# Method development for MR-guided HIFU applications in oncology

*Document status and date:*
Published: 28/10/2020

*Document Version:*
Publisher's PDF, also known as Version of Record (includes final page, issue and volume numbers)

*Please check the document version of this publication:*

• A submitted manuscript is the version of the article upon submission and before peer-review. There can be important differences between the submitted version and the official published version of record. People interested in the research are advised to contact the author for the final version of the publication, or visit the DOI to the publisher's website.
• The final author version and the galley proof are versions of the publication after peer review.
• The final published version features the final layout of the paper including the volume, issue and page numbers.

Link to publication

# METHOD DEVELOPMENT
## for
## MR–GUIDED
## HIFU APPLICATIONS
## in
## ONCOLOGY



**Lukas Christian Sebeke**

# Method Development for MR-guided HIFU Applications in Oncology

*To remember a friend*

**Lukas Christian Sebeke**

# Method Development for MR-guided HIFU Applications in Oncology

PROEFSCHRIFT

ter verkrijging van de graad van doctor aan de Technische Universiteit Eindhoven, op gezag van de rector magnificus prof.dr.ir. F.P.T. Baaijens, voor een commissie aangewezen door het College voor Promoties, in het openbaar te verdedigen op woensdag 28 oktober 2020 om 16:00 uur

door

**Lukas Christian Sebeke**

geboren te Hannover, Duitsland

Dit proefschrift is goedgekeurd door de promotoren en de samenstelling van de promotiecommissie is als volgt:

Voorzitter:             prof.dr. M. Merkx

1e promotor:          prof.dr. H. Grüll

Copromotor(en):     prof.dr. P.A.J. Hilbers
                     dr.ir. E. Heijman (Philips Research)

Leden:                prof.dr. J.H. Hwang (Stanford University)
                     prof.dr.Med. D. Maintz (Universitätsklinikum Köln)
                     dr.ir. R.G.P. Lopata
                     prof.dr.ir. W.P.M.H. Heemels

# TABLE OF CONTENTS

# Chapter 1

## Introduction

# THERMAL THERAPY FOR CANCER TREATMENT

At present, the National Cancer Institute divides cancer treatments into the categories surgery, radiation therapy, chemotherapy, immunotherapy, hormone therapy, stem cell transplant, targeted therapy, and personalized medicine [1]. The variety of existing approaches and especially the development of precision medicine [2] reflects that cancer is a multi-factorial disease. Hence, it is a highly personal condition which requires careful deliberation and weighing of treatments with oftentimes debilitating side effects. Thermal therapies take on a special role in this setting.

One of the roles of thermal therapy is that of a thermal knife [3]. The application of temperatures in excess of 56 °C, which is usually referred to as ablation [4], rapidly induces coagulative necrosis and/or thermal fixation. Unlike conventional surgery, which invasively excises locally confined tumors, the malignant tissue is destroyed *in-situ* [5,6]. This allows the body to break down the necrotic tissue by itself and enables the treatment of some tumors that may not be resectable [7]. If supported by immunomodulation, the remaining fragments of malignant cells may even lead to a systemic response in a so-called abscopal effect [8,9]. The invasiveness of the techniques used for ablation ranges from minimally invasive to completely noninvasive [4], although some thermal ablative techniques are also applied during surgery [10].

The application of temperatures between 40 and 44 °C is referred to as mild hyperthermia [11]. While hyperthermia may produce a cytotoxic effect by itself depending on the temperature and duration [12], mild hyperthermia is mostly used as an adjuvant treatment to chemotherapy [13] and radiotherapy [14]. Several clinical trials and meta-analyses have found that the addition of hyperthermia acts as sensitizer for these treatments, enhancing their effectiveness [15-22]. The thermal enhancement of radiotherapy arises from the inhibition of DNA repair mechanisms [23,24] and the stimulation of perfusion in the tumor. The latter effect results in the reoxygenation of poorly perfused and thereby hypoxic tumor regions [25,26], which are highly resistant to radiotherapy [27]. The effectiveness of chemotherapy is likewise enhanced *via* the stimulation of blood flow, as well as enhancement of vessel permeability, both improving the availability of the drug in malignant tissue [28-30]. The potency of thermal enhancement of chemotherapy depends on the drug and varies between independent, additive and synergistic [31].

Both in ablation and hyperthermia, the outcome of the treatment depends on the thermal history of the treated tissue. It was recognized early on that the surviving fraction of cells undergoing a heat treatment follows an Arrhenius relationship [32]. This led to the development of the thermal dose concept [33], which is still in use today and enables the comparison of results among studies utilizing different equipment and heating

regimes [34]. The thermal dose $D$ accumulated between the start of the treatment $t_0$ and a timepoint $t$ depends on the temperature evolution $T(t')$ [33]:

$$D(t) = \int_{t_0}^{t} R^{\frac{43\,°C - T(t')}{1\,°C}} dt'$$

$$R = \begin{cases} 0.5, & T > 43\,°C \\ 0.25, & T \leq 43\,°C \end{cases}$$

[1]

The break in the Arrhenius curve at around 43 °C is thought to arise from the gradual formation of thermotolerance in cells treated at lower temperatures [35]. It is important to note that the value of $R$ and the breakpoint temperature are a convention and may vary situationally, i.e., the thermal dose required to induce cell death depends on the type of cells or tissue treated. It was found, however, that a thermal dose of 240 **C**umulative **E**quivalent **M**inutes at 43 °C (CEM43) is sufficient to induce coagulative necrosis in most tissues and is therefore often used as a threshold to predict necrosis [36,37]. For ablation treatments, this translates to a treatment time of less than a second at 57 °C. Hyperthermia treatments are not aimed at reaching 240 CEM43 in a single application. Nonetheless, a positive correlation between the complete response rate and the delivered thermal dose has been observed in many studies [34,38-41]. In cases where this correlation was not found, inadequate heating techniques were often cited as the cause [34].

## MEDICAL HEATING TECHNOLOGIES

One of the oldest references to thermal therapy is found in the Edwin Smith Surgical Papyrus, which is dated to a period around 1600 BC [42,43]. It mentions the use of cautery and hot stones, which in modern terms could be classified as medical devices for conductive heating, i.e., devices that rely on the diffusion of heat into the tissue to effect a temperature increase. The most recent examples of techniques utilizing conductive heating employ magnetic nanoparticles and rapidly switching magnetic fields [44,45] to heat adjacent tissue. Exploratory clinical studies with magnetic particles as heat source have shown feasibility [46-48] and have explored a potential survival benefit [49] in patients with recurrent glioblastoma multiforme. However, the control this technique provides over the heating rate and its spatial distribution is currently severely limited [48]. Consequently, they are suited neither for the controlled induction of mild hyperthermia nor for uniform ablation. Furthermore, the magnetic nanoparticles injected into the patient are degraded only very slowly and will be retained for a long time, which precludes the use of magnetic resonance imaging (MRI) in the target region in the future

due to the induced imaging [49]. In addition, other metal (e.g. dental implants) must be removed from the treated body part as the use of a switching magnetic field would lead to unintentional heating [49]. Therefore, broad adoption of magnetic nanoparticles for thermal therapy currently appears unlikely.

Hyperthermic perfusion as a heating method is related to conductive heating as it also relies on the diffusion of heat into the malignant tissue. However, instead of introducing heated objects or particles, a warm solution of a cytostatic is circulated through the vascular system of an isolated limb (isolated limb perfusion, ILP [50]), the peritoneum (Hyperthermic IntraPeritoneal Chemotherapy, HIPEC [51]), the thorax (Hyperthermic IntraThoracic Chemotherapy, HITHOC [52]), a cavity, or a lumen (Hyperthermic IntraVEsical Chemotherapy, HIVEC) [53]. Within their respective niche, ILP, HIPEC and HITHOC have improved the clinical outcomes of patients significantly compared to control treatments [54-59], while a pilot study of HIVEC has concluded with promising results [60]. However, due to the slow diffusion of drugs into the tissue [61] and the sharp drop of the temperature away from the perfused space [62], all approaches except ILP are limited to the treatment of small tumors that are in direct contact with the circulated solution. In the case of bladder cancer, the limited penetration depth of conductive heating can be augmented *via* the addition of an intracavity microwave antenna [63].

Electromagnetic waves, such as microwaves, are one of the two approaches which allow for the creation of temperature elevation at a distance from a medical device. Instead of bringing a heated body or fluid into close contact with the intended treatment volume, the required energy is delivered to the tissue in the form of electromagnetic radiation where it dissipates and thereby effects an increase in temperature [64]. One mode of use is superficial hyperthermia, in which electromagnetic radiation is applied directly to the skin [65]. The used wavelength lies between infrared and microwaves [66,67], depending on the required penetration depth. Due to the strong attenuation of electromagnetic waves at these wavelengths, this technique is not used for tumors that extend to more than a few millimeters deep under the skin [67]. For the treatment of tumors that are seated deeper, electromagnetic interstitial heating devices, i.e., antennas in the form of needles, can be inserted into or close to the intended treatment volume [68,69]. These interstitial devices are usually operated at high output powers to ablate the surrounding tissue volume, though the use for hyperthermia has also been demonstrated [70]. The ablation of tissue using these devices is referred to as radiofrequency ablation (RFA) and microwave ablation (MWA). RFA is already in regular use for the treatments of metastases in the liver [10].

For the application of hyperthermia to deep seated tumors, extracorporeal radiative phased array systems are used [11]. Here, the antennas are arranged around the patient and coupled to the patient's skin *via* water boluses. The center of heating can be chosen *via* the

antennas' relative amplitude and phase [71]. The applied frequencies result in heating foci with diameters between 10 and 15 cm [72]. This allows the induction of mild hyperthermia in exceptionally large tissue volumes, referred to as locoregional hyperthermia. These devices have been successfully used in numerous clinical trials demonstrating the added benefit of HT to radio, chemo- or radiochemotherapy [15,16,19,20,73-75]. However, the long wavelengths necessary for this technique also inherently limit the capability to create uniform heating patterns and to counteract localized heat sinks like blood vessels. Apart from pre-heating of blood entering the target area by enlarging the heated volume [76], this problem cannot be addressed using electromagnetic radiation as wavelengths on the required millimeter scale are strongly attenuated in water-rich tissues [77].

Currently, the only means for controlling temperature on such small scales noninvasively is therapeutic ultrasound. When targeting deep tissue regions with extracorporeal transducers, therapeutic ultrasound is usually applied at frequencies around 1 MHz, which amounts to a wavelength of about 1.6 mm in muscle tissue [78]. Compared to electromagnetic radiation of this wavelength, the attenuation coefficient of ultrasound is lower by a factor of about 0.3 [77,79]. This enables the creation of very small heating foci deep inside the body with the help of extracorporeal ultrasound transducers [80]. This technique is referred to as High Intensity Focused Ultrasound (HIFU). Extracorporeal HIFU transducers are bowl-shaped, which leads to constructive interference at the geometrical focus by default. In many modern transducers, the bowl additionally is populated by a high number of independently operating piezo elements, which also allows the deflection of the focal region from the geometrical focus in three dimensions [81]. A distinguishing feature of HIFU is the capability to noninvasively apply both local hyperthermia and thermal ablation in a single treatment [82-84]. Higher ultrasound frequencies of up to 10 MHz are applied in interstitial ultrasound heating devices, which aim at treating tissues closer to the transducer. This technique is under investigation for the focal and whole-gland treatment of prostate cancer [85]. For applications that require even higher precision like the treatment of glaucoma in the eye, miniature HIFU transducers operating at frequencies of up to 21 MHz have been developed [86,87].

## THE DEVELOPMENT OF NONINVASIVE THERMAL THERAPY USING FOCUSED ULTRASOUND

The biological effects of high-intensity ultrasound waves on living organisms were investigated as early as 1927 by Wood and Loomis [88]. They described the mechanical destruction of cells by constructively interfering ultrasound waves and speculated that the applied ultrasound may lead to heating inside organisms. They used a planar

piezoelectric emitter and plates of glass or metal fixed in parallel to the emitter to generate constructive interference, resulting in planar standing waves between the emitter and the reflector plates. The first article discussing a device for focusing ultrasound waves in a point was published in 1935 by Johannes Gruetzmacher [89]. Instead of a planar emitter, he presented two piezo crystals in the form of concave mirrors. According to his article, this resulted in a 150-fold enhancement of the ultrasound intensity compared to the intensity measured near the emitter. Gruetzmacher already speculated that such transducers may prove valuable for clinical applications in his original publication.

The first article presenting the effect of high-intensity focused ultrasound (HIFU) on tissue was published in 1942 by Lynn *et al.* [90], who showed that HIFU can be used to induce coagulation in *ex-vivo* bovine liver without harming the prefocal tissue. A phase of preclinical research followed, focusing mainly on fundamental research concerned with the effect of focused ultrasound on the brain [91-93]. This finally led to the first clinical applications for the treatment of Parkinson's disease reported in the late 1950s by Meyers and the brothers Fry [94,95]. The results of these interventions were promising, with a large proportion of patients reporting a sustained relief of rigidity symptoms. However, verification of the HIFU focus location was not yet possible and the treatment still required a craniotomy. Simultaneously, a drug for the treatment of Parkinson's disease, L-DOPA, became available, offering a treatment that was much more acceptable for patients [96]. Therefore, HIFU treatment of neurological diseases was not clinically adopted. Instead, the 1960s and 1970s saw the first oncological applications of HIFU in thyroid, breast, and brain tumors [97,98] as well as a brief adoption in eye surgery [99]. In this period, Francis Fry also presented a first HIFU system with an integrated sonography probe [100], pioneering noninvasive image-guided therapy.

The next big step in the development of image-guided HIFU intervention began with the publication of the first image of a human body created *via* nuclear magnetic resonance (NMR) in 1977 by Damadian *et al.* [101]. From their technique, magnetic resonance imaging (MRI) was developed. This allowed Hynynen *et al.* to present the first combination of HIFU with a magnetic resonance imaging scanner in 1993 [102]. This was closely followed by the invention of the proton resonance frequency shift (PRFS)-based MRI-thermometry by Ishihara *et al.* and De Poorter *et al.* in 1995 [103,104], which would facilitate the first completely noninvasive, feedback-controlled hyperthermia treatment presented in 1999 by Vimeux *et al.* [105]. Apart from these resounding successes, the 1990s also marked the beginning of broad commercialization of focused ultrasound technology with the founding of two prominent manufacturers of HIFU equipment, Chongqing Haifu and Insightec, as well as the resurgence of interest in HIFU for neurological applications with the demonstration of transcranial HIFU by Kynynen and Jolesz [106].

The technological leaps and the advent of commercially available HIFU systems in the 1990s was followed by the formation of the first organization dedicated to the support

and promotion of HIFU research in 2001, namely the International Society for Therapeutic Ultrasound (ISTU), and the formation of the Focused Ultrasound Foundation (FUSF) in 2006, which is dedicated to accelerating of the adoption of HIFU into clinical practice. Since then, the number of research articles published each year reporting on focused ultrasound has been increasing rapidly, along with the breadth of clinical applications of HIFU.

## CLINICAL APPLICATIONS OF MR-HIFU

Focused ultrasound has great potential for a wide variety of indications. In 2020, more than 100 clinical applications of this heating method have reached at least the stage of pilot trials [107]. MR-HIFU, as a subspecies of focused ultrasound techniques, is the only medical heating modality that enables the noninvasive application of both hyperthermia and ablation to both deep and superficial tissue regions. The first two applications for which MR-HIFU was approved in the EU were uterine fibroids and painful bone metastases [108]. These two applications exemplify two core capabilities of HIFU, tumor debulking and pain palliation, which are of importance for a promising upcoming application, i.e., pancreatic cancer. Here, we briefly explore these three conditions and the role of MR-HIFU in their treatment.

### Uterine Fibroids

Uterine fibroids (UF) are extremely common. The GDB 2017 [109] study estimates a global prevalence of 139 million, but there are large regional differences as ethnicity has a strong influence on the incidence and the severity of the symptoms [110,111]. Approximately 15 % to 30 % of UF are symptomatic [112]. Symptoms of UF include abnormal uterine bleeding, anemia, discomfort, urinary incontinence, and potentially severe problems related to reproduction [113].

The options for treatment can be divided into pharmaceutical management, inter-ventional radiology (selective uterine artery embolization and HIFU), and surgical management (hysterectomy, myomectomy, radiofrequency ablation, and endometrial ablation) [112]. Pharmaceutical management is often the first step, but it is aimed primarily at reducing and mitigating uterine bleeding [112]. Further steps depend on the patient's situation and preference. The most commonly applied treatment is hysterectomy, i.e., the surgical removal of the uterus, as it has the lowest rate of needing reintervention and is associated with a low rate of complications [114,115]. However, the recovery time of about four weeks after open hysterectomy is substantial. This can be shortened to about 3 weeks if a minimally invasive approach is used [116], but the required equipment is not yet universally available, and a hysterectomy precludes future pregnancy [117]. As the

mean age of childbearing in Europe has been increasing steadily since 1985 [118], the wish to retain one's uterus will very likely continue to become more prevalent. Furthermore, the emotional impact of a hysterectomy can also be a reason to reject the procedure.

The most commonly used fertility-preserving treatments are myomectomy, i.e., the surgical removal of fibroids, uterine artery embolization (UAE, blocking of the fibroids' blood supply) and thermal ablation *via* HIFU or RF. A recent review found that in the published literature, myomectomy still exhibits the highest rate of live births (75.6 %), followed by thermal ablation (70.5 %) and UAE (60.6 %) [119]. Fertility data on HIFU ablation specifically is still scarce due to the relatively recent introduction of the technology and the FDA's explicit ban of offering HIFU to patients desiring to preserve fertility until 2015 [120]. However, initial results are promising [121]. As opposed to myomectomy, HIFU-ablation is a completely noninvasive treatment without the need for general anesthesia and can be performed on an outpatient basis [122]. This results in hospital stays and median recovery times of only two days [123], which is extremely short compared to the average recovery time of 22.1 days for myomectomy [124,125]. The tumor shrinkage after HIFU ablation occurs over a timespan of up to one year and appears to depend on the fraction of the UF that is nonperfused immediately after the treatment [126]. On average, a shrinkage to approximately 60 % of the original volume can be expected [127,128]. Even though there seems to be a learning curve with the application of HIFU [128], one of the first clinical studies by Funaki *et al.* already showed a considerable and sustained decrease in the symptom severity score (SSS) to an average value that was close to the SSS of a healthy control group. HIFU ablation of UF is also not associated with severe adverse events [123,128] and may even be more cost effective compared to other treatments [129]. Consequently, MR-HIFU is being seen as a tool with high potential for the fertility-preserving management of uterine fibroids [130].

**Bone metastases**

Bone metastases (BM) frequently develop from breast cancer (73 % of cases at time of death) and prostate cancer (68 % of cases at time of death), which respectively are the cancer types with the highest incidence in women and men [131], as well as from a number of other common solid tumors [132]. The mean survival time after the diagnosis of BM in prostate- and breast cancer patients lies between two and three years [133-135]. BM can manifest as osteolytic, i.e., destroying normal bone, or osteoblastic, i.e., leading to the abnormal formation of additional bone, or mixed. BM from prostate cancer are mostly osteoblastic [136], while BM arising from breast cancer mostly manifest as osteolytic but can also show mixed or osteoblastic behavior [137]. The symptoms of BM include pain, hypercalcemia, fractures, spinal cord compression, and spinal instability [138].

Treatments focus primarily on symptom prevention and palliation and the prevention of BM spread. For the latter, the administration of bisphosphonates has shown

promise, prolonging the disease-free survival in breast cancer patients [139,140]. In terms of symptom prevention, bones are reinforced *via* medication aimed at supporting bone regeneration and eligible patients can undergo surgery to reinforce affected bones [138]. BM-related pain may originate from inflammation or mechanical stress, either exerted by the tumor directly or due to strain on weakened bones [141]. As a first step, this pain should be managed pharmaceutically [142,143], as antineoplastic treatments only take effect after several weeks. Depending on whether the disease is localized or diffuse, the choice of antineoplastic treatment is most often between palliative radiotherapy (localized disease) or radiopharmaceuticals (diffuse disease) [144,145].

For management of pain induced by localized BM, HIFU may offer an alternative to palliative radiotherapy (RT). RT yields a median time to response of two weeks and may even take up to nine weeks to take effect [146,147]. The median reported complete response rate is 26 % (range: 13 % - 58 %), the median reported overall response rate is 71 % (range: 53 % - 78 %), and the median reported rate of acute toxicity is 29 % (range: 5 % - 37 %) [148]. Acute toxicities of RT include nausea, vomiting, diarrhea, skin reactions, tiredness and a temporary increase in pain at the tumor site [149]. If no pain palliation is achieved, patients may undergo repeated irradiation. However, re-irradiation appears to be less effective [150] and radiation toxicity may compound. The mechanism of pain relief in RT is not yet entirely clear [149].

The analgesic effect of HIFU therapy for painful bone metastases stems from the denervation of the periosteum and from tumor debulking [151,152]. Thus far, two prospective clinical studies have been published with encouraging results. Hurwitz *et al.* reported complete and overall pain palliation responses in 23.2 % and 64.3 % of the 112 patients enrolled in the study, some of which had previously undergone RT without complete pain relief [153]. Napoli *et al.* even reported complete and overall response rates of 72.2 % and 88.9 %, respectively, albeit in a smaller cohort of 18 patients [152]. Napoli *et al.* also reported the complete absence of adverse events, while Hurwitz *et al.* reported adverse events in 45 % of patients, 60.3 % of which resolved on the day of treatment and may in a large part have been prevented by stronger analgesia during treatment. The most frequent adverse event was sonication pain (32.1 %), followed by pain arising from patient positioning (8 %). Other less frequent events included skin numbness (0.9 %), myositis (0.9 %), skin burns (1.8 %), fractures (1.8 %), neuropathy (1.8 %) and postprocedural pain (4.5 %).

The toxicity profile of HIFU compares favorably with RT [153,154] and as HIFU does not rely on ionizing radiation, repetition of the treatment is unproblematic. Pain relief sets in within the first days after treatment, rather than weeks [146,153]. The rapid onset of pain relief and the absence of ionizing radiation is especially noteworthy, as many patients suffering from BM are both in urgent need of effective analgesia and may still have several years to live. Further clinical evidence is needed to establish HIFU as an alternative

1

to RT, but the evidence accumulated so far paints a very favorable picture with potential benefits in time to pain relief, response rate, and toxicity profile. The effectiveness of HIFU for pain palliation is being recognized and further analgesic applications are explored, such as osteoid osteoma, desmoid tumors, osteoarthritis, neuropathic pain, and pancreatic cancer [7,108,155-159].

## Upcoming application: Pancreatic cancer

The first established applications of HIFU are treatment of benign diseases such as UF or osteoid osteoma, neurological diseases, or in a palliative setting such as pain treatment associated with bone metastasis. Treatment of malignant cancers has been explored for almost all types of solid tumors that are acoustically accessible, such as prostate, breast, liver, kidney, as well as pancreatic cancer [107]. Especially for pancreatic cancer, HIFU may offer a unique treatment option as first clinical studies with US-guided HIFU suggest [7,160,161].

Compared to other cancers, pancreatic cancer (PaC) has a relatively low age-standardized incidence at 7.7 per 100,000 people in Europe in 2018, putting it at 13th place. Nonetheless, PaC was the 4th most likely cause of cancer-related death in Europe and caused 4.5 % of all cancer fatalities worldwide in that year [162]. Its 5-year survival rate is the lowest of any cancer and while the mortality of most other cancers has been falling over the last thirty years, the mortality of PaC has risen and may become the second leading cause of cancer related death in the USA by 2030 [131,163,164]. This trend will not remain confined to the USA. The median age of diagnosis of PaC is 71 years [165]. The average global life expectancy at birth has passed this threshold in the latter half of the past decade and is predicted to continue to increase, which could lead to a surge in the global mortality of PaC [118]. The high mortality of PaC is attributed to the interplay of several unfavorable characteristics. It is typically diagnosed at a late stage due to its unspecific symptoms and their late onset [166]. Therefore, the tumor has often already formed metastases and encased the adjacent arteries, making resection impossible [167]. Even in patients who undergo resection of the primary tumor, median survival is extremely short due to the high morbidity of the procedure and frequent recurrence [168]. The expanding tumor mass exerts growing pressure on surrounding structures, leading to duodenal and biliary obstruction, nausea, and pain in the abdomen and back [169,170].

The treatment approach in PaC heavily depends on the stage of the disease at the time of diagnosis and the patient's status. Resection with subsequent chemotherapy is the only curative option at the moment and only about one in six patients is eligible [169]. This leaves palliative chemotherapy as the only option for the majority of patients, as a recent study did not find a survival benefit of added radiotherapy [171,172]. However, pancreatic ductal adenocarcinoma (PDA), which is the most common type

of PaC, forms a dense matrix of stromal cells, inhibiting the penetration of systemically administered drugs into the tumor, adding to its high resistance to chemotherapy [173]. mFOLFIRINOX, a combination of oxaliplatin, irinotecan, leucovorin, and fluorouracil has recently shown a significant and considerable advantage over the previous standard of care, gemcitabine, but many patients are considered too sick to cope with the extreme toxicity and side effects [174]. Medicinal pain management is often insufficient and is therefore supported by celiac plexus block or celiac plexus neurolysis [169], but these techniques have not demonstrated a significant benefit over a placebo treatment in a double-blinded randomized control trial [175]. PaC patients are therefore in urgent need for a treatment option that reliably alleviates pain, reduces tumor volume, and induces minimal additional toxicity. These are all hallmarks of HIFU, as has already been shown in its application in uterine fibroids and bone metastases.

Consequently, HIFU is being explored as a treatment modality for pancreatic cancer in China since the early 2000s [176-181] and has since sparked interest in Europe and the US [7,160,182,183]. The accumulated evidence shows that HIFU ablation of pancreatic tumors induces long-lasting pain relief in about 4 of 5 patients [179,180,184-192], and improves local tumor control [180,186,188,190]. The mechanism by which HIFU induces pain relief is not yet clear. It has been speculated that the analgesic effect may stem from the ablation of nerve fibers in the tumor, the inactivation of the solar plexus, the shrinkage of the tumor, and/or the reduction of the inflammatory environment *via* the expression of cytokines [7,193]. A recent study of Marinova *et al.* [7] in fifty pancreatic cancer patients (stages three and four) found that the pain relief already began at the one-week follow up after HIFU ablation and thereby preceded the shrinkage of the tumor. The reported pain scores furthermore continued to improve over several months, possibly suggesting a combination of the mechanisms mentioned above. The same study also found that the patients experienced a swift and sustained decrease of the impact the pain had on their daily life, and the complete absence of major or long-lasting side-effects [7]. The comparison with historical data also suggests a survival benefit over chemotherapy alone [7,160,194]. Independent of whether the survival benefit of HIFU ablation will be confirmed or not, it is already an extremely valuable modality for analgesia in pancreatic cancer patients today.

Clinical studies concerning the HIFU-ablation of pancreatic cancer have mostly been performed using HIFU under sonography guidance [185], while examples for MR-HIFU are scarce [195,196]. In treating abdominal organs like the pancreas, sonography has the advantage that acoustically opaque targets like ribs or pockets of air and solids in the bowels can be identified directly and the high frame rate allows real-time monitoring of organ motion. If such objects intersect the HIFU beam, the ultrasound is strongly absorbed and reflected, leading to heating outside of the target volume. The main drawback of sonography guidance for thermal therapy is the lack of reliable temperature

feedback beyond 50 °C [197]. The operator must therefore rely on a-priori estimations of the required energy and changes in the echogenicity and elasticity of ablated tissue to control exposure [197]. The presence of nearby critical structures furthermore limits the fraction of the tumor that can be ablated safely without temperature feedback [198]. This directly impacts the pain palliation that can be achieved, as the ablated tumor fraction correlates with the pain response [196]. Magnetic resonance imaging is a natural solution to this problem as MR-thermometry is not limited in this fashion, potentially improving patient safety and the palliative effect. Reliable temperature feedback also allows the application of local hyperthermia for the intratumoral release and enhancement of chemotherapy, which might help to overcome the high resistance to chemotherapy of PaC [84].

## GUIDANCE, MONITORING AND CONTROL OF HIFU TREATMENTS UNDER MAGNETIC RESONANCE IMAGING

Magnetic Resonance (MR) guidance yields high soft-tissue contrast [199], allows near-real time volumetric temperature measurements [103], and can visualize non-perfused areas [200]. This provides interventional radiologists with a potent tool for treatment planning, treatment monitoring and post-procedural evaluation of treatment success. Since the first demonstration of an MR-HIFU concept by Hynynen *et al.* in 1993 [102], several commercial platforms capable of delivering HIFU under MRI guidance have become available. The most prominent clinical MR-HIFU devices are the ExAblate® (Insightec, Haifa, Israel) and the Sonalleve® (Profound Medical, Mississauga, Canada) systems. Both systems employ a phased array transducer that is integrated into an MRI patient table and therefore offer near-real time MR thermometry to monitor ablation. The major difference between the systems is that the Sonalleve® transducer allows the treatment of larger volumes using electronic beam steering in all directions and utilizes MR-thermometry measurements in a closed feedback loop to make online adjustments to the sonication protocol. Though the CE label for both systems is currently restricted to ablative treatments, the Sonalleve system is inherently capable to induce local hyperthermia over a prolonged timespan *via* a controller that uses MR-thermometry feedback [83].

**Thermometry**

The cornerstone of MR-HIFU Hyperthermia treatments and controlled ablation is the accurate, near-real time, and completely noninvasive temperature mapping enabled by MRI. While many parameters that can be measured *via* MRI are temperature dependent [201-206], the proton resonance frequency of water molecules is the most widely used in MR-thermometry. This is due to the high attainable framerate and the proton resonance frequency's linear evolution with temperature, which is largely independent of tissue type [103,207].

The temperature dependence of the resonance frequency of protons in water molecules was first discovered by Hindman in 1966 [208] and its use for temperature monitoring was first investigated by Ishihara *et al.* and De Poorter *et al.* in 1995 [103,104]. It arises from the change in the magnetic field experienced by the water proton, which in turn is temperature dependent. The local magnetic field $B_{loc}$ depends on the external magnetic field $B_0$ and the shielding that is mediated by the chemical environment:

$$B_{loc} = B_0 \cdot (1 - \sigma) \qquad [2]$$

where $\sigma$ is called the screening- or shielding constant. It varies as an approximately linear function of the local temperature. This behavior arises from the deformation and weakening of the hydrogen bond to the oxygen atom in the water molecule [208,209]:

$$\sigma(T) = \alpha T \qquad [3]$$

In the range between -15 °C and 100 °C, the proportionality constant $\alpha$ is about $-1.03 \pm 0.02 \cdot 10^{-8} \, {}^1/_K$. This results in a linear dependence of the protons' Larmor frequency $\omega$ on temperature:

$$\omega(T) = \gamma B_0 (1 - \sigma) \qquad [4]$$

where $\gamma$ is the gyromagnetic ratio of the proton. This relation can be used to calculate the local temperature either *via* the difference in frequency to a temperature-independent reference peak like the proton peak in lipids (spectroscopic thermometry) [210] or *via* the difference compared to an earlier timepoint [103]. The latter method is commonly referred to as proton resonance frequency shift (PRFS) thermometry. While it is more susceptible to measurement artifacts caused by changes in the magnetic field than spectroscopic thermometry, it is much faster and therefore it is the method of choice for real-time applications.

In PRFS thermometry, the difference in Larmor frequency is determined *via* the phase shift in gradient-recalled echo (GRE) images. Before the start of the treatment, the phase distribution in thermal equilibrium $\varphi_0$ is measured, referred to as the baseline. $\varphi_0$

is subtracted from the phase distribution $\varphi(T)$ at subsequent timepoints to eliminate the influence of other parameters affecting the Larmor frequency:

$$\Delta T = \frac{\varphi(T) - \varphi_0}{\gamma \alpha B_0 TE}$$

[5]

where $TE$ is the echo time of the used GRE sequence. For this formula to be valid, $B_0$ must remain constant, which is not the case as the main magnetic field of the MRI slowly changes over time due to imperfections in the superconducting material and due to the heavy use of gradients in GRE sequences. Furthermore, motion of the patient also leads to an immediate alteration of the local magnetic field. The former problem can be addressed *via* phase drift correction (PDC). In PDC, the induced offset is identified by fitting a two-dimensional polynomial to the spatial distribution of phase difference in areas that have remained at a constant temperature, like distant tissue or reference phantoms [104]. Solutions to the problem of motion include the use of multiple baselines for different motion states [211], interpolation of the phase distribution from unheated tissue into the heated area [212], modelling of the magnetic field distribution [213], and the suspension of motion *via* phases of induced apnea [214].

### Control in MR-HIFU treatments

Before noninvasive real time feedback *via* MR-thermometry was possible, treatment planning routines for MR-HIFU hyperthermia were developed that are similar in nature what is still used for the preparation of hyperthermia treatments *via* radiative phased array systems today [215]. The basic approach was to develop an exact patient tissue model and to deliver an upfront calculated ultrasound energy to the target tissue to achieve the desired heating. However, the results indicated that heating could not be predicted accurately, and that multiple potential points of failure related to inadequate model detail and anatomical deviations were present [215]. Therefore, automated control systems aimed at completely noninvasive temperature- and thermal dose regulation using MR-HIFU were developed shortly after the MR-thermometry was introduced in 1995 [103]. While they showed excellent control, the tissue volume that could be heated uniformly with these approaches was only on the scale of a few millimeters due to the tight focusing of energy in HIFU [105,216,217]. As the point-by-point method of sonicating one focal volume at a time is time-consuming and wastes a large proportion of the energy applied to the patient [82], a method of extending the heated volume by repositioning the HIFU transducer laterally to the transducer axis in a spiral trajectory optimized for uniform heating was developed early on by Salomir *et al.* [218]. In 2004, Mougenot *et al.* combined this method with a model-based controller also developed by Salomir *et al.* [217,219] and

later extended the approach to a three-dimensional target volume [220]. However, the heated volumes were inherently limited by the need of physically moving the transducer to address the entire target location. This restriction was loosened with MR-compatible phased array transducers capable of deflecting the focal volume by up to 8 mm from the natural focus using electronic beam steering [82]. This enabled the controlled heating of a target volume up to 16 mm in diameter while keeping the transducer stationary. This was first exploited by Enholm *et al.*, who designed a control algorithm for ablation that would switch to a new circular focus trajectory with a larger radius once a temperature or thermal dose threshold inside the previous radius is met [221]. The larger focus deflection also enabled the implementation of the first control scheme for hyperthermia which allowed the simultaneous heating of clinically relevant volumes of up to 58 mm in diameter [83]. In that approach, Tillander *et al.* regulated the temperature in each of seven sub-volumes using a binary feedback algorithm, which would enable or disable heating to each point on a predefined grid based on a temperature threshold. Once a sub-volume had reached the target temperature, the transducer would be repositioned to the sub-volume with the lowest mean temperature.

It is now possible to both induce controlled ablation and hyperthermia using MR-HIFU. A few challenges remain, however, mainly concerning the management of near-field heating in prolonged ablation treatments and the compensation of local heat sinks in hyperthermia treatments. These have both been approached using Model Predictive Control (MPC) [222-225]. MPC algorithms minimize a given objective function, which reflects a goal like the minimization of the difference between the actual temperature and a target temperature, by varying the available control inputs while maintaining a set of constraints. These constraints always include the model constraint, which is a representation of how the controlled system behaves over time and in response to the control inputs. Further constraints that represent safety thresholds or limits to the maximum power of a control input can also be included. Each time a new measurement of the system's state becomes available, the MPC calculates with which inputs the objective function becomes minimal over a given number of future timesteps, enabling the MPC to anticipate the ramifications of applied control actions. Finally, the control action for the upcoming timestep is applied and the next feedback is awaited. The MPC scheme has been used by de Bever *et al.* to minimize the time required to ablate a given volume while limiting the thermal buildup in the near field [223]. It is furthermore used in this thesis to improve upon the binary hyperthermia controller of Tillander *et al.* by calculating the optimal distribution of heating power to achieve a highly uniform temperature distribution [224].

## AIM OF THIS THESIS

The overall **aim** of this thesis is the clinical translation of MR-HIFU hyperthermia and ablation for the treatment of pancreatic cancer and other malignant tumors that are refractory to chemo- and radiotherapy. The envisioned treatment scheme comprises the combination of hyperthermia-induced drug delivery and the subsequent thermal ablation of the tumor. This scheme would allow to treat and sensitize the tumor border zones and other regions that cannot be ablated safely. In this thesis several steps towards that goal are addressed, such as the improvement of MR-HIFU hyperthermia technology and the establishment of a suitable clinical workflow for the ablation of the pancreas.

In **chapter 2**, a preclinical feasibility study on the MR-HIFU ablation of the pancreas in a healthy swine model is presented. This animal study was set-up and conducted with the aim to develop a suitable clinical workflow, to evaluate potential side effects, and to identify technological challenges that may be encountered. The study included the design and application of an acoustically transparent compression device that facilitates access to the pancreas *via* the displacement and compression of the bowels. The effect of this compression device on the acoustic beam path is evaluated on MR images. Furthermore, the predictive power for the size of the induced thermal lesions of MR-thermometry, contrast enhanced MRI, and the applied energy is analyzed. The study serves as a feasibility study to obtain regulatory approval for a planned clinical trial scheduled for start in early 2021. The implications of using a swine model for clinical translation are discussed in detail.

In **chapter 3**, a newly developed model-based controller for the application in MR-HIFU hyperthermia is described in detail. The aim was to develop a controller which would fully leverage the control MR-guided HIFU provides over the spatial distribution of heat in a target tissue to create highly uniform temperature distributions. As the controller relies on a computational model of the target tissue to predict the development of the temperature distribution in response to HIFU heating, its sensitivity to potential model mismatches was thoroughly investigated both *in-silico* and *in-vitro*. Finally, its performance is compared to the current state-of-the-art MR-HIFU hyperthermia controller in a perfused tissue-mimicking phantom.

In **chapter 4**, the performance of the developed model-predictive controller is evaluated in a series of large animal experiments performed in a healthy swine model. During the experiments, target volumes were defined in the biceps femori of the animals and were heated to hyperthermic temperatures for up to thirty minutes using the newly developed controller. The performance of the controller was assessed using MR-thermometry data. The effect of blood vessels acting as local heat sinks on heating power allocation was evaluated using a thermal model and contrast enhanced MRI.

Furthermore, the influence of hyperthermia on the perfusion and effect of the perfusion on the performance of the controller was investigated.

In **chapter 5**, the application of MR-HIFU based hyperthermia as a trigger for local drug delivery in combination with temperature sensitive liposomes is presented. The study was performed in healthy pigs with the biceps femori as target tissue. Hyperthermia was maintained for 30 minutes using the model predictive control algorithm. The aim was to establish a clinically translatable protocol for MR-HIFU-induced drug delivery of doxorubicin using temperature sensitive liposomes for a planned future clinical trial. Thus, aspects of possible adverse immune reaction to the infusion of liposomes and their management as well as the entire treatment workflow were important aspects of this study. A further important aspect of the study was the analysis of the pharmacokinetics and biodistribution of doxorubicin and the liposomal carrier, and the comparison of the doxorubicin concentration in treated and untreated muscle volumes in particular. The study concludes with an analysis of the effect the scheduling of the infusion and hyperthermia treatment has on the drug dose accumulated in the target area.

In **chapter 6**, a general discussion is presented, starting with a concise statement of the rationale for the research presented in this thesis. The obtained results are summarized, and their implications are discussed. Finally, an outlook on the clinical translation of MR-HIFU ablation for pancreatic cancer and MR-HIFU hyperthermia-mediated drug delivery is provided, and the final conclusions are drawn.

1

# REFERENCES

[1] NIH/National Cancer Institute. Types of Cancer Treatment [Internet]. [cited 2020 Jul 7]. Available from: https://www.cancer.gov/about-cancer/treatment/types.

[2] Ginsburg GS, Phillips KA. Precision Medicine: From Science To Value. Health Aff. 2018;37:694–701.

[3] Tempany CMC, McDannold NJ, Hynynen K, et al. Focused ultrasound surgery in oncology: Overview and principles. Radiology. 2011;259:39–56.

[4] Webb H, Lubner MG, Hinshaw JL. Thermal Ablation. Semin. Roentgenol. 2011;46:133–141.

[5] Ikeda M. Radiofrequency Ablation and Percutaneous Ethanol Injection in Patients with Small Hepatocellular Carcinoma: a Comparative Study. Jpn. J. Clin. Oncol. 2001;31:322–326.

[6] Coad JE, Kosari K, Humar A, et al. Radiofrequency ablation causes "thermal fixation" of hepato-cellular carcinoma: A post-liver transplant histo-pathologic study. Clin. Transplant. 2003;17:377–384.

[7] Marinova M, Huxold HC, Henseler J, et al. Clinical Effectiveness and Potential Survival Benefit of US-Guided High-Intensity Focused Ultrasound Therapy in Patients with Advanced-Stage Pancreatic Cancer. Ultraschall Med. 2019;40:625–637.

[8] Takaki H, Cornelis F, Kako Y, et al. Thermal ablation and immunomodulation: From preclinical experiments to clinical trials. Diagn. Interv. Imaging. 2017;98:651–659.

[9] Lemdani K, Mignet N, Boudy V, et al. Local immunomodulation combined to radiofrequency ablation results in a complete cure of local and distant colorectal carcinoma. Oncoimmunology. 2019;8:1550342.

[10] Takahashi H, Berber E. Role of thermal ablation in the management of colorectal liver metastasis. Hepatobiliary Surg. Nutr. 2020;9:49–58.

[11] Datta NR, Kok HP, Crezee H, et al. Integrating Loco-Regional Hyperthermia Into the Current Oncology Practice: SWOT and TOWS Analyses. Front. Oncol. 2020;10:819.

[12] Hildebrandt B. The cellular and molecular basis of hyperthermia. Crit. Rev. Oncol. Hematol. 2002;43:33–56.

[13] Issels RD. Hyperthermia Adds to Chemotherapy. Eur. J. Cancer. 2008;44:2546–2554.

[14] Horsman MR, Overgaard J. Hyperthermia: A Potent Enhancer of Radiotherapy. Clin. Oncol. 2007;19:418–426.

[15] Issels RD, Lindner LH, Verweij J, et al. Neo-adjuvant Chemotherapy Alone or with Regional Hyperthermia for Localised High-Risk Soft-Tissue Sarcoma: A Randomised Phase 3 Multicentre Study. Lancet Oncol. 2010;11:561–570.

[16] Issels RD, Lindner LH, Verweij J, et al. Effect of Neoadjuvant Chemotherapy Plus Regional Hyperthermia on Long-Term Outcomes Among Patients With Localized High-Risk Soft Tissue Sarcoma. JAMA Oncol. 2018;4:483–492.

[17] Vernon CC, Hand JW, Field SB, et al. Radiotherapy with or without hyperthermia in the treatment of superficial localized breast cancer: Results from five randomized controlled trials. Int. J. Radiat. Oncol. Biol. Phys. 1996;35:731–744.

[18] Van der Zee J, González González D, Van Rhoon GC, et al. Comparison of Radiotherapy Alone with Radiotherapy plus Hyperthermia in Locally Advanced Pelvic Tumours: A Prospective, Randomised, Multicentre Trial. Lancet. 2000;355: 1119–1125.

[19] Datta NR, Rogers S, Ordóñez SG, et al. Hyper-thermia and Radiotherapy in the Management of Head and Neck Cancers: A Systematic Review and Meta-Analysis. Int. J. Hyperth. 2016;32:31–40.

[20] Datta NR, Rogers S, Klingbiel D, et al. Hyperthermia and Radiotherapy with or without Chemotherapy in Locally Advanced Cervical Cancer: A Systematic Review with Conventional and Network Meta-Analyses. Int. J. Hyperth. 2016;32:809–821.

[21] Hu Y, Li Z, Mi D-H, et al. Chemoradiation combined with regional hyperthermia for advanced oesop-hageal cancer: a systematic review and meta-analysis. 2017;

[22] De Haas-Kock DFM, Buijsen J, Pijls-Johannesma M, et al. Concomitant hyperthermia and radiation therapy for treating locally advanced rectal cancer. Cochrane Database Syst. Rev. 2009;

[23] Oei AL, Vriend LEM, Crezee J, et al. Effects of hyperthermia on DNA repair pathways: One treatment to inhibit them all. Radiat. Oncol. 2015;10.

[24] Krawczyk PM, Eppink B, Essers J, et al. Mild hyperthermia inhibits homologous recombination, induces BRCA2 degradation, and sensitizes cancer cells to poly (ADP-ribose) polymerase-1 inhibition. Proc. Natl. Acad. Sci. U. S. A. 2011;108:9851–9856.

[25] Jones EL, Prosnitz LR, Dewhirst MW, et al. Thermochemoradiotherapy Improves Oxygenation in Locally Advanced Breast Cancer. Clin. Cancer Res. 2004;10:4287–4293.

[26] Vujaskovic Z, Song CW. Physiological mechanisms underlying heat-induced radio-sensitization. Int. J. Hyperth. 2004. p. 163–174.

[27] Horsman MR, Overgaard J. The impact of hypoxia and its modification of the outcome of radiotherapy. J. Radiat. Res. 2016;57:i90–i98.

[28] Dewhirst MW, Secomb TW. Transport of drugs from blood vessels to tumour tissue. Nat. Rev. Cancer. 2017;17:738–750.

[29] De Smet M, Langereis S, Van den Bosch S, et al. SPECT/CT Imaging of Temperature-Sensitive Liposomes for MR-Image Guided Drug Delivery with High Intensity Focused Ultrasound. J. Control. Release. 2013;169:82–90.

[30] Lokerse WJM, Bolkestein M, Hagen TLM, et al. Investigation of Particle Accumulation, Chemosensitivity and Thermosensitivity for Effective Solid Tumor Therapy Using Thermo-sensitive Liposomes and Hyperthermia. Theranostics. 2016;6:1717–1731.

[31] Issels R. Hyperthermia Combined with Chemotherapy – Biological Rationale, Clinical Application, and Treatment Results. Oncol. Res. Treat. 1999;22:374–381.

[32] Westra A, Dewey WC. Variation in sensitivity to heat shock during the cell-cycle of chinese hamster cells in vitro. Int. J. Radiat. Biol. 1971;19:467–477.

[33] Sapareto S a., Dewey WC. Thermal Dose Determination in Cancer Therapy. Int. J. Radiat. Oncol. 1984;10:787–800.

[34] Van Rhoon GC. Is CEM43 Still a Relevant Thermal Dose Parameter for Hyperthermia Treatment Monitoring? Int. J. Hyperth. 2016;6736:1–13.

[35] Sapareto SA, Hopwood LE, Dewey WC. Effects of Hyperthermia on Survival and Progression of Chinese Hamster Ovary Cells. Cancer Res. 1978;38:393–400.

[36] Van Rhoon GC, Samaras T, Yarmolenko PS, et al. CEM43℃ Thermal Dose Thresholds: A Potential Guide for Magnetic Resonance Radiofrequency Exposure Levels? Eur. Radiol. 2013;23:2215–2227.

[37] Yarmolenko PS, Moon EJ, Landon C, et al. Thresholds for Thermal Damage to Normal Tissues: An Update. Int. J. Hyperth. 2011;27:320–343.

[38] Franckena M, Fatehi D, Bruijne M de, et al. Hyperthermia dose-effect relationship in 420 patients with cervical cancer treated with combined radiotherapy and hyperthermia. Eur. J. Cancer. 2009;45:1969–1978.

[39] Sherar M, Liu FF, Pintilie M, et al. Relationship between thermal dose and outcome in thermoradiotherapy treatments for super-ficial recurrences of breast cancer: Data from a phase III trial. Int. J. Radiat. Oncol. Biol. Phys. 1997;39:371–380.

[40] Thrall DE. Thermal Dose Is Related to Duration of Local Control in Canine Sarcomas Treated with Thermoradiotherapy. 2005;11:5206–5214.

[41] Van Der Zee J, Van Der Holt B, Rietveld PJM, et al. Reirradiation combined with hyperthermia in recurrent breast cancer results in a worthwhile local palliation. Br. J. Cancer. 1999;79:483–490.

[42] Allen JP. The Art of Medicine in Ancient Egypt. New York/New Haven: The Metropolitan Museum of Art/Yale University Press; 2005.

[43] Kosack W. Der medizinische Papyrus Edwin Smith: The New York Academy of Medicine, Inv. 217: Neu in Hieroglyphen übertragen, übersetzt und bearbeitet (in German). Berlin: Christoph Brunner Verlag Basel; 2011.

[44] Gilchrist RK, Medal R, Shorey WD, et al. Selective Inductive Heating of Lymph Nodes. Ann. Surg. 1957;146:596–606.

[45] Wieringen N Van, Dijk JDP Van, Nieuwenhuys GJ, et al. Power absorption and temperature control of multi-filament palladium – nickel thermoseeds for interstitial hyperthermia. Phys. Med. Biol. 1996;41:2367–2380.

1

[46] Wust P, Gneveckow U, Johannsen M, et al. Magnetic nanoparticles for interstitial thermotherapy – feasibility, tolerance and achieved temperatures. Int. J. Hyperth. 2006;22:673–685.

[47] Johannsen M, Gneveckow U, Eckelt L, et al. Clinical hyperthermia of prostate cancer using magnetic nanoparticles: Presentation of a new interstitial technique. Int. J. Hyperth. 2005;21:637–647.

[48] Maier-Hauff K, Rothe R, Scholz R, et al. Intracranial Thermotherapy using Magnetic Nanoparticles Combined with External Beam Radiotherapy: Results of a Feasibility Study on Patients with Glioblastoma Multiforme. J. Neurooncol. 2007;81: 53–60.

[49] Maier-Hauff K, Ulrich F, Nestler D, et al. Efficacy and safety of intratumoral thermotherapy using magnetic iron-oxide nanoparticles combined with external beam radiotherapy on patients with recurrent glioblastoma multiforme. J. Neurooncol. 2011;103:317–324.

[50] Eggermont AM, De Wilt JH, Ten Hagen TL. Current uses of isolated limb perfusion in the clinic and a model system for new strategies. Lancet Oncol. 2003;4:429–437.

[51] Helderman RFCPA, Löke DR, Kok HP, et al. Variation in clinical application of hyperthermic intraperitoneal chemotherapy: A review. Cancers (Basel). 2019;11.

[52] De Bree E, Van Ruth S, Baas P, et al. Cytoreductive Surgery and Intraoperative Hyperthermic Intrathoracic Chemotherapy in Patients With Malignant Pleural Mesothelioma or Pleural Metastases of Thymoma. Chest. 2002;121:480–487.

[53] Sousa A, Piñeiro I, Rodríguez S, et al. Recirculant hyperthermic IntraVEsical chemotherapy (HIVEC) in intermediate–high-risk non-muscle-invasive bladder cancer. Int. J. Hyperth. 2016;32:374–380.

[54] Koops HS, Vaglini M, Suciu S, et al. Prophylactic isolated limb perfusion for localized, high-risk limb melanoma: results of a multicenter randomized phase III trial. European Organization for Research and Treatment of Cancer Malignant Melanoma Cooperative Group Protocol 18832, the World Hea. J. Clin. Oncol. 1998;16:2906–2912.

[55] Jakob J, Smith HG, Wilkinson MJ, et al. Regional chemotherapy by isolated limb perfusion prior to surgery compared with surgery and post-operative radiotherapy for primary, locally advanced extremity sarcoma: a comparison of matched cohorts. Clin. Sarcoma Res. 2018;8.

[56] Zhou H, Wu W, Tang X, et al. Effect of hyperthermic intrathoracic chemotherapy (HITHOC) on the malignant pleural effusion. Medicine (Baltimore). 2017;96:e5532.

[57] Van Driel WJ, Koole SN, Sikorska K, et al. Hyperthermic Intraperitoneal Chemotherapy in Ovarian Cancer. N. Engl. J. Med. 2018;378:230–240.

[58] Bonnot P-E, Piessen G, Kepenekian V, et al. Cytoreductive Surgery With or Without Hyperthermic Intraperitoneal Chemotherapy for Gastric Cancer With Peritoneal Metastases (CYTO-CHIP study): A Propensity Score Analysis. J. Clin. Oncol. 2019;37:2028–2040.

[59] Verwaal VJ, Van Ruth S, De Bree E, et al. Randomized Trial of Cytoreduction and Hyperthermic Intraperitoneal Chemotherapy Versus Systemic Chemotherapy and Palliative Surgery in Patients With Peritoneal Carcinomatosis of Colorectal Cancer. J. Clin. Oncol. 2003;21:3737–3743.

[60] Sousa A, Inman BA, Piñeiro I, et al. A clinical trial of neoadjuvant hyperthermic intravesical chemotherapy (HIVEC) for treating inter-mediate and high-risk non-muscle invasive bladder cancer. 2014;30:166–170.

[61] Carlier C, Mathys A, De Jaeghere E, et al. Tumour tissue transport after intraperitoneal anticancer drug delivery. Int. J. Hyperth. 2017;33:534–542.

[62] Schooneveldt G, Bakker A, Balidemaj E, et al. Thermal dosimetry for bladder hyperthermia treatment. An overview. 2016;32:417–433.

[63] Colombo R, Lev A, Da Pozzo LF, et al. A New Approach Using Local Combined Microwave Hyperthermia and Chemotherapy in Superficial Transitional Bladder Carcinoma Treatment. J. Urol. 1995;153:959–963.

[64] Wust P, Seebass M, Nadobny J, et al. Electro-magnetic deep heating technology. In: Seegenschmiedt M, Fessenden P, Vernon C, editors. Thermoradiotherapy Thermochem. Vol. 1 Biol. Physiol. Phys. Berlin: Springer Verlag; 1995. p. 219–251.

[65] Dobšíček Trefná H, Crezee J, Schmidt M, et al. Quality assurance guidelines for superficial hyperthermia clinical trials. Strahlentherapie und Onkol. 2017;193:351–366.

[66] Notter M, Piazena H, Vaupel P. Hypofractionated re-irradiation of large-sized recurrent breast cancer with thermography-controlled, contact-free water-filtered infrared-A hyperthermia: a retrospective study of 73 patients. Int. J. Hyperth. ISSN. 2016;33:227–236.

[67] Stauffer PR, Maccarini P, Arunachalam K, et al. Conformal microwave array (CMA) applicators for hyperthermia of diffuse chest wall recurrence. Int. J. Hyperth. 2010;26:686–698.

[68] Fallahi H, Prakash P. Antenna designs for microwave tissue ablation. Crit. Rev. Biomed. Eng. 2018;46:495–521.

[69] Ryan TP, Brace CL. Interstitial microwave treatment for cancer: historical basis and current techniques in antenna design and performance. Int. J. Hyperth. ISSN. 2016;33:3–14.

[70] Van Vulpen M, Raaymakers BW, Lagendijk JJW, et al. Three-dimensional controlled interstitial hyperthermia combined with radiotherapy for locally advanced prostate carcinoma – a feasibility study. Int. J. Radiat. Oncol. Biol. Phys. 2002;53:116–126.

[71] Paulsen KD, Geimer S, Tang J, et al. Optimization of pelvic heating rate distributions with electromagnetic phased arrays. Int. J. Hyperth. 1999;15:157–186.

[72] Mulder HT, Curto S, Paulides MM, et al. Systematic Quality Assurance of the BSD2000-3D MR-Compatible Hyperthermia Applicator Performance Using MR Temperature Imaging. Int. J. Hyperth. 2018;35:305–313.

[73] Wessalowski R, Schneider DT, Mils O, et al. Regional Deep Hyperthermia for Salvage Treatment of Children and Adolescents with Refractory or Recurrent Non-Testicular Malignant Germ-Cell Tumours: An Open-Label, Non-Randomised, Single-Institution, Phase 2 Study. Lancet Oncol. 2013;14:843–852.

[74] Datta NR, Stutz E, Gomez S, et al. Efficacy and Safety Evaluation of the Various Therapeutic Options in Locally Advanced Cervix Cancer: A Systematic Review and Network Meta-Analysis of Randomized Clinical Trials. Int. J. Radiat. Oncol. [Internet]. 2019;103:411–437. Available from: http://10.0.3.248/j.ijrobp.2018.09.037.

[75] Datta NR, Puric E, Klingbiel D, et al. Hyperthermia and Radiation Therapy in Locoregional Recurrent Breast Cancers: A Systematic Review and Meta-analysis. Int. J. Radiat. Oncol. Biol. Phys. 2016;94:1073–1087.

[76] Lagendijk JJW. The influence of bloodflow in large vessels on the temperature distribution in hyperthermia. Phys. Med. Biol. 1982;27:17–23.

[77] Johnson CC, Guy AW. Nonionizing electromagnetic wave effects in biological materials and systems. Proc. IEEE. 1972;60:692–718.

[78] Dussik K, Fritch D, Kyriazidou M, et al. Measurements of articular tissues with ultrasound. Am. J. Phys. Med. 1958.

[79] Duck FA. Physical Properties of Tissue. A Comprehensive Reference Book. Med. Phys. 1990.

[80] Fry WJ, Barnard JW, Fry FJ, et al. Ultrasonic Lesions in the Mammalian Central Nervous System. Science (80-. ). 1955;122:517–518.

[81] Hynynen K, Jones RM. Image-guided ultrasound phased arrays are a disruptive technology for non-invasive therapy. Phys. Med. Biol. 2016;61:R206–R248.

[82] Köhler M, Mougenot C, Quesson B, et al. Volumetric HIFU Ablation under 3D Guidance of Rapid MRI Thermometry. Med. Phys. 2009;36: 3521–3535.

[83] Tillander M, Hokland S, Koskela J, et al. High Intensity Focused Ultrasound Induced In Vivo Large Volume Hyperthermia under 3D MRI Temperature Control. Med. Phys. 2016;43:1539–1549.

[84] Hijnen N, Kneepkens E, De Smet M, et al. Thermal Combination Therapies for Local Drug Delivery by Magnetic Resonance-Guided High-Intensity Focused Ultrasound. Proc. Natl. Acad. Sci. 2017;114:E4802–E4811.

[85] Chopra R, Colquhoun A, Burtnyk M, et al. MR Imaging–controlled Transurethral Ultrasound Therapy for Conformal Treatment of Prostate Tissue: Initial Feasibility in Humans. Radiology. 2012;265:303–313.

[86] Aptel F, Lafon C. Therapeutic applications of ultrasound in ophthalmology. Int. J. Hyperth. 2012;28:405–418.

[87] Aptel F, Béglé A, Razavi A, et al. Short- and Long-Term Effects on the Ciliary Body and the Aqueous Outflow Pathways of High-Intensity Focused Ultrasound Cyclocoagulation. Ultrasound Med. Biol. 2014;40:2096–2106.

1

[88] Wood RW, Loomis AL. The physical and biological effects of high-frequency sound-waves of great intensity. London, Edinburgh, Dublin Philos. Mag. J. Sci. 1927;4:417–436.

[89] Gruetzmacher J. Piezoelektrischer Kristall mit Ultraschallkonvergenz. Zeitschrift fuer Phys. 1935;96:342–349.

[90] Lynn JG, Zwemer RL, Chick AJ, et al. A new method for the generation and use of focused ultrasound in experimental biology. J. Gen. Physiol. 1942;26:179–193.

[91] Fry WJ, Wulff VJ, Tucker D, et al. Physical Factors Involved in Ultrasonically Induced Changes in Living Systems: I. Identification of Non?Temperature Effects. J. Acoust. Soc. Am. 1950;22:867–876.

[92] Barnard JW, Fry WJ, Fry FJ, et al. Effects of high intensity ultrasound on the central nervous system of the cat. J. Comp. Neurol. 1955;103:459–484.

[93] Bakay L, Hueter TF, Ballantine HT, et al. Ultrasonically Produced Changes in the Blood-Brain Barrier. Arch. Neurol. Psychiatry. 1956;76:457–467.

[94] Meyers R, Fry WJ, Fry FJ, et al. Early Experiences with Ultrasonic Irradiation of the Pallidofugal and Nigral Complexes in Hyperkinetic and Hypertonic Disorders. J. Neurosurg. 1959;16:32–54.

[95] Fry WJ, Fry FJ. Fundamental Neurological Research and Human Neurosurgery Using Intense Ultrasound. IRE Trans. Med. Electron. 1960;ME-7:166–181.

[96] Ter Haar G, Coussios C. High Intensity Focused Ultrasound: Physical Principles and Devices. Int. J. Hyperth. 2007;23:89–104.

[97] Oka M. Application of intense focused ultrasound in brainsurgery and other fields. Clin. All-Round. 1964;13:1514.

[98] Heimburger RF. Ultrasound augmentation of central nervous system tumor therapy. Indiana Med. 1985;78:469–476.

[99] Coleman DJ, Lizzi FL, Jakobiec FA. Therapeutic ultrasound in the production of ocular lesions. Ophthalmology. 1979;86:185–192.

[100] Fry WJ. Ultrasonic Visualization of Ultrasonically Produced Brain Lesions. Confin. Neurol. 1970;32: 38–52.

[101] Damadian R, Golsmith M, Minkoff L. NMR in cancer: XVI. FONAR image of the live human body. Physiol. Chem. Phys. 1977;9:97–100.

[102] Hynynen K, Darkazanli A, Unger E, et al. MRI-Guided Noninvasive Ultrasound Surgery. Med. Phys. 1993;20:107–115.

[103] Ishihara Y, Calderon A, Watanabe H, et al. A Precise and Fast Temperature Mapping Using Water Proton Chemical Shift. Magn. Reson. Med. 1995;34:814–823.

[104] De Poorter J, De Wagter C, De Deene Y, et al. Noninvasive MRI Thermometry with the Proton Resonance Frequency (PRF) Method: In Vivo Results in Human Muscle. Magn. Reson. Med. 1995;33:74–81.

[105] Vimeux F, De Zwart JA, Palussiére J, et al. Real-Time Control of Focused Ultrasound Heating Based on Rapid MR Thermometry. Invest. Radiol. 1999;34:190–193.

[106] Hynynen K, Jolesz FA. Demonstration of potential noninvasive ultrasound brain therapy through an intact skull. Ultrasound Med. Biol. 1998;24:275–283.

[107] Focused Ultrasound Foundation. State of the Technology [Internet]. [cited 2020 Jun 25]. Available from: https://www.fusfoundation. org/the-technology/state-of-the-technology.

[108] Siedek F, Yeo SY, Heijman E, et al. Magnetic Resonance-Guided High-Intensity Focused Ultra-sound (MR-HIFU): Technical Background and Overview of Current Clinical Applications (Part 1). RöFo. 2019;191:522–530.

[109] James SL, Abate D, Abate KH, et al. Global, regional, and national incidence, prevalence, and years lived with disability for 354 Diseases and Injuries for 195 countries and territories, 1990-2017: A systematic analysis for the Global Burden of Disease Study 2017. Lancet. 2018;392:1789–1858.

[110] Baird DD, Dunson DB, Hill MC, et al. High cumulative incidence of uterine leiomyoma in black and white women: Ultrasound evidence. Am. J. Obstet. Gynecol. 2003;188:100–107.

[111] Stewart E, Cookson C, Gandolfo R, et al. Epidemiology of uterine fibroids: a systematic review. BJOG An Int. J. Obstet. Gynaecol. 2017;124:1501–1512.

[112] Catherino WH, Parrott E, Segars J. Proceedings from the National Institute of Child Health and Human Development Conference on the Uterine Fibroid Research Update Workshop. Fertil. Steril. 2011;95:9–12.

[113] Bulun SE. Uterine Fibroids. N. Engl. J. Med. 2013;369:1344–1355.

[114] Cardozo ER, Clark AD, Banks NK, et al. The estimated annual cost of uterine leiomyomata in the United States. Am. J. Obstet. Gynecol. 2012;206:211.e1-211.e9.

[115] Sandberg EM, Tummers FHMP, Cohen SL, et al. Reintervention risk and quality of life outcomes after uterine-sparing interventions for fibroids: a systematic review and meta-analysis. Fertil. Steril. 2018;109:698-707.e1.

[116] Holzer A, Jirecek ST, Illievich UM, et al. Laparoscopic Versus Open Myomectomy: A Double-Blind Study to Evaluate Postoperative Pain. Pain Med. 2006;102:1480–1484.

[117] Pitter MC, Simmonds C, Seshadri-Kreaden U, et al. The impact of different surgical modalities for hysterectomy on satisfaction and patient reported outcomes. J. Med. Internet Res. 2014;3:e11.

[118] ONU. World Population Prospects 2019. Dep. Econ. Soc. Aff. World Popul. Prospect. 2019. 2019.

[119] Khaw SC, Anderson RA, Lui M-W. Systematic review of pregnancy outcomes after fertility-preserving treatment of uterine fibroids. Reprod. Biomed. Online. 2020;40:429–444.

[120] Kohi M, Sridhar D. Updates on MR-Guided Focused Ultrasound for Symptomatic Uterine Fibroids. Semin. Intervent. Radiol. 2018;35:17–22.

[121] Rabinovici J, David M, Fukunishi H, et al. Pregnancy outcome after magnetic resonance-guided focused ultrasound surgery (MRgFUS) for conservative treatment of uterine fibroids. Fertil. Steril. 2010;93:199–209.

[122] Kim Y-S. Clinical application of high-intensity focused ultrasound ablation for uterine fibroids. Biomed. Eng. Lett. 2017;7:99–105.

[123] Verpalen IM, De Boer JP, Linstra M, et al. The Focused Ultrasound Myoma Outcome Study (FUMOS); a retrospective cohort study on long-term outcomes of MR-HIFU therapy. Eur. Radiol. 2020;30:2473–2482.

[124] Mara M, Maskova J, Fucikova Z, et al. Midterm Clinical and First Reproductive Results of a Randomized Controlled Trial Comparing Uterine Fibroid Embolization and Myomectomy. Cardiovasc. Intervent. Radiol. 2008;31:73–85.

[125] Xiromeritis P, Kalogiannidis I, Papadopoulos E, et al. Improved recovery using multimodal perioperative analgesia in minimally invasive myomectomy: A randomised study. Aust. New Zeal. J. Obstet. Gynaecol. 2011;51:301–306.

[126] Dobrotwir A, Pun E. Clinical 24 month experience of the first MRgFUS Unit for treatment of uterine fibroids in Australia. J. Med. Imaging Radiat. Oncol. 2012;56:409–416.

[127] Funaki K, Fukunishi H, Sawada K. Clinical out-comes of magnetic resonance-guided focused ultrasound surgery for uterine myomas: 24-month follow-up. Ultrasound Obstet. Gynecol. 2009;34:584–589.

[128] Verpalen IM, Anneveldt KJ, Nijholt IM, et al. Magnetic resonance-high intensity focused ultrasound (MR-HIFU) therapy of symptomatic uterine fibroids with unrestrictive treatment protocols: A systematic review and meta-analysis. Eur. J. Radiol. 2019;120:108700.

[129] Babashov V, Palimaka S, Blackhouse G, et al. Magnetic resonance-guided high-intensity focused ultrasound (MRgHIFU) for treatment of symptomatic uterine fibroids: An economic analysis. Ont. Health Technol. Assess. Ser. 2015;15:1–61.

[130] Chodankar R, Allison J. New Horizons in Fibroid Management. Curr. Obstet. Gynecol. Rep. 2018;7:106–115.

[131] Siegel RL, Miller KD, Jemal A. Cancer Statistics, 2019. CA. Cancer J. Clin. 2019;69:7–34.

[132] Galasko C. The anatomy and pathways of skeletal metastases. In: Weiss L, Gilbert A, editors. Bone metastases. Boston: GK Hall; 1981. p. 49–63.

[133] Domchek SM, Younger J, Finkelstein DM, et al. Predictors of skeletal complications in patients with metastatic breast carcinoma. Cancer. 2000;89:363–368.

[134] Eisenberger MA, Blumenstein BA, Crawford ED, et al. Bilateral Orchiectomy with or without Flutamide for Metastatic Prostate Cancer. N. Engl. J. Med. 1998;339:1036–1042.

[135] Huang J-F, Shen J, Li X, et al. Incidence of patients with bone metastases at diagnosis of solid tumors in adults: a large population-based study. Ann. Transl. Med. 2020;8:482.

[136] Guise TA, Yin JJ, Mohammad KS. Role of endothelin-1 in osteoblastic bone metastases. Cancer. 2003;97:779–784.

[137] Pulido C, Vendrell I, Ferreira AR, et al. Bone metastasis risk factors in breast cancer. Ecancermedicalscience. 2017;11:715.

[138] Coleman RE. Clinical Features of Metastatic Bone Disease and Risk of Skeletal Morbidity. Clin. Cancer Res. 2006;12:6243s-6249s.

[139] Coleman R, Cameron D, Dodwell D, et al. Adjuvant zoledronic acid in patients with early breast cancer: final efficacy analysis of the AZURE (BIG 01/04) randomised open-label phase 3 trial. Lancet Oncol. 2014;15:997–1006.

[140] Gnant M, Mlineritsch B, Stoeger H, et al. Zoledronic acid combined with adjuvant endocrine therapy of tamoxifen versus anastrozol plus ovarian function suppression in premenopausal early breast cancer: Final analysis of the Austrian Breast and Colorectal Cancer Study Group Trial 12. Ann. Oncol. 2015;26:313–320.

[141] Selvaggi G, Scagliotti G V. Management of bone metastases in cancer: A review. Crit. Rev. Oncol. Hematol. 2005;56:365–378.

[142] Smith HS, Barkin RL. Painful Boney Metastases. Am. J. Ther. 2014;21:106–130.

[143] Janjan NA, Payne R, Gillis T, et al. Presenting Symptoms in Patients Referred to a Multidisciplinary Clinic for Bone Metastases. J. Pain Symptom Manage. 1998;16:171–178.

[144] Macedo F, Ladeira K, Pinho F, et al. Bone metastases: an overview. Oncol. Rev. 2017; 11:321.

[145] World Health Organization. WHO Guidelines for the Pharmacological and Radiotherapeutic Management of Cancer Pain in Adults and Adolescents. Geneva; 2018.

[146] Yarnold JR. 8 Gy single fraction radiotherapy for the treatment of metastatic skeletal pain: Randomised comparison with a multifraction schedule over 12 months of patient follow-up. Radiother. Oncol. 1999;52:111–121.

[147] Meeuse JJ, Van Der Linden YM, Van Tienhoven G, et al. Efficacy of radiotherapy for painful bone metastases during the last 12 weeks of life. Cancer. 2010;116:2716–2725.

[148] Lutz S, Berk L, Chang E, et al. Palliative Radiotherapy for Bone Metastases: An ASTRO Evidence-Based Guideline. Int. J. Radiat. Oncol. 2011;79:965–976.

[149] De Felice F, Piccioli A, Musio D, et al. The role of radiation therapy in bone metastases management. Oncotarget. 2017;8:25691–25699.

[150] Huisman M, Van Den Bosch MAAJ, Wijlemans JW, et al. Effectiveness of reirradiation for painful bone metastases: A systematic review and meta-analysis. Int. J. Radiat. Oncol. Biol. Phys. 2012;84:8–14.

[151] Yeo SY, Elevelt A, Donato K, et al. Bone metastasis treatment using magnetic resonance-guided high intensity focused ultrasound. Bone. 2015;81:513–523.

[152] Napoli A, Anzidei M, Marincola BC, et al. Primary pain palliation and local tumor control in bone metastases treated with magnetic resonance-guided focused ultrasound. Invest. Radiol. 2013;48:351–358.

[153] Hurwitz MD, Ghanouni P, Kanaev S V., et al. Magnetic Resonance–Guided Focused Ultrasound for Patients With Painful Bone Meta-stases: Phase III Trial Results. J. Natl. Cancer Inst. 2014;106:1–9.

[154] Chow E, Zeng L, Salvo N, et al. Update on the Systematic Review of Palliative Radiotherapy Trials for Bone Metastases. Clin. Oncol. 2012;24: 112–124.

[155] Siedek F, Yeo SY, Heijman E, et al. Magnetic Resonance-Guided High-Intensity Focused Ultrasound (MR-HIFU): Overview of Emerging Applications (Part 2). RöFo. 2019;191:531–539.

[156] Napoli A, Bazzocchi A, Scipione R, et al. Non-invasive Therapy for Osteoid Osteoma: A Prospective Developmental Study with MR Imaging–guided High-Intensity Focused Ultrasound. Radiology. 2017;285:186–196.

[157] Arrigoni F, Barile A, Zugaro L, et al. Intra-articular benign bone lesions treated with Magnetic Resonance-guided Focused Ultra-sound (MRgFUS): imaging follow-up and clinical results. Med. Oncol. 2017;34:55.

[158] Weeks EM, Platt MW, Gedroyc W. MRI-guided focused ultrasound (MRgFUS) to treat facet joint osteoarthritis low back pain – case series of an innovative new technique. Eur. Radiol. 2012;22:2822–2835.

[159] Jeanmonod D, Werner B, Morel A, et al. Transcranial magnetic resonance imaging–guided focused ultrasound: noninvasive central lateral thalamotomy for chronic neuro-pathic pain. Neurosurg. Focus. 2012;32:E1.

[160] Vidal-Jove J, Perich E, Del Castillo MA. Ultrasound Guided High Intensity Focused Ultrasound for Malignant Tumors: The Spanish Experience of Survival Advantage in Stage III and IV Pancreatic Cancer. Ultrason. Sonochem. 2015;27:703–706.

[161] Strunk HM, Henseler J, Rauch M, et al. Clinical Use of High-Intensity Focused Ultrasound (HIFU) for Tumor and Pain Reduction in Advanced Pancreatic Cancer. RöFo. 2016;188:662–670.

[162] Bray F, Ferlay J, Soerjomataram I, et al. Global Cancer Statistics 2018: GLOBOCAN Estimates of Incidence and Mortality Worldwide for 36 Cancers in 185 Countries. CA. Cancer J. Clin. 2018;68:394–424.

[163] Islami F, Siegel RL, Jemal A. The changing landscape of cancer in the USA – opportunities for advancing prevention and treatment. Nat. Rev. Clin. Oncol. 2020;

[164] Rahib L, Smith BD, Aizenberg R, et al. Projecting cancer incidence and deaths to 2030: The unexpected burden of thyroid, liver, and pancreas cancers in the united states. Cancer Res. 2014;74:2913–2921.

[165] Ryan DP, Hong TS, Bardeesy N. Pancreatic Adenocarcinoma. N. Engl. J. Med. 2014;371:1039–1049.

[166] Zhang Q, Zeng L, Chen Y, et al. Pancreatic Cancer Epidemiology, Detection, and Management. Gastroenterol. Res. Pract. 2016;2016:1–10.

[167] Isaji S, Mizuno S, Windsor JA, et al. International Consensus on Definition and Criteria of Borderline Resectable Pancreatic Ductal Adenocarcinoma 2017. Pancreatology. 2018;18:2–11.

[168] Hidalgo H. Pancreatic cancer. N. Engl. J. Med. 2010;362:1605–1617.

[169] Moffat GT, Epstein AS, O'Reilly EM. Pancreatic Cancer – A Disease in Need: Optimizing and Inte-grating Supportive Care. Cancer. 2019;0:1–9.

[170] Vincent A, Herman J, Schulick R, et al. Pancreatic Cancer. Lancet. 2011;378:607–620.

[171] Springfeld C, Jäger D, Büchler MW, et al. Chemo-therapy for pancreatic cancer. Presse Med. 2019;48:e159–e174.

[172] Hammel P, Huguet F, Van Laethem J-L, et al. Effect of Chemoradiotherapy vs Chemotherapy on Survival in Patients With Locally Advanced Pancreatic Cancer Controlled After 4 Months of Gemcitabine With or Without Erlotinib. JAMA. 2016;315:1844.

[173] Neesse A, Michl P, Frese KK, et al. Stromal biology and therapy in pancreatic cancer. Gut. 2011;60:861–868.

[174] Conroy T, Hammel P, Hebbar M, et al. FOLFIRINOX or Gemcitabine as Adjuvant Therapy for Pancreatic Cancer. N. Engl. J. Med. 2018;379:2395–2406.

[175] Wong GY, Schroeder DR, Carns PE, et al. Effect of Neurolytic Celiac Plexus Block on Pain Relief, Quality of Life, and Survival in Patients with Unresectable Pancreatic Cancer: A Randomized Controlled Trial. J. Am. Med. Assoc. 2004;291:1092–1099.

[176] Xiong L. The Preliminary Clinical Results of the Treatment for Advanced Pancreatic Carcinoma by High Intensity Focused Ultrasound. Chin J Gen Surg. 2001;16:345–347.

[177] Xu Y, Wang G, Gu Y, et al. The Acesodyne Effect of High Intensity Focused Ultrasound on the Treatment of Advanced Pancreatic Carcinoma. Clin Med J China. 2003;10:322–323.

[178] Yuan C, Yang L, Cheng Y. Observation of High Intensity Focused Ultrasound Treating 40 Cases of Cancer of Pancreas. Chlin J Clin Hep. 2003;19:145–146.

[179] Xiong LL, Hwang JH, Huang XB, et al. Early Clinical Experience using High Intensity Focused Ultrasound for Palliation of Inoperable Pancreatic Cancer. J. Pancreas. 2009;10:123–129.

[180] Gao HF, Wang K, Meng ZQ, et al. High Intensity Focused Ultrasound Treatment for Patients with Local Advanced Pancreatic Cancer. Hepatogastroenterology. 2013;60:1906–1910.

[181] Ji Y, Zhang Y, Zhu J, et al. Response of Patients with Locally Advanced Pancreatic Adenocarcinoma to High-Intensity Focused Ultrasound Treatment: A Single-Center, Prospective, Case Series in China. Cancer Manag. Res. 2018;10:4439–4446.

[182] Dimcevski G, Kotopoulis S, Bjånes T, et al. A Human Clinical Trial Using Ultrasound and Microbubbles to Enhance Gemcitabine Treatment of Inoperable Pancreatic Cancer. J. Control. Release. 2016;243:172–181.

[183] Marinova M, Rauch M, Mücke M, et al. High-Intensity Focused Ultrasound (HIFU) for Pancreatic Carcinoma: Evaluation of Feasibility, Reduction of Tumour Volume and Pain Intensity. Eur. Radiol. 2016;26:4047–4056.

[184] Thudium M, Bette B, Tonguc T, et al. Multidisciplinary management and outcome in pancreatic cancer patients treated with high-intensity focused ultrasound. Int. J. Hyperth. 2020;37:456–462.

1

[185] Dababou S, Marrocchio C, Rosenberg J, et al. A Meta-Analysis of Palliative Treatment of Pancreatic Cancer with High Intensity Focused Ultrasound. J. Ther. Ultrasound. 2017;5:9.

[186] Zhao H, Yang G, Wang D, et al. Concurrent Gemcitabine and High-Intensity Focused Ultrasound Therapy in Patients with Locally Advanced Pancreatic Cancer. Anticancer. Drugs. 2010;21:447–452.

[187] Orsi F, Zhang L, Arnone P, et al. High-Intensity Focused Ultrasound Ablation: Effective and Safe Therapy for Solid Tumors in Difficult Locations. Am. J. Roentgenol. 2010;195:W245-252.

[188] Wang K, Chen Z, Meng Z, et al. Analgesic Effect of High Intensity Focused Ultrasound Therapy for Unresectable Pancreatic Cancer. Int. J. Hyperth. 2011;27:101–107.

[189] Sung HY, Jung SE, Cho SH, et al. Long-Term Outcome of High-Intensity Focused Ultrasound in Advanced Pancreatic Cancer. Pancreas. 2011;40:1080–1086.

[190] Sofuni A, Moriyasu F, Sano T, et al. Safety Trial of High-Intensity Focused Ultrasound Therapy for Pancreatic Cancer. World J. Gastroenterol. 2014;20:9570–9577.

[191] Li P-Z, Zhu S-H, He W, et al. High-Intensity Focused Ultrasound Treatment for Patients with Unresectable Pancreatic Cancer. Hepatobiliary Pancreat. Dis. Int. 2012;11:655–660.

[192] Orgera G, Krokidis M, Monfardini L, et al. High Intensity Focused Ultrasound Ablation of Pancreatic Neuroendocrine Tumours: Report of Two Cases. Cardiovasc. Intervent. Radiol. 2011;34:419–423.

[193] Zhou Y. High-intensity focused ultrasound treatment for advanced pancreatic cancer. Gastroenterol. Res. Pract. 2014;2014.

[194] Lv W, Yan T, Wang G, et al. High-Intensity Focused Ultrasound Therapy in Combination with Gemcitabine for Unresectable Pancreatic Carcinoma. Ther. Clin. Risk Manag. 2016;12:687–691.

[195] Anzidei M, Napoli A, Sandolo F, et al. Magnetic Resonance-Guided Focused Ultrasound Ablation in Abdominal Moving Organs: A Feasibility Study in Selected Cases of Pancreatic and Liver Cancer. Cardiovasc. Intervent. Radiol. 2014;37:1611–1617.

[196] Anzidei M, Marincola BC, Bezzi M, et al. Magnetic Resonance-Guided High-Intensity Focused Ultrasound Treatment of Locally Advanced Pancreatic Adenocarcinoma: Preliminary Experience for Pain Palliation and Local Tumor Control. Invest Radiol. 2014;49:759–765.

[197] Lewis MA, Staruch RM, Chopra R. Thermometry and Ablation Monitoring with Ultrasound. Int. J. Hyperth. 2015;31:163–181.

[198] Mahadevan V. Anatomy of the Pancreas and Spleen. Surgery. 2016;34:261–265.

[199] Lauterbur PC. Image Formation by Induced Local Interactions: Examples Employing Nuclear Magnetic Resonance. Nature. 1973;242:190–191.

[200] Lauterbur PC, Dias MHM, Rudin AM. Augmentation of Tissue Water Proton Spin-Lattice Relaxation Rates By in Vivo Addition of Paramagnetic Ions. Electrons to Tissues. 1978;1:752–759.

[201] Graham SJ, Bronskill MJ, Henkelman RM. Time and temperature dependence of MR parameters during thermal coagulation ofex vivo rabbit muscle. Magn. Reson. Med. 1998;39:198–203.

[202] Gensler D, Fidler F, Ehses P, et al. MR safety: Fast T 1 thermometry of the RF-induced heating of medical devices. 2012;68:1593–1599.

[203] Chen J, Daniel BL, Pauly KB. Investigation of proton density for measuring tissue temperature. J. Magn. Reson. Imaging. 2006;23:430–434.

[204] Baron P, Ries M, Deckers R, et al. In vivo T2-based MR thermometry in adipose tissue layers for high-intensity focused ultrasound near-field monitoring. Magn. Reson. Med. [Internet]. 2014;72:1057–1064. Available from: http://10.0.3.234/mrm.25025.

[205] Samulski T V, Macfall J, Zhang Y, et al. Non-invasive thermometry using magnetic resonance diffusion imaging: Potential for application in hyperthermic oncology. Int. J. Hyperth. 1992;8:819–829.

[206] Graham SJ, Stanisz GJ, Kecojevic A, et al. Analysis of changes in MR properties of tissues after heat treatment. Magn. Reson. Med. 1999;42:1061–1071.

[207] Rieke V, Pauly KB. MR thermometry. J. Magn. Reson. Imaging. 2008;27:376–390.

[208] Hindman JC. Proton Resonance Shift of Water in the Gas and Liquid States. 1966;44:4582.

[209] NéMethy G, Scheraga HA. Structure of Water and Hydrophobic Bonding in Proteins. I. A Model for the Thermodynamic Properties of Liquid Water. 1962;36:3382.

[210] Kuroda K, Oshio K, Chung AH, et al. Temperature Mapping using the water proton chemical shift: A chemical shift selective phase mapping method. Magn. Reson. Med. [Internet]. 1997;38:845–851. Available from: http://10.0.3.234/mrm.1910380523.

[211] Vigen KK, Daniel BL, Pauly JM, et al. Triggered, Navigated, Multi-Baseline Method for Proton Resonance Frequency Temperature Mapping With Respiratory Motion. Magn. Reson. Med. 2003;50:1003–1010.

[212] Rieke V, Vigen KK, Sommer G, et al. Referenceless PRF shift thermometry. Magn. Reson. Med. 2004;51:1223–1231.

[213] Salomir R, Viallon M, Kickhefel A, et al. Reference-free PRFS MR-thermometry using near-harmonic 2-D reconstruction of the background phase. IEEE Trans. Med. Imaging. 2012;31:287–301.

[214] Bing C, Cheng B, Staruch RM, et al. Breath-hold MR-HIFU hyperthermia: phantom and in vivo feasibility. Int. J. Hyperth. 2019;36:1084–1097.

[215] McGough RJ. Treatment planning for hyperthermia with ultrasound phased arrays. IEEE Trans. Ultrason. Ferroelectr. Freq. Control. 1996;43:1074–1084.

[216] Daum DR, Hynynen K. Thermal Dose Optimization via Temporal Switching in Ultrasound Surgery. IEEE Trans. Ultrason. Ferroelectr. Freq. Control. 1998;45:208–215.

[217] Salomir R, Vimeux FC, De Zwart JA, et al. Hyperthermia by MR-Guided Focused Ultrasound: Accurate Temperature Control Based on Fast MRI and a Physical Model of Local Energy Deposition and Heat Conduction. Magn. Reson. Med. 2000;43:342–347.

[218] Salomir R, Palussire J, Vimeux FC, et al. Local Hyperthermia with MR-Guided Focused Ultrasound: Spiral Trajectory of the Focal Point Optimized for Temperature Uniformity in The Target Region. J. Magn. Reson. Imaging. 2000;12:571–583.

[219] Mougenot C, Salomir R, Palussie J, et al. Automatic spatial and temporal temperature control for MR-guided focused ultrasound using fast 3D MR thermometry and multispiral trajectory of the focal point. Magn. Reson. Med. 2004;52:1005–1015.

[220] Mougenot C, Quesson B, De Senneville BD, et al. Three-dimensional spatial and temporal temperature control with MR thermometry-guided focused ultrasound (MRgHIFU). Magn. Reson. Med. 2009;61:603–614.

[221] Enholm JK, Köhler M, Quesson B, et al. Improved Volumetric MR-HIFU Ablation by Robust Binary Feedback Control. IEEE Trans. Biomed. Eng. 2010;57:103–113.

[222] Arora D, Minor M a, Skliar M, et al. Control of thermal therapies with moving power deposition field. Phys. Med. Biol. 2006;51:1201–1219.

[223] De Bever J, Todd N, Payne A, et al. Adaptive Model-Predictive Controller for Magnetic Resonance Guided Focused Ultrasound Therapy. Int. J. Hyperth. 2014;30:456–470.

[224] Sebeke L, Deenen DA, Maljaars E, et al. Model predictive control for MR-HIFU-mediated uniform hyperthermia. Int. J. Hyperth. 2019;36:1040–1050.

[225] Deenen DA, Maljaars E, Sebeke L, et al. Offset-free model predictive control for enhancing MR-HIFU hyperthermia in cancer treatment. IFAC-PapersOnLine. 2018;51:191–196.

1

# Chapter 2

## Feasibility Study of MR-Guided Pancreas Ablation Using High Intensity Focused Ultrasound in a Healthy Swine Model

# ABSTRACT

**Purpose:** Pancreatic cancer is typically diagnosed in a late stage with limited therapeutic options. For those patients, ultrasound-guided high-intensity focused ultrasound (US-HIFU) can improve local control and alleviate pain. However, MRI-guided HIFU (MR-HIFU) has not yet been studied extensively in this context. To facilitate related research and accelerate clinical translation, we report a workflow for the *in-vivo* HIFU ablation of the porcine pancreas under MRI-guidance.

**Materials and Methods:** The pancreases of five healthy German landrace pigs (35-58 kg) were sonicated using a clinical MR-HIFU system. Acoustic access to the pancreas was supported by a specialized diet and a hydrogel compression device for bowel displacement. Organ motion was suspended using periods of apnea. The size of the resulting thermal lesions was assessed using the thermal threshold- and dose profiles, non-perfused volume, and gross examination. The effect of the compression device on beam path length was assessed using MRI imaging.

**Results:** Eight of ten treatments resulted in clearly visible damage in the target tissue upon gross examination. Five treatments resulted in coagulative necrosis. Good agreement between the four metrics for lesion size and a clear correlation between the delivered energy dose and the resulting lesion size were found. The compression device notably shortened the intraabdominal beam path.

**Conclusions:** We demonstrated a workflow for HIFU-treatment of the porcine pancreas *in-vivo* under MRI-guidance. This development bears significance for the development of MR-guided HIFU interventions on the pancreas as the pig is the preferred animal model for the translation of pre-clinical research into clinical application.

## INTRODUCTION

Despite its moderately low incidence, pancreatic cancer (PaC) caused 4.5 % of all cancer fatalities worldwide in 2018, making it the 7th most likely cause of cancer related deaths [1]. PaC exhibits the lowest 5-year relative survival rate of any cancer [2]. This stems from a confluence of unfavorable characteristics, namely the late onset of symptoms, rapid involvement of the adjacent arteries, early development of metastases, and the ineffectiveness of systemic therapy [3-6]. As a result, resection is often impossible at time of diagnosis, leaving patients with limited therapeutic options, such as palliative chemotherapy [7]. The growing tumor mass often leads to complications, including duodenal- or biliary obstruction that require the placement of stents or surgical inter-vention [7,8]. Furthermore, the pressure exerted on the surrounding nerves often induces abdominal and back pain, which is currently treated according to the WHO guidelines recommending a combination of analgesics escalating from non-opioids to strong opioids and adjuvant treatments [9,10]. In case the pain cannot be alleviated in this manner, celiac plexus block (CPB) and celiac plexus neurolysis (CPN) are applied [7]. However, the effectiveness of these techniques has been questioned and has not shown a significant benefit in quality of life over a placebo in a double-blinded randomized control trial [11]. Thus, patients diagnosed with advanced PaC are in urgent need of alternative treatment options and effective analgesia free of debilitating side-effects. Thermal ablation of PaC using high-intensity focused ultrasound (HIFU) offers a non-invasive method for tumor debulking and pain reduction and has therefore been explored in several clinical studies since the beginning of the century [12-21].

In HIFU treatments, ultrasound waves produced by a purpose-built transducer are focused inside the target tissue. Energy dissipation in the focus leads to a sharp temperature increase in a small ellipsoid-shaped volume of a few millimeters in diameter and length, rapidly inducing a lesion of coagulative necrosis and even thermal fixation [22,23]. Accumulated evidence shows that HIFU-mediated tumor ablation leads to long-term pain relief in a large proportion of patients suffering from PaC [15,16,24-31], improves local control [16,25,27,29], and may even offer survival benefits over chemo- and radio-chemotherapy [17,21,32].

During ablation, the accumulated thermal damage in the target tissue is commonly estimated using the thermal dose concept introduced by Sapareto *et al*. The thermal dose is measured in cumulative equivalent minutes at 43 °C, CEM43 [33,34]:

$$CEM43 = \int_0^t R^{(43-T)} \, dt$$
$$R = \begin{cases} 0.50 \ for \ T > 43°C \\ 0.25 \ for \ T \le 43°C \end{cases}$$

[1]

where $T$ is the temperature in °C, $t$ is the time of the thermal exposure in minutes, and $R$ is the base of the exponential expression which determines the dose rate. Though sensitivity to thermal damage is tissue dependent, several experimental studies showed that 240 CEM43 is a thermal dose threshold at which coagulative necrosis is induced in most tissues [35-40]. Consequently, most tissues heated to temperatures above 57 °C undergo coagulative necrosis within less than a second. The exponential temperature dependence of the thermal dose provides a strong argument for accurate temperature monitoring of the target tissue together with feedback-controlled heating to ensure swift, safe, and complete ablation [36,41,42].

HIFU treatments can be guided by diagnostic ultrasound (US-HIFU) [43] or magnetic resonance imaging (MR-HIFU) [44]. In treating abdominal organs like the pancreas, US-guidance is convenient because acoustically opaque obstacles like gas pockets and bones, which would block the HIFU beam and thereby lead to prefocal heating and tissue damage, can easily be identified. Monitoring of target tissue ablation is based on changes in echogenicity and elasticity that are associated with coagulative tissue necrosis [43,45-47]. However, an ultrasound-based method for measuring tissue temperatures above 50 °C for the purpose of monitoring the treatment and off-site heating has not yet been reported [48-51].

During MR-guided thermal therapy, the proton resonance frequency of water, which shifts linearly with $\alpha$ = −0.01 ppm per Kelvin of temperature increase in all water-rich tissues [52], is often exploited for temperature monitoring. Proton Resonance Frequency Shift (PRFS)-thermometry therefore provides non-invasive, volumetric, and radiation-free monitoring of the temperature along the beam path in the full temperature range that is of interest for thermal ablation [53]. Consequently, MR-guided HIFU systems that allow near-real time imaging of the induced temperature elevation have been developed [36,42,54]. Moreover, the use of MR-thermometry data in a feedback controller enables ablation of tissue defined by a given thermal dose [36,41,55]. Among other indications, MR-guided HIFU is currently clinically approved for ablation of uterine fibroids, ablation of prostate cancer and the treatment of essential tremor as well as several musculoskeletal conditions [56-58]. Despite the success of MR-HIFU in treating these conditions and the good results that have been achieved with US-HIFU in treating pancreatic cancer, only one study in six patients has been published describing MR-HIFU ablation of PaC [59].

In preparation for a planned clinical trial using MR-HIFU for ablation of PaC, we performed a feasibility study in a healthy swine model to establish a protocol for MR-guided ablation of the porcine pancreas using a commercially available MR-HIFU device that is already approved for the treatment of uterine fibroids and bone metastasis. The porcine pancreas differs from the human pancreas in that it is larger and that its main duct drains into the duodenum directly instead of joining the common bile duct [60,61]. It consists of the duodenal lobe, the connecting lobe and the splenic lobe, which

resemble the head, uncinate process, and the body and tail of the pancreas in humans in their anatomical arrangement, respectively [62]. As in humans, the head of the porcine pancreas (duodenal lobe) is connected to the duodenum, the body (splenic lobe) follows the curvature of the stomach, passes the portal vein on the anterior side and extends to the left kidney (tail end of the splenic lobe) [63,64]. The unique anatomical arrangement of the colon in pigs complicates ventral acoustic access to the pancreas compared to humans. In the latter, only the transverse mesocolon overlaps the head and neck of the pancreas while in the former, most of the colon is arranged in a series of spirals located in the upper left quadrant of the abdomen, blocking access to the duodenal lobe of the pancreas [61,63]. Thorough bowel preparation is therefore required to minimize feces and air pockets in the colon. Despite this obstacle, the similarity in anatomical dimensions and the structural resemblance of the human and porcine pancreas make the pig the predominant model for preclinical studies on HIFU treatment of PaC [65-71].

    Here, we describe the developed protocol and discuss the difficulties which arose from the anatomical location of the pancreas during our experiments using MR-HIFU. The predictive power of the applied ultrasound energy and the measurement of the lesion size *via* the diameter of the thermal dose- and thermal threshold profiles and contrast enhanced MRI are evaluated as well. Acoustic access to the pancreas was supported by a custom compression spacer and its effect on the distance from the skin to the pancreas was assessed.

## MATERIALS AND METHODS

### Animal Model

In this study, the feasibility of selective ablation of the porcine pancreas using MR-HIFU was investigated in five healthy, female German landrace pigs between 35 and 58 kg in weight. The experimental protocol was approved by the State Agency for Nature, Environment and Consumer Protection of North Rhine Westphalia. The animals underwent bowel preparation starting 96 h prior to induction of anesthesia ($t = -96$ h). From that time point on, they were fed Dutch vanilla custard ("Vla") exclusively with free access to water. Starting at $t = -96$ h and ending at $t = -48$ h, a laxative was added to the custard (200 g per animal and day; Agiolax® Madaus, MEDA Pharma). From $t = -12$ h until the experiment, the pigs were fasted with free access to water and were fed three capsules of Simeticone (Lefax Intense 250 mg, Bayer, Germany) to promote elimination of gas pockets.

    At the beginning of the experiment, the animals received an intramuscular injection of Atropine (0.02 mg/kg; WDT, Germany) and Tiletamin/Zolazepam (10 mg/kg; Zoletil, Virbac, Germany). Anesthesia was induced and maintained intravenously using Propofol (induction: 1.66 mg/kg i.v., maintenance: 4.0–9.5 mg/kg/h as required; Fresenius,

Bad Homburg, Germany). Analgesia was achieved by intravenous administration of buprenorphine (0.02 mg/kg; Buprenovet Multidose, Bayer, Germany). The pigs were intubated and ventilated under pressure-control (Hamilton C1, Heinen + Löwenstein, Switzerland) at 30 % oxygen, 14 breaths/min, and a positive end-expiratory pressure (PEEP) of 5–8 mmHg. The tidal volume was adjusted as needed to maintain normocapnia (PaCO2 35–45 mmHg). A catheter (18G; Arrow International, Reading, USA) for the continuous administration of propofol and Ringer's solution (5 ml/kg/h; Fresenius Kabi, Germany) was placed in the right external jugular vein using the Seldinger technique. The transportation to the MR-HIFU lab was performed with the animal in prone position. During the experiment, several phases of apnea at 10 mbar of airway pressure were induced to suspend motion for imaging and sonication. To prevent hypoxia, all animals were ventilated with 100 % oxygen beforehand for preoxygenation and denitrogenisation until end expiratory oxygen concentrations reached >85 %. Before the first sonication, a dose of Buscopan (2 mg/kg i.v., Sanofi, Paris, France) was administered to suppress peristaltic movement. After the sonications, animals were euthanized using sodium-pentobarbital (150 mg/kg i.v., Euthadorm®, CP-Pharma, Burgdorf, Germany). Laparotomy was performed and sites of thermal injury along the beam path were documented if present.

The study was preceded by a pilot study in three animals in which the used MRI sequences and anesthesia protocols were optimized (data not shown), the depth of the pancreas inside the animal without a compression spacer was assessed, and sonication of the pancreas without the addition of a compression spacer was attempted, which proved to be unfeasible due to the lack of acoustic access to the pancreas. The animals in the pilot study were prepared in the same way as the animals in the subsequent feasibility study, with the exception that these animals instead were fed Calshake (Fresenius, Bad Homburg, Germany) and were not given a laxative.

### Experimental setup

The experiments were performed using a clinical MR-HIFU system (3T Achieva®, Philips Healthcare, Best, The Netherlands, and Sonalleve® V2 HIFU, Profound Medical, Mississauga, Canada), which was operated using the Sonalleve® software release 3.5.1271.1817. The employed Sonalleve® V2 HIFU System has not yet been approved by the FDA for the treatment of pancreatic cancer. The patient table of the used system contains a 256-element phased array transducer immersed in an oil bath with a radius of curvature of 140 mm and an aperture of 135.9 mm [72].

A polyacrylamide spacer with a drop-shaped dome, which displaced the bowels and thereby facilitated acoustic access to the pancreas, was interposed between the HIFU window and the animal (Figure 1). The influence of a similar spacer on the quality of temperature mapping was studied previously by Ferrer *et al.* [73]. A thin layer of degassed

and demineralized water was applied to the HIFU window to establish acoustic coupling to the spacer. The compression spacer was positioned on the HIFU window with the dome's point towards the intended cranial direction of the animal. The spacer was held in place using a frame of adhesive tape applied to the edges of the HIFU window. Acoustic coupling was further optimized by shaving and washing of the pig's abdomen as well as the application of degassed ultrasound gel to both the pig's abdomen and the spacer. The animal was rolled onto the spacer along the head-tail axis to prevent the trapping of air bubbles, bringing it into prone position with the xiphoid process at the cranial end of the HIFU window.
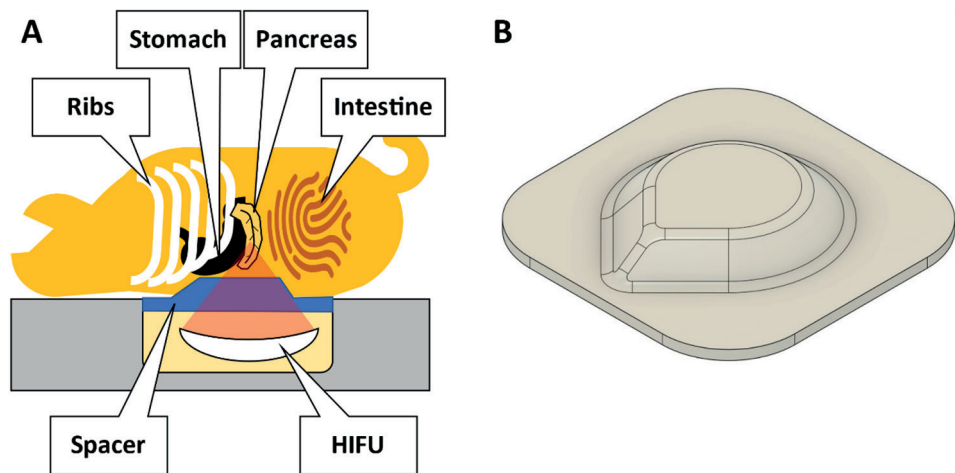


**Figure 1:** (**A**) Experimental setup. The pigs were positioned on the patient table in prone position. The abdomen was compressed using a custom-made hydrogel spacer (**B**) inserted between the animal and the table's acoustic membrane.

*Spacer fabrication*

All chemicals used to create the spacers were purchased from Sigma Aldrich (Sigma-Aldrich Corporation, St. Louis, Missouri, USA) and their respective ratios are detailed in Table 1. The shape of the spacer was chosen based on T1-weighted MRI imaging data from the pilot study and was modeled in Fusion 360 (Autodesk, San Rafael, CA, USA). Using a 3D-printer (Prusa i3 MK3, Prusa Research, Czech Republic), a model of the spacer was manufactured from polylactic acid. Using this model, a mold of the spacer was created from silicone (HS620, Versandhandel Blioch, Ahrensburg, Germany). All necessary ingredients for the hydrogel were mixed under stirring. APS was added last to initialize polymerization and the solution was poured into the mold. Ten minutes after the onset of polymerization, the spacer was removed from the mold and stored in an

airtight container. For a technical drawing of the spacer and the acoustic properties of the material, see supplementary information S1 and S2.

**Table 1:** Composition of the spacers used in this study.

| Component | Product code | Fraction of volume |
|---|---|---|
| De-ionized & degassed water | – | 82.24% (v/v) |
| Acrylamide/bis-acrylamide (ratio: 19:1), 40% (w/v) solution | A9926-5L | 17.55% (v/v) |
| TEMED | T7024-100ML | 0.21% (v/v) |
| APS | 248614-500G | 0.21% (w/v) |

*Abbreviations:* **EMED**: N,N,N',N'-tetra-metylethylenediamine; **APS**: ammonium peroxydisulfate.

## MR Imaging

All images were acquired using the HIFU table's window coil and the HIFU pelvis coil (Model 905051-F, Philips Healthcare, Best, The Netherlands). Motion artefacts and organ displacement were avoided by inducing apnea. All scan protocols and sonications were started with a delay of about 5 s after reaching the set apnea pressure to provide enough time for the settlement of organ movement.

*Treatment planning*

The treatments were planned using 3D T1-weighted turbo field echo (TFE) sequences with and without spectral attenuated inversion recovery (SPAIR) fat suppression. The used parameters were TE = 1.46 ms, TR = 3.2 ms, FA = 10°, slice thickness = 4 mm, number of slices = 150, TFE factor = 69, NSA = 1, SENSE factor (RL, FH) = (2, 1.5) , ACQ (RECON) voxel MPS = 1.79 x 1.82 (1.52 x 1.53) mm, water-fat shift = 0.7 pixels, startup echoes = 0, fold-over direction = RL, and no TFE pre-pulses. This resulted in an acquisition duration of 13.4 s.

*Treatment monitoring*

All sonications were monitored using PRFS-thermometry *via* an RF-spoiled gradient echo sequence (T1-FFE) with TR = 30 ms, TE = 19.5 ms (animals 1, 2 and 3) or 15 ms (animals 4 and 5), FOV (RL, HF) = 400 x 250 mm, EPI factor = 9, number of slices = 6, reconstructed voxel dimensions = 2.5 x 2.5 x 7 mm$^3$, resulting in an acquisition time of 2.66 s (animals 1, 2 and 3) or 2.25 s (animals 4 and 5) for a full set of slices. Fat suppression was performed using selective excitation. The MR thermometry slices were positioned in four stacks, namely the focus- (3 slices), sagittal- (1 slice), near field- (1 slice), and far field (1 slice) stacks. The focus stack was positioned at the HIFU focus point and was oriented perpendicular to the transducer axis to provide a complete view of the volumetric temperature distribution in

the target area. The sagittal stack was positioned to show the long axis of the HIFU focus. The nearfield stack was positioned deep to the subcutaneous fat layer to monitor excess heat generation in the abdominal muscles. The far field stack was positioned behind the focus to monitor heat generation at the spine.

### Post-interventional MRI

The sonications were evaluated using the 3D T1-weighted TFE sequences described above, both before and one minute after intravenous contrast agent injection (0.1 mmol/kg, Dotagraf, Jenapharm GmbH & Co. KG, Jena, Germany). The parameters and field of view of the post-treatment scans were kept the same as the planning scans. For evaluation, the images acquired after contrast agent injection were subtracted from their pre-injection counterpart to reveal non-perfused volumes (NPVs).

### Treatment protocol

The splenic and duodenal lobes of the pancreas were identified using the planning images and one target point was selected in each. Care was taken to maintain 1.5 cm between the two target points and to avoid intersection of the ultrasound beam with air pockets, feces, and bones. Cessation of peristaltic motion was verified by continuous temperature mapping. Each sonication was preceded by test sonications (fixed focus position, 1.2 MHz) using an acoustic output power between 100 and 150 W, depending on the observed heating efficiency, to verify acoustic coupling and alignment of the focus point with the target volume. Offsets between the observed and intended center of heating were corrected by the adjustment of the transducer position and beam steering. Next, the target points were sonicated in two separate apnea phases using a sonication protocol with fixed acoustic output power of either 300 W or 400 W and a circular eight-point focus trajectory with a diameter of 4 mm (4 mm regular sonication cell, max. sonication time 60 s, 1.2 MHz, first described by Köhler *et al.* [42]). According to simulations performed by the manufacturer, this sonication protocol results in a spatial peak, time-averaged intensity of 3.64 W/cm$^2$ per Watt of acoustic output power in water. The sonication power was chosen based on clinical research published on US-HIFU treatment of PaC [26,31,32,74]. The sonications were stopped manually when a safety hazard, such as spontaneous breathing or excessive off-target heating, was observed or when the temperature in the target area was deemed high enough by the operator to achieve rapid ablation. This resulted in sonication times between 7.5 s and 29.9 s and thermal lesions of various diameters.

## Data analysis

*Evaluation of sublethal sonications*

The sonications that did not lead to a visible or palpable thermal lesion in the pancreas upon excision of the organ were documented and possible causes were analyzed. The scheme displayed in Figure 2 shows possible explanations for the absence of a thermal lesion in the pancreas and the observations that were considered in judging the most likely explanation for each individual case. The threshold of 3.99 kJ was used for judging the applied energy insufficient to create a thermal lesion as this was the smallest energy which led to a thermal lesion in the experiments.
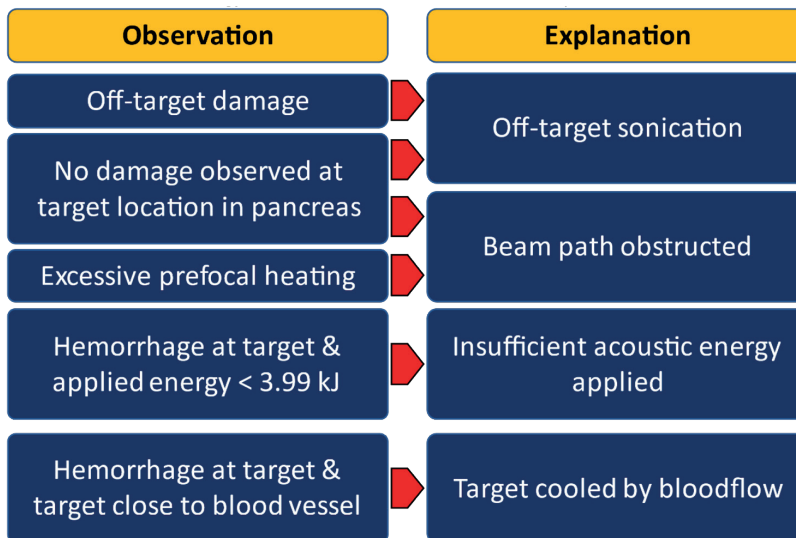


| Observation | Explanation |
|---|---|
| Off-target damage | Off-target sonication |
| No damage observed at target location in pancreas | |
| Excessive prefocal heating | Beam path obstructed |
| Hemorrhage at target & applied energy < 3.99 kJ | Insufficient acoustic energy applied |
| Hemorrhage at target & target close to blood vessel | Target cooled by bloodflow |

**Figure 2:** Explanations for the absence of coagulative necrosis at the target location of the pancreas (right column) and supporting evidence (left column). The complete absence of damage may be due to off-target sonication or an obstruction of the beam.

*Histology*

The pancreas was excised in toto. The treated areas of the pancreas were marked with surgical clips and fixated in a 4 % v/v solution of formaldehyde. Rapid fixation of the pancreas is essential due to the early onset of autolysis in this organ and the slow penetration of formaldehyde into bulky tissue samples [75,76]. After 48 h, the samples were transferred to phosphate-buffered saline and stored until gross examination (see *Analysis of the lesion size*). After gross examination, the fixated tissue samples were trimmed and sliced through the center of the target area, perpendicular to the sample's surface. They were dehydrated using increasing concentrations of alcohol (2-propanol,

Th. Geyer Hamburg GmbH, Hamburg, Germany), treated with an intermedium (Histo-Clear, National Diagnostics, Atlanta, Georgia, USA) and embedded in paraffin (Paraplast Plus, Sigma Life Sciences, Darmstadt, Germany). The embedded samples were sliced and stained using hematoxylin and eosin. Examination was performed using a brightfield microscope (BX53, Olympus, Japan).

*Analysis of the lesion size*
For the evaluation of the lesion size by gross examination, each piece was placed on an even surface next to a ruler and a photograph was taken to generate a near-isometric view of the sample with a reference scale. The photographs were then analyzed using the *Measure* tool of ImageJ, Version 1.52a (National Institutes of Health, USA; http://imagej.nih.gov/ij). The longest and the shortest axis of the ablated area visible as white necrotic core on the tissue piece's surface were measured. The average of both measurements will be referred to as the lesion size. The lesion size was correlated with the applied acoustic energy (transducer output x sonication time) and the acoustic energy after attenuation by the spacer and the prefocal tissue. The acoustic energy after attenuation will be referred to as the delivered energy $E_D$ and is calculated from the applied power $P_{applied}$ and the sonication time $t$ based on the combined attenuation coefficient $\alpha$ of the spacer at 37 °C and the prefocal tissue, using the parameters determined by Hwang *et al.* [67] for the latter:

$$E_D = P_{delivered} \cdot t \tag{2}$$

$$P_{delivered} = P_{applied} \cdot 10^{-\frac{\alpha(l_1, l_2, l_3)}{10 \text{ dB}}} \tag{3}$$

$$\alpha(l_1, l_2, l_3) = 0.04 \frac{\text{dB}}{\text{cm}} \cdot l_1 + 1.44 \frac{\text{dB}}{\text{cm}} \cdot l_2 + 0.96 \frac{\text{dB}}{\text{cm}} \cdot (l_3 - l_2) \tag{4}$$

where $l_1$ is the thickness of the spacer along the transducer axis, $l_2$ is the thickness of the abdominal wall (skin to the deep surface of the abdominal muscles) and $l_3$ is the total length of the prefocal beam path inside the animal along the transducer axis. The attenuation coefficients reported by Hwang *et al.* were measured for the acoustic frequency of 1 MHz and were therefore adjusted to 1.2 MHz using a linear model of the attenuation coefficient's frequency ($\omega$) dependence [77]:

$$\alpha(\omega) = \alpha_0 \omega^b, \qquad b = 1 \tag{5}$$

For the thermal threshold- and dosimetry-based prediction of the lesion size, the spatial extent of the area which exceeded 57 °C at any time during the treatment and the extent

of the area which accumulated a thermal dose of 240 CEM43 was assessed. To this end, the lengths along the longest and the shortest axes of the corresponding contour plots in the central slice of the focus stack were measured using a custom python application (thermal threshold) and the Sonalleve GUI measurement tool (thermal dose). The arithmetic mean of the respective measurements will be referred to as the thermal threshold prediction $d_{57}$ and the dosimetry prediction $d_{240}$ of the lesion size. The measurements were performed on the first slice acquired after the end of the respective sonication. The NPV diameter was measured perpendicular to the transducer axis in the transverse imaging planes of the contrast enhanced MR scans. The measurements were performed from the center of one hyperemic rim to the other and will be referred to as the NPV prediction of the lesion size $d_{NPV}$. The quality of $d_{57}$, $d_{240}$ and $d_{NPV}$ as predictors for the lesion size was assessed *via* the mean squared deviation (MSD) from the lesion size found in gross examination.

*Analysis of the compression spacer's influence on the intraabdominal beam path length*
The depth of each pig's pancreas as shown in the acquired anatomical MRI images was measured using the "Measurements and Tools > Length" tool of the RadiAnt software (Medixant, Poznan, Poland). Both the distance of the organ's surface closest to the HIFU window (ventral limit) and the organ's surface farthest from the HIFU window (dorsal limit) to the skin of the abdomen were measured in a vertical line. Additionally, each measurement was repeated between the respective surface of the organ and the HIFU window. The measured distances were then used to assess the effect of the spacer's influence on the length of the beam path inside the abdominal cavity.

## Statistics

The correlation of the lesion size with $E_A$ and $E_D$ was analyzed *via* linear regression and the coefficient of determination using the linear_model.LinearRegression module and the LinearRegression.score method of the sklearn python 2.7 package (version 0.20.1). The spacer's influence on the length of the beam path was analyzed *via* Welch's t-test using the stats.ttest_ind module of the scipy python 2.7 package (version 1.1.0).

## RESULTS

### Overview

The sonication results of the study group are summarized in Table 2. Eight out of ten sonications resulted in visible damage at the target site. Five sonications induced a lesion of coagulative necrosis, which was confirmed by histology. Injury of the abdominal skin, abdominal wall, the spleen, or the stomach was not observed in any of the animals. One sonication resulted in clearly discernible bowel damage (animal 3). Hyperemia

**Table 2:** Sonication results overview.

| Pig number / sonication number | 1/1 | 1/2 | 2/1 | 2/2 | 3/1 | 3/2 | 4/1 | 4/2 | 5/1 | 5/2 |
|---|---|---|---|---|---|---|---|---|---|---|
| Pig Weight [kg] | 36.5 | 36.5 | 38 | 38 | 35 | 35 | 39 | 39 | 58 | 58 |
| Applied Acoustic Power [W] | 300 | 300 | 300 | 300 | 300 | 400 | 300 | 300 | 300 | 300 |
| Applied Energy [J] | 3720 | 2250 | 8190 | 5550 | 5610 | 11960 | 7620 | 4620 | 3990 | 8160 |
| Delivered Energy [J] | 1521 | 829 | 2078 | 1548 | 1400 | 2862 | 2484 | 1649 | 940 | 1965 |
| Maximum target temperature [°C] | 61.90 | 68.09 | 94.90 | 50.10 | 57.70 | 62.91 | 66.90 | 63.95 | 53.51 | 52.68 |
| Damage induced in pancreas | - | + | + | - | + | + | + | + | + | + |
| Coagulative necrosis induced in pancreas | - | - | + | - | + | - | + | + | - | - |
| Lesion size min/max/mean [mm] | -/- | -/- | 7.5/ 8.7 / 8.10 | -/- | 2.9/ 4.3 / 3.60 | -/- | 9.4/ 11.8 / 10.60 | 5.7/ 8.0 / 6.85 | 1.7/ 1.7 / 1.70 | -/- |
| Threshold measurement min/max/mean [mm] | 5.3/ 6.1 / 5.7 | 7.6/ 9.5 / 8.55 | 7.5/ 10.3 / 8.90 | 4.4/ 9.0 / 6.70 | 2.8/ 8.2 / 5.50 | 2.5/ 8.0 / 5.25 | 8.3/ 9.8 / 9.05 | 5.6/ 6.8 / 6.20 | -/- | -/- |
| Dosimetry measurement min/max/mean [mm] | 7.2/ 9.8 / 8.50 | 9.8/ 11.7 / 10.75 | 7.4/ 9.5 / 8.45 | -/- | 2.9/ 6.6 / 4.75 | 8.6/ 10.1 / 9.35 | 10.4/ 12.3 / 11.35 | 7.4/ 9.9 / 8.65 | -/- | -/- |
| NPV measurement [mm] | 0.0 | 0.0 | 8.4 | 0.0 | 3.4 | 0.0 | 8.0 | 6.7 | 0.0 | 0.0 |
| Prefocal heating >56 °C | + | - | - | - | + | + | + | - | - | - |
| Damage in adjacent organs | - | - | - | - | + | - | - | - | - | - |
| PV within 1 cm of target volume | - | - | - | - | - | - | - | - | - | + |

*Abbreviations:* **NPV:** non-perfused volume; **PV:** Portal vein.

in the omental fat adjacent to the pancreas was observed in two cases (animals 3 and 4). In sonication 3/2, 400 W of acoustic power were applied as the selected volume lay particularly deep inside the animal, resulting in poor heating efficiency during the test sonications.

## Analysis of sublethal sonications

Of the five target sites that did not show a thermal lesion, two exhibited no damage at all (1/1 and 2/2). According to the arguments outlined in Figure 2, this may have been caused by insufficient heating or a migration of the pancreas out of the HIFU focus. Sonication 1/1 showed very minor heating at the target location in both the focus slice and the sagittal slice, but strong prefocal heating and heating offset from the target volume (Figure 3A), which prompted early cancellation with low overall energy being delivered. We therefore believe that the acoustic energy deposited in the pancreas was not sufficient to induce damage. During sonication 2/2, spontaneous breathing occurred due to insufficient depth of anesthesia. As a result, the target volume was displaced out of the HIFU focus and the sonication was canceled before damage was induced (Figure 3C).

Sonications 1/2, 3/2 and 5/2 resulted in damage at the target site but did not lead to the formation of a thermal lesion. In sonication 1/2, this can be attributed to the relatively small amount of acoustic energy that reached the pancreas. The sagittal temperature map also shows a small deviation of the heated area's shape from the usual elongated form. It is therefore possible that the ultrasound was absorbed mainly before the pancreas (Figure 3B). Sonication 3/2 was performed with the highest amount of energy among all experiments and prefocal heating was observed only close to the intended focal volume. The target volume was placed in an area of the pancreas directly adjacent to the bowels, which sustained damage that was clearly discernible during gross examination. It is therefore likely that a large part of the acoustic energy was absorbed by stool in the adjacent bowel loop, leading only to hyperemia in the pancreas (Figure 3D). Sonication 5/2 was performed with high acoustic energy compared to other sonications, exhibited limited prefocal heating (Figure 3E), did not induce any visible damage to other organs, and did not lead to a thermal lesion. MR-imaging showed that the center of the target volume was located at a distance of only 5 mm to the surface of the portal vein. It is therefore likely that the perfusion and cooling of the target volume by the nearby blood vessel prevented sufficient buildup of heat (Figure 3F).

Coagulative necrosis was predicted by the thermal dose measurement in three sonications that did not produce a thermal lesion in the pancreas (1/1, 1/2, and 3/2). In sonication 3/2, this can be attributed to the displacement of the pancreas out of the HIFU focus as damage was induced in the bowels. During sonications 1/1 and 1/2, no motion or erratic temperature measurements were observed in the target volume. Creation of

a false positive by thermometry artifacts can therefore be ruled out. Damage to other organs was not observed during examination.
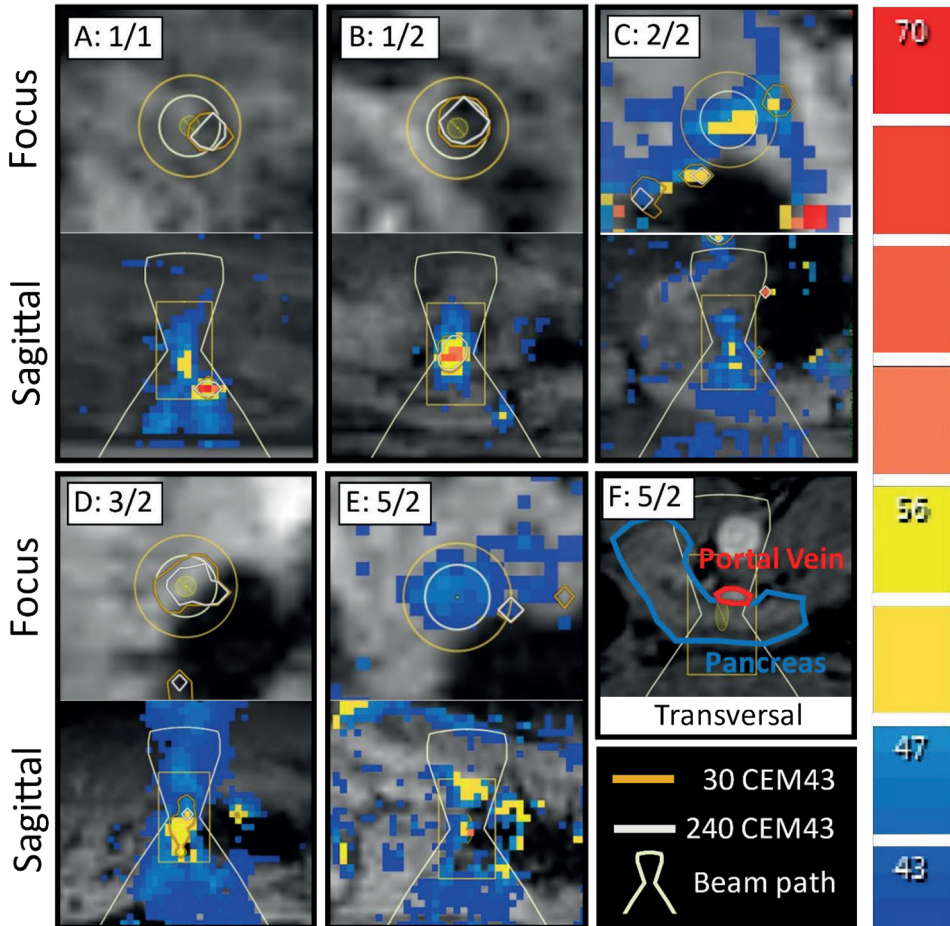


**Figure 3:** Snapshots of thermometry maps acquired during sublethal sonications. (**A**) Sonication 1/1: Offset of thermal dose profile in focus slice and prefocal heating in sagittal slice. (**B**) Sonication 1/2: Strong focal heating despite small amount of delivered energy and irregular shape of heated volume. (**C**) Sonication 2/2: Motion artifacts due to respiration in focus slice; insufficient heating measured in sagittal slice before movement. (**D**) Sonication 3/2: Signal void indicative of air or solid near focus observed in focus slice and strong prefocal heating in sagittal slice. (**E**) Sonication 5/2: Limited heating in the focus, only mild prefocal heating. (**F**) Sonication 5/2: Proximity of the target area to the portal vein likely prevented sufficient heating for the creation of a thermal lesion.

## Histology

Coagulative necrosis in the focal area was confirmed by histology in all samples which showed a white necrotic core in gross examination (2/1, 3/2, 4/1, 4/2, and 5/1). The focal areas of these samples exhibited coherent cell bodies with fragmented nuclei and no hemorrhage, indicative of coagulative necrosis (Figure 4A). The focal areas were surrounded by a border region of low cellular cohesion (Figure 4B) and hemorrhage (Figure 4C), which then transitioned into healthy pancreas parenchyma (Figure 4D).
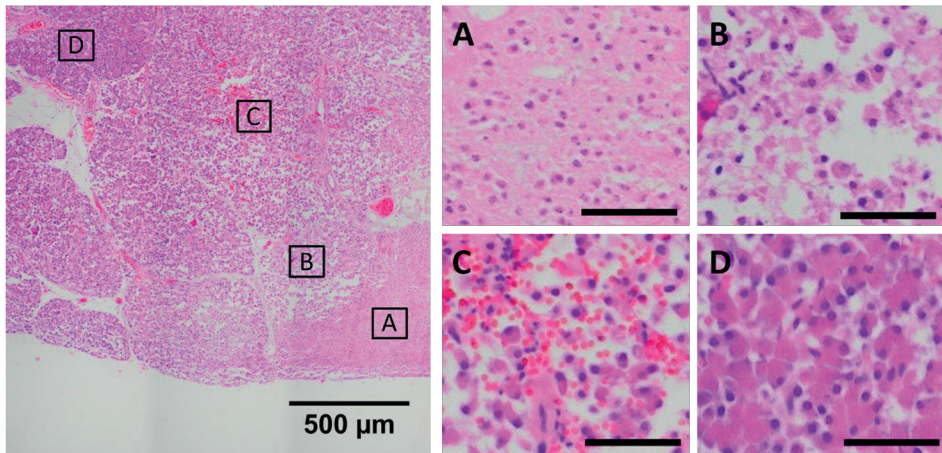


**Figure 4:** Representative images of the different degrees of thermal damage induced by HIFU in the porcine pancreas, from sample 4/2. The scale bars in the subfigures represent 50 µm. (**A**) Center of the focal area, exhibiting coherent cells with fragmented nuclei and no hemorrhage. (**B**, **C**) Border region, exhibiting a loss of cohesion between cells and hemorrhage. (**D**) Healthy pancreas parenchyma.

## Analysis of the lesion size

The fixated pancreas samples are shown in Figure 5. In Figure 6A-B, the diameters of the thermal lesions created throughout the experiments are drawn versus the applied ultrasound energy $E_A$ and the delivered ultrasound energy $E_D$. The coefficients of determination $R^2$ of the ordinary least squares (OLS) regression for the applied and the delivered energy are 0.61 and 0.96, respectively. The resulting linear approximations $D_{AE}$ and $D_{DE}$ are:

$$D_{AE} = 1.33 \, \frac{\text{mm}}{\text{kJ}} \cdot (E_A - 0.77 \text{ kJ}) \tag{6}$$

$$D_{DE} = 6.08 \, \frac{\text{mm}}{\text{kJ}} \cdot (E_D - 3.84 \text{ kJ}) \tag{7}$$

The MSD of the thermal threshold monitoring, thermal dose monitoring and NPV measurement were 2.01 mm², 1.60 mm², and 1.98 mm², respectively. The corresponding lesion size predictions $d_{57}$, $d_{240}$, and $d_{NPV}$ are plotted against the results of gross examination in Figure 6C-E.
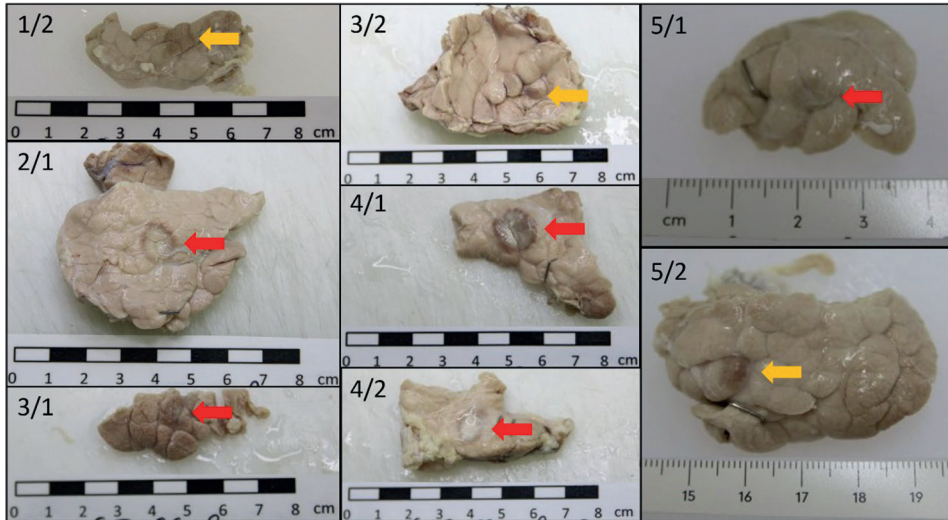


**Figure 5:** Fixated pancreas samples. Red arrows indicate thermal lesions of coagulative necrosis. Yellow arrows indicate non-ablative tissue damage.

### Analysis of the compression spacer's influence on the beam path length

Only two animals from the pilot study were included in the analysis to obtain data on the length of the beam path without a spacer as an error in the positioning of the third animal prevented the measurement of the pancreas' depth in the manner described above. Instead, pig 4 was scanned both with and without a spacer. The weight of the animals appeared to have an influence of approximately $1.05 \frac{mm}{kg}$ on the ventral limit of the pancreas without a spacer and $0.29 \frac{mm}{kg}$ with a spacer (Figure 7A-B).

The depths of the ventral and dorsal limits of the pancreas with and without spacer are shown in Figure 7C. The average depth of the ventral limit from the skin with and without the addition of a spacer were 41 ± 4 mm and 65 ± 10 mm, respectively. The depths of the dorsal limits of the pancreas from the skin with and without spacer were 79 ± 4 mm and 114 ± 11 mm, respectively. On average, the acoustic beam path from the skin was therefore shortened by 24 ± 6 mm for the most ventral part of the pancreas and by 35 ± 6 mm for the most dorsal part. The average depths of the ventral and dorsal limits of the pancreas from the surface of the table's acoustic window with a spacer were 76 ± 6 mm and 112 ± 5 mm, respectively. The overall length of the beam path from the acoustic window therefore remained largely unaffected by the addition of a spacer.
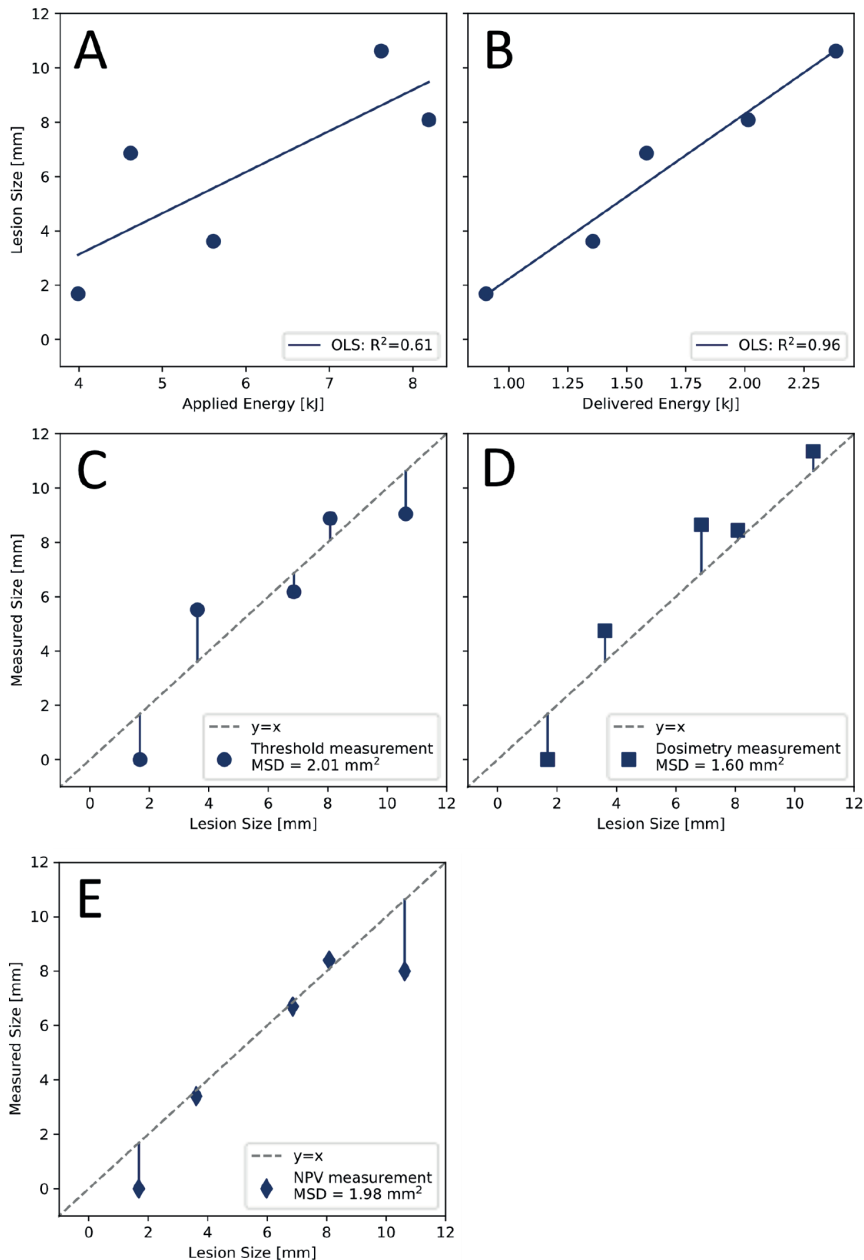
**Figure 6:** Predictive power of different parameters for the lesion size found in gross examination after fixation. Lesion size versus (**A**) applied acoustic energy, (**B**) delivered acoustic energy. Measurement of the lesion size *via* (**C**) temperature threshold monitoring (57 °C), (**D**) thermal dose monitoring (240 CEM43), and (**E**) post-treatment contrast enhanced MRI. **OLS**: ordinary least squares; **MSD**: mean squared deviation; **NPV**: non-perfused volume.

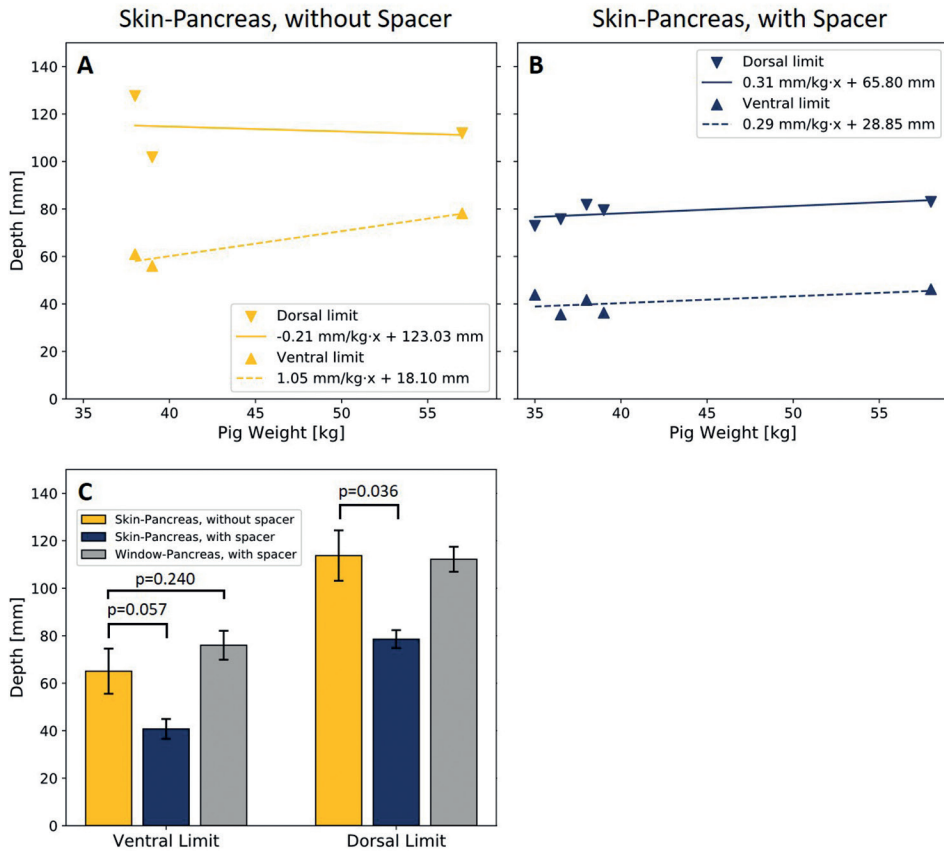**Figure 7:** (**A**) Depth of the pancreas from the skin without a spacer (n = 3) and (**B**) the depth from the skin and from the acoustic window with a spacer (n = 5) versus animal weight. (**C**) Side-by-side comparison of ventral and dorsal limits. Probability values were obtained using Welch's t-test.

## DISCUSSION

We introduced an experimental setup and procedure which enables sonication of the porcine pancreas under MR-guidance using a clinical MR-HIFU system. The use of a custom hydrogel spacer appeared a necessary addition to create an acoustic window by compressing tissue located in front of the pancreas and to displace bowel loops. The spacer notably shortened the distance that needed to be penetrated by the ultrasound inside the animals' abdomen, reducing ultrasound attenuation and the risk of bowel loop interposition without significantly increasing the overall distance between the HIFU window and the pancreas. Furthermore, bowel preparation prior to treatment appeared to be crucial as the presence of feces or air pockets in the bowel led to strong

prefocal absorption of ultrasound with off-target heating in the pilot study (data not shown). If bowel loop interposition occurred despite the use of bowel preparation and a compression spacer, this could often be resolved by massaging the animal's abdomen with hand motions in caudal direction. Ablations were performed during short periods of apnea in expiration, using a PEEP of 10 mbar. This allowed the use of established MRI sequences for planning, PRFS-thermometry, and post-interventional imaging as well as the use of standard sonication protocols without the need for motion compensation in imaging or treatment. Above protocol allowed successful MR-guided HIFU sonication of the porcine pancreas in eight out of ten attempts. One sonication likely failed to induce damage in the pancreas due to the partial obstruction of the beam path and one failed due to insufficient suppression of respiration, leading to movement of the pancreas. In three of the eight successful sonications, the acoustic energy delivered to the pancreas was insufficient to induce coagulative necrosis in the focal area. The reasons that were identified for this were the application of too little acoustic energy, the displacement of the pancreas out of the HIFU focus after acquisition of the planning images, and the rapid cooling of the target tissue by the adjacent portal vein.

The successful delivery of focused ultrasound energy to the porcine pancreas achieved with this technique shows that MRI has potential for the planning and monitoring of HIFU treatments of the pancreas: Acoustically opaque areas, i.e., gas pockets in the stomach or bowels, solid bowel content, and bones, can be identified and avoided due to the capability to display them in high-contrast, high-resolution cross-sections with an overlay of the exact HIFU beam path. In PaC patients, nearby critical organs, i.e., the stomach, major blood vessels and the common bile duct (possibly containing a stent), can also be made visible using MRI [78-80] and should not be in the focal area during sonication, but successful US-HIFU treatments close to these structures have already been demonstrated [26]. Fiducial markers, which may be present due to prior radiotherapy, can also be visualized [81,82] and should be avoided. During the sonication, MR-guidance enables near-real-time monitoring of the temperature in the target volume and adjacent tissue. These measurements were used to track the areas that received the lethal thermal dose of 240 CEM43 and the areas which exceeded the temperature threshold of 57 °C. The diameter of these areas matched the diameter of the thermal lesions found upon gross examination on the scale of the voxel size, with the thermal dose performing slightly better than the threshold. In this study we used sonication protocols with fixed acoustic power and beam trajectories and no feedback mechanisms to control the lesion size. Since a good agreement was found between the diameter of the thermal dose profile and the diameter of the resulting thermal lesion, it should be feasible to create thermal lesions of a specific size in the pancreas with high accuracy using feedback algorithms, such as previously published by Enholm *et al.* [41]. We have also found that the size of the created thermal lesions correlated well with the applied acoustic energy after accounting

for attenuation by the spacer and prefocal tissue, opening the possibility to control the lesion size *via* this parameter. This can easily be implemented in the current workflow as the required measurements can be extracted directly from the imaging data used for treatment planning.

The main limitations of this study are the absence of a pancreatic tumor in the treated animals, the small number of the induced thermal lesions, and that tissues may change in volume during fixation by a certain percentage [83]. The linear models and predictive powers we derived in this study will therefore not necessarily be representative of the relationships in the clinical application. Furthermore, as the animals were euthanized without an observation period following the treatments, the study does not allow conclusions concerning the frequency and severity of potential adverse events. This is of note as the thermal lesions of two sonications in which coagulative necrosis was indicated by thermal dosimetry were not accounted for during dissection of the animals, leaving open the question of where exactly they formed. Finally, with one exception, the depth of each animal's pancreas was assessed only either with or without a spacer. While there is little doubt that the spacer does shorten the intraabdominal beam path to the pancreas, the magnitude of the observed difference may have been distorted by differences in the weight, anatomy, and preparation of the animals.

In conclusion, despite some inherent limits to its transferability, the pig is the best preclinical model for the translational development of HIFU technology targeting PaC due to the resemblance of the porcine and human pancreas as well as the similar anatomical dimensions. We have therefore established a treatment protocol which allows the HIFU sonication of the porcine pancreas using a clinical MR-HIFU system and described it here in detail. The size of the thermal lesions created in the pancreas correlated well with the attenuation-corrected ultrasound energy and can be monitored using PRFS-thermometry. Apart from the compression spacer, the software and hardware employed is already in clinical use for the MR-guided HIFU treatment of uterine fibroids and bone metastases. The presented methods and findings should therefore facilitate further research and thereby accelerate clinical translation of this promising application.
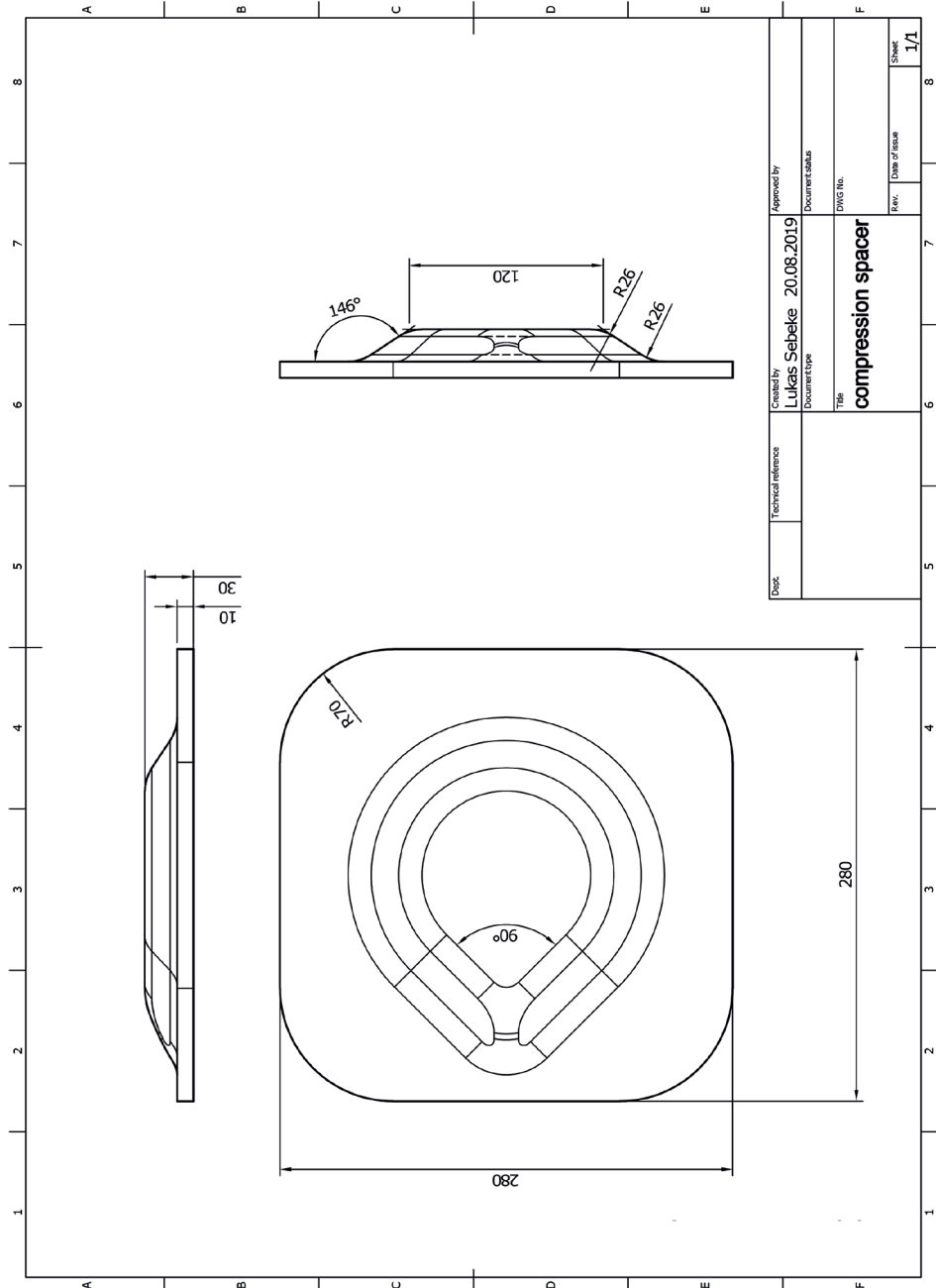
## ACKNOWLEDGEMENT

# SUPPLEMENTARY INFORMATION

## S1: Technical drawing of the compression spacer

## S2: Acoustic properties

The polyacrylamide material from which the spacers were manufactured was characterized using the finite-amplitude insertion-substitution (FAIS) method. The measurements were performed by the Therapy Ultrasound team of the Joint Department of Physics / Division of Radiotherapy and Imaging at the Institute of Cancer Research, London, UK. Measurements at different temperatures were taken in ascending order up to 50 °C. Two additional measurements were performed during cooldown at 37 °C and 25 °C.

**Table S3:** Acoustic Properties of the polyacrylamide material used in manufacturing the spacer. The rows "37 down" and "25 down" were measured during cooldown.

| Temperature [°C] | Thickness [cm] | SoS [m/s] | Attenuation coefficient [dB/cmMHz] | Exponent of attenuation coefficient |
|---|---|---|---|---|
| 20 | 1.55 ± 0.02 | 1516 ± 0.5 | 0.044 ± 0.006 | 1.75 ± 0.11 |
| 25 | 1.55 ± 0.03 | 1528 ± 0.7 | 0.036 ± 0.005 | 1.83 ± 0.08 |
| 30 | 1.54 ± 0.03 | 1539 ± 0.8 | 0.036 ± 0.005 | 1.69 ± 0.08 |
| 37 | 1.54 ± 0.03 | 1552 ± 0.9 | 0.031 ± 0.005 | 1.78 ± 0.11 |
| 50 | 1.54 ± 0.03 | 1567 ± 0.8 | 0.019 ± 0.005 | 2.03 ± 0.17 |
| 37 down | 1.58 ± 0.02 | 1553 ± 0.8 | 0.031 ± 0.005 | 1.82 ± 0.08 |
| 25 down | 1.59 ± 0.02 | 1529 ± 0.8 | 0.034 ± 0.004 | 1.82 ± 0.08 |

*Abbreviation:* **SoS:** Speed of Sound.

# REFERENCES

[1]   Bray F, Ferlay J, Soerjomataram I, et al. Global Cancer Statistics 2018: GLOBOCAN Estimates of Incidence and Mortality Worldwide for 36 Cancers in 185 Countries. CA. Cancer J. Clin. 2018;68:394–424.

[2]   Siegel RL, Miller KD, Jemal A. Cancer Statistics, 2019. CA. Cancer J. Clin. 2019;69:7–34.

[3]   Zhang Q, Zeng L, Chen Y, et al. Pancreatic Cancer Epidemiology, Detection, and Management. Gastroenterol. Res. Pract. 2016;2016:1–10.

[4]   Ryan DP, Hong TS, Bardeesy N. Pancreatic Adenocarcinoma. N. Engl. J. Med. 2014;371:1039–1049.

[5]   Isaji S, Mizuno S, Windsor JA, et al. International Consensus on Definition and Criteria of Borderline Resectable Pancreatic Ductal Adenocarcinoma 2017. Pancreatology. 2018;18:2–11.

[6]   Feig C, Gopinathan A, Neesse A, et al. The Pancreas Cancer Microenvironment. Clin Cancer Res. 2012;18:4266–4276.

[7]   Moffat GT, Epstein AS, O'Reilly EM. Pancreatic Cancer – A Disease in Need: Optimizing and Integrating Supportive Care. Cancer. 2019;0:1–9.

[8]   Vincent A, Herman J, Schulick R, et al. Pancreatic Cancer. Lancet. 2011;378:607–620.

[9]   Carlson CL. Effectiveness of the World Health Organization Cancer Pain Relief Guidelines: an Iterative Review. J. Pain Res. 2016;9:515–534.

[10]  WHO. Cancer Pain Relief With a Guide to Opioid Availability. 2nd ed. Cancer Pain Reli. Geneva, Switzerland: World Health Organization; 1996.

[11]  Wong GY, Schroeder DR, Carns PE, et al. Effect of Neurolytic Celiac Plexus Block on Pain Relief, Quality of Life, and Survival in Patients with Unresectable Pancreatic Cancer: A Randomized Controlled Trial. J. Am. Med. Assoc. 2004;291:1092–1099.

[12]  Xiong L. The Preliminary Clinical Results of the Treatment for Advanced Pancreatic Carcinoma by High Intensity Focused Ultrasound. Chin J Gen Surg. 2001;16:345–347.

[13]  Xu Y, Wang G, Gu Y, et al. The Acesodyne Effect of High Intensity Focused Ultrasound on the Treatment of Advanced Pancreatic Carcinoma. Clin Med J China. 2003;10:322–323.

[14]  Yuan C, Yang L, Cheng Y. Observation of High Intensity Focused Ultrasound Treating 40 Cases of Cancer of Pancreas. Chlin J Clin Hep. 2003;19:145–146.

[15]  Xiong LL, Hwang JH, Huang XB, et al. Early Clinical Experience using High Intensity Focused Ultrasound for Palliation of Inoperable Pancreatic Cancer. J. Pancreas. 2009;10:123–129.

[16]  Gao HF, Wang K, Meng ZQ, et al. High Intensity Focused Ultrasound Treatment for Patients with Local Advanced Pancreatic Cancer. Hepatogastroenterology. 2013;60:1906–1910.

[17]  Vidal-Jove J, Perich E, Del Castillo MA. Ultrasound Guided High Intensity Focused Ultrasound for Malignant Tumors: The Spanish Experience of Survival Advantage in Stage III and IV Pancreatic Cancer. Ultrason. Sonochem. 2015;27:703–706.

[18]  Dimcevski G, Kotopoulis S, Bjånes T, et al. A Human Clinical Trial Using Ultrasound and Microbubbles to Enhance Gemcitabine Treatment of Inoperable Pancreatic Cancer. J. Control. Release. 2016;243:172–181.

[19]  Marinova M, Rauch M, Mücke M, et al. High-Intensity Focused Ultrasound (HIFU) for Pancreatic Carcinoma: Evaluation of Feasibility, Reduction of Tumour Volume and Pain Intensity. Eur. Radiol. 2016;26:4047–4056.

[20]  Ji Y, Zhang Y, Zhu J, et al. Response of Patients with Locally Advanced Pancreatic Adenocarcinoma to High-Intensity Focused Ultrasound Treatment: A Single-Center, Prospective, Case Series in China. Cancer Manag. Res. 2018;10:4439–4446.

[21]  Marinova M, Huxold HC, Henseler J, et al. Clinical Effectiveness and Potential Survival Benefit of US-Guided High-Intensity Focused Ultrasound Therapy in Patients with Advanced-Stage Pancreatic Cancer. Ultraschall Med. 2019;40:625–637.

[22]  Wu F, Wang ZB, Cao Y De, et al. Heat Fixation of Cancer Cells Ablated with High-Intensity-Focused Ultrasound in Patients with Breast Cancer. Am. J. Surg. 2006;192:179–184.

[23]  Ter Haar G, Coussios C. High Intensity Focused Ultrasound: Physical Principles and Devices. Int. J. Hyperth. 2007;23:89–104.

2

[24] Dababou S, Marrocchio C, Rosenberg J, et al. A Meta-Analysis of Palliative Treatment of Pancreatic Cancer with High Intensity Focused Ultrasound. J. Ther. Ultrasound. 2017;5:9.

[25] Zhao H, Yang G, Wang D, et al. Concurrent Gemcitabine and High-Intensity Focused Ultrasound Therapy in Patients with Locally Advanced Pancreatic Cancer. Anticancer. Drugs. 2010;21:447–452.

[26] Orsi F, Zhang L, Arnone P, et al. High-Intensity Focused Ultrasound Ablation: Effective and Safe Therapy for Solid Tumors in Difficult Locations. Am. J. Roentgenol. 2010;195:W245-252.

[27] Wang K, Chen Z, Meng Z, et al. Analgesic Effect of High Intensity Focused Ultrasound Therapy for Unresectable Pancreatic Cancer. Int. J. Hyperth. 2011;27:101–107.

[28] Sung HY, Jung SE, Cho SH, et al. Long-Term Outcome of High-Intensity Focused Ultrasound in Advanced Pancreatic Cancer. Pancreas. 2011;40:1080–1086.

[29] Sofuni A, Moriyasu F, Sano T, et al. Safety Trial of High-Intensity Focused Ultrasound Therapy for Pancreatic Cancer. World J. Gastroenterol. 2014;20:9570–9577.

[30] Li P-Z, Zhu S-H, He W, et al. High-Intensity Focused Ultrasound Treatment for Patients with Unresectable Pancreatic Cancer. Hepatobiliary Pancreat. Dis. Int. 2012;11:655–660.

[31] Orgera G, Krokidis M, Monfardini L, et al. High Intensity Focused Ultrasound Ablation of Pancreatic Neuroendocrine Tumours: Report of Two Cases. Cardiovasc. Intervent. Radiol. 2011;34:419–423.

[32] Lv W, Yan T, Wang G, et al. High-Intensity Focused Ultrasound Therapy in Combination with Gemcitabine for Unresectable Pancreatic Carcinoma. Ther. Clin. Risk Manag. 2016;12:687–691.

[33] Sapareto SA, Hopwood LE, Dewey WC. Combined Effects of X Irradiation and Hyperthermia on CHO Cells for Various Temperatures and Orders of Application. Radiat. Res. 1978;73:221–233.

[34] Sapareto S a., Dewey WC. Thermal Dose Determination in Cancer Therapy. Int. J. Radiat. Oncol. 1984;10:787–800.

[35] Damianou C, Hynynen K. The Effect of Various Physical Parameters on the Size and Shape of Necrosed Tissue Volume During Ultrasound Surgery. J. Acoust. Soc. Am. 1994;95:1641–1649.

[36] Chung AH, Jolesz FA, Hynynen K. Thermal Dosimetry of a Focused Ultrasound Beam In Vivo by Magnetic Resonance Imaging. Med. Phys. 1999;26:2017–2026.

[37] McDannold N, Hynynen K, Wolf D, et al. MRI Evaluation of Thermal Ablation of Tumors with Focused Ultrasound. J. Magn. Reson. Imaging. 1998;8:91–100.

[38] Van Rhoon GC, Samaras T, Yarmolenko PS, et al. CEM43℃ Thermal Dose Thresholds: A Potential Guide for Magnetic Resonance Radiofrequency Exposure Levels? Eur. Radiol. 2013;23:2215–2227.

[39] Yarmolenko PS, Moon EJ, Landon C, et al. Thresholds for Thermal Damage to Normal Tissues: An Update. Int. J. Hyperth. 2011;27:320–343.

[40] Dewhirst MW, Viglianti BL, Lora-Michiels M, et al. Basic Principles of Thermal Dosimetry and Thermal Thresholds for Tissue Damage from Hyperthermia. Int. J. Hyperth. 2003;19:267–294.

[41] Enholm JK, Köhler M, Quesson B, et al. Improved Volumetric MR-HIFU Ablation by Robust Binary Feedback Control. IEEE Trans. Biomed. Eng. 2010;57:103–113.

[42] Köhler M, Mougenot C, Quesson B, et al. Volumetric HIFU Ablation under 3D Guidance of Rapid MRI Thermometry. Med. Phys. 2009;36:3521–3535.

[43] Ebbini ES, Ter Haar G. Ultrasound-Guided Therapeutic Focused Ultrasound: Current Status and Future Directions. Int. J. Hyperth. 2015;31:77–89.

[44] Hynynen K. MRIgHIFU: A Tool for Image-Guided Therapeutics. J. Magn. Reson. Imaging. 2011;34:482–493.

[45] Shahmirzadi D, Hou GY, Chen J, et al. Ex Vivo Characterization of Canine Liver Tissue Viscoelasticity After High-Intensity Focused Ultrasound Ablation. Ultrasound Med. Biol. 2014;40:341–350.

[46] Zhang S, Zhou F, Wan M, et al. Feasibility of Using Nakagami Distribution in Evaluating the Formation of Ultrasound-Induced Thermal Lesions. J. Acoust. Soc. Am. 2012;131:4836–4844.

[47] Shankar PM. Ultrasonic Tissue Characterization Using a Generalized Nakagami Model. IEEE Trans. Ultrason. Ferroelectr. Freq. Control. 2001;48:1716–1720.

[48] Lewis MA, Staruch RM, Chopra R. Thermometry and Ablation Monitoring with Ultrasound. Int. J. Hyperth. 2015;31:163–181.

[49] Bamber J, Hill C. Ultrasonic Attenuation and Propagation Speed in Mammalian Tissues as a Function of Temperature. Ultrasound Med. Biol. 1979;5:149–157.

[50] Teixeira CA, Alvarenga A V., Cortela G, et al. Feasibility of Non-Invasive Temperature Estimation by the Assessment of the Average Gray-Level Content of B-Mode Images. Ultrasonics. 2014;54:1692–1702.

[51] Maraghechi B, Kolios MC, Tavakkoli J. Feasibility of Detecting Change in Backscattered Energy of Acoustic Harmonics in Locally Heated Tissues. Int. J. Hyperth. 2019;36:964–974.

[52] Ishihara Y, Calderon A, Watanabe H, et al. A Precise and Fast Temperature Mapping Using Water Proton Chemical Shift. Magn. Reson. Med. 1995;34:814–823.

[53] Hall LD, Talagala SL. Mapping of pH and Temperature Distribution Using Chemical-Shift-Resolved Tomography. J. Magn. Reson. 1985;65:501–505.

[54] Vimeux F, De Zwart JA, Palussiére J, et al. Real-Time Control of Focused Ultrasound Heating Based on Rapid MR Thermometry. Invest. Radiol. 1999;34:190–193.

[55] Daum DR, Hynynen K. Thermal Dose Optimization via Temporal Switching in Ultrasound Surgery. IEEE Trans. Ultrason. Ferroelectr. Freq. Control. 1998;45:208–215.

[56] Siedek F, Yeo SY, Heijman E, et al. Magnetic Resonance-Guided High-Intensity Focused Ultrasound (MR-HIFU): Technical Background and Overview of Current Clinical Applications (Part 1). RöFo. 2019;191:522–530.

[57] Siedek F, Yeo SY, Heijman E, et al. Magnetic Resonance-Guided High-Intensity Focused Ultrasound (MR-HIFU): Overview of Emerging Applications (Part 2). RöFo. 2019;191:531–539.

[58] Focused Ultrasound Foundation. State of the Technology [Internet]. [cited 2019 Aug 15]. Available from: https://www.fusfoundation.org/the-technology/state-of-the-technology.

[59] Anzidei M, Marincola BC, Bezzi M, et al. Magnetic Resonance-Guided High-Intensity Focused Ultrasound Treatment of Locally Advanced Pancreatic Adenocarcinoma: Preliminary Experience for Pain Palliation and Local Tumor Control. Invest. Radiol. 2014;49:759–765.

[60] Ligresti D, Kuo YT, Baraldo S, et al. EUS Anatomy of the Pancreatobiliary System in a Swine Model: The WISE Experience. Endosc. Ultrasound. 2019;8:249–254.

[61] Swindle MM, Makin A, Herron AJ, et al. Swine as Models in Biomedical Research and Toxicology Testing. Vet. Pathol. 2012;49:344–356.

[62] Ferrer J, Iii WES, Weegman BP, et al. Pig Pancreas Anatomy: Implications for Pancreas Procurement, Preservation and Islet Isolation. Transplantation. 2008;86:1503–1510.

[63] Mahadevan V. Anatomy of the Pancreas and Spleen. Surgery. 2016;34:261–265.

[64] Swindle MM, Smith AC. Comparative Anatomy and Physiology of the Pig. Scand. J. Lab. Anim. Sci. 1998;25:11–21.

[65] Khokhlova TD, Hwang JH. HIFU for Palliative Treatment of Pancreatic Cancer. J. Gastrointest. Oncol. 2011;2:83–95.

[66] Liu CX, Gao XS, Xiong LL, et al. A Preclinical In Vivo Investigation of High-Intensity Focused Ultrasound Combined with Radiotherapy. Ultrasound Med. Biol. 2011;37:69–77.

[67] Hwang JH, Wang YN, Warren C, et al. Preclinical In Vivo Evaluation of an Extracorporeal HIFU Device for Ablation of Pancreatic Tumors. Ultrasound Med. Biol. 2009;35:967–975.

[68] Xie B, Li YY, Jia L, et al. Experimental Ablation of the Pancreas with High Intensity Focused Ultrasound (HIFU) in a Porcine Model. Int. J. Med. Sci. 2011;8:9–15.

[69] Dupré A, Melodelima D, Pflieger H, et al. Thermal Ablation of the Pancreas with Intraoperative High-Intensity Focused Ultrasound: Safety and Efficacy in a Porcine Model. Pancreas. 2017;46:219–224.

[70] Chang W, Lee JY, Lee JH, et al. A Portable High-Intensity Focused Ultrasound System for the Pancreas with 3D Electronic Steering: A Preclinical Study in a Swine Model. Ultrasonography. 2018;37:298–306.

2

[71] Li T, Khokhlova T, Maloney E, et al. Endoscopic High-Intensity Focused US: Technical Aspects and Studies in an In Vivo Porcine Model. Gastrointest. Endosc. 2015;81:1243–1250.

[72] Kothapalli SVVN, Altman MB, Partanen A, et al. Acoustic field characterization of a clinical magnetic resonance-guided high-intensity focused ultrasound system inside the magnet bore. Med. Phys. 2017;44:4890–4899.

[73] Ferrer CJ, Bartels LW, van Stralen M, et al. Fluid Filling of the Digestive Tract for Improved Proton Resonance Frequency Shift-Based MR Thermometry in the Pancreas. J. Magn. Reson. Imaging. 2018;47:692–701.

[74] Strunk HM, Henseler J, Rauch M, et al. Clinical Use of High-Intensity Focused Ultrasound (HIFU) for Tumor and Pain Reduction in Advanced Pancreatic Cancer. RöFo. 2016;188:662–670.

[75] Shimizu M, Hayashi T, Saitoh Y, et al. Postmortem Autolysis in the Pancreas. Pancreas. 1990;5:91–94.

[76] Eltoum I, Fredenburgh J, Myers RB, et al. Introduction to the Theory and Practice of Fixation of Tissues. J. Histotechnol. 2001;24:173–190.

[77] Szabo TL. Time Domain Wave Equations for Lossy Media Obeying a Frequency Power Law. J. Acoust. Soc. Am. 1994;96:491–500.

[78] Bottomley PA. In-Vivo Soft Tissue NMR Imaging of the Rat Thorax and Abdomen. Experientia. 1981;37:768–770.

[79] Wallner BK, Schumacher KA, Weidenmaier W, et al. Dilated Biliary Tract: Evaluation with MR Cholangiography with a T2- Weighted Contrast-Enhanced Fast Sequence. Radiology. 1991;181:802–808.

[80] Wedeen V, Meuli R, Edelman R, et al. Projective Imaging of Pulsatile Flow With Magnetic Resonance. Science. 1985;230:946–948.

[81] Mougenot C, Moonen C. Magnetic Resonance-Guided High Intensity Focused Ultrasound in the Presence of Biopsy Markers. J. Ther. Ultrasound. 2017;5:4–13.

[82] Gurney-Champion OJ, Lens E, Van Der Horst A, et al. Visibility and Artifacts of Gold Fiducial Markers Used for Image Guided Radiation Therapy of Pancreatic Cancer on MRI. Med. Phys. 2015;42:2638–2647.

[83] Stowell RE. Effect on Tissue Volume of Various Methods of Fixation, Dehydration, and Embedding. Biotech. Histochem. 1941;16:67–83.

# Chapter 3

## Model Predictive Control for MR-HIFU-Mediated, Uniform Hyperthermia

# ABSTRACT

**Purpose:** In local hyperthermia, precise temperature control throughout the entire target region is key for swift, safe, and effective treatment. In this article we present a model predictive control (MPC) algorithm providing voxel-level temperature control in magnetic resonance guided, high intensity focused ultrasound (MR-HIFU) and assess the improvement in performance it provides over the current state of the art.

**Materials and Methods:** The influence of model detail on the prediction quality and runtime of the controller is evaluated and a tissue mimicking phantom is characterized using the resulting model. Next, potential problems arising from modelling errors are evaluated *in-silico* and in the characterized phantom. Finally, the controller's performance is compared to the current state-of-the-art hyperthermia controller in side-by-side experiments.

**Results:** Modelling diffusion by heat exchange between four neighboring voxels achieves high predictive performance and results in runtimes suited for real-time control. Erroneous model parameters deteriorate the MPC's performance. Using models derived from thermometry data acquired during low powered test sonications, however, high control performance is achieved. In a direct comparison with the state-of-the-art hyperthermia controller, the MPC produces smaller tracking errors and tighter temperature distributions, both in a homogeneous target and near a localized heat sink.

**Conclusions:** Using thermal models deduced from low-powered test sonications, the proposed MPC algorithm provides good performance in phantoms. In direct comparison to the current state-of-the-art hyperthermia controller, MPC performs better due to the more finely tuned heating patterns and therefore constitutes an important step towards stable, uniform hyperthermia.

## INTRODUCTION

Mild local heating of tumor tissue to hyperthermic temperature in the range of 41–43 °C has been shown to have strong synergistic effects on radio- and chemotherapy, acting on cellular and tissue level [1-6]. Besides a plethora of preclinical evidence, several clinical trials demonstrated the synergistic effects of hyperthermia on radio-, chemo-, and chemoradiotherapy leading to improved outcome such as local control, disease free-, and long term survival [7-16]. As clinical studies also revealed that the outcome is sensitive to the applied thermal dose throughout the treatment, various measures have been introduced to describe and characterize the obtained temperatures over time and across the target tissue [17]. Induction of uniform hyperthermia across a treatment area is impeded by two major obstacles: First, the obtained temperatures depend on spatially and temporally varying tissue properties such as perfusion and heat diffusion. The former often leads to lower than intended heating close to blood vessels, while hyperthermia devices utilizing radiofrequency heating intrinsically lack the ability to compensate for local heat loss on the associated millimeter scale [18]. Second, temperature monitoring is currently performed using thermocouples inside or near the heated tissue [19], which only provides sparse spatial sampling of the temperature. Radiofrequency-based hyperthermia devices integrated into a magnetic resonance imaging (MRI) scanner could address some of above shortcomings and are currently evaluated for use in clinical settings [20,21].

      Focused ultrasound was already explored in the 1930s and was employed early on for local non-invasive heating of deep-seated tissue to induce brain lesions [22,23]. Clinical application of high intensity focused ultrasound (HIFU), however, was only achieved after image guidance was added for spatial targeting and therapy control using diagnostic ultrasound or MRI [24-27]. The integration of an extracorporeal HIFU transducer into the patient bed of an MRI scanner (MR-HIFU) in particular enables both the *in-situ* localization of the target tissue and the optimization of the transducer position before the treatment. Furthermore, the MRI provides near real-time temperature maps while the HIFU heating is ongoing. This is exploited for closed-loop feedback to the HIFU transducer, allowing to deliver a well-defined thermal dose and to maintain stable temperatures [28]. HIFU was recognized and tested as a hyperthermia device early on [24,29-31], but only MR-feedback enabled a stable hyperthermia over an extended period of time [32-34]. With a focus point of 2–3 mm in diameter and 5–7 mm in height, HIFU enables the local heating of tissue on the millimeter scale. For heating of larger volumes, electronic beam steering by coordinated ultrasound phase shifts was implemented to move the focus point over predefined circular perimeters [35]. In combination with MR thermometry and a simple binary feedback loop, electronic beam steering has been used to achieve MR-HIFU mediated, regional hyperthermia. The feasibility of this technique has been

demonstrated in several preclinical studies [36-42] and recently in a first clinical trial using the MR-HIFU system Sonalleve® (Profound Medical Inc., Toronto, Canada) [43]. By adding mechanical transducer movement facilitated by a robotic positioning system, a first large volume hyperthermia application based on MR-HIFU has been demonstrated *in vivo* [44] and applied clinically [45]. The feedback algorithm used in the referenced demonstration periodically repositions the transducer to heat different parts of the target region of interest (treatment cell) based on the lowest average temperature inside seven predefined sub-cells. Within the sub-cells, heating is regulated by adjusting the power delivered to the sub-cell as a whole and skipping points inside the sub-cell which are already above the target temperature. It is non-parametric in nature, i.e. it is designed to perform reliably without any prior knowledge of the particular tissue properties if they fall inside the anticipated range. Algorithms which do utilize tissue models for thermal therapies, however, can be more effective in achieving their respective control objective. Salomir *et al.* [32] as well as Quesson *et al.* [33], for instance, used physical models to calculate optimal HIFU intensities and thereby induced predefined temperature evolutions in the HIFU's natural focus spot with high accuracy. Model predictive control (MPC) [46,47], a well-established control scheme using mathematical models of the to-be-controlled system in constrained optimization problems to calculate optimal control strategies, has been applied successfully as well: In ablation treatments, MPC has been shown to enable increased speed and patient safety in the delivery of a target thermal dose [48-50]. An MPC scheme for mild regional hyperthermia, which aims to directly control the temperature in a target ROI, has been introduced as well but was only demonstrated *in-silico* thus far [51].

Here, we explore a novel control algorithm for MR-HIFU mediated mild hyperthermia applications, following the MPC paradigm. It aims to improve upon the existing binary control option by Tillander *et al.* [44], which we consider to be the state of the art, by optimizing the heat delivered to each individual voxel inside the target ROI based on a mathematical model of the tissue. As the appropriate model parameters for any individual case are generally unknown beforehand, the extent to which errors in the controller's model can lead to problematic controller behavior was investigated *in-silico*, followed by the quantification of the performance attainable with pre-treatment model identification in phantom experiments. Since the controller was implemented on a clinical MR-HIFU system, a direct performance comparison between the MPC and the existing binary control algorithm of Tillander *et al.* [44] was also performed and is presented last.

## MATERIALS AND METHODS

### Model Predictive Control

MPC is a form of control that exploits a mathematical model of the system to be controlled (the state-space model) to predict its future state depending on the applied control actions. At each sampling instant, the state variables of the system, e.g. the temperatures in a set of voxels, are measured. This measurement is then used as a starting point to calculate the next control actions, e.g. a sequence of heating patterns, that minimize the objective function over a certain control horizon. The objective function's minimum reflects the goals of the controller and depends on the predicted future state of the system. This calculation is usually done *via* constrained optimization, where the objective function is optimized by varying the control inputs while constraining the variables describing the system's state (the state variables) to behave according to the model [46,47,52].

### Controller architecture

*State-space model*

The state-space model that will be used in the MPC scheme is based on the Pennes bioheat transfer equation (PBE) [53]:

$$\rho C \frac{\partial T}{\partial t} = \nabla \cdot (K \nabla T) - W_b C_b (T - T_a) + Q \qquad [1]$$

where $\rho$ is the density of the tissue [kg/m³], $K$ is the diffusion coefficient [m²/s], $C$ and $C_b$ are the specific heat capacities of tissue and blood [J/(kg °C)], $W_b$ is the perfusion rate [kg/(m³s)], $T$ is the tissue's temperature [°C], $T_a$ is the arterial temperature [°C], and $Q$ is the heating power density delivered to the tissue [W/m³].

Our implementation aims to control the temperature inside the target region using a single thermometry slice, which is acquired repeatedly alongside other slices that are required for monitoring purposes. A linear discrete-time state-space model of the temperature evolution in two spatial dimensions is therefore required. The discrete timestep size equals the acquisition time of one feedback cycle (i.e. the acquisition of a full set of thermometry slices) and the discrete space step size equals the voxel size in the acquired two-dimensional temperature maps. Summarizing diffusion and perfusion effects into dimensionless parameters, one obtains a simplified model for the predicted temperature elevation $\hat{T}'_{t+1}$ with:

$$\hat{T}'_{t+1}(m,n) = A_0 T'_t(m,n)$$
$$+A_1\big(T'_t(m+1,n) + T'_t(m-1,n) + T'_t(m,n+1) + T'_t(m,n-1)\big)$$
$$+\sum_{i=1}^{N_p} q \cdot p_{t,i} \cdot f_i(m,n) \tag{2}$$

where $T'_t(m,n) = T_t(m,n) - T_a$ is the temperature elevation above the arterial blood temperature $T_a$ at time and discrete location $(m,n)$ [°C], $A_0$ is the per-cycle heat loss coefficient, which incorporates the loss due to perfusion and the diffusion out of the voxel, and $A_1$ is the per-dynamic inter-voxel heat transfer coefficient. $q$ is the per-cycle, single-voxel temperature increase per Watt of acoustic power, $p_{t,i}$ is the acoustic power applied targeting the sonication point with index $i$ at timepoint $t$, $f_i(m,n)$, is the distribution of heating power among voxel coordinates $(m,n)$ when targeting sonication point with index $i$, and $N_p$ is the number of available sonication points. The discretization was performed under the assumptions that heat diffusion is homogenous in all observed voxels, the heat delivered in one feedback cycle is affected by diffusion and perfusion only from the next cycle on, and that heat is exchanged between nearest neighbors only.

The state variables are the temperature elevation $T'_t(m,n)$ of the voxels at the locations $(m,n)$, $(m,n) \in O$ at timepoint $t$, where $O$ is the set of voxel coordinates inside the ROI which is passed to the controller (observed ROI). The input variables $p_{t,i}$, $i = 1, ..., N_p$, are constrained to be greater than or equal to zero and to total no more than a certain maximum power $p_{max}$ at each timestep $t$ within the control horizon $H$:

$$0 \le p_{t,i} \text{ for } t = 1, ..., H \text{ and } i = 1, ..., N_p \tag{3}$$

$$\sum_{i=1}^{N_p} p_{t,i} \le p_{max}, \text{for } t = 1, ..., H \tag{4}$$

Each allowed sonication point is chosen to coincide with the middle of an MRI voxel and is assumed to heat that particular voxel exclusively, i.e. $f_i(m,n)$ is assumed to be one at the targeted voxel's coordinates and zero everywhere else.

## Focal spot calibration and model identification

The transducer's alignment with the MRI's coordinate system was verified using multiple low-powered test sonications before each experiment. During the test sonication, the HIFU focus is moved by electronic beam steering on a trajectory consisting of the transducer's natural focus point and eight points equally distributed on an 8 mm circle around the natural focus. Using these nine heated points as reference, errors in the transducer's alignment are identified *via* spatial shifts from the expected heating pattern and are corrected by adjusting the transducer's position inside the table accordingly.

The use of this multipoint test sonication pattern also creates a large number of warm voxels throughout the target area. The MRI thermometry maps gathered during the test sonications can therefore be used to calibrate the state-space model's parameters to the target material. The estimation of the $A_0$ and $A_1$ parameters is performed *via* linear regression, for which all voxels within a radius of 2 cm around the target area are included. The voxels' temperatures at each timestep $k + 1$ after transducer shutoff were used as the dependent variable. The respective voxel's temperature at time $k$ (parameter $A_0$) as well as the sum of the nearest neighbors' temperatures at time $k$ (parameter $A_1$) were used as the regressors. The model used therefore has the following form:

$$T'_{k+1}(m, n) = A_0\big(T'_k(m, n)\big)$$
$$+A_1\big(T'_k(m + 1, n) + T'_k(m - 1, n) + T'_k(m, n + 1) + T'_k(m, n - 1)\big)$$

[5]

The linear regression was performed using the open source Python package scikit-learn, version 0.18.1 [54].

After the calculation of $A_0$ and $A_1$ is complete, the per-dynamic single-voxel heating rate $q$ is calculated by linear regression. Here, the total temperature increase across all voxels in a radius of 20 mm around the natural focus at each cycle $l$ serves as the dependent variable and the retained fraction of the power added to the target slice is used as the regressor. This results in a linear model of the form:

$$\sum_{(m,n)\in M} T'_l(m, n) = q \cdot P \cdot \sum_{i=0}^{l} (A_0 + 4A_1)^l$$

[6]

where $P$ is the acoustic output power selected for the sonication, $M$ is the set of voxel coordinates within a radius of 20 mm around the transducer's natural focus and $(A_0 + 4A_1)$ is the fraction of power retained in the focus slice from one cycle to the next.

**Cost function**

In MPC, the optimal control actions are determined *via* constrained optimization of the cost function, which is chosen to reflect the control objectives. For this controller, it has been given the form:

$$J_t = \sum_{j=1}^{H} \sum_{(m,n)\in R} \frac{1}{H \cdot N_R}\left(\frac{T'_{obj} - \hat{T}'_{t+j}(m, n)}{5\ \text{K}}\right)^2$$

[7]

where $H$ is the control horizon, $R$ is the set of coordinates belonging to the voxels inside the target ROI, $N_R$ is the number of voxels inside $R$, and $T'_{obj}$ is the target temperature elevation.

## Implementation

All phantom experiments were performed on a clinical MR-HIFU system (3T Achieva®, Philips Healthcare, Best, The Netherlands, and Sonalleve® V2 HIFU, Profound Medical, Toronto, Canada). We developed a custom MR-HIFU software providing treatment planning- and monitoring capabilities tailored to the MPC algorithm. The program was written in Python, version 2.7.13 [55]. PyQt 5.6.0 [56] was used to create the GUI and pyqtgraph 0.10.0 [57] provided efficient real-time visualization of the captured data. The communication with the MRI scanner and the HIFU system was achieved using the pyMRI and pyHIFU toolboxes [58]. The calculation of the optimal control actions was done using the python interface of Gurobi 7.5 [59]. The experiments employing the existing binary controller were performed using the Hyperthermia Release 3.5.955.1215 of the Sonalleve® software (Profound Medical, Toronto, Canada).

## MR thermometry

The imaging sequence used to monitor the treatment progress was an RF-spoiled gradient echo sequence with TR = 30 ms, TE = 19.5 ms, FA = 19.5°, FOV = 296 mm, 5 slices, and voxel dimensions = 1.8 x 1.8 x 7 $mm^3$, resulting in a dynamic scan time of 3.5 s ('one cycle') and a resolution of 160 x 160 voxels per slice. The temperature maps were acquired exploiting the proton resonance frequency shift (PRFS) [60]. The coils used for image acquisition were the HIFU table's window coil and the HIFU Pelvis Coil (Model 905051-F, Philips Healthcare, Best, The Netherlands). In particular, the calculation included masking of low SNR voxels, masking of expected heating areas, baseline subtraction, and a second order baseline drift correction. The MRI slices were positioned in four stacks, namely the focus, sagittal, near field, and far field stacks. The focus stack was positioned at the HIFU focus point and contained three slices to provide a complete view of the volumetric temperature distribution in the target ROI, with the center slice of the focus stack functioning as feedback for the controller. The sagittal slice was positioned to intersect the focus spot and provides information on the vertical alignment of the focus. The nearfield slice was positioned at the phantom's acoustic window to monitor excess heat generation on the phantom's surface or, in a hypothetical clinical setting, a patient's skin. The far field slice was positioned near the ultrasound absorber at the far side of the phantom and is intended as a monitoring modality for organs and bone surfaces behind the focus.

## Preparatory work

### Phantom manufacturing process

All phantom experiments were performed with polyacrylamide hydrogels sealed in polypropylene containers. The containers can be opened on one side to provide an acoustic window and are lined with an ultrasound absorber on the opposite side to

prevent reflections. The phantoms also contained a hollow channel of 5 mm diameter, which can be perfused with water to mimic a medium-sized blood vessel. The phantoms were manufactured in-house using a variation of the tissue-mimicking formulation by Negussie *et al.* [61]. The used chemicals were purchased from Sigma Aldrich (Sigma-Aldrich Corporation, St. Louis, Missouri, USA) and are detailed with their respective ratios in Table 1.

**Table 1:** Chemical composition of the phantoms used in this study.

| Component | Product code | Fraction of volume |
|---|---|---|
| De-ionized water | – | 82.24% (v/v) |
| Acrylamide/bis-acrylamide (ratio: 19:1), 40% (w/v) solution | A9926-5L | 17.54% (v/v) |
| TEMED | T7024-100ML | 0.21% (v/v) |
| APS | 248614-500G | 0.21% (w/v) |
| SiO2 | S5631-1KG | 2.00% (w/v) |

*Abbreviations:* **TEMED:** N,N,N0,N0-tetra-metyl-ethylenediamine; **APS**: Ammonium peroxydisulfate; **SiO2**: Silicon dioxide particles, sizes 0.5–10 μm.

*Model selection and identification*

Ten test sonications with 60 W of acoustical power and 16 s duration were performed in the phantom to be used in the experiments, far away from the water channel. These test sonications employed the nine-point heating pattern described above. While the transducer was active and for ten cycles after transducer shutoff, thermometry slices were acquired to provide training data for the thermal model.

As the detail of the inter-voxel heat exchange in the state-space model has a strong impact on the runtime of the controller, the chosen model must be simple enough to provide real-time control. The predictive quality of models with increasing numbers of nearest neighbors included in the prediction was therefore assessed and the peak runtimes required for solving the constrained optimization problem of the MPC at these different levels of detail was measured in simulations with fifty timesteps each. The simulations were run on the HIFU console (HP Z800 Workstation, Intel® Xeon® CPU X5650 @ 2.67 GHz) using the otherwise unchanged controller. The level of detail resulting in the shortest peak runtime while still providing markedly better predictive performance on the test set than all simpler models was selected for use in the remaining *in-silico* and *in-vitro* experiments. Half of all recorded voxel temperature measurements inside the observed 20 mm radius around the natural focus were assigned to the test set. Using the selected level of detail, the model parameters to be used in the following robustness experiments were determined.

*Performance metrics*

Controller performance was assessed in the steady state, which was established after 400s at the latest in all experiments. The used metrics were the average steady-state performance $J$, the average steady-state tracking error $T_{Off}$, and the average steady-state temperature distribution width $T_{Range}$ and are defined as:

$$J = \frac{1}{N_S \cdot N_R} \sum_{t \in S} \sum_{(m,n) \in R} \left(T_t(m,n) - T_{obj}\right)^2 \tag{8}$$

$$T_{Off} = \frac{1}{N_S \cdot N_R} \sum_{t \in S} \sum_{(m,n) \in R} T_t(m,n) - T_{obj} \tag{9}$$

$$T_{Range} = \frac{1}{N_S} \sum_{t \in S} T_{90}(t) - T_{10}(t) \tag{10}$$

where $S$ is the set of timepoints measured in the steady state ($400\ s < t < 600\ s$) and $N_S$ is the number of timepoints in $S$. $T_{90}(t)$ and $T_{10}(t)$ denote the 90th and 10th percentile of voxel temperatures measured inside the target ROI at timepoint t.

## Simulations

*Influence of model errors in-silico*

*In-silico* experiments allow the isolation of controller-specific errors from other sources of complications, such as alignment errors of HIFU- and MRI coordinate systems. The effect of plant-model mismatch, i.e. discrepancies between the model and the controlled system's behavior, was therefore investigated *in-silico*.

The controller's model was initialized with a set of models containing varying $A_1$ and $q$ parameters while the properties of the simulated target tissue remained unchanged. The controller's parameters were $q_{MPC} = (q_{sim}/3,\ q_{sim},\ 3 \cdot q_{sim})$ and $A_{1,MPC} = (0.0,\ A_{1,sim},$ 0.2) with respect to the simulated tissue's parameters $q_{sim}$ and $A_{1,sim}$. The simulations were performed by solving the finite difference equation (2) on a two-dimensional grid of 1.8 mm spatial resolution and a 3.5 s temporal resolution. The used model was selected beforehand using thermometry data acquired during test-sonications on the polyacrylamide phantom described above. For these simulations, the controller was operated on a circular target ROI with a diameter of 18 mm. $T_{obj}$ was set to 5 °C above the baseline. To simulate noise, normally distributed random numbers with a standard deviation of 0.4 K were added to the temperature maps passed to the controller as feedback.

**Phantom Experiments**

*Influence of model errors in-vitro*

Nine hyperthermia experiments were performed on the previously characterized polyacrylamide phantom using MPCs initialized with all possible combinations of the average value found for $A_1$, the case of negligible perfusion ($A_1 = 0.0$) and immediate leveling of temperature gradients between nearest neighbors ($A_1 = 0.2$) with the average value found for $q$ and $q$-mismatches by the factors 1/3 and 3. Heat loss other than in-plane diffusion was excluded from the starting model by setting ($A_0 = 1 - 4A_1$). Each hyperthermia experiment was run for 10 minutes with $T_{obj} = 5$ K, $P_{max} = 60$ W, and $H = 5$. For these experiments, the target area was placed far from the water channel and the channel's perfusion was disabled.

*Performance comparison: MPC and binary controller*

The MPC's performance was assessed by comparison with the current state-of-the-art controller introduced by Tillander *et al.* [44], which will be referred to as the binary controller. For the comparison in a homogeneous target area, the water supply of the phantom was disabled and a round target ROI with 18mm diameter was placed several centimeters away from the water channel. For the comparison in an inhomogeneous target area, the phantom was perfused with de-ionized water at 2.4 ml/s and the target ROI was positioned 1 mm away from the water channel. Both target ROIs were sonicated with the MPC as well as the binary control algorithm. For both experiments, the MPC was initialized with parameters identified from test sonication data acquired before the experiment in the respective configuration. Each hyperthermia experiment was run for 10 minutes with $T_{obj} = 5$ K, $P_{max} = 60$ W, and $H = 5$.

## RESULTS

### Preparatory work

*Model selection and identification*

First, the coefficient of determination as well as the controller runtimes were measured using increasing numbers of nearest neighbors in the prediction of voxel temperatures (Figure 1). The model incorporating four nearest neighbors (N = 4) shows a significantly higher coefficient of determination than the model neglecting diffusion (N = 0) and led to a peak runtime of 390 ms. The model with eight nearest neighbors required a 55.6 % longer peak runtime of 608 ms and improved the predictive quality only slightly ($R^2 = 0.946$ vs 0.947 on average). Models with more nearest neighbors did not further

improve the coefficient of determination significantly but only increased peak run time. The chosen model therefore incorporated four nearest neighbors only. The $A_1$ and $q$ parameters derived from the test sonications using this model were $0.126 \pm 0.008$ and $0.882 \pm 0.094$, respectively.
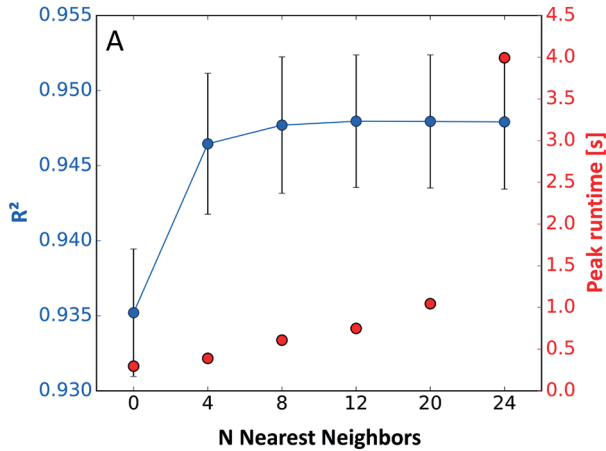


**Figure 1:** Coefficient of determination on the test set vs. the number of nearest neighbors used in the model and corresponding peak runtimes required for optimization.

## Simulations

*Influence of model errors in-silico*

The simulated temperature evolutions in the target ROI for plant-model mismatches in $A_1$ and $q$ are displayed in Figure 2. Regardless of the used $A_{1,MPC}$, the controller performs best in the cases with $q_{MPC} = q_{sim}$. In the case of severely underestimated heating ($q_{MPC} = q_{sim}/3$), the temperature distributions are much broader than in the matched heating case for all $A_1$ parameters and show heat spikes throughout the duration of the sonication. Additionally, positive tracking errors between 304 and 542 mK are observed. In the overestimated heating case ($q_{MPC} = 3 \cdot q_{sim}$), the widths of the temperature distributions are larger than for the matched heating case as well for all $A_1$ parameters and negative tracking errors between 285 and 353 mK are observed. The best performance $J$ was achieved using the correct model parameters.

The controller's responsiveness to measured temperature deficits is shown in Figure 3 for varying model parameters. Over- and underestimation of the $q$ parameter leads to under- and overcompensation of measured temperature deficits, respectively. For the case of neglected diffusion ($A_{1,MPC} = 0.0$), the controller aggressively counteracts

measured temperature deficits while in the case of immediate leveling of temperature gradients ($A_{1,MPC}$ = 0.2), the controller is much less responsive.
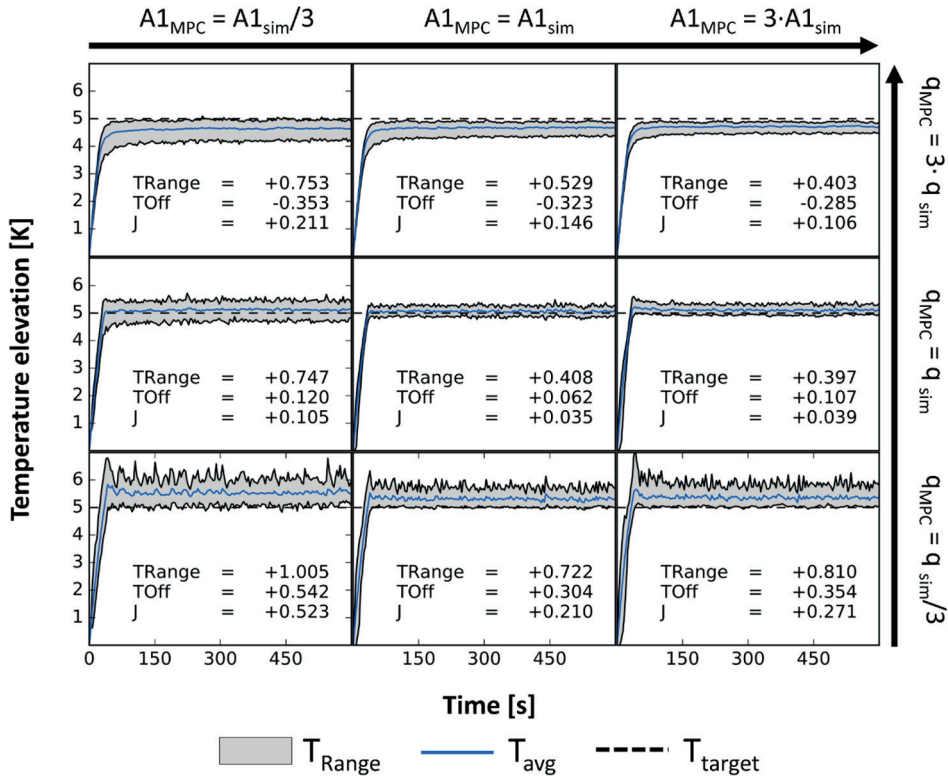


**Figure 2:** Simulated temperature curves in the target ROI vs. time, not including the noise added to the feedback signal. In each simulation, the controller was given a different model while the simulated tissue remained unchanged. The eight panels around the center represent the mismatched cases with the used parameter displayed at the respective row and column.

*Abbreviations: $T_{Range}$*: average steady-state temperature distribution width; $T_{off}$: average steady-state tracking error; *J*: average steady-state performance.
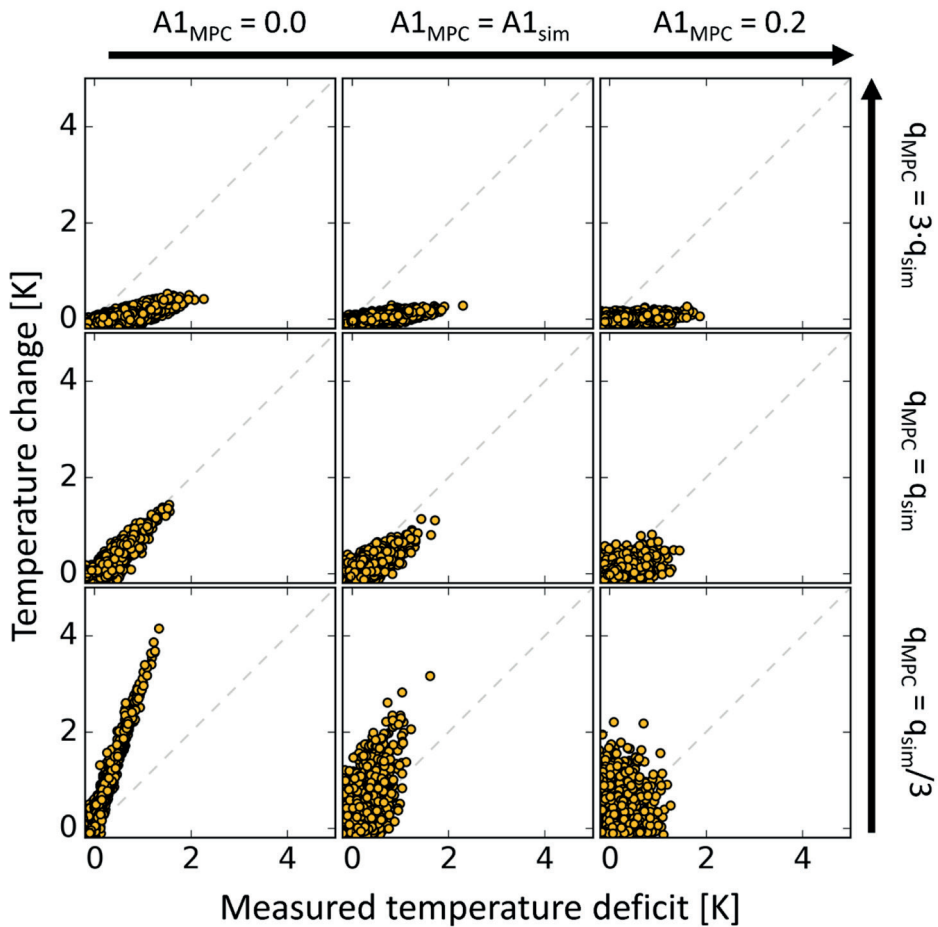
**Figure 3:** Temperature change of voxels inside the target ROI vs. measured temperature deficit at the previous timestep *in-silico*. The eight panels around the center represent the mismatched cases with the used parameter displayed at the respective row and column. The used $q$ parameter determines the magnitude of the response while the used $A_1$ parameter influences the stringency with which measured temperature deficits are compensated.

**Phantom experiments**

*Influence of model errors in-vitro*

The evolution of the temperature distributions during nine *in-vitro* experiments with varying model parameters is shown in Figure 4. Across all experiments, the average absolute steady-state tracking error $T_{off}$ was 138 mK and the average steady-state width of the temperature distribution $T_{Range}$ was 740 mK. In all tested cases, an underestimation

of the heating power led to $T_{off}$ and $T_{Range}$ values above 144 mK and 754 mK while an overestimation led to $T_{off}$ and $T_{Range}$ values below -185 mK and above 785 mK. Experiments using the experimentally identified $q$ parameter performed better in both aspects with $T_{off}$ and $T_{Range}$ values smaller than 62 mK and 676 mK. The use of the experimentally identified $A_1$ parameter led to the best performance $J$ for two out of three different $q$ parameters and the second-best result in one case. The best performance $J$ was achieved using the experimentally identified parameters.



**Figure 4:** Temperature curves in the target ROI vs. time for varying controller models in nine otherwise identical phantom experiments. The used values for the $A_1$ and $Q$ parameters are given for each row and column.

*Abbreviations:* $T_{Range}$: average steady-state temperature distribution width; $T_{off}$: average steady-state tracking error; $J$: average steady-state performance.
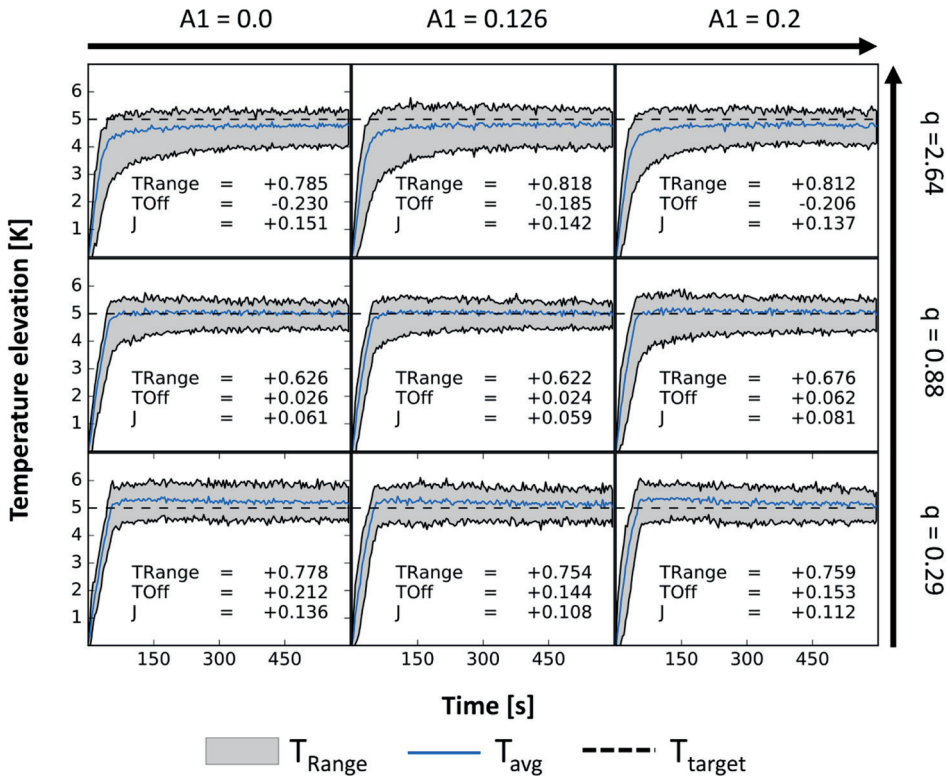
*Performance comparison: MPC and binary controller*

The MPC's performance was rated in a direct comparison to the current state-of-the-art controller for MR-HIFU mediated mild hyperthermia. The comparison was made both for a homogenous target ROI (Figure 5) and a target ROI adjacent to the water channel inside the phantom material (Figure 6). The steady-state (400 s < $t$ <600 s) performance metrics $T_{off}$ and $T_{Range}$ for the homogeneous case were 67 mK and 698 mK for the MPC and 605 mK and 1734 mK for the binary controller, respectively. The steady-state performance metrics $T_{off}$ and $T_{Range}$ for the inhomogeneous case were 49 mK and 862 mK for the MPC and 646 mK and 1629 mK for the binary controller, respectively. The average spatial temperature profiles through the centers of the target ROI in steady state (Figures 5B and 6B) showed bell shapes for the binary controller and plateaus for the MPC controller. The MPC allocated heating power mainly to the edges of the target ROI and increased heating at the edge of the ROI bordering the water channel in the inhomogeneous case. Information on the power distribution used by the binary controller could not be obtained from the clinical software and is therefore not shown here.
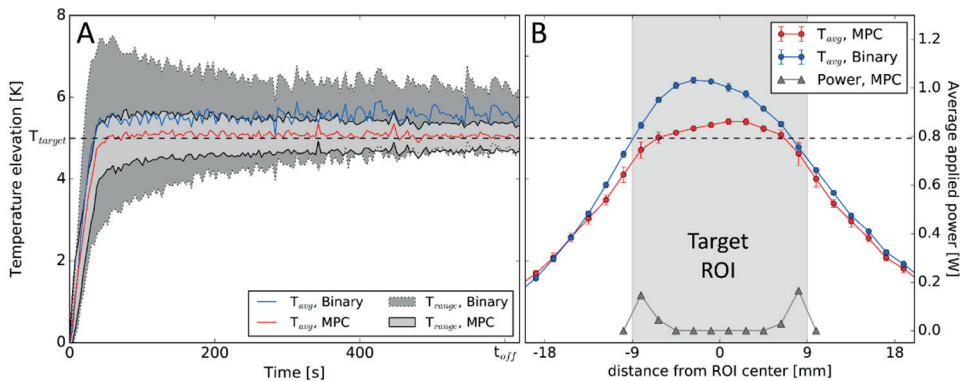


**Figure 5: (A**) Temperature distribution vs. time achieved with the binary controller and the MPC algorithm in a homogeneous region of the phantom. (**B**) Spatial temperature profiles and the MPC's power distribution profile through the center of the target region, average for 400 s < $t$ < 600 s. Target area is shaded.
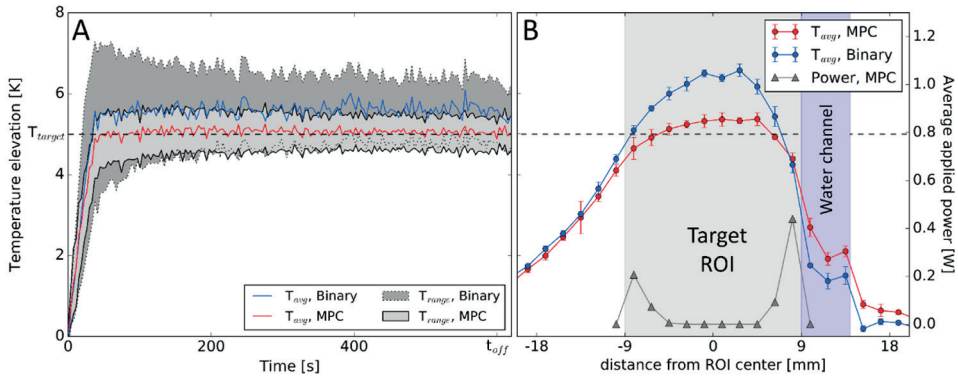
**Figure 6:** (**A**) Temperature distribution vs. time achieved with the binary controller and the MPC algorithm near the water channel of the phantom. (**B**) Spatial temperature profiles and the MPC's power distribution profile through the center of the target region perpendicular to the water channel, average for 400 s < $t$ < 600 s. Target area (grey) and water channel (purple) are shaded.

## DISCUSSION

The impact of errors in the estimation of tissue properties were explored *in-silico* and *in-vitro*. Both investigations showed that mismatches of the $A_1$ parameter have a weaker influence on steady-state controller performance compared to the influence of the heating parameter $q$. This observation can be explained by the diminished influence of diffusion inside the target ROI once a highly homogeneous temperature distribution has been reached. Neglect of diffusion in the model ($A_1 = 0$) together with a severe under- or overestimation of $q$, however, led to increased tracking errors of up to 542 mK *in-silico* and 230 mK *in-vitro*, caused by an aggressive overcompensation of measured temperature deficits. While these errors are smaller than the tracking errors that were encountered using the binary controller, this still shows the necessity of modelling diffusion for precise temperature control. At the same time, modelling diffusion between a large number of voxels offers only small benefits beyond the already very good predictive performance achievable with four nearest neighbors.

Besides the expected tracking errors, the underestimation of $q$ caused heat spikes which were observed prominently *in-silico*, where the feedback noise could be masked. This influence of the mismatch in $q$ arises from the resulting controllers' overcompensation of measured temperature deficits induced by noise. Higher heating estimates, on the other hand, will lead to insufficient heating in response to any measured temperature deficit. This led to a smoother temperature evolution in the corresponding simulations, but not to an improvement in control performance over the matched case. One avenue

that could be pursued in the future to reduce tracking errors and the controller's responsiveness to noise in a controlled manner is the extension of the MPC algorithm to a full offset-free implementation, which is used in other control problems where the system's state cannot be measured directly or the controller input is noisy [52,62].

In the direct comparison between the MPC and the binary control algorithm, the MPC implementation outperformed the binary controller both in terms of the tracking error and width of the temperature distribution after establishment of the steady state. In the homogeneous case, the MPC's $T_{off}$ and $T_{Range}$ were only 11.1 % and 40.3 % of the binary controller's $T_{off}$ and $T_{Range}$. The reason for this becomes evident in the spatial temperature profiles produced by the two controllers (Figure 5B). The MPC's profile shows a flat plateau inside the target area, while the binary controller gives rise to a bell shape, indicative of excess heating in the center of the target ROI. The MPC avoids this problem by optimizing the applied heating pattern at each time step, thereby shifting all applied power to the edge of the controlled area automatically after the ROI center is sufficiently heated. In the inhomogeneous case, where the heated region is placed adjacent to a perfused water channel, both controllers produce a skewed distribution (Figure 6B). The MPC's advantage is considerable in this case as well with $T_{off}$ and $T_{Range}$ at 7.6 % and 52.9 % of the binary controller's $T_{off}$ and $T_{Range}$, respectively. Analogous to the homogeneous case, this is a consequence of the flexible heating patterns used by the MPC, allowing to allocate additional heating power to the edge of the target ROI bordering the water channel. This capability might prove particularly useful in a clinical setting where regions of enhanced perfusion or variations in ultrasound absorption might not be detectable in advance or might arise during the treatment, e.g. by the heat-induced stimulation of blood flow.

The controlled environment that was used to show the MPC's advantages over the current state-of-the-art in the absence of such unpredictable effects and to assess the problems particular to this new MPC algorithm is at the same time a limitation of this study. It cannot demonstrate adequately how the MPC would perform when encountering problems that are particular to the *in-vivo* setting. Most of these problems, first and foremost those related to patient safety, e.g. protection of the skin, the detection of thermometry artifacts, and detection of patient motion, must be addressed by appropriate patient preparation, patient monitoring and dedicated safety software modules separate from the controller, however. Nonetheless, validation of the controller's performance in an *in-vivo* setting, where perfusion might change over time or tissue properties may vary spatially in unpredictable ways, is required and will be performed in a dedicated study.

In conclusion, we presented the structure, implementation, and *in-vitro* evaluation of an MPC algorithm for improved uniform hyperthermia using MR-HIFU, which employs personalized thermal models derived from low-powered test sonications for each

treatment. The MPC outperforms the current state-of-the-art controller *in-vitro* both in terms of target tracking performance as well as spatial homogeneity of the resulting temperature distribution. This is made possible *via* the automatic and flexible redistribution of heating power by repeated model-based optimization. This also holds in the presence of a localized heat sink, which was counteracted by the MPC *via* automatic allocation of additional heating power. We therefore believe that the proposed MPC solution will further advance MR-HIFU based hyperthermia and may be key for applications where tight control of the temperature is essential, such as device-targeted drug delivery.

## ACKNOWLEDGEMENT

3

# REFERENCES

[1]   Datta NR, Ordóñez SG, Gaipl US, et al. Local Hyperthermia Combined with Radiotherapy and-/or Chemotherapy: Recent Advances and Promises for the Future. Cancer Treat. Rev. 2015;41:742–753.

[2]   Issels RD. Hyperthermia Adds to Chemotherapy. Eur. J. Cancer. 2008;44:2546–2554.

[3]   Horsman MR, Overgaard J. Hyperthermia: A Potent Enhancer of Radiotherapy. Clin. Oncol. 2007;19:418–426.

[4]   Dewhirst MW, Vujaskovic Z, Jones E, et al. Re-setting the Biologic Rationale for Thermal Therapy. Int. J. Hyperth. 2005;21:779–790.

[5]   Wust P, Hildebrandt B, Sreenivasa G, et al. Hyperthermia in Combined Treatment of Cancer. Lancet Oncol. 2002;3:487–497.

[6]   Falk MH, Issels RD. Hyperthermia in Oncology. Int. J. Hyperth. 2001;17:1–18.

[7]   Issels RD, Lindner LH, Verweij J, et al. Effect of Neoadjuvant Chemotherapy Plus Regional Hyperthermia on Long-Term Outcomes Among Patients With Localized High-Risk Soft Tissue Sarcoma. JAMA Oncol. 2018;4:483–492.

[8]   Datta NR, Rogers S, Klingbiel D, et al. Hyperthermia and Radiotherapy with or without Chemotherapy in Locally Advanced Cervical Cancer: A Systematic Review with Conventional and Network Meta-Analyses. Int. J. Hyperth. 2016;32:809–821.

[9]   Datta NR, Rogers S, Ordóñez SG, et al. Hyperthermia and Radiotherapy in the Management of Head and Neck Cancers: A Systematic Review and Meta-Analysis. Int. J. Hyperth. 2016;32:31–40.

[10]  Maluta S, Kolff MW. Role of Hyperthermia in Breast Cancer Locoregional Recurrence: A Review. Breast Care. 2015;10:408–412.

[11]  Wessalowski R, Schneider DT, Mils O, et al. Regional Deep Hyperthermia for Salvage Treatment of Children and Adolescents with Refractory or Recurrent Non-Testicular Malignant Germ-Cell Tumours: An Open-Label, Non-Randomised, Single-Institution, Phase 2 Study. Lancet Oncol. 2013;14:843–852.

[12]  Issels RD, Lindner LH, Verweij J, et al. Neo-adjuvant Chemotherapy Alone or with Regional Hyperthermia for Localised High-Risk Soft-Tissue Sarcoma: A Randomised Phase 3 Multicentre Study. Lancet Oncol. 2010;11:561–570.

[13]  Franckena M, Lutgens LC, Koper PC, et al. Radiotherapy and Hyperthermia for Treatment of Primary Locally Advanced Cervix Cancer: Results in 378 Patients. Int. J. Radiat. Oncol. Biol. Phys. 2009;73:242–250.

[14]  Franckena M, Stalpers LJA, Koper PCM, et al. Long-Term Improvement in Treatment Outcome After Radiotherapy and Hyperthermia in Locoregionally Advanced Cervix Cancer: An Update of the Dutch Deep Hyperthermia Trial. Int. J. Radiat. Oncol. Biol. Phys. 2007;70:1176–1182.

[15]  Van der Zee J, Van Rhoon GC. Cervical Cancer: Radiotherapy and Hyperthermia. Int. J. Hyperth. 2006;22:229–234.

[16]  Van der Zee J, González González D, Van Rhoon GC, et al. Comparison of Radiotherapy Alone with Radiotherapy plus Hyperthermia in Locally Advanced Pelvic Tumours: A Prospective, Randomised, Multicentre Trial. Lancet. 2000;355:1119–1125.

[17]  Pearce JA. Comparative Analysis of Mathematical Models of Cell Death and Thermal Damage Processes. Int. J. Hyperth. 2013;29:262–280.

[18]  Craciunescu OI, Samulski T V., MacFall JR, et al. Perturbations in Hyperthermia Temperature Distributions Associated with Counter-Current Flow: Numerical Simulations and Empirical Verification. IEEE Trans. Biomed. Eng. 2000;47:435–443.

[19]  Fatehi D, Van der Zee J, Van der Wal E, et al. Temperature Data Analysis for 22 Patients with Advanced Cervical Carcinoma Treated in Rotterdam Using Radiotherapy, Hyperthermia and Chemotherapy: A Reference Point is Needed. Int. J. Hyperth. 2006;22:353–363.

[20]  Mulder HT, Curto S, Paulides MM, et al. Systematic Quality Assurance of the BSD2000-3D MR-Compatible Hyperthermia Applicator Performance Using MR Temperature Imaging. Int. J. Hyperth. 2018;35:305–313.

[21] Paulides MM, Numan WCM, Drizdal T, et al. Feasibility of MRI-Guided Hyperthermia Treatment of Head and Neck Cancer. 8th Eur. Conf. Antennas Propagation, EuCAP 2014. 2014. p. 1474–1477.

[22] Gruetzmacher J. Piezoelektrischer Kristall mit Ultraschallkonvergenz. Zeitschrift fuer Phys. 1935;96:342–349.

[23] Fry WJ, Barnard JW, Fry FJ, et al. Ultrasonic Lesions in the Mammalian Central Nervous System. Science (80-. ). 1955;122:517–518.

[24] Hynynen K, Roemer R, Anhalt D, et al. A Scanned, Focused, Multiple Transducer Ultrasonic System for Localized Hyperthermia Treatments. Int. J. Hyperth. 2010;26:1–11.

[25] Shimm DS, Hynynen KH, Anhalt DP, et al. Scanned Focussed Ultrasound Hyperthermia: Initial Clinical Results. Int. J. Radiat. Oncol. Biol. Phys. 1988;15:1203–1208.

[26] Schenck JF, Unger E. MRI-Guided Noninvasive Ultrasound Surgery. Med. Phys. 1993;20:107–115.

[27] Cline HE, Schenck JF, Hynynen K, et al. MR-Guided Focused Ultrasound Surgery. J. Comput. Assist. Tomogr. 1992;16:956–965.

[28] Salomir R, Palussire J, Vimeux FC, et al. Local Hyperthermia with MR-Guided Focused Ultrasound: Spiral Trajectory of the Focal Point Optimized for Temperature Uniformity in The Target Region. J. Magn. Reson. Imaging. 2000;12:571–583.

[29] Hynynen K, Deyoung D. Temperature Elevation at Muscle-Bone Interface During Scanned, Focused Ultrasound Hyperthermia. Int. J. Hyperth. 1988;4:267–279.

[30] Anhalt D, Hynynen K, Roemer R. Patterns of Changes of Tumour Temperatures During Clinical Hyperthermia: Implications for Treatment Planning, Evaluation and Control. Int. J. Hyperth. 1995;11:426–436.

[31] Benkeser PJ, Frizzell LA, Ocheltree KB, et al. A Tapered Phased Array Ultrasound Transducer for Hyperthermia Treatment. IEEE Trans. Ultrason. Ferroelectr. Freq. Control. 1987;34:446–453.

[32] Salomir R, Vimeux FC, De Zwart JA, et al. Hyperthermia by MR-Guided Focused Ultrasound: Accurate Temperature Control Based on Fast MRI and a Physical Model of Local Energy Deposition and Heat Conduction. Magn. Reson. Med. 2000;43:342–347.

[33] Quesson B, Vimeux F, Salomir R, et al. Automatic Control of Hyperthermic Therapy Based on Real-Time Fourier Analysis of MR Temperature Maps. Magn. Reson. Med. 2002;47:1065–1072.

[34] Vanne A, Hynynen K. MRI Feedback Temperature Control for Focused Ultrasound Surgery. Phys. Med. Biol. 2003;48:31–43.

[35] Palussière J, Salomir R, Le Bail B, et al. Feasibility of MR-Guided Focused Ultrasound with Real-Time Temperature Mapping and Continuous Sonication for Ablation of VX2 Carcinoma in Rabbit Thigh. Magn. Reson. Med. 2003;49:89–98.

[36] Kneepkens E, Heijman E, Keupp J, et al. Interleaved Mapping of Temperature and Longitudinal Relaxation Rate to Monitor Drug Delivery During Magnetic Resonance-Guided High-Intensity Focused Ultrasound-Induced Hyperthermia. Invest. Radiol. 2017;52:620–630.

[37] Hijnen N, Kneepkens E, De Smet M, et al. Thermal Combination Therapies for Local Drug Delivery by Magnetic Resonance-Guided High--Intensity Focused Ultrasound. Proc. Natl. Acad. Sci. 2017;114:E4802–E4811.

[38] Kneepkens E. Preclinical Evaluation of Paramagnetic Temperature Sensitive Liposomes for Image-Guided Drug Delivery [dissertation]. Eindhoven, the Netherlands: Technische Universiteit Eindhoven; 2017.

[39] De Smet M, Langereis S, Van den Bosch S, et al. SPECT/CT Imaging of Temperature-Sensitive Liposomes for MR-Image Guided Drug Delivery with High Intensity Focused Ultrasound. J. Control. Release. 2013;169:82–90.

[40] De Smet M, Hijnen NM, Langereis S, et al. Magnetic Resonance Guided High-Intensity Focused Ultrasound Mediated Hyperthermia Improves the Intratumoral Distribution of Temperature-Sensitive Liposomal Doxorubicin. Invest. Radiol. 2013;48:395–405.

[41] De Smet M, Heijman E, Langereis S, et al. Magnetic Resonance Imaging of High Intensity Focused Ultrasound Mediated Drug Delivery from Temperature-Sensitive Liposomes: An In Vivo Proof-of-Concept Study. J. Control. Release. 2011;150:102–110.

3

[42] Hijnen NM, Heijman E, Köhler MO, et al. Tumour Hyperthermia and Ablation in Rats Using a Clinical MR-HIFU System Equipped with a Dedicated Small Animal Setup. Int. J. Hyperth. 2012;28:141–155.

[43] Chu W, Staruch RM, Pichardo S, et al. MR-HIFU Mild Hyperthermia for Locally Recurrent Rectal Cancer: Temperature Mapping and Heating Quality in First Patient. 12th Int. Congr. Hyperthermic Oncol. 2016. p. 144.

[44] Tillander M, Hokland S, Koskela J, et al. High Intensity Focused Ultrasound Induced In Vivo Large Volume Hyperthermia under 3D MRI Temperature Control. Med. Phys. 2016;43:1539–1549.

[45] Heijman E, Yeo SY, Sebeke L, et al. Volumetric Hyperthermia of Soft Tissue Sarcoma using MR-Guided High Intensity Focussed Ultrasound. 6th Int. Symp. Focus. Ultrasound. 2018.

[46] Mayne DQ, Rawlings JB, Rao C V., et al. Constrained Model Predictive Control: Stability and Optimality. Automatica. 2000;36:789–814.

[47] Lee JH. Model Predictive Control: Review of the Three Decades of Development. Int. J. Control. Autom. Syst. 2011;9:415–424.

[48] Arora D, Skliar M, Roemer RB. Model Predictive Control of Ultrasound Hyperthermia Treatments of Cancer. Proc. 2002 Am. Control Conf. (IEEE Cat. No.CH37301). 2002;4:2897–2902.

[49] Blankespoor A, Payne A, Todd N, et al. Model Predictive Control of HIFU Treatments in 3D for Treatment Time Reduction. AIP Conf. Proc. 2009;1113:215–219.

[50] De Bever J, Todd N, Payne A, et al. Adaptive Model-Predictive Controller for Magnetic Resonance Guided Focused Ultrasound Therapy. Int. J. Hyperth. 2014;30:456–470.

[51] Luo X, De Jager B, Heijman E, et al. Set-Based MPC with an Application to Enhanced Local Hyperthermia for Cancer Treatment. IFAC-PapersOnLine. 2013;48–23:477–482.

[52] Pannocchia G, Gabiccini M, Artoni A. Offset-Free MPC Explained: Novelties, Subtleties, and Applications. IFAC-PapersOnLine. 2015;48:342–351.

[53] Pennes HH. Analyis of Tissue and Arterial Blood Temperatures in the Resting Human Forearm. J. Appl. Physiol. 1985;1:93–122.

[54] Pedregosa F, Varoquaux G, Gramfort A, et al. Scikit-learn: Machine Learning in Python. J. Mach. Learn. Res. 2011;12:2825–2830.

[55] Van Rossum G. Python tutorial. Amsterdam: Centrum voor Wiskunde en Informatica (CWI); 1995.

[56] Riverbank Computing Limited. PyQt5 Reference Guide.

[57] Campagnola L. PyQtGraph - Scientific Graphics and GUI Library for Python: www.pyqtgraph.org. 2014.

[58] Zaporzan B, Waspe AC, Looi T, et al. MatMRI and MatHIFU: Software Toolboxes for Real-Time Monitoring and Control of MR-Guided HIFU. J. Ther. Ultrasound. 2013;1:7.

[59] Gurobi Optimization LLC. Gurobi Optimizer Reference Manual. 2018.

[60] Ishihara Y, Calderon A, Watanabe H, et al. A Precise and Fast Temperature Mapping Using Water Proton Chemical Shift. Magn. Reson. Med. 1995;34:814–823.

[61] Negussie AH, Partanen A, Mikhail AS, et al. Thermochromic Tissue-Mimicking Phantom for Optimisation of Thermal Tumour Ablation. Int. J. Hyperth. 2016;6736:1–5.

[62] Deenen DA, Maljaars E, Sebeke L, et al. Offset-Free Model Predictive Control for Enhancing MR-HIFU Hyperthermia in Cancer Treatment. 6th IFAC Conf. Nonlinear Model Predict. Control. 2018. p. 223–228.

# Chapter 4

## Visualization of Thermal Washout due to Spatiotemporally Heterogeneous Perfusion in the Application of a Model-Based Control Algorithm for MR-HIFU Mediated Hyperthermia

## ABSTRACT

**Purpose:** This article will report results from the *in-vivo* application of a model-predictive control algorithm for MR-HIFU hyperthermia that was presented in a previous article. The focus of the investigation lies on the interplay between the controller's performance and the spatiotemporally heterogeneous perfusion.

**Materials and Methods:** Hyperthermia at 42 °C was induced and maintained for up to 30 minutes in the biceps femori of German landrace pigs (N = 5) using a commercial MR-HIFU system and a recently developed MPC algorithm. The influence of blood vessels on the heating power allocation was investigated by superimposing the applied heating pattern and calculated heat sink maps on contrast-enhanced MRI images. A lower bound for the hyperthermia-induced increase in perfusion was estimated based on the power required to maintain hyperthermia and its influence on the controller's performance was assessed.

**Results:** The MPC algorithm allocates additional heating power to sub-volumes with elevated heat sink effects, which are colocalized with blood vessels visible on contrast-enhanced MRI. The perfusion appeared to have increased by at least a factor of approximately 1.86 on average. The controller performed well throughout the treatments.

**Conclusions:** The MPC controller generates uniform temperature distributions despite the presence of spatiotemporally heterogeneous perfusion due to the rapid thermometry feedback available with MR-HIFU and the flexible allocation of heating power. The visualization of spatiotemporally heterogeneous perfusion presents new research opportunities for the investigation of stimulated perfusion in hypoxic tumor regions.

## INTRODUCTION

Mild hyperthermia, i.e., the heating of malignant tissue to temperatures between 40 and 43 °C, sensitizes tumors for chemo- and radiotherapy (RT and CT) without introducing additional systemic toxicity [1,2]. This thermal enhancement effect has already been demonstrated in several clinical trials targeting a wide variety of tumors [3-9]. It arises from direct denaturation of proteins [10], the inhibition of repair mechanisms [11-13], and the killing of cells that are RT- and CT-resistant, but vulnerable to heat, i.e., cells in the "S-phase" [14,15] or in environments that are hypoxic and acidic due to inadequate perfusion [16-20]. The vasodilation following hyperthermia can also lead to increased perfusion in the tumor, resulting in sensitization to RT and CT *via* reoxygenation [21,22] and enhanced drug availability [23-26]. However, heating must be carefully controlled to avoid vascular shutdown, which would negatively impact the clinical outcome [27].

Devices used for clinical hyperthermia applications are currently based on extracorporeal antenna systems emitting electromagnetic waves in the radiofrequency and microwave range, while temperature is typically monitored using thermocouples placed into target tissue [28]. These devices enable the application of energy across regions with diameters of tens of centimeters (regional hyperthermia, RHT), allowing to heat large tumor volumes. However, maintaining a high degree of temperature control throughout the tumor is of vital importance as there is a clear correlation between the applied thermal dose [29] and treatment outcome [30-33]. The extent of the volume to which energy can be applied homogeneously with a clinical radiative phased array system depends on the used wavelength and antenna geometry, and is in the range of centimeters [34,35]. The resulting temperature distribution is also affected by the local tissue properties, such as electrical conductivity and perfusion rate. Radiative phased array systems have limited capacity for the compensation of inhomogeneous heating rates and local heat sinks due to the lack of spatially resolved real-time feedback and the inherent lower limit to the size of the focus [34,36,37]. Dedicated tools for better planning of RF-induced regional hyperthermia that utilize tissue models to optimize energy delivery have been developed [35,36] and the recent integration of RF hyperthermia devices into MRI scanners enables non-invasive thermometry during heating. Despite these advances, precise control of the temperature distribution with RF devices remains challenging in the absence of closed-loop feedback control and clinicians still must rely on patient feedback to avoid local overheating [38].

Magnetic Resonance-guided High-Intensity Focused Ultrasound (MR-HIFU) presents a solution to the challenge of uniformity in the presence of heterogeneous tissue properties. Clinical HIFU transducers generate coherent ultrasound fields with frequencies in the range of approx. 0.35 to 2 MHz that interfere constructively in a focal volume [39]. Dissipation of ultrasound energy results in a sharp temperature increase in

4

the focal volume, which resembles an axisymmetric ellipsoid of around 7 mm in length along the transducer axis and 2 mm in diameter for a frequency of 1.2 MHz [40]. The heated volume can be increased by moving the focus, either *via* mechanical repositioning of the transducer (mechanical beam steering) or *via* coordinated phase shifts among the piezo elements on phased array transducers (electronic beam steering) [41,42]. The integration into an MRI patient table complements the precision of HIFU with high soft-tissue contrast and near-real-time- and spatially resolved MR-thermometry feedback. Currently, MR-thermometry is typically based on the proton resonance frequency shift (PRFS) method, which exploits the linear correlation between the Larmor frequency of protons in water molecules and the local temperature. PRFS thermometry allows to acquire temperature maps of non-fatty tissues with millimeter-resolution at sub-second timescales [43,44], which can serve as input for feedback-controlled HIFU sonications.

Using PRFS thermometry feedback and mechanical as well as electronic beam steering, Tillander *et al.* recently demonstrated the feasibility of stabilizing hyperthermic temperature elevations throughout clinically relevant volumes in highly perfused porcine thigh muscle *via* a binary feedback control algorithm [45]. This technique has already been applied clinically by Chu *et al.* and Heijman *et al.* for recurrent rectal cancer and dedifferentiated liposarcoma, respectively [46,47]. However, earlier calculations already showed that the high spatial control in power deposition of HIFU allows to compensate for differences in local tissue cooling due to tissue perfusion and around thermally significant vessels, which is not feasible using a binary control algorithm together with electronic beams steering along fixed trajectories [48]. The logical next step in the development of HIFU technology for the application in hyperthermia is therefore to fully leverage the precision of HIFU and spatially resolved MR-thermometry by a transition from binary feedback control to a controller that calculates optimal sonication patterns. Model predictive control (MPC) is a modern control scheme that is widely used in the industry [49,50] and has already been applied in algorithms for thermal ablation therapy [51-53]. MPC algorithms use a model of the system's dynamic behavior (the state-space model) to predict the state of the system at a future timepoint in response to the available control inputs. Using a cost function to define the target state of the system, the best control action at a given timepoint is found *via* the variation of the control inputs such that the cost function assumes its minimum and all state- and input variables satisfy their respective constraints. This allows the processing of multidimensional inputs like temperature maps into multidimensional outputs like heating power distributions, thereby enabling the online adaption of sonication patterns to the current distribution and strength of heat sinks.

Recently we presented the architecture of an MPC algorithm for MR-HIFU mediated local hyperthermia and characterized its performance in a perfused tissue-mimicking phantom in comparison to the current state-of-the-art binary feedback controller [45,54].

We showed that the MPC algorithm yields superior performance *in-vitro via* the targeted compensation of heat loss due to diffusion and local heat loss induced by an artificial blood vessel. In this study, we present results from the *in-vivo* application of the MPC algorithm in porcine thigh muscle. The aim is to evaluate the controller's performance in live tissue and to investigate the interplay between its flexible heating power allocation and spatiotemporally varying perfusion.

## MATERIALS AND METHODS

### Animal model

The performance of an MPC algorithm for the creation and maintenance of local hyperthermia was investigated in muscle tissue of the biceps femori of five healthy, female German landrace pigs between 35 and 39.5 kg in weight. The experimental protocol was approved by the State Agency for Nature, Environment and Consumer Protection of North Rhine Westphalia, Germany.

Starting 12 hours prior to the experiment, the pigs were fasted with free access to water. At the beginning of the experiment, the animals received an intramuscular injection of Atropine (0.02 mg/kg; WDT, Germany), Tiletamin/Zolazepam (10 mg/kg; Zoletil, Virbac, Germany), and Xylazin (2 mg/kg; Rompun 2 %; Bayer; Germany). Anesthesia was induced and maintained intravenously using Propofol (induction: 1.66 mg/kg i.v., maintenance: 4.0–9.5 mg/kg/h as required; Fresenius, Bad Homburg, Germany). Analgesia was achieved by intravenous administration of buprenorphine (0.02 mg/kg; Buprenovet Multidose, Bayer, Germany). The pigs were intubated and ventilated under pressure control (Hamilton C1, Heinen + Löwenstein, Switzerland) at 30 % oxygen, 14 breaths/min, and a positive end-expiratory pressure (PEEP) of 5–8 mmHg. The tidal volume was adjusted as needed to maintain normocapnia (PaCO2 35–45 mmHg). A catheter with three lumens (18G; Arrow International, Reading, USA) for the continuous administration of propofol and Ringer's solution (5 ml/kg/h; Fresenius Kabi, Germany) and the administration of other medication was placed in the right external jugular vein using the Seldinger technique.

The animals were placed inside the MRI scanner in right lateral recumbency with the biceps femori above the acoustic window of the HIFU table (Figure 1A). A rubber tube containing MR-visible oil capsules was affixed to the right thigh to allow localization of the targeted volumes during dissection (Figure 2B). Acoustic contact was achieved by shaving, the application of degassed ultrasound gel and the interposition of an acoustic coupling gel pad (Aquaflex® Ultrasound Gel Pad 4 x 27.5 x 27.5 cm, Parker Laboratories, Farfield, NJ, USA). Degassed and deionized water was used to ensure acoustic coupling between the acoustic membrane of the HIFU table and the gel pad. After positioning of the animal in the scanner was completed, a muscle relaxant (initial bolus: 0.1 mg/kg,

4

infusion: 36 mg/h/kg; Pancuroniumbromid Rotexmedica 2 mg/ml, Panpharma GmbH, Trittau, Germany) was administered to prevent shivering and a custom GaAs temperature sensor (Neoptix Inc, Quebec City, Quebec, Canada) encased in a carbon needle was placed in the biceps femori of the right leg.

Up to three hyperthermia treatments with a target temperature of 42 °C were performed in each session and were continued for up to 30 minutes, targeting a disc-shaped volume with a diameter of 18 mm and a thickness of 7 mm in the biceps femori. After the end of each treatment, temperature mapping was continued for up to 15 minutes and a minimum waiting time of 30 minutes was maintained between individual treatments to ensure the restoration of thermal equilibrium. To ensure the presence of large blood vessels in the vicinity of the target volume, areas close to the femur were targeted (Figure 1C). The animals were returned to the stable eight hours after the beginning of anesthesia and were allowed to recover for 48h under observation. Finally, the animals were euthanized using sodium-pentobarbital (150 mg/kg i.v., Euthadorm®, CP-Pharma, Burgdorf, Germany).

## Experimental setup

The hyperthermia treatments were performed on a clinical MR-HIFU system (3T Achieva®, Philips Healthcare, Best, The Netherlands, and Sonalleve® V2 HIFU, Profound Medical, Mississauga, Canada). Treatment planning and feedback control of the temperature during treatment was performed using a python-based software developed in-house and a model predictive control algorithm. The python-based software provides a user interface with tools for the planning and monitoring of treatments and communicates with the hardware using the pyMRI and pyHIFU packages of Zaprozan *et al.* [55].
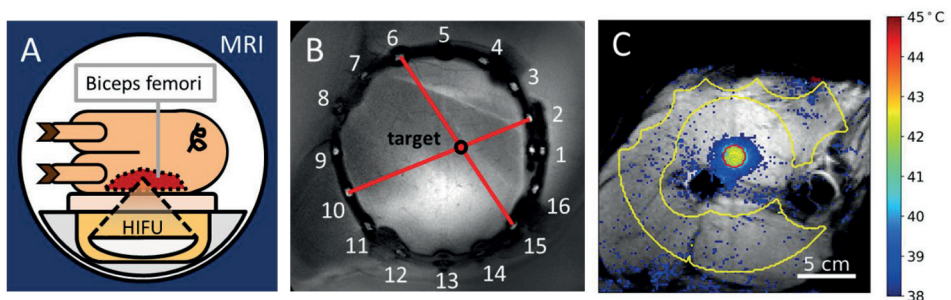


**Figure 1:** Experimental Setup. (**A**) The animal is positioned on the HIFU table such that the biceps femori can be sonicated. (**B**) The rubber tube containing fish oil capsules is visible in MRI and is used to document the target site. (**C**) MRI with temperature map overlay. Yellow contour: Drift correction ROI with manually excluded areas. Red contour: Target ROI.

## Controller architecture

The controller follows the MPC paradigm and was described in detail in a previous article [54], see chapter 2 of this thesis. The description here will therefore be brief.

*State-space model*

The state-space model that will be used in the MPC scheme is based on the Pennes bioheat transfer equation (PBE) [56], incorporating heat loss via local perfusion, diffusion of heat and heating by an external source:

$$\rho_t C_t \frac{\partial T}{\partial t} = \nabla \cdot (K\nabla T) - W_b C_b (T - T_a) + Q \tag{1}$$

where $\rho_t$ is the density of the tissue [kg/m³], $K$ is the thermal conductivity [W/(K · m)], $C_t$ and $C_b$ are the specific heat capacities of tissue and blood [J/(kg · K)], $W_b$ is the perfusion rate [kg/(m³ · s)], $T$ is the tissue's temperature [°C], $T_a$ is the arterial temperature [°C], and $Q$ is the heating power density delivered to the tissue [W/m³]. The MPC controls the temperature in the target volume using a thermometry slice bisecting its center in perpendicular orientation to the HIFU beam axis. The temperature elevation above the baseline temperature at timestep $k + 1$ in the voxel at the grid position $(m, n)$, denoted by $\hat{T}'_{t+1}(m, n)$, is described by:

$$\hat{T}'_{k+1}(m, n) = A_0 T'_k(m, n)$$
$$+A_1\big(T'_k(m + 1, n) + T'_k(m - 1, n) + T'_k(m, n + 1) + T'_k(m, n - 1)\big)$$
$$+\sum_{i=1}^{N_p} q \cdot p_{k,i} \cdot f_i(m, n) \tag{2}$$

$$A_0 = \left(1 - 4 \cdot \frac{K}{\rho_t C_t h^2}\Delta t - \frac{W_b C_b}{\rho C}\Delta t\right)$$
$$A_1 = \frac{K}{\rho_t C_t h^2}\Delta t \tag{3}$$

where $A_0$ is the heat retention coefficient, which incorporates the loss due to perfusion and the diffusion out of the voxel, $A_1$ is the per-dynamic inter-voxel heat transfer coefficient, and $\Delta t$ is the timestep length. The variable $q$ represents the absorption coefficient [K/W], $p_{k,1}$ is the acoustic power applied targeting the sonication point with index $i$ at timepoint $k$, $f_i(m, n)$, is the spatial distribution of heating power among voxel coordinates $(m, n)$ when targeting the sonication point with index $i$, and $N_p$ is the number of available sonication points. The input variables $p_{k,i}$, $i = 1, ..., N_p$, are constrained to be greater than or equal to zero and to total no more than a specified maximum power $p_{max}$ at each timestep $k$:

$$0 \leq p_{k,i} \text{ for } i = 1, \dots, N_p$$

$$\sum_{i=1}^{N_p} p_{k,i} \leq p_{max} \qquad [4]$$

Each allowed sonication point is chosen to coincide with the middle of an MRI voxel and is assumed to heat that particular voxel exclusively, i.e. $f_i(m, n)$ is assumed to be one at the targeted voxel's coordinates and zero everywhere else. The allowed sonication points were all voxels belonging to the target ROI's edge and were arranged in a checker-pattern everywhere else inside the target ROI.

## Cost function

The optimal distribution of heating power was determined *via* constrained optimization of the cost function. For this controller, it has been given the form:

$$\omega(T) = \gamma B_0(1 - \sigma) \qquad [5]$$

where $H$ is the control horizon, $R$ is the set of coordinates belonging to the voxels inside the target ROI, $N_R$ is the number of voxels inside $R$, and $T'_{obj}$ is the target temperature elevation. The control horizon determines how many future timesteps are considered in the optimization. For this study, $H$ was set to 5.

## Focal spot calibration and model identification

The transducer's alignment with the MRI's coordinate system was verified using multiple 16 s long test sonications at 60 W of acoustic output power before each experiment. During the test sonication, the HIFU focus was rapidly moved on a trajectory consisting of the transducer's natural focus and eight points equally distributed on an 8 mm circle around the natural focus by electronic beam steering. Offsets from the intended centers of heating were corrected by adjusting the transducer's position inside the HIFU table.

After alignment was verified, the MRI thermometry maps gathered during three additional test sonications were used to calibrate the state-space model's parameters. The estimation of the $A_0$ and $A_1$ parameters is performed *via* linear regression, for which all voxels within a radius of 2 cm around the target area are included. The voxels' temperatures at each timestep $k + 1$ after transducer shutoff were used as the dependent variable. The respective voxel's temperature at time $k$ (parameter $A_0$) as well as the sum of the nearest neighbors' temperatures at time $k$ (parameter $A_1$) were used as the regressors. The model used therefore has the following form:

$$T'_{k+1}(m, n) = A_0\left(T'_k(m, n)\right)$$
$$+A_1\left(T'_k(m + 1, n) + T'_k(m - 1, n) + T'_k(m, n + 1) + T'_k(m, n - 1)\right) \qquad [6]$$

The linear regression was performed using the Python package scikit-learn, version 0.18.1 [57].

After the calculation of $A_0$ and $A_1$ is complete, the absorption coefficient $q$ is calculated *via* linear regression. Here, the total temperature increase across all voxels in a radius of 20 mm around the natural focus at each timestep $k$ serves as the dependent variable and the retained fraction of the power added to the target slice is used as the regressor. This results in a linear model of the form

$$\sum_{(m,n)\in M} T_k'(m,n) = q \cdot P \cdot \Delta t \cdot \sum_{i=0}^{k} (A_0 + 4A_1)^k \qquad [7]$$

where $P$ is the acoustic output power selected for the sonication, $M$ is the set of voxel coordinates within a radius of 20 mm around the transducer's natural focus and $(A_0 + 4A_1)$ is the fraction of power retained in the focus slice from one cycle to the next.

In the first two animals, $q$ was calculated by dividing the accumulated thermal load in the last temperature map of the test sonication by the total test sonication duration at the time of acquisition. However, the resulting absorption coefficients were notably higher than expected and exhibited large variability, prompting the development of the method described above.

**Magnetic Resonance Imaging**

All images were acquired using the HIFU table's window coil and the HIFU pelvis coil (Model 905051-F, Philips Healthcare, Best, The Netherlands) on a 3T MRI scanner (3T Achieva®, Philips Healthcare, Best, The Netherlands).

*Pre-treatment imaging*

The treatment planning was performed using a 3D T1-weighted fast field echo (FFE) without fat suppression. The used parameters were TE = 2.3 ms, TR = 6.1 ms, FA = 20°, acquisition matrix = 88 x 166, number of slices = 167, reconstructed (acquired) voxel dimensions = 0.49 x 0.49 x 1.50 mm (1.52 x 1.53 x 3.00 mm), FOV = 140 x 261 x 250 mm, fold-over direction = RL. Constant Level Appearance (CLEAR) was used to achieve higher signal homogeneity and Sensitivity Encoding (SENSE, P reduction = 1.2, S reduction = 1) was used to accelerate imaging. This resulted in an acquisition duration of 5.5 minutes.

*MR thermometry*

The imaging sequence used to monitor the treatment progress was an RF-spoiled gradient echo sequence with TR = 30 ms, TE = 19.5 ms, FA = 19.5°, FOV = 288 x 288 mm, 6 slices, and voxel dimensions = 1.8 x 1.8 x 7 mm, resulting in an acquisition time of 3.7 s for a full set of slices and a resolution of 160 x 160 voxels per slice. The temperature maps

4

were acquired *via* the proton resonance frequency shift (PRFS) [43]. In particular, the calculation included masking of low SNR voxels, masking of the expected heating area and of areas exhibiting strong thermometry artifacts, baseline subtraction, and a second order baseline drift correction. The MRI slices were positioned in four stacks, namely the focus, sagittal, near field, and far field stacks. The focus stack contained three slices, all other stacks contained one slice. The focus stack was oriented perpendicular to the transducer axis, centered on the HIFU focus point and contained three slices to provide a complete view of the volumetric temperature distribution in the target ROI, with the center slice of the focus stack functioning as feedback for the MPC algorithm. The sagittal stack was oriented in sagittal orientation and was centered on the focus spot. It provides information on the vertical alignment of the focus. The near-field stack was positioned at the pig's skin to monitor excess heat generation in the hydrogel spacer, indicative of excessive absorption. The far-field stack was positioned deep to the focal area.

## Postinterventional imaging

The sonications were evaluated by contrast-enhanced (CE) MRI, using the 3D T1-weighted FFE sequences described above for treatment planning. For this purpose, the images were acquired twice, both before and one minute after intravenous contrast agent injection (0.1 mmol/kg gadoteric acid, Dotagraf®, Jenapharm GmbH & Co. KG, Jena, Germany). The parameters and field of view of the post-treatment scans were kept the same as the planning scans. The presence of non-perfused volumes (NPVs) was determined by subtracting pre- and post-injection CE MR images.

## Data Analysis

### Sonication metrics

The quality of the hyperthermic temperature control during the sonications was evaluated using parameters that were calculated from the temperature voxel values within the target ROI. The target ROI was placed in the center temperature mapping slice of the focus stack. The steady-state performance of the MPC were calculated from PRFS voxel temperature data acquired between 300s and the end of the sonication. The used parameters were the mean temperature in the target ROI $\bar{T}_s$, the 10th and 90th percentile of the voxel temperature distribution $T_{90s}$ and $T_{10s}$, the standard deviation of the voxel temperatures in the target ROI $\sigma_s$ and the mean squared tracking error of all voxels in the target ROI $\delta^2$, which corresponds to the cost function for a control horizon $H$ of 1.

## MR thermometry validation

In all treatments, temperature mapping was maintained for 15 minutes after the conclusion of the sonication to identify the presence of excessive phase drift. If the

temperature in the target ROI converged back to baseline (± 1 K), the temperature maps acquired during the sonication were judged valid.

One sonication was performed close to the temperature sensor instead of the femur to validate the conversion from phase shift to temperature increase. The readings of the temperature sensor were recorded every 10 s using a multichannel signal conditioner (Neoptix Reflex, Neoptix Inc, Québec, Canada). For the thermometry validation, the PRFS temperature measurements of all voxels in a radius of twice the voxel size around the location of the temperature sensor's tip were extracted using a custom Python application. The extracted PRFS temperature values were averaged for each timestep to obtain the PRFS temperature measurement at the sensor's tip over time. The mean absolute error between each sensor reading and the PRFS temperature closest in time was calculated to evaluate the performance. The effect of viscous heating [58] on the temperature sensor's measurements was not subtracted from the sensor measurements as the applied HIFU power decreased sharply after the initial warmup phase, necessarily diminishing viscous heating.

*Spatial power allocation and apparent perfusion*
The ability of the controller to counteract localized heat loss was investigated by superimposing the average power applied to each voxel on the contrast-enhanced MRI scans that were acquired after the conclusion of the treatments. Additionally, the combined effect of heat diffusion and perfusion on the temperature of each voxel during cooldown was determined *via* linear regression. This apparent perfusion rate $W_a$ was superimposed on the same MRI slices to verify the colocalization of local heat sinks and blood vessels. $W'_a$ (mass flow of blood per volume of tissue) was calculated according to equation (8) and converted to the more commonly used $W_a$ (volume flow of blood per mass of tissue, equation (9)):

$$W_a'(m,n) = \left(1 - \frac{T_{k+1}(m,n)}{T_k(m,n)}\right) \cdot \frac{\rho_t \cdot C_t}{C_b \cdot \Delta t} \qquad [8]$$

$$W_a = \frac{W_a'}{\rho_t \rho_b} \qquad [9]$$

*Analysis of the model error over time*
The temperature distribution predicted by equation (2) was calculated for each temperature map from the temperature map and the applied heating pattern of the previous timestep. The resulting prediction was subtracted from the measured temperature distribution to obtain the prediction error in each voxel at each timestep. The arithmetic mean of the prediction error in each voxel of the target ROI was calculated in each timestep to obtain the mean target ROI prediction error $\Omega_{ROI}$. Additionally, the prediction error in a sub-

volume of each target ROI $\Omega_{sub}$ was investigated. The sub-volumes consisted of the voxel in the target ROI to which most energy had been allocated throughout the sonication and those of its nearest neighbors which also contained an allowed sonication point. The behavior of $\Omega_{ROI}$ and $\Omega_{sub}$ was modeled as a linear combination of the prediction errors arising from a time-dependent perfusion parameter mismatch $\Delta w$ and an absorption parameter mismatch $\Delta q$:

$$\Omega(t, p) = \Delta w(t) + \Delta q \cdot p + \Omega_0$$
$$\Delta w(t) = m_w t$$
[10]

where $p$ is the total power applied to the respective area and $m_w$ is the slope of the temporal change. The intercept $\Omega_0$ incorporates the perfusion- and heat diffusion parameter errors arising from the a-priori model identification and the equilibration of diffusion losses. The diffusion losses were assumed to reach equilibrium by 300s. Therefore, all timepoints between 300s and the end of the sonication were considered for this analysis. Experiments that were terminated prematurely and experiments that exhibited signs of phase drift were excluded.

## RESULTS

A series of hyperthermia experiments (N = 10) were performed, targeting a disk-shaped volume of 18 mm in diameter and 7 mm in height. This results in a diameter of the heated volume of approximately 3.3 cm along the transducer axis. The target temperature was set to 42 °C and heating was maintained for up to 30 minutes. The target volumes were placed in the biceps femori of healthy landrace pigs (N = 5). Before each hyperthermia experiment, three 16 s long test sonications at 60 W of acoustic power were performed under continuous MR-thermometry. The acquired thermometry data served to spatially align the coordinate systems of the MRI and the HIFU, and to derive the model parameters to initialize the MPC controller for the subsequent hyperthermia experiments. In addition to MR-thermometry, absolute temperature measurements were acquired using a temperature sensor inserted into the thigh muscle of the animal.

### Model identification

The model parameters calculated from the PRFS temperature maps acquired during the test sonications and the derived thermal properties are listed in Table 2. The listed parameters were used as model parameters in the hyperthermia experiments following the respective model identification, see subsection *Focal spot calibration and model identification* in the *Materials and Methods* section.

**Table 1:** Identified model parameters and corresponding physiological quantities. Bracketed and values were calculated using a previous algorithm utilizing only the final temperature map of the test sonication and are not included in the calculation of the respective averages.

| Animal Number/ Experiment Number | $A_0$ | $A_1$ | $q$ [K/J] | $K_1$ [W/m/K] | $W_b$ [ml/s/kg] | $\alpha$ [mm³K/J] |
|---|---|---|---|---|---|---|
| 1/1 | 0.520 | 0.120 | [0.827] | 0.39 | 0 | [43.62] |
| 2/1 | 0.500 | 0.110 | [0.558] | 0.35 | 14.51 | [28.23] |
| 2/2 | 0.510 | 0.110 | [0.478] | 0.35 | 12.09 | [26.29] |
| 3/1 | 0.513 | 0.117 | 0.397 | 0.38 | 4.37 | 21.27 |
| 3/2 | 0.500 | 0.117 | 0.330 | 0.38 | 7.64 | 17.43 |
| 4/1 | 0.540 | 0.110 | 0.403 | 0.35 | 4.84 | 20.46 |
| 4/2 | 0.570 | 0.100 | 0.356 | 0.32 | 7.25 | 17.76 |
| 4/3 | 0.503 | 0.117 | 0.374 | 0.38 | 7.01 | 19.53 |
| 5/1 | 0.507 | 0.107 | 0.295 | 0.35 | 15.70 | 16.34 |
| 5/2 | 0.533 | 0.110 | 0.335 | 0.35 | 6.53 | 16.87 |
| Average (SD) | 0.520 (0.021) | 0.112 (0.006) | 0.356 (0.036) | 0.36 (0.02) | 7.99 (4.58) | 18.51 (1.76) |

*Abbreviations:* $A_0$: Heat retention parameter; $A_1$: Heat exchange parameter; $q$: voxel absorption coefficient; $K$: thermal conductivity; $W_b$: Perfusion rate; $\alpha$: absorption coefficient

## Hyperthermia Experiments

The controller performance for all hyperthermia experiments is detailed in Table 2. A representative PRFS temperature curve and corresponding PRFS temperature maps for different phases of the hyperthermia sonication are shown in Figure 2. The controller first reached a mean temperature of 42 °C in the target area at 53.7 ± 9.0 s after the start of the sonication. The average absolute tracking error of the average temperature during steady-state was 0.2 K. Treatment 4/3 was cancelled prematurely due to time constraints in the animal protocol. NPVs were not observed in post-treatment CE MRI. Animals 2 and 3 exhibited localized erythema and swelling on the treated leg. The erythema was colocalized with air bubbles visible on MRI and resolved within 24 hours in both animals. Limping or other behaviors indicating discomfort in the treated leg were not observed in any animal.

**Table 2:** Overview of sonication metrics. The target temperature was always 42 °C. All values are averages over the timespan from 300s from initiation to the end of the sonication.

| Animal number/ experiment number | Animal weight [kg] | $\overline{T}_s$ [°C] | $T_{10s}$ [°C] | $T_{90s}$ [°C] | $T_{10s} - T_{9s}$ [°C] | $\sigma_s$ [°C] | $\delta^2$ (x $10^3$) |
|---|---|---|---|---|---|---|---|
| 1/1 | 37 | 41.6 | 42.1 | 41.0 | 1.02 | 0.42 | 23 |
| 2/1 | 39 | 42.1 | 42.7 | 41.4 | 1.30 | 0.51 | 22 |
| 2/2 | | 41.9 | 42.6 | 41.1 | 1.57 | 0.70 | 30 |
| 3/1 | 39 | 42.1 | 42.7 | 41.4 | 1.34 | 0.52 | 32 |
| 3/2 | | 42.4 | 43.1 | 41.6 | 1.55 | 0.60 | 32 |
| 4/1 | 37 | 42.3 | 43.3 | 41.3 | 1.98 | 0.82 | 42 |
| 4/2 | | 42.1 | 42.6 | 41.4 | 1.21 | 0.48 | 24 |
| 4/3 | | 41.8 | 42.5 | 41.0 | 1.46 | 0.61 | 65 |
| 5/1 | 35 | 42.0 | 42.5 | 41.6 | 0.90 | 0.41 | 15 |
| 5/2 | | 42.1 | 42.7 | 41.6 | 1.13 | 0.45 | 17 |
| Average (SD) | 37.4 | 42.04 (0.22) | 42.68 (0.33) | 41.34 (0.21) | 1.35 (0.30) | 0.55 (0.12) | 30 (14) |

*Abbreviations:* $\overline{T}_s$: Mean temperature in target ROI; $T_{90s}$, $T_{10s}$: 90th and 10th percentile of voxel temperatures in the target ROI; $\sigma_s$: standard deviation of the voxel temperatures in the target ROI; $\delta^2$: Mean squared tracking error.

## Spatial power allocation and apparent perfusion

Figure 4 shows the average spatial heating power allocation per PRFS thermometry voxel during all sonications superimposed on the CE MRI scans of the respective area. Heating power was allocated to the edges of the target ROI and was increased in areas which showed elevated perfusion in the CE MRI scans. This effect was especially prominent in cases where blood vessels adjoined or penetrated the target ROI. Accordingly, Figure 5 shows that the apparent voxel perfusion value exhibited clear regions of elevation in highly perfused areas, see subsection *Spatial power allocation and apparent perfusion* in the *Materials and Methods* section.
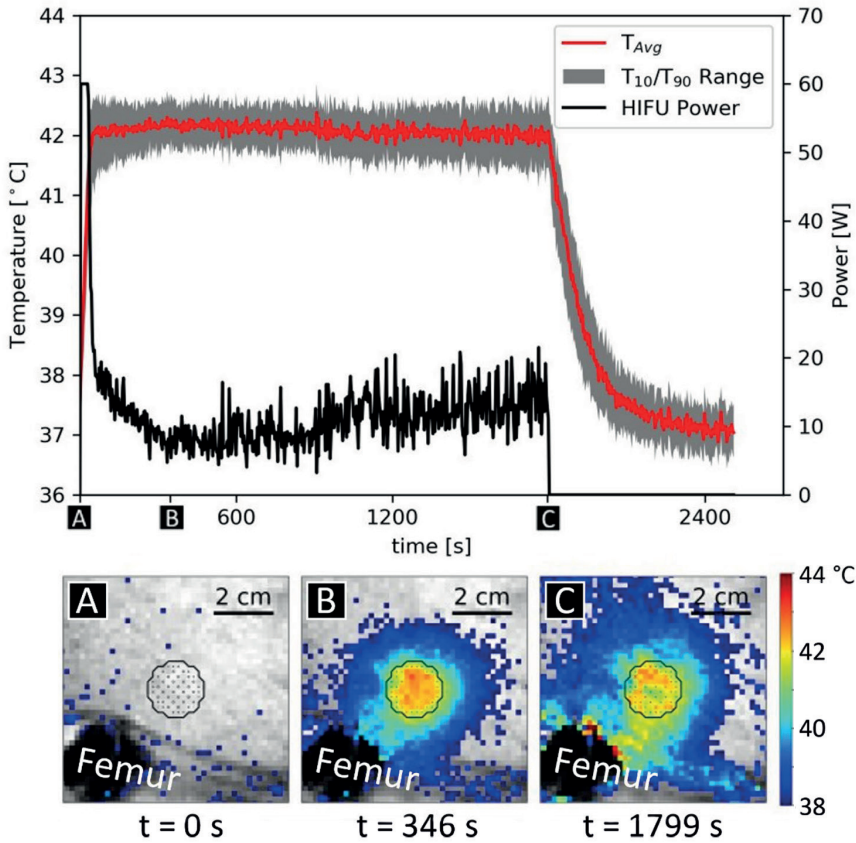
**Figure 2:** Example of temperature evolution and spatial temperature/power distribution during different control phases during a sonication, treatment 5/1. The black outline shows target ROI and the points inside the target ROI indicate power allocation. (**A**) Warmup phase, power is allocated primarily to the ROI's center. (**B**) Beginning of steady-state phase; power is allocated primarily to the edges of the target ROI. (**C**) Late steady-state phase, immediately before the end of the sonication. Power is allocated to the edge and heterogeneously throughout the target ROI.

4
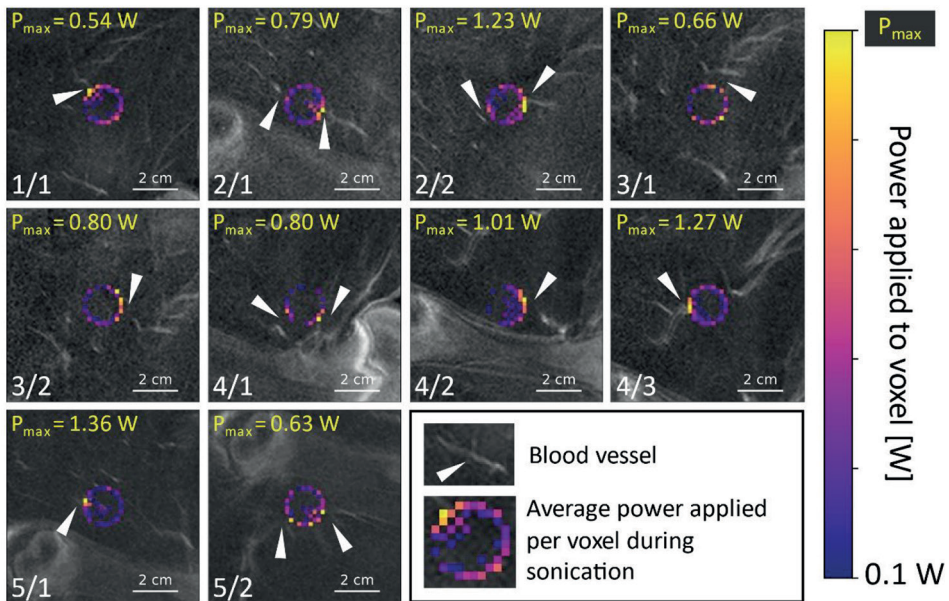
**Figure 3:** Average spatial heating power allocation per PRFS thermometry voxel for all experiments superimposed on contrast-enhanced MRI images. White arrowheads mark regions with elevated heating power allocation.



**Figure 4:** Apparent voxel perfusion per PRFS thermometry voxel for all experiments superimposed on contrast-enhanced MRI images. White arrowheads match arrowheads in Figure 4.
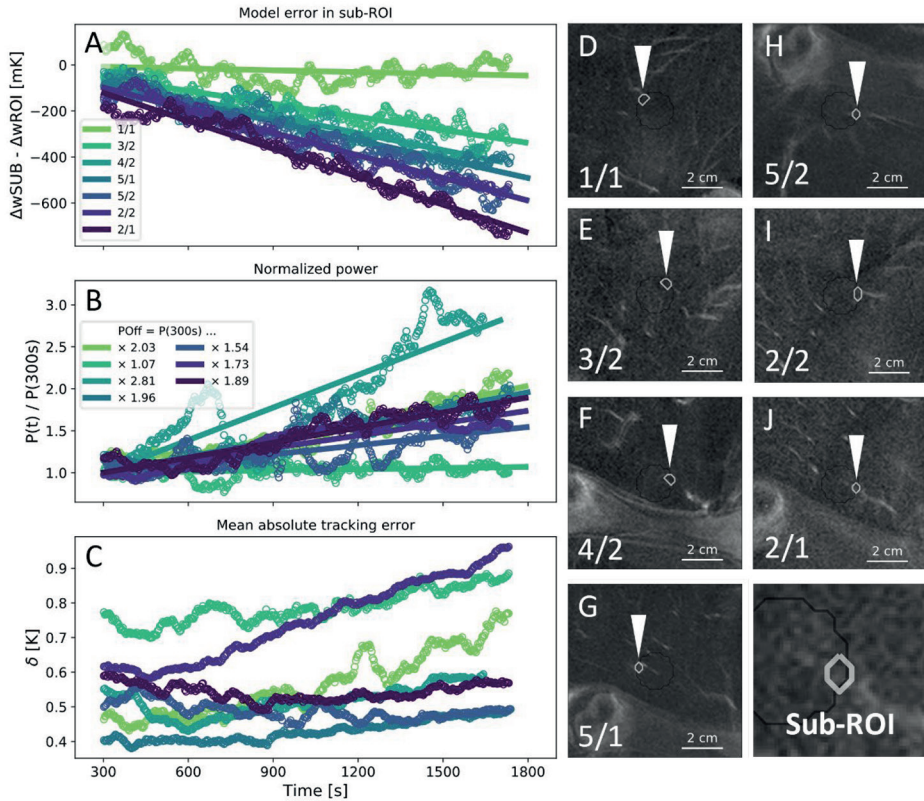
**Figure 5:** (**A**) The time-dependent model error in the sub-volumes around the voxel that had received the highest amount of heating energy minus the time-dependent model error in the entire ROI. (**B**) Total applied HIFU power normalized by the output pow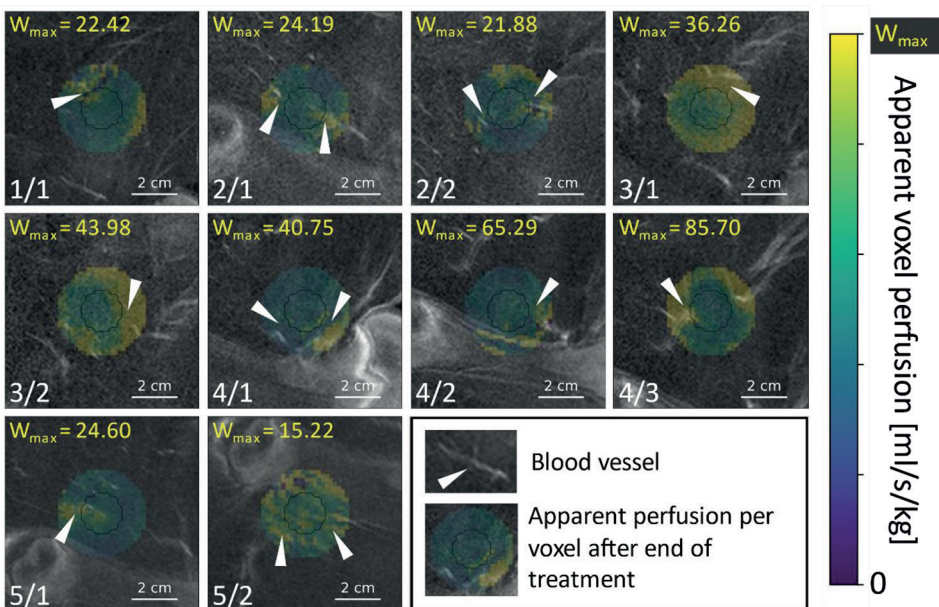er at 300 s. (**C**) Mean absolute tracking error in the target ROI. A one-minute moving average was applied to all data points in (**A**-**C**) to enhance clarity. (**D**-**J**) Contrast-enhanced MRI with superimposed outlines of the investigated sub-volumes in order from smallest to largest slope in (**A**). White arrowheads indicate the sub-volumes' locations.

## Analysis of dynamic processes

The difference between time-dependent prediction errors $\Delta w$ of the sub-volumes and of target ROIs between the equilibration at 300 s and the end of the sonication show a clear negative correlation with time (Figure 5A). Over the course of the 25 minutes between equilibration and the end of the sonication, five of nine power levels rose by a factor between 1.54 and 2.03. One power level rose by a factor of 2.81 (treatment 4/2) and one power level rose by a factor of 1.07 (treatment 3/2). On average, the power level required to maintain hyperthermia rose by a factor of 1.86 (Figure 5B). Changes in the mean absolute tracking error in the target ROI $\delta$ were small in five of the seven treatments with changes in the range of 0.1 K. Two treatments (1/1, 2/2) showed an increase in $\delta$ of more

than 0.2 K (Figure 5C). All sub-volumes were at least in proximity to a blood vessel and the presence of a large blood vessel inside the target ROI appears to result in a steeper slope of $\Delta w(t)$ (Figure 5D-J).



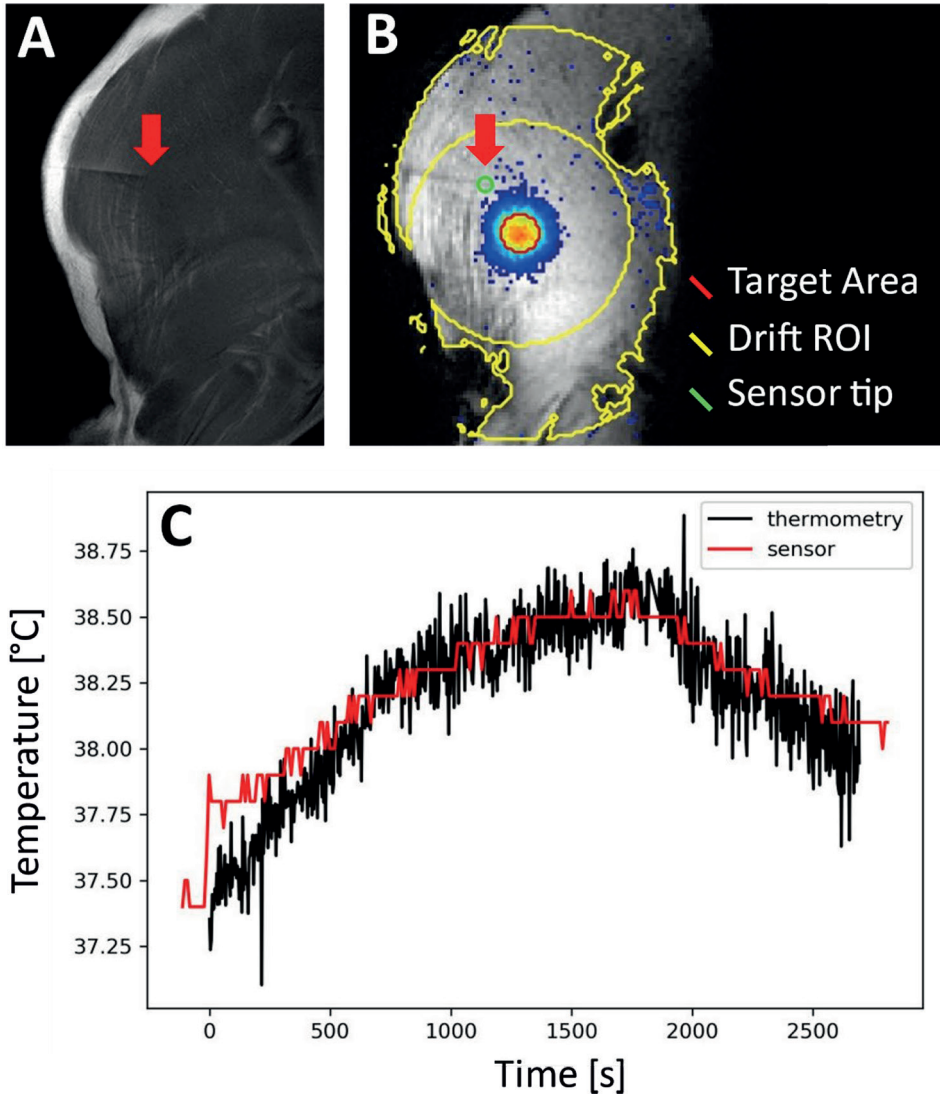**Figure 6:** Thermometry validation during experiment 3/2. (**A**) High-resolution T1-weighted slice showing the location of the temperature sensor needle's tip. (**B**) Magnitude image with PRFS thermometry overlay, showing the location of the PRFS temperature readout. (**C**) Readings of the temperature sensor and the PRFS thermometry at the sensor tip's location.

**Thermometry**

Except for experiments 4/1 and 5/1, the average PRFS thermometry readings in the target ROI returned to baseline in all experiments, indicating the absence of excessive phase drift. The results from the thermometry validation are shown in Figure 3. Viscous heating introduced a sudden temperature increase by + 0.4 °C at the temperature sensor at the beginning of the sonication, which diminished over time. The temporal arithmetic mean (SD) of the absolute thermometry error was 0.12 (0.02) °C.

## DISCUSSION

We have investigated the performance of a model-predictive controller for MR-HIFU-mediated local hyperthermia at 42 °C for up to 30 minutes in a series of *in-vivo* studies. The controller quickly stabilized the temperature in the target area with small steady-state tracking errors and narrow temperature distributions. While the heating power was uniformly distributed across the target area at the start of each experiment, the controller gradually allocated additional heating power to areas with local heat sinks caused by blood vessels. Analysis of the modelling error at these localized heat sinks revealed a time-dependent component to the modelling error with a negative slope, which accumulated considerable magnitude in some cases. Validation of the MR-thermometry *via* the insertion of a fiber-optic temperature probe into the vicinity of one target volume exhibited good agreement between thermometry- and probe readings.

In a previous article, we have shown that the MPC outperforms the state-of-the-art binary hyperthermia controller in a tissue-mimicking phantom both in terms of tracking error and uniformity of the temperature distribution [45,54]. The *in-vivo* results presented here also indicate a smaller average absolute tracking error and a narrower temperature distribution in comparison to the values reported for the binary controller. The main advantage of the MPC is the more tightly controlled temperature distribution ($T_{10} - T_{90}$) 1.35 ± 0.30 K vs. 2.15 ± 0.40 K for the MPC and the binary controller, respectively). The binary scheme only permits the application of one power level per feedback cycle throughout the target ROI, while the MPC allows more flexible allocation of heating power. Consequently, the MPC algorithm can compensate perfusion-induced differences in local heat loss more effectively and can react to the increase of perfusion that occurs during hyperthermia [27,59] by adapting the used sonication pattern. The targeted compensation of local heat sinks should allow to adequately heat heterogeneously perfused tumors without causing vascular shutdown due to overheating, which is still a challenge today [19,60].This is also made possible in part by the rapid feedback provided by PRFS thermometry, which allowed the controller to maintain high performance

4

despite the pronounced local enhancement of perfusion over time that was observed in this study.

Any results regarding perfusion obtained in this study must be considered qualitative due to the lack of a gold standard measurement like radioactive microspheres, and the mismatch of the calculated perfusion and diffusion parameters with values reported in the literature [61–63]. Nonetheless, a thermoregulation response can clearly be seen via the increase in heat drain close to blood vessels compared to the rest of the heated region. Working under the assumption that diffusion heat loss remains constant after 300s, we can establish a lower bound for the thermoregulation response in the target area. If the heat loss at 300s is attributed to perfusion exclusively, the increase in heating power by a factor of 1.86 translates into an increase in perfusion by the same factor, which is close to the responses reported by Lokshina *et al.* for the leg muscles of male Sprague-Dawley rats [64]. To our knowledge, comparable results have not yet been published for large animals or human subjects. The visualization and real-time estimation of perfusion changes as a response to hyperthermia presents an opportunity for future research. Most studies concerning the physiological response of tumor vasculature to elevated temperatures was conducted in the 1980s and only quantified averages across the whole tumor [60]. Using a high-performance controller for MR-HIFU hyperthermia and thermal modelling, it may be possible to gather new insight on the optimal conditions for the reperfusion and reoxygenation of tumor entities that are highly refractory to chemo- and radiotherapy. A suitable thermal model for this purpose may be the discrete vasculature (DIVA) model originally developed by Kotte *et al*. [65,66]. In thermal simulations, the results obtained with models featuring discrete vasculature differ substantially from results obtained with models based on Pennes bioheat equation [67] and the former show much better agreement with noninvasive thermometry data [68]. In the DIVA model, the vasculature is represented by a series of buckets which exchange heat with the surrounding tissue *via* a set of voxels containing at least a part of the vessel. Temporally varying blood flow rates can be modelled *via* the adjustment of the blood velocity and/or the vessel radius, allowing the representation of stimulated vasodilation in healthy and tumor tissue [65].

The comparison of the PRFS thermometry readings and the temperature sensor measurements showed good agreement, indicating correct translation from phase shifts to temperature shifts. The viscous heating caused by the interaction of the peripheral ultrasound with the temperature sensor was not discernible in the PRFS thermometry readings. The likely reasons for this include the small size of the affected volume in comparison to the overall PRFS measurement volume, the small associated temperature elevation and the partial volume effect [69]. The second-order drift correction worked well in all but two cases where the temperature did not return to an equilibrium in the range of one Kelvin around the baseline within 15 minutes after the end of the sonication.

These failures resulted from a problem with the phase unwrapping step that was used in the drift correction algorithm.

Future avenues for improvement therefore clearly include a more robust thermometry feedback algorithm. This will become especially important for applications in abdominal organs, where both periodic and aperiodic motion will be encountered [70]. We therefore deem thermometry that is robust against both motion and field drift the most urgent concern. Furthermore, this control algorithm currently does not include transducer movement for the enlargement of the targetable area and a strategy for near-field temperature management that would be necessary to safely treat very large or highly perfused volumes [45]. An integration of these features will be indispensable to the clinical translation of the controller. Finally, we have shown that the thermoregulation response to hyperthermia can locally lead to considerable deviations from the expected thermal behavior of the heated region. While this does not necessarily lead to a substantial decline in controller performance thanks to the rapid thermometry feedback available with MR-HIFU, it warrants the investigation of offset-free control strategies [71]. These may be of special interest for drug delivery applications with temperature sensitive liposomes, where the rate of release depends on the temperature of the blood [72].

The main limitation of this study is the lack of a tumor in the target area. The perfusion of tumors is heterogeneous [60], generally reacts less strongly to heating than muscle tissue [73,74] and considerable variability among preclinical tumor entities has been observed [75,76]. Tumors may also have acoustic characteristics distinct from healthy surrounding tissue [77]. The controller performance reported here may therefore not be representative of the performance that would be observed in the clinical case. Nonetheless, the developed MPC exhibits high performance in the presence of spatially heterogeneous and time-dependent perfusion. We therefore believe that this control algorithm will maintain a high degree of temperature control in tumor tissue as well.

In conclusion, we have demonstrated the use of an MPC algorithm for MR-HIFU-mediated hyperthermia in a large animal model. The MPC algorithm provides uniform temperature distributions in the presence of heterogeneous perfusion by allocating additional heating power to localized heat sinks. MR-HIFU-mediated highly uniform hyperthermia holds the promise of detailed insight into the interplay between spatiotemporally heterogeneous perfusion and heating, and the thermal enhancement effect. Clinically, it may become a tool for the treatment of deep-seated tumors that cannot be heated uniformly with other modalities.

4

## ACKNOWLEDGEMENT

# REFERENCES

[1] Issels RD. Hyperthermia Adds to Chemotherapy. Eur. J. Cancer. 2008;44:2546–2554.

[2] Horsman MR, Overgaard J. Hyperthermia: A Potent Enhancer of Radiotherapy. Clin. Oncol. 2007;19:418–426.

[3] Issels RD, Lindner LH, Verweij J, et al. Effect of Neoadjuvant Chemotherapy Plus Regional Hyperthermia on Long-Term Outcomes Among Patients With Localized High-Risk Soft Tissue Sarcoma. JAMA Oncol. 2018;4:483–492.

[4] Franckena M, Stalpers LJA, Koper PCM, et al. Long-Term Improvement in Treatment Outcome After Radiotherapy and Hyperthermia in Locoregionally Advanced Cervix Cancer: An Update of the Dutch Deep Hyperthermia Trial. Int. J. Radiat. Oncol. Biol. Phys. 2008;70:1176–1182.

[5] Van der Zee J, González González D, Van Rhoon GC, et al. Comparison of Radiotherapy Alone with Radiotherapy plus Hyperthermia in Locally Advanced Pelvic Tumours: A Prospective, Randomised, Multicentre Trial. Lancet. 2000;355:1119–1125.

[6] Overgaard J, Bentzen SM, Overgaard J, et al. Randomised trial of hyperthermia as adjuvant to radiotherapy for recurrent or metastatic malignant melanoma. Lancet. 1995;345:540–543.

[7] Vernon CC, Hand JW, Field SB, et al. Radiotherapy with or without hyperthermia in the treatment of superficial localized breast cancer: Results from five randomized controlled trials. Int. J. Radiat. Oncol. Biol. Phys. 1996;35:731–744.

[8] Jones EL, Oleson JR, Prosnitz LR, et al. Randomized Trial of Hyperthermia and Radiation for Superficial Tumors. J. Clin. Oncol. 2005;23:3079–3085.

[9] Cihoric N, Tsikkinis A, Rhoon G Van, et al. Hyperthermia-related clinical trials on cancer treatment within the ClinicalTrials. gov registry. Int. J. Hyperth. 2015;31:609–614.

[10] Dewey WC, Hopwood LE, Sapareto SA, et al. Cellular responses to combinations of hyperthermia and radiation. Radiology. 1977;123:463–474.

[11] Eppink B, Krawczyk PM, Stap J, et al. Hyperthermia-induced DNA repair deficiency suggests novel therapeutic anti-cancer strategies. Int. J. Hyperth. 2012;28:509–517.

[12] Konings AWT. Interaction of Heat and Radiation In Vitro and In Vivo. Princ. Pract. Thermoradiotherapy Thermochem. 1995. p. 89–102.

[13] Powell SN, Kachnic LA. Homologous recombination research is heating up and ready for therapy. Proc. Natl. Acad. Sci. U. S. A. 2011;108:9731–9732.

[14] Westra A, Dewey WC. Variation in sensitivity to heat shock during the cell-cycle of chinese hamster cells in vitro. Int. J. Radiat. Biol. 1971;19:467–477.

[15] Malyapa RS, Sawada S. Variation in heat sensitivity through the cell cycle of M10 and Burkitt P3HR-1 cells. Int. J. Hyperth. 1992;8:463–473.

[16] Gerweck LE. Modification of Cell Lethality at Elevated Temperatures The pH Effect. Radiat. Res. 1977;70:224–235.

[17] Freeman ML, Dewey WC, Hopwood LE. Effect of pH on Hyperthermic Cell Survival: Brief Communication 2. JNCI J. Natl. Cancer Inst. 1977;58:1837–1839.

[18] Horsman MR, Overgaard J. The impact of hypoxia and its modification of the outcome of radiotherapy. J. Radiat. Res. 2016;57:i90–i98.

[19] Datta NR, Kok HP, Crezee H, et al. Integrating Loco-Regional Hyperthermia Into the Current Oncology Practice: SWOT and TOWS Analyses. Front. Oncol. 2020;10:819.

[20] Vaupel P. Pathophysiology of Solid Tumors. Impact Tumor Biol. Cancer Treat. Multidiscip. Strateg. 2009. p. 51–92.

[21] Zywietz F, Reeker W, Kochs E. Changes in tumor oxygenation during a combined treatment with fractionated irradiation and hyperthermia: An experimental study. Int. J. Radiat. Oncol. Biol. Phys. 1997;37:155–162.

[22] Vujaskovic Z, Song CW. Physiological mechanisms underlying heat-induced radiosensitization. Int. J. Hyperth. 2004;20:163–174.

[23] Dewhirst MW, Secomb TW. Transport of drugs from blood vessels to tumour tissue. Nat. Rev. Cancer. 2017;17:738–750.

4

[24] De Smet M, Langereis S, Van den Bosch S, et al. SPECT/CT Imaging of Temperature-Sensitive Liposomes for MR-Image Guided Drug Delivery with High Intensity Focused Ultrasound. J. Control. Release. 2013;169:82–90.

[25] Lokerse WJM, Bolkestein M, Hagen TLM, et al. Investigation of Particle Accumulation, Chemosensitivity and Thermosensitivity for Effective Solid Tumor Therapy Using Thermosensitive Liposomes and Hyperthermia. Theranostics. 2016;6:1717–1731.

[26] Farr N, Wang Y-N, D'Andrea S, et al. Hyperthermia-enhanced targeted drug delivery using magnetic resonance-guided focussed ultrasound: a pre-clinical study in a genetic model of pancreatic cancer. Int. J. Hyperth. 2018;34:284–291.

[27] Vujaskovic Z, Poulson JM, Gaskin AA, et al. Temperature-dependent changes in physiologic parameters of spontaneous canine soft tissue sarcomas after combined radiotherapy and hyperthermia treatment. Int. J. Radiat. Oncol. Biol. Phys. 2000;46:179–185.

[28] Kok HP, Cressman ENK, Ceelen W, et al. Heating technology for malignant tumors: a review. Int. J. Hyperth. 2020;37:711–741.

[29] Sapareto S a., Dewey WC. Thermal Dose Determination in Cancer Therapy. Int. J. Radiat. Oncol. 1984;10:787–800.

[30] Franckena M, Fatehi D, Bruijne M de, et al. Hyperthermia dose-effect relationship in 420 patients with cervical cancer treated with combined radiotherapy and hyperthermia. Eur. J. Cancer. 2009;45:1969–1978.

[31] Bakker A, Van Der Zee J, Van Tienhoven G, et al. Temperature and thermal dose during radiotherapy and hyperthermia for recurrent breast cancer are related to clinical outcome and thermal toxicity: a systematic review. Int. J. Hyperth. 2019;36:1023–1038.

[32] Ohguri T, Harima Y, Imada H, et al. Relationships between thermal dose parameters and the efficacy of definitive chemoradiotherapy plus regional hyperthermia in the treatment of locally advanced cervical cancer: data from a multicentre randomised clinical trial. Int. J. Hyperth. 2018;34:461–468.

[33] Kroesen M, Mulder HT, Van Holthe JML, et al. Confirmation of thermal dose as a predictor of local control in cervical carcinoma patients treated with state-of-the-art radiation therapy and hyperthermia. Radiother. Oncol. 2019;140:150–158.

[34] Crezee J, Lagendijk JJW. Temperature uniformity during hyperthermia: The impact of large vessels. Phys. Med. Biol. 1992;37:1321–1337.

[35] Mulder HT, Curto S, Paulides MM, et al. Systematic Quality Assurance of the BSD2000-3D MR-Compatible Hyperthermia Applicator Performance Using MR Temperature Imaging. Int. J. Hyperth. 2018;35:305–313.

[36] Kok H, Wust P, Stauffer P, et al. Current state of the art of regional hyperthermia treatment planning: a review. Radiat. Oncol. 2015;10.

[37] Curto, Aklan, Mulder, et al. Quantitative, Multi-institutional Evaluation of MR Thermometry Accuracy for Deep-Pelvic MR-Hyperthermia Systems Operating in Multi-vendor MR-systems Using a New Anthropomorphic Phantom. Cancers (Basel). 2019;11:1709.

[38] Kok HP, Korshuize- Van Straten L, Bakker A, et al. Online Adaptive Hyperthermia Treatment Planning During Locoregional Heating to Suppress Treatment-Limiting Hot Spots. Int. J. Radiat. Oncol. Biol. Phys. 2017;99:1039–1047.

[39] Ter Haar G, Coussios C. High Intensity Focused Ultrasound: Physical Principles and Devices. Int. J. Hyperth. 2007;23:89–104.

[40] Civale J, Rivens I, Shaw A, et al. Focused Ultrasound Transducer Spatial Peak Intensity Estimation: A Comparison of Methods. Phys. Med. Biol. 2018;63:055015.

[41] Cain CA, Umemura S-I. Concentric-Ring Phased-Array Ultrasound. IEEE Trans. Microw. Theory Tech. 1986;34:542–551.

[42] Ebbini ES, Cain CA. A Spherical-Section Ultrasound Phased Array Applicator for Deep Localized Hyperthermia. IEEE Trans. Biomed. Eng. 1991;38:634–643.

[43] Ishihara Y, Calderon A, Watanabe H, et al. A Precise and Fast Temperature Mapping Using Water Proton Chemical Shift. Magn. Reson. Med. 1995;34:814–823.

[44] Rieke V, Pauly KB. MR thermometry. J. Magn. Reson. Imaging. 2008;27:376–390.

[45] Tillander M, Hokland S, Koskela J, et al. High Intensity Focused Ultrasound Induced In Vivo Large Volume Hyperthermia under 3D MRI Temperature Control. Med. Phys. 2016;43:1539–1549.

[46] Heijman E, Yeo SY, Sebeke L, et al. Volumetric Hyperthermia of Soft Tissue Sarcoma using MR-Guided High Intensity Focussed Ultrasound. 6th Int. Symp. Focus. Ultrasound. 2018.

[47] Chu W, Huang Y, Pichardo S, et al. A phase I study of MR-HIFU hyperthermia (HT) with radiation (RT) and chemotherapy (CT) for recurrent rectal cancer. J. Glob. Oncol. 2019;

[48] Lagendijk JJW, Crezee J, Hand JW. Dose uniformity in scanned focused ultrasound hyperthermia. Int. J. Hyperth. 1994;10:775–784.

[49] Mayne DQ. Model predictive control: Recent developments and future promise. Automatica. 2014;50:2967–2986.

[50] Lee JH. Model Predictive Control: Review of the Three Decades of Development. Int. J. Control. Autom. Syst. 2011;9:415–424.

[51] Arora D, Skliar M, Roemer RB. Model-Predictive Control of Hyperthermia Treatments. IEEE Trans. Biomed. Eng. 2002;49:629–639.

[52] Blankespoor A, Payne A, Todd N, et al. Model Predictive Control of HIFU Treatments in 3D for Treatment Time Reduction. AIP Conf. Proc. 2009;1113:215–219.

[53] De Bever J, Todd N, Payne A, et al. Adaptive Model-Predictive Controller for Magnetic Resonance Guided Focused Ultrasound Therapy. Int. J. Hyperth. 2014;30:456–470.

[54] Sebeke LC, Deenen DA, Maljaars E, et al. Model Predictive Control for MR-HIFU-Mediated Uniform Hyperthermia. Int. J. Hyperth. 2019;36:1040–1050.

[55] Zaporzan B, Waspe AC, Looi T, et al. MatMRI and MatHIFU: Software Toolboxes for Real-Time Monitoring and Control of MR-Guided HIFU. J. Ther. Ultrasound. 2013;1:7.

[56] Pennes HH. Analyis of Tissue and Arterial Blood Temperatures in the Resting Human Forearm. J. Appl. Physiol. 1985;1:93–122.

[57] Pedregosa F, Varoquaux G, Gramfort A, et al. Scikit-learn: Machine Learning in Python. J. Mach. Learn. Res. 2011;12:2825–2830.

[58] Morris H, Rivens I, Shaw A, et al. Investigation of the viscous heating artefact arising from the use of thermocouples in a focused ultrasound field. Phys. Med. Biol. 2008;53:4759–4776.

[59] Bicher HI, Hetzel FW, Sandhu TS, et al. Effects of hyperthermia on normal and tumor microenvironment. Radiology. 1980;137:523–530.

[60] Vaupel PW, Kelleher DK. Pathophysiological and vascular characteristics of tumours and their importance for hyperthermia: hetero-geneity is the key issue. Int. J. Hyperth. 2010;26:211–223.

[61] Wyler F, Käslin M, Hof R, et al. Das Göttinger Miniaturschwein als Versuchstier. 1979;36:31–36.

[62] Tranquilli WJ, Parks CM, Thurmon JC, et al. Organ blood flow and distribution of cardiac output in nonanesthetized swine. Am. J. Vet. Res. 1982;43:895–897.

[63] Henriques FCJ, Moritz AR. Studies of Thermal Injury. Am. J. Pathol. 1946;530–549.

[64] Lokshina AM, Song CW, Rhee JG, et al. Effect of fractionated heating on the blood flow in normal tissues. Int. J. Hyperth. 1985;1:117–129.

[65] Kotte A, Van Leeuwen G, De Bree J, et al. A description of discrete vessel segments in thermal modelling of tissues. Phys. Med. Biol. [Internet]. 1996;41:865–884. Available from: https://dx.doi.org/10.1088/0031-9155/41.

[66] [66] Kotte ANTJ, Van Leeuwen GMJ, Lagendijk JJW. Modelling the thermal impact of a discrete vessel tree. Phys. Med. Biol. [Internet]. 1999;44:57–74. Available from: https://dx.doi.org/10.1088/0031-9155/44.

[67] [67] Van Den Berg CAT, Van De Kamer JB, De Leeuw AAC, et al. Towards patient specific thermal modelling of the prostate. Phys. Med. Biol. 2006;51:809–825.

[68] [68] Craciunescu OI, Raaymakers BW, Kotte ANTJ, et al. Discretizing large traceable vessels and using DE-MRI perfusion maps yields numerical temperature contours that match the MR noninvasive measurements. Med. Phys. 2001;28:2289–2296.

[69] Todd N, Vyas U, De Bever J, et al. The Effects of Spatial Sampling Choices on MR Temperature Measurements. Magn. Reson. Med. 2011;65:515–521.

[70] Aubry J-F, Pauly K, Moonen C, et al. The road to clinical use of high-intensity focused ultrasound for liver cancer: technical and clinical consensus. J. Ther. Ultrasound. 2013;1:13.

4

[71]  Deenen DA, Maljaars E, Sebeke L, et al. OffsetFree Model Predictive Control for Enhancing MR-HIFU Hyperthermia in cancer treatment. IFAC-PapersOnLine. 2018;51:191–196.

[72]  Lokerse WJM, Kneepkens ECM, ten Hagen TLM, et al. In depth study on thermosensitive liposomes: Optimizing formulations for tumor specific therapy and in vitro to in vivo relations. Biomaterials. 2016;82:138–150.

[73]  Song CW, Kang MS, Rhee JG, et al. Effect of Hyperthermia on Vascular Function in Normal and Neoplastic Tissues. Ann. N. Y. Acad. Sci. 1980;335:35–47.

[74]  Vaupel P. Pathophysiological Mechanisms of Hyperthermia in Cancer Therapy. Biol. Basis Oncol. Thermother. 1990.

[75]  Song CWC. Effect of Local Hyperthermia on Blood Flow and Microenvironment: A Review. Cancer Res. 1984;44:4721–4730.

[76]  Rossmanna C, Haemmerich D. Review of Temperature Dependence of Thermal Properties, Dielectric Properties, and Perfusion of Biological Tissues at Hyperthermic and Ablation Temperatures. Crit. Rev. Biomed. Eng. 2014;42:467–492.

[77]  Duck FA. Physical Properties of Tissue. A Comprehensive Reference Book. Med. Phys. 1990.

# Chapter 5

# Liposomal Drug Delivery of Doxorubicin using MR-HIFU Hyperthermia in a Large Animal Model

## ABSTRACT

**Purpose:** Encapsulation of cytostatic drugs for a localized release is an effective way to increase the therapeutic width of such agents. In this article we present the localized release of doxorubicin (DOX) from a novel formulation of thermosensitive liposomes using MR-HIFU mediated hyperthermia in a large animal model.

**Materials and Methods:** German landrace pigs of weights between 37.5 and 53.5 kg received an infusion of DOX containing temperature sensitive Liposomes (100 mg/m²/h, 30 min). The pigs' biceps femori was treated locally in two target areas with mild hyperthermia using magnetic resonance guided high intensity focused ultrasound, starting 10 minutes and 60 minutes after initiation of the infusion, respectively. The pharmacokinetics and biodistribution of the drug were determined and an analysis of the treatment parameters' influence was performed.

**Results:** Compared to untreated tissue, we found a 15-fold and a 7-fold increase in DOX concentration in the muscle volumes that had undergone hyperthermia starting 10 min and 60 min after the beginning of the infusion, respectively. The pharmacokinetic analysis showed a slow clearance of the liposomal carrier and a drug leakage half-life of approximately 25 minutes. A linear relationship was found between the AUC of the free drug in the target volume and the resulting drug concentration in the tissue.

**Conclusions:** HIFU-Hyperthermia is a suitable method for local drug release of DOX using thermosensitive liposomes in non-moving targets in large animals. This study is an important milestone towards clinical translation.

## INTRODUCTION

Mild local heating of tumor tissue to hyperthermic temperature in the range of 41–43 °C has been shown to have strong synergistic effects on radio- and chemotherapy, acting on cellular and tissue level [1-6]. Besides a plethora of preclinical evidence, several clinical trials demonstrated the synergistic effects of hyperthermia on radio-, chemo-, and chemoradiotherapy leading to improved outcome such as local control, disease free-, and long-term survival [7-16]. Another important application of hyperthermia is its use as a trigger for local drug delivery in combination with temperature sensitive drug carrier systems such as liposomes. This concept was first proposed by Yatvin and Weinstein *et al*. in the late seventies using temperature sensitive liposomes (TSLs) for delivery of neomycin and methotrexate [17,18]. The hydrophilic drug is first loaded into the interior aqueous lumen and remains stably encapsulated at body temperature as it cannot pass the lipophilic lipid bilayer. When exposed to hyperthermic temperatures, the lipid bilayer goes through a sol-gel to liquid-crystalline melting transition (Tm) inducing a destabilization and transient porosity of the liposomal membrane that mediates a rapid release of the drug [19-21]. For local drug delivery, the malignant tissue is heated to hyperthermic temperatures while the drug-loaded TSLs are infused. As long as the TSLs keep circulating, local and continuous release of the drug from its liposomal carrier is triggered within the vessels of the heated target tissue which is followed by subsequent drug uptake into the tumor tissue. Preclinical studies performed with different doxorubicin (DOX)-loaded TSLs (DOX -TSLs) demonstrated an increase of intratumoral DOX concentration by a factor of approx. 5–25 depending on the exact experimental parameters, such as TSL formulation, employed hyperthermia device as well as tumor models [20-25]. Several factors and parameters play a decisive role in the concept of temperature induced drug delivery, which are related to the properties of the TSLs, the drug itself, and, most importantly, to the *in-vivo* situation. Ideally, drug leakage from the TSLs at body temperature should be minimal while the liposomal carrier itself should be cleared as slowly as possible. Furthermore, release of the drug from TSLs should be rapid and complete at hyperthermic temperatures. Together, these parameters determine the amount of "free drug" that is available during hyperthermia [26]. The drug itself should have molecular properties which allow a rapid extravasation and subsequent uptake into the tumor tissue, without suffering from excessive washout. The complex interplay of TSL clearance, drug leakage at body temperature, release kinetics, rates of uptake, and clearance of the free drug together with tissue perfusion during hyperthermia-mediated drug delivery with TSLs has been studied *in-silico* [27]. Importantly, recent experimental data obtained in a rat sarcoma for hyperthermia-induced drug delivery followed by thermal ablation using MR-HIFU as a heating device are well in agreement with the simulations [28]. Much experimental work was devoted

5

to the development of improved TSL formulations and their preclinical testing, mainly using doxorubicin as active pharmaceutical ingredient (API) [20]. Meanwhile, first TSL formulation of DOX (Thermodox®, Celsion coorp., New Jersey, United States) comprising a mixture of the lyso-lipid 1-monostearoyl-2-hydroxy-sn-glycero-3-phosphocholine (MSPC) with 1.2-dipalmitoyl-sn-glycero-3-phosphocholine (DPPC) and a pegylated lipid 1,2-distearoyl-sn-glycero-3-phosphoethanolamine-N-[amino(polyethylene glycol)-2000] (DSPE-PEG) has been used in clinical studies in combination with radiofrequency ablation (RFA) of liver lesions and local regionally recurrent breast cancer [19,29-32]. An alternative formulation was introduced by Lindner *et al*., using the novel glycerol-based phospholipid 1.2-dipalmitoyl-sn-glycero-3-phosphoglyceroglycerol (DPPG$_2$) in combination with DPPC and 1.2-distearoyl-sn-glycero-3-phosphocholine (DSPC) omitting lyso-lipids as well as pegylated lipids [33]. The release-temperature of DPPG$_2$ based TSLs can be adjusted within the hyperthermic temperature range by varying the molar fractions of the lipid constituents. Importantly, DPPG$_2$-TSLs loaded with carboxyfluorescin as a model drug showed a substantially prolonged circulation time in rats although no pegylated lipids are incorporated in the lipid bilayer [33]. A doxorubicin-loaded DPGG2-TSL formulation (DPPG$_2$-TSL-DOX) has been developed and preclinically tested in rat sarcoma model and in privately owned cats suffering from spontaneous feline soft tissue sarcoma [34]. The dose-escalation study in cats showed a positive correlation between the infused dose and the plasma concentration as well as the half-life of DOX. More importantly, an objective tumor response was already observed even at a low dose of 0.6 mg DOX/kg bodyweight [34]. The studies in a sarcoma rat model also demonstrated a long plasma half-life of DOX, pointing at slow clearance of the DPPG$_2$-TSL carrier as well as a slow leakage of DOX from the TSL. DOX quantification revealed an approximately 10–17 fold increase in tumor DOX concentration depending on the hyperthermia devices used [34-36]. Higher intratumoral DOX concentrations were found when a laser device was used to establish local hyperthermia confined to the tumor tissue compared to regional hyperthermia employing a water bath. While the clinical use of laser-based hyperthermia is limited to superficial targets, magnetic resonance guided high intensity focused ultrasound (MR-HIFU) can be used as a hyperthermia device to locally heat deep seated tissue noninvasively. The use of MR-HIFU for local drug delivery in combination with TSLs has been demonstrated in several preclinical studies in mice, rats and rabbits [28,37-50]. The distinguishing feature and strength of MR-HIFU is the tight temperature control which can be achieved thanks to near-real time MR-thermometry together with a closed feedback loop to the HIFU controller [51-55]. A recently introduced control algorithm further improved the attainable uniformity of the temperature distribution using a model-predictive control implementation [55], see chapters 2 and 3 of this thesis. Notably, the MPC algorithm in combination with MR-HIFU allowed to compensate for perfusion

induced heat loss occurring at blood vessels, which may be of special importance to TSL-based drug delivery as blood temperature and perfusion are key parameters.

The central aim of this study is a step towards clinical translation of temperature-triggered drug delivery using the promising formulation DPPG$_2$-TSL-DOX in combination with MR-HIFU as a device to induce conformal and uniform hyperthermia. The study was performed in healthy pigs as a large animal model to establish a suitable clinical workflow such as TSL infusion, management of possible adverse immune reactions, and prolonged hyperthermia. Our special interest was to investigate the timing of hyperthermia with respect to the infusion of TSLs as the drug uptake in the heated target tissue is expected to scale with the plasma level of free DOX.

## MATERIALS AND METHODS

### Liposomes and Chemicals

DOX containing liposomes (DPPG$_2$-TSL-DOX) were provided by Thermosome GmbH (Munich, Germany). The lipid bilayer consisted of the lipids 1,2-Dipalmitoyl-sn-Glycero-3-Phosphocholine (DPPC), 1,2-Distearoyl-sn-Glycero-3-Phosphocholine (DSPC) and 1,2-dipalmitoyl-sn-glycero-3-phosphodiglycerol (DPPG$_2$). The molar ratios of these lipids in the formulation was 50:20:30 (DPPC:DSPC:DPPG$_2$). The DOX concentration was 1.6 mg/ml and the lipid to drug molar ratio was 0.082 (mmol/mmol). The diameter of the liposomes was determined by dynamic light scattering (DLS using non-invasive backscattering with a scattering angle of 173° and a wavelength of 633 nm) to be 115 nm and the calculated PDI was 0.088. The external buffer used was PBF (pH 7.4). All other substances were purchased from commercial vendors and used without further purification unless otherwise stated.

### MR-HIFU Hyperthermia Setup

The hyperthermia treatments were performed on a clinical MR-HIFU system (3T Achieva®, Philips Healthcare, Best, The Netherlands) and Sonalleve® V2 HIFU, (Profound Medical, Mississauga, Canada). Treatment planning and feedback control of the temperature during treatment was performed using a custom MPC algorithm and software presented in a previous article [55]. The controller uses a model of the tissue's dynamic thermal behavior to predict the temperature at future timepoints in response to the available control inputs. The objective of the controller is defined using a cost function that assumes its minimum when all voxels in the target volume are at the target temperature. The best sonication pattern at a given timepoint is found *via* the variation of the control inputs, i.e., the heating power distribution, such that the cost function assumes its minimum. Simultaneously, the behavior of the voxel temperature variables is constrained to behave

5

according to the thermal model of the tissue and the heating power is limited to a given maximum. The resulting power distribution is translated to a sonication pattern which is then applied by the HIFU transducer. In combination with the rapid temperature feedback enabled by MR-thermometry, this control scheme generates highly uniform temperature distributions in phantom material and *in-vivo* [55], see chapters 2 and 3 of this thesis.

**Animal model**

In this study, the release of DOX from temperature sensitive liposomes using MR-HIFU hyperthermia was investigated in four healthy, female German landrace pigs between 37.5 and 53.5 kg in weight. The experimental protocol was approved by the State Agency for Nature, Environment and Consumer Protection of North Rhine Westphalia ('Landesamtes für Natur, Umwelt- und Verbraucherschutz des Landes Nordrhein-Westfalen', LANUV). An overview of the experimental timeline is presented in Figure 1.

Potential anaphylactic reactions to the liposomes were prevented by administration of methylprednisolone acetate (3 mg/kg i.m.; Depo-Medrol® ad us vet., Zoetis Schweiz GmbH, 2800 Delémont, Switzerland) 24h prior to the start of the liposome infusion as well as methylprednisolone (3 mg/kg i.v.; Medrate® Solubile ad us. vet., Zoetis Schweiz GmbH, Delémont, Switzerland), diphenhydramine (1 mg/kg i.v.; Diphenhydramin-Hevert®, Hevert-Arzneimittel GmbH & Co. KG, Nußbaum, Germany), and ranitidine (1 mg/kg i.v., Ranitidin-ratiopharm® 50 mg/5 ml, Ratiopharm GmbH, Ulm, Germany) 1h prior to the start of the liposome infusion. Starting 12 hours prior to the experiment, the pigs were fasted with free access to water. At the beginning of the experiment, the animals received an intramuscular injection of Atropine (0.02 mg/kg; WDT, Germany) and Tiletamin/Zolazepam (10 mg/kg; Zoletil, Virbac, Germany). Anesthesia was induced and maintained intravenously using Propofol (induction: 1.66 mg/kg i.v., maintenance: 4.0–9.5 mg/kg/h as required; Fresenius, Bad Homburg, Germany). Analgesia was achieved by intravenous administration of buprenorphine (0.02 mg/kg; Buprenovet Multidose, Bayer, Germany). The pigs were intubated and ventilated under pressure-control (Hamilton C1, Heinen + Löwenstein, Switzerland) at 30% oxygen, 14 breaths/min, and a positive end-expiratory pressure (PEEP) of 5–8 mmHg. The tidal volume was adjusted as needed to maintain normocapnia ($PaCO_2$ 35–45 mmHg). A catheter with three lumens (18G; Arrow International, Reading, USA) for the continuous administration of propofol and Ringer's solution (5 ml/kg/h; Fresenius Kabi, Germany) and for the administration of the liposomes, was placed in the right external jugular vein using the Seldinger technique. The animals were placed inside the MRI scanner in left lateral recumbency with the biceps femori above the acoustic window of the HIFU table (Figure 2A). Acoustic contact and sufficient distance of the biceps femori from the ultrasound window was achieved by shaving, applying degassed ultrasound gel and the interposition of an acoustic coupling gel pad (Aquaflex® Ultrasound Gel Pad 4 x 27.5 x 27.5 cm, Parker Laboratories,

Farfield, NJ, USA). After positioning the animal in the scanner, a muscle relaxant (initial bolus: 0.1 mg/kg, infusion: 36 mg/h/kg; Pancuroniumbromid Rotexmedica 2 mg/ml, Panpharma GmbH, Trittau, Germany) was administered to prevent shivering. After MR-HIFU treatment planning was finished, DPPG$_2$-TSL-DOX (Thermosome GmbH, Planegg, Germany) was infused for 30 minutes at 100 mg/m²/h (for a total dose of 50 mg/m²). Two local hyperthermia treatments with target temperatures of 42 °C were initiated at 10 minutes and 60 minutes after beginning of the DPPG$_2$-TSL-DOX infusion. The targets for the hyperthermia treatment were disc-shaped volumes with a diameter of 18 mm and a thickness of 7 mm in the left biceps femori. After the end of the second HT treatment, i.e, approx. 110 minutes after the start of the infusion, the centers of both treated volumes and a separate piece of muscle that did undergo hyperthermia were marked *via* ablation. This resulted in coagulated volumes of ellipsoid shape with axis lengths of about 4 x 4 x 15 mm³. The ablated tissue in the hyperthermia-treated muscle was used as visual markers to localize the hyperthermia-treated volumes during dissection. The ablated tissue in the untreated muscle was used as a control to study any possible additional effects of the ablation on the DOX concentration. The animals were euthanized using sodium-pentobarbital (150 mg/kg i.v., Euthadorm®, CP-Pharma, Burgdorf, Germany) three hours after the start of the DPPG$_2$-TSL-DOX infusion.
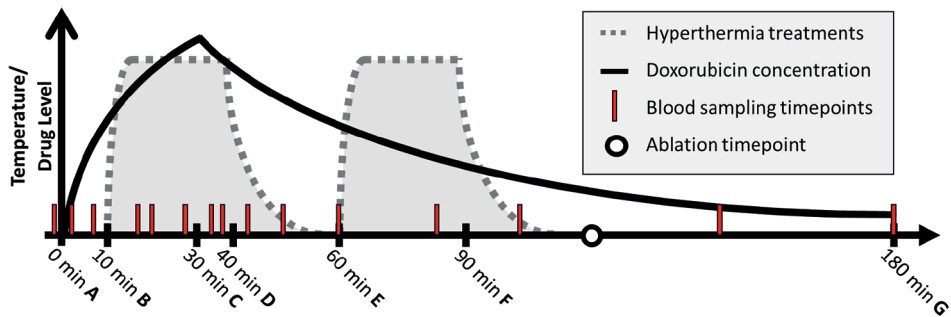


**Figure 1:** Experimental Timeline. Blood was sampled at 0, 2, 8, 15, 20, 28, 32, 38, 45, 50, 60, 80, 100, 140 and 180 minutes after start of infusion. **A:** Start of infusion, **B:** Start of first hyperthermia treatment, **C:** End of infusion, **D:** End of first hyperthermia treatment, **E:** Start of second hyperthermia treatment, **F:** End of second hyperthermia treatment, **G:** Euthanasia.
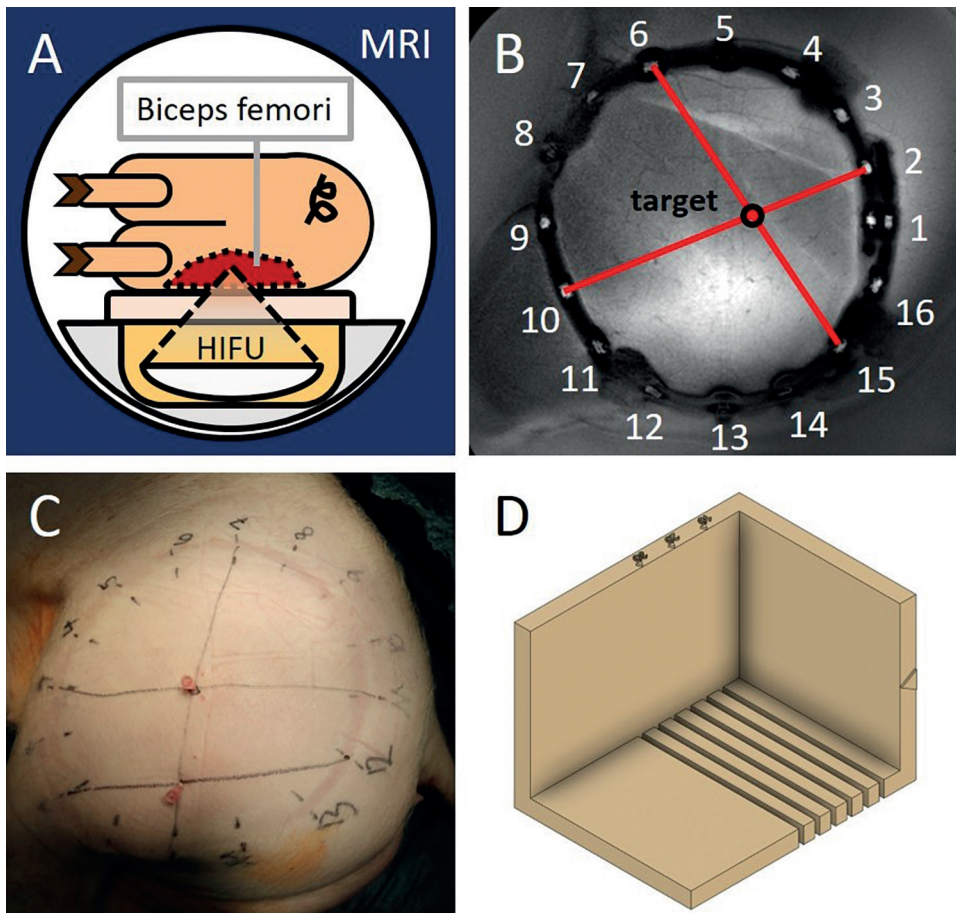
**Figure 2:** Experimental setup. (**A**) Positioning of the pig in lateral recumbency. The hind limb is positioned above the HIFU transducer and an acoustically transparent gel pad is interposed to facilitate acoustic coupling. (**B**) Example for the localization of the treated areas *via* MR-visible markers. The intersection of the line connecting the markers 6 and 15 as well as the line connecting markers 2 and 10 marks the point on the pig's skin directly lateral to the targeted area. (**C**) Localization of the targeted areas using marks on the skin. (**D**) Cutting guide used for slicing excised muscle samples into 5 mm thick slices.

## Sampling for Pharmacokinetics and Biodistribution analysis

Blood samples of approx. 4 ml were drawn using monovettes containing K3 EDTA (S-Monovette® 9 ml, Sarstedt AG & Co. KG, Nümbrecht, Germany) at 0, 2, 8, 15, 20, 28, 32, 38, 45, 50, 60, 80, 100, 140 and 180 minutes after start of the infusion which were split into three samples, one of which was centrifuged at 1500 g for 15 minutes to isolate the

serum. All fractions were kept on ice until the end of the experiment and afterwards were frozen at -20 °C until analysis. The blood samples were drawn from the most proximal lumen of the catheter while the DPPG$_2$-TSL-DOX infusion was administered *via* the most distal lumen to prevent contamination of the samples by the infusion.

After euthanization of the animal, the lungs, heart, liver, spleen, kidneys, pancreas were excised and collected in pre-weighted boxes. Bone marrow samples were obtained from the humerus. Samples of untreated muscle where obtained from the muscle tissue surrounding the humerus. Rough localization of the treated muscle volumes and the ablated area in the biceps femori was achieved using a tube with seventeen equidistant markers visible on T1-weighted MRI images which was affixed to the left leg before positioning of the animals (Figure 2B). Before excision of the sonicated volumes, their location was determined using the markers on the pig's skin and needles were pierced into the biceps femori perpendicular to the skin through the marked location (Figure 2C). The volume around the target area was excised along the full thickness of the biceps femori which was then cut into slices of 5 mm thickness along the former HIFU beam axis to find the target area marked with a visible ablation. The slicing was done using a band saw (EXAKT 300 CL, EXAKT Advanced Technologies GmbH, Norderstedt, Germany) and a 3D printed cutting guide with notches marking slice thickness in 5 mm steps (Figure 2D). Upon finding the ablated area marking the treated volume, the more medial slice was frozen in 2-Methylbutane (Product Code 427730025, Thermo Fisher Scientific, Waltham, Massachusetts, USA) cooled by liquid nitrogen and preserved at -80 °C until processing. The tissue around the ablated area in the more lateral slice was excised in a radius of 5 mm to be used in determination of the drug level. All obtained organs and tissue samples were kept frozen at -20 °C until analysis.

## Determination of Doxorubicin concentration

For the determination of the DOX concentration the pre-weighted organs were blended. Samples of 500 µg were taken out of the blended organs and further homogenized at 30 Hz for 30 min using a TissueLyzer II® (Qiagen, Hilden, Germany) after spiking with a daunorubicin (DAUN) solution (product number D8809, Sigma-Aldrich, 5 mg/l, 1.5 ml in water) as an internal standard. Each homogenized mixture was then treated with a silver nitrate solution (Merck, Product number 1.01512.0250, 33 % w/v, 0.7 ml) for 10 min. The formed precipitate was centrifugated off (3000 rpm, 4 °C, 30 min) and the solution was passed through a preconditioned Strata-X SPE column (Phenomenex, Aschaffenburg, Germany). The column was then washed first with 1.2 ml of water and subsequently with 1.2 ml of 10 % methanol in water and the 1.2 ml of 30 % methanol in water. After drying the columns shortly under air flow, the desired compounds were eluted out of the column with 2 times 600 µl of formic acid solution (2 % in methanol). The eluate was collected separately and evaporated to dryness under nitrogen flow. The resulting residue was

5

then redissolved in 300 µl of a 0.1 % TFA solution in water and analyzed *via* HPLC. The blood, muscle, and bone marrow samples were treated according to the same procedure, except that the tissue was homogenized directly without pre-blending.

HPLC Chromatograms were measured using an Agilent 1200 System consisting of a degasser (G1322A), a binary pump (G1312A), a WPS autosampler (G1367B), and a FLD fluorescence detector (G1321A). A Kinetex® C8 100 Å LC column (00B-4497-AN) was used for separation of the compounds. The running solvents were 0.1 % TFA in Water, and 0.1 % TFA in acetronitrile. The used gradient was optimized to achieve an optimal separation of the compounds. The excitation and emission wavelengths for the fluorescence detector were 485 nm and 590 nm respectively.

Quantification was performed by comparison of the fluorescence peak intensities of DOX and DAUN to a previously performed calibration curve with spiked blood and tissue samples.

## Determination of DPPG$_2$ concentration

The DPPG$_2$ concentration in serum samples was determined by Nano-Electrospray Ionization Tandem Mass Spectrometry (Nano-ESI-MS/MS) with direct infusion of the lipid extract (*Shotgun Lipidomics*). Samples were thawed on ice, and an aliquot of 50 µl was used for analysis. 5 µl of 12.43 µM 1-heptadecanoyl-2-(5Z,8Z,11Z,14Z-eicosatetraenoyl)-sn-glycero-3-phospho-(1′-rac-glycerol) (PG 37:4) (Avanti Polar Lipids, Product number LM1202, Alabama, USA) were added to each sample as internal standard. Lipids were extracted using a modified one step MTBE extraction [56]. Extracts were dried under a stream of nitrogen, redissolved in 300 µl of methanol and stored at -20 °C.

For MS analysis, 20 µl of the lipid extract in methanol were loaded into 96-well plates and diluted with 40 µl of 10 mM ammonium acetate in methanol. Lipid infusion and ionization was conducted using Nano-ESI chips with the TriVersa NanoMate operated by the ChipSoft Software (Advion, Ithaca, NY, USA) under the following settings: sample infusion volume: 14 µL, volume of air to aspirate after sample: 1 µL, air gap before chip: enabled, aspiration delay: 0 sec, pre-piercing: with mandrel, spray sensing: enabled, cooling temperature: 14 °C, gas pressure: 0.5 psi, ionization voltage: 1.4 kV, vent headspace: enabled. Pre-wetting was done once. Mass spectrometric analysis was performed using a QTRAP 6500 mass spectrometer (SCIEX, Framingham, MA, USA) operated by Analyst 1.6.3. The following instrument-dependent settings were used: curtain gas: 40 psi, CAD gas: medium, interface heater temperature: 100 °C. DPPG$_2$ was monitored in the positive ion mode using its specific Multiple Reaction Monitoring (MRM) transitions m/z 814.6 to 551.4 (quantifier) and 814.6 to 313.2 (qualifier). For the detection of the internal standard PG 37:4 the MRM transitions m/z 802.5 to 613.5 was used. For all MRM transitions the values for declustering potential, entrance potential, collision energy, and cell exit potential were 28 V, 10 V, 35 V, and 8 V, respectively. The quantifier MRM transition of

DPPG$_2$ and the one of PG 37:4 were integrated using the MultiQuant 3.0.2 software (AB SCIEX). DPPG$_2$ was quantified on the basis of an external calibration curve which was calculated from MS/MS measurements of serum samples obtained after spiking pure blood samples with 6 different concentrations of the same liposomal formulation used for the animal experiments.

**Magnetic Resonance Imaging**

All images were acquired using the HIFU table's window coil and the HIFU pelvis coil (Model 905051-F, Philips Healthcare, Best, The Netherlands) on a 3T MRI scanner (3T Achieva®, Philips Healthcare, Best, The Netherlands).

**Pre-treatment imaging**

The treatment planning was performed using a 3D T1-weighted fast field echo (FFE) without fat suppression. The used parameters were TE = 2.3 ms, TR = 6.1 ms, FA = 20°, acquisition matrix = 88 x 166, number of slices = 167, reconstructed (acquired) voxel dimensions = 0.49 x 0.49 x 1.50 mm (1.52 x 1.53 x 3.00 mm), FOV = 140 x 261 x 250 mm, fold-over direction = RL. Constant Level Appearance (CLEAR) was used to achieve higher signal homogeneity and Sensitivity Encoding (SENSE, P reduction = 1.2, S reduction = 1) was used to accelerate imaging. This resulted in an acquisition duration of 331.3 s.

**MR thermometry**

The imaging sequence used to monitor the treatment progress was an RF-spoiled gradient echo sequence with TR = 30 ms, TE = 19.5 ms, FA = 19.5°, FOV = 288 x 288 mm, 6 slices, and voxel dimensions=1.8 x 1.8 x 7 mm, resulting in an acquisition time of 3.7 s for a full set of slices and a resolution of 160 x 160 voxels per slice. The temperature maps were acquired *via* the proton resonance frequency shift (PRFS) [42]. In particular, the calculation included masking of low SNR voxels, masking of the expected heating area and of areas exhibiting strong thermometry artifacts, baseline subtraction, and a second order baseline drift correction. The MRI slices were positioned in four stacks, namely the focus, sagittal, near field, and far field stacks. The focus stack contained three slices, all other stacks contained one slice. The focus stack was oriented perpendicular to the transducer axis, centered on the HIFU focus point and contained three slices to provide a complete view of the volumetric temperature distribution in the target ROI, with the center slice of the focus stack functioning as feedback for the MPC algorithm. The sagittal stack was oriented in sagittal orientation and was centered on the focus spot. It provides information on the vertical alignment of the focus. The near-field stack was positioned at the pig's skin to monitor excess heat generation in the hydrogel spacer, indicative of excessive absorption. The far-field stack was positioned deep to the focal area.

5

## Postinterventional imaging

The sonications were evaluated using the same 3D T1-weighted FFE sequences described above for treatment planning, both before and one minute after intravenous contrast agent injection (0.1 mmol/kg gadoteric acid, Dotagraf®, Jenapharm GmbH & Co. KG, Jena, Germany). The parameters and field of view of the post-treatment scans were kept the same as the planning scans. For evaluation, the images acquired after contrast agent injection were subtracted from their pre-injection counterpart to reveal non-perfused volumes (NPVs).

## Fluorescence Microscopy

The samples preserved for fluorescence microscopy were cut in 10 µm thick slices using a cryotome (CM 1950, Leica Biosystems Nussloch GmbH, Nussloch, Germany) and transferred to microscope slides (Paul Marienfeld GmbH & Co. KG, Lauda-Königshofen, Germany). The slices were left untreated apart from applying fluorescence-compatible mountant and were covered with a coverslip which was secured using a clear nail enamel. The finished slides were kept dark at -20 °C until examination. Examination of the slides was done using a fluorescence microscope (DM6000B microscope equipped with a DFC310FX camera, Leica Microsystems GmbH, Wetzlar, Germany) and a custom DOX fluorescence filter set (excitation, 480/40 nm; emission, 600/60 nm; dichroic, 505 lp). A muscle sample from an animal which underwent the same treatment described above with liposomes not containing DOX was used as control.

## Models and statistics

*Pharmacokinetics*

The concentrations of total DOX and $DPPG_2$ in the blood after the end of the infusion $c_{decay}$ and during the infusion $c_{Inf}$ were modeled using a two-compartment model $c_{decay}$ follows Equation 1 with the macro-parameters $A$ and $B$ and the corresponding decay times $\tau_\alpha$ and $\tau_\beta$ [57]. The half-life $t_{1/2}$ of each component of the biexponential function is calculated according to Equation 2.

$$c_{decay}(t) = A \cdot e^{-(t-t_{Inf})/\tau_\alpha} + B \cdot e^{-(t-t_{Inf})/\tau_\beta} \qquad [1]$$

$$t_{1/2} = ln2 \cdot \tau \qquad [2]$$

$c_{Inf}(t)$ is described by Equation 3 with the steady-state serum concentration $C_{ss}$ and the balancing factors $X_1$ and $X_2$ [58]:

$$c_{Inf}(t) = C_{ss} \cdot \left(1 - X_1 e^{-t/\tau_\alpha} - X_2 e^{-t/\tau_\beta}\right) \tag{3}$$

The fitting was performed with the minimize function of the lmfit python 3.8 package (version 1.0.0) applying a cauchy optimization model (reduce_fcn argument: 'neglogcauchy'), which minimizes the effect of outliers [59]. All parameters were constrained to be greater or equal to zero $C_{ss}$ was constrained such that $c_{Inf}(t=30\,min) = c_{decay}$ ($t = 30$ min) and $X_1 + X_2$ were constrained such that $X_1 + X_2 = 1$. The equation to calculate the sum of the error to be minimized using this model ($f_{cau}$) can be found in equation (4):

$$f_{cau}(t) = \sum_{t=1}^{n} -\ln\left(\frac{1}{\pi \cdot (1 + (c(t) - c_{real}(t))^2)}\right) \tag{4}$$

Here $c$ is either $c_{inf}$ or $e_{decay}$ and $c_{real}$ is the actual measured concentration at the experimental timepoint $t$.

*Calculation of leaked DOX concentration*
Currently, there is no method for measuring the fraction of total DOX that has already left the liposomes and is therefore free to extravasate. It must consequently be estimated. The total concentration of DOX in the blood stream $c_{D,tot}$ comprises both DOX encapsulated in liposomes and free DOX, with the respective concentrations $c_{D,lip}$ and $c_{D,free}$:

$$c_{D,tot}(t) = c_{D,lip}(t) + c_{D,free}(t) \tag{5}$$

The concentration $c_{D,lip}$ is connected to the concentration of liposomes in the blood *via* the fraction of total DOX present in the liposomes $F(t)$. We assume that $F(t)$ decays over the leakage time $\tau_{leak}$ [26] after the end of the infusion at timepoint $t_{inf}$:

$$c_{D,lip} = F(t) \cdot c_{lip}(t) \tag{6}$$

$$F(t) = F\left(t_{inf}\right) \cdot e^{\frac{-(t-t_{inf})}{\tau_{leak}}} \tag{7}$$

$C_{D,lip}$ is influenced by the infusion of liposomes, the elimination of DOX-carrying liposomes and the leakage of DOX from the liposomes. As a simplification, the infusion, clearance and leakage of liposomal DOX during infusion are assumed to result in an effective constant infusion rate $m$ until the end of the infusion is reached at $t_{inf}$. This leads to the following differential equation (equation 7) and solution (equation 8):

$$\begin{aligned}
c'_{D,lip}(t) &= F(t) \cdot \frac{d}{dt} c_{lip}(t) + c_{lip}(t) \cdot \frac{d}{dt} F(t) \\
c'_{D,lip}(t) &= m \cdot \vartheta(t_{inf} - t) - \frac{c_{D,lip}(t)}{\tau_{leak}}
\end{aligned} \tag{8}$$

5

$$c_{D,lip}(t) = \begin{cases} m \cdot \tau_{leak} \cdot \left(1 - e^{-t/\tau_{leak}}\right) & \text{for } t < t_{inf} \\ m \cdot \tau_{leak} \left(1 - e^{-t_{inf}/\tau_{leak}}\right) \cdot e^{-(t-t_{inf})/\tau_{leak}} & \text{for } t > t_{inf} \end{cases} \quad [9]$$

where $\vartheta(t)$ denotes the Heaviside step function. $c_{D,free}$ is influenced by the leakage of DOX from the liposomes and the elimination with elimination time $\tau_{free}$, leading to the following differential equation (equation 10) and solution (equation 11):

$$c'_{D,free}(t) = \frac{c_{D,lip}(t)}{\tau_{leak}} - \frac{c_{D,free}(t)}{\tau_{D,free}} \quad [10]$$

$$c_{D,free}(t) = \begin{cases} \frac{m \cdot \tau_{free}}{\tau_{leak} - \tau_{free}} \cdot \left( \tau_{leak}\left(1 - e^{\frac{-t}{\tau_{leak}}}\right) - \tau_{free}\left(1 - e^{\frac{-t}{\tau_{free}}}\right) \right) & \text{for } t < t_{inf} \\ \frac{m \cdot \tau_{free}}{\tau_{leak} - \tau_{free}} \left( \tau_{leak}\left(1 - e^{\frac{-30}{\tau_{leak}}}\right) e^{\frac{-(t-30)}{\tau_{leak}}} - \tau_{free}\left(1 - e^{\frac{-30}{\tau_{free}}}\right) e^{\frac{-(t-30)}{\tau_{free}}} \right) & \text{for } t > t_{inf} \end{cases} \quad [11]$$

The sum of $c_{D,lip}$ and $c_{D,free}$ was fitted to the total concentration of DOX *via* the variation of $m$, $\tau_{leak}$ and $\tau_{free}$ using the minimize function of the lmfit python 3.8 package (version 1.0.0) [59]. All parameters were constrained to be greater or equal to zero.

*AUC of bioavailable ("free") DOX*
The amount of drug delivered to a target volume depends on multiple factors, including the plasma concentration of free DOX $c_{D,free}$, the plasma concentration of liposomal doxorubicin $c_{D,lip}$, the retention factor $r$, describing the diffusion of the drug into and out of the tissue, the release fraction $f$, which describes the fraction of drug released from the liposome while it passes through the target zone, and the ratio between the plasma flow $w_{target}$ and the volume of plasma $v_{target}$ in the target volume [60]. It can be approximated using an integral over the timespan between the start of the infusion at $t_{start}$ and the timepoint of euthanasia $t_{stop}$.

$$[Dox]_{target} = \frac{w_{target}}{v_{target}} \int_{t_{start}}^{t_{stop}} \left( c_{free} + c_{D,lip}(t) \cdot f(t) \right) \cdot r(t)\, dt \quad [12]$$

As these parameters are generally unknown, equation (11) was simplified under the following assumptions: 1; The retention factor $r$ is constant. 2; The release fraction is a step-function which assumes the value 1 as long as the average temperature in the target area exceeds 40 °C and is 0 otherwise:

$$f(t) = \theta(t), \qquad \theta(t) = \begin{cases} 1 & \text{if } T(t) > 40 \text{ °C} \\ 0 & \text{otherwise} \end{cases} \quad [13]$$

This leads to the following proportionality between the concentration of DOX in the target area and the area under the time-curve of the concentration of free DOX in the target area, $AUC_{freeDox}$:

$$[DOX]_{target} \propto AUC_{freeDox} = \int_{t_{start}}^{t_{stop}} c_{D,free} + c_{D,lip}(t) \cdot \theta(t) \, dt \qquad [14]$$

This proportionality was tested using linear regression *via* the linear_model. LinearRegression function of the sklearn python 2.7 package (version 0.20.1) [61]. $c_{D,free}$ and $c_{D,lip}$ were modeled according to equations 8 and 10 and the parameters were assumed to be equal among all animals.

## Statistics of Biodistribution

The difference in concentration of DOX between the untreated muscle and the treated muscle areas was tested for statistical significance using the stats.ttest_rel module of the scipy python 2.7 package (version 1.1.0) [62] to perform a paired t-test.

## RESULTS

### Vital parameters and body temperature

One animal showed a transient increase in arterial blood pressure by 10 mmHg following the initiation of the liposome infusion. Other signs of anaphylactic reactions were not observed and were well managed with given premedication. Body temperatures were maintained with heating blankets around 37.5 °C (range: 37.0–38.2 °C) as measured with a temperature probe (Expression MR400, Invivo Corp., Orlando, FL, USA) in the esophagus, see Table 1.

5

Table 1: Esophageal temperatures measured at the beginning and the end of each hyperthermia treatment.

| Pig number | $t_{start}$ = 10 min | | $t_{start}$ = 60 min | |
| | $t_{start}$ (10 min) | $t_{start}$ (40 min) | $t_{start}$ (60 min) | $t_{start}$ (90 min) |
|---|---|---|---|---|
| 1 | 37.8 | 37.7 | 38.0 | 38.0 |
| 2 | 36.8 | 37.0 | 37.2 | 37.4 |
| 3 | 37.0 | 37.1 | 37.1 | 37.4 |
| 4 | 38.2 | 38.2 | 38.0 | 38.1 |
| mean | 37.5 | 37.5 | 37.6 | 37.7 |

## Pharmacokinetics

The pharmacokinetic parameters of the two-compartment model for DOX and DPPG$_2$ are shown in Table 2 and the resulting fits are shown in Figure 3A. The curves were fitted using the negative logarithmic cauchy likelihood, as described in equation (4), to reduce the effect of outliers. The peak plasma concentrations of DOX and DPPG$_2$ were 57.5 %ID and 61.8 %ID, respectively. After the small initial decay of the alpha phase, the liposomes exhibited a beta phase with very long $\tau_\beta$, maintaining a high plasma concentration of the TSL carrier. The DPPG$_2$ concentration at the end of the experiment was approx. 40 %ID, which is only 65% of the maximum concentration reached. The projected experimental half life $t_{1/2,exp}$ according to the used fitting model is 637 min (10.6 h).

DOX exhibited shorter decay times and a more substantial decay during the initial alpha phase, leading to a halving of the blood concentration from the maximum value concentration after an experimental half-life $t_{1/2,exp}$ of 16.4 min only. The modelling of the DOX pharmacokinetic using equations (9) and (11) yielded an effective infusion rate $m$ of 2.61 %ID/min, a leakage time $\tau_{leak}$ of 24.91 min and an elimination time $\tau_{free}$ of 4.89 min (Figure 3B).

**Table 2:** Pharmacokinetic parameters of DPPG$_2$-TSL-DOX obtained using a two-compartment model.

| Substance | A | $\tau_\alpha$ [min] | $t_{1/2,\alpha}$ [min] | B | $t_\beta$ [min] | $t_{1/2,\beta}$ [min] | $t_{1/2,exp}$ [min] | AUC [%ID·min] |
|---|---|---|---|---|---|---|---|---|
| DOX | 52.0 | 20.7 | 14.36 | 5.6 | 221.4 | 153.5 | 16.4 | 2568.0 |
| DPPG$_2$ | 20.0 | 49.3 | 34.2 | 41.8 | 2107.9 | 1461.1 | 637.0 | 7929.6 |

*Abbreviations: A,B*: Macro parameters; $\tau_\alpha$, $\tau_\beta$: decay times of the alpha and beta phases; $t_{1/2,\alpha}$, $t_{1/2,\beta}$: Half-lifes of the alpha and beta-phases; $t_{1/2,exp}$: Experimental half-life; Balancing parameters were $X_1 = 0$ and $X_2 = 1$

## Biodistribution

The results of the biodistribution analysis are shown in Figure 4. In the muscle samples treated during the first and the second hyperthermia periods, DOX concentrations were higher than in the untreated muscle samples by factors of 15 (p = 0.0048) and 7 (p = 0.049), respectively. No significant difference was observed between the untreated muscle samples and the ablated control samples that had not undergone hyperthermia.

The organs with the highest concentration of the API at the end of the experiments were the kidneys (0.051 ± 0.033 %ID/g) and the spleen (0.0253 ± 0.0069 %ID/g). The concentrations in all other relevant measured organs (heart pancreas, liver, lung) were between 0.01 and 0.025 %ID/g. The lowest concentrations were found in the bone marrow (0.0066 ± 0.0043 %ID/g) and the untreated and ablated muscle samples (both at ca. 0.025 %ID/g).

## Two-compartment model



## Leakage model
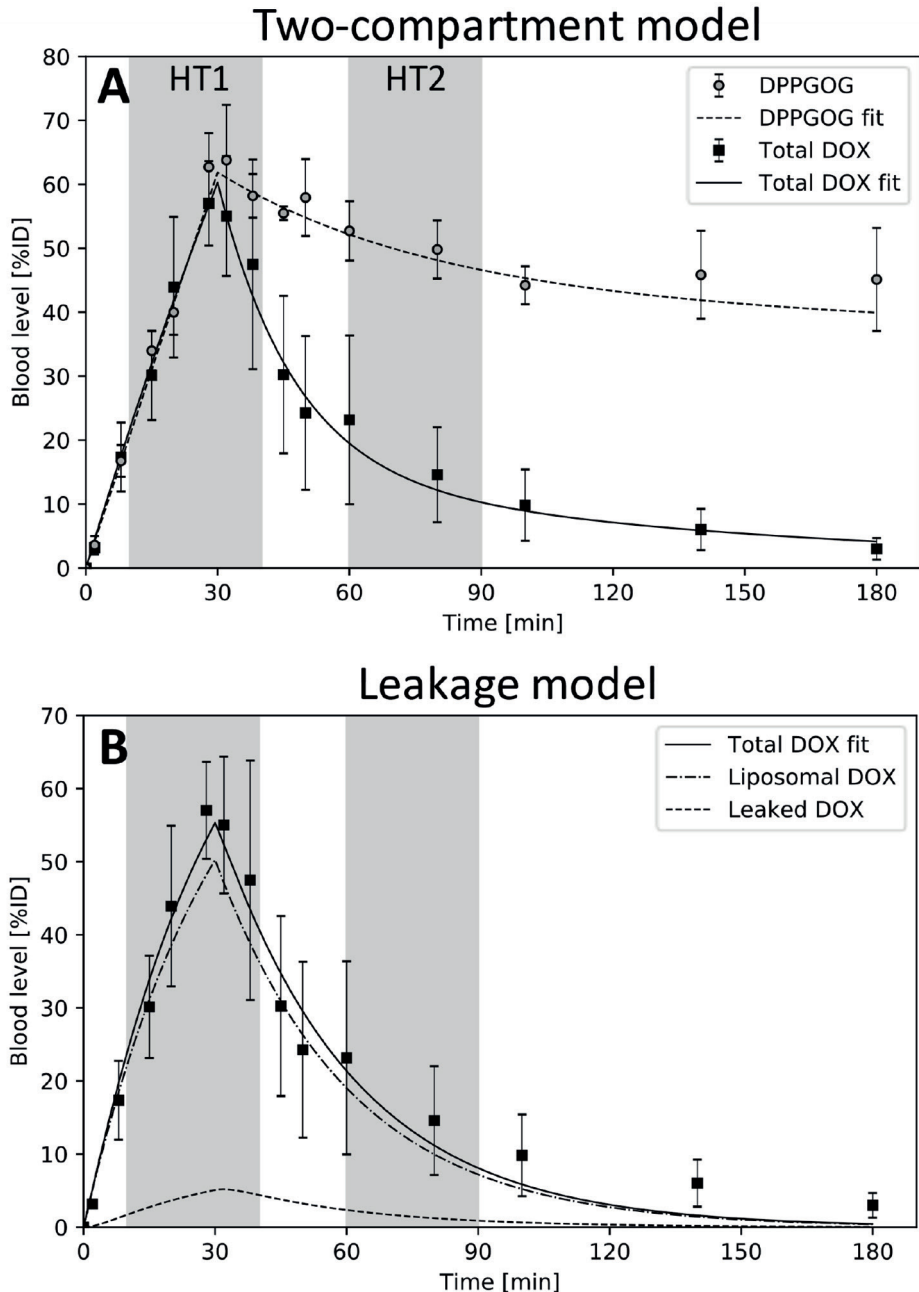


**Figure 3:** Pharmacokinetics of $DPPG_2$ and DOX (DOX dose: 50 mg/m$^2$; DOX n = 5, $DPPG_2$ n = 3). The grey areas mark the times during which hyperthermia was applied. (**A**) $DPPG_2$ and DOX blood concentrations with fits according to a two-compartment model using a cauchy optimization. (**B**) DOX blood concentration fitted with a model incorporating only the infusion and the leakage of DOX from the liposomes and subsequent elimination pf the API from the blood stream.

5
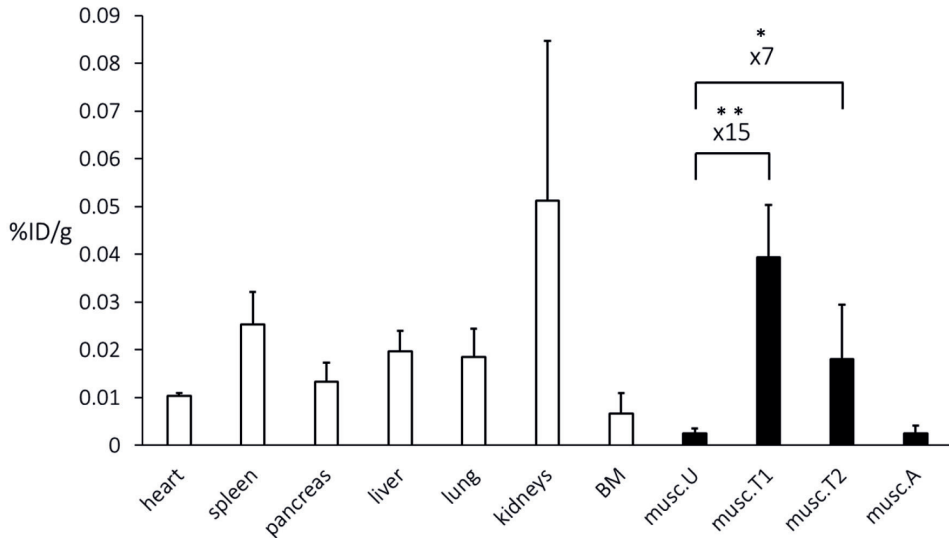
**Figure 4:** Biodistribution of DOX 3 h after start of infusion of DPPG$_2$-TSL-DOX in pigs. Dose: 50 mg/m². n = 4 for muscle samples (black), n = 5 organ samples (white). BM: Bone Marrow. Musc.U: Muscle untreated; **Musc.T1**: muscle volume sonicated during hyperthermia treatment starting 10 min after DPPG$_2$-TSL-DOX infusion start; **Musc.T2**: muscle volume sonicated during hyperthermia treatment starting 60 min after DPPG2-TSL-DOX infusion start; **Musc.A**: ablated muscle samples that had not undergone hyperthermia.

**Table 3:** Hyperthermia treatment metrics. Hyperthermia duration denotes the amount of time over which hyperthermic temperatures of at least 40 °C were sustained in the target ROI.

| Pig Nr. | Weight [kg] | Hyperthermia parameters | | | |
| --- | --- | --- | --- | --- | --- |
| | | Hyperthermia duration [min] | $T_{mean}$ [°C] | $T_{10}$ [°C] | $T_{10}$ [°C] |
| $t_{Start}$ = 10 min | | | | | |
| 1 | 39.5 | 24.1 | 42.07 | 41.33 | 42.72 |
| 2 | 37.5 | 19.6 | 41.72 | 40.91 | 42.44 |
| 3 | 46 | 33.1 | 42.08 | 41.36 | 42.80 |
| 4 | 53.5 | 30.3 | 42.01 | 41.36 | 42.59 |
| $t_{Start}$ = 60 min | | | | | |
| 1 | 39.5 | 30.4 | 41.73 | 41.25 | 42.16 |
| 2 | 37.5 | 29.3 | 41.36 | 40.58 | 42.11 |
| 3 | 46 | 26.7 | 41.25 | 40.41 | 41.04 |
| 4 | 53.5 | 25.3 | 41.83 | 41.06 | 42.52 |

*Abbreviations:* $T_{mean}$, $T_{10}$, $T_{90}$: arithmetic mean, 10th percentile and 90th percentile of voxel temperatures inside the target ROI during sonication.

### Influence of Hyperthermia treatment parameters on drug accumulation

A summary of the hyperthermia treatment parameters is shown in Table 3. The average hyperthermia duration was 27.3 minutes. Across all experiments, the arithmetic mean, the 90th percentile and 10th percentile of voxel temperatures in the target ROI while the HIFU was active were 41.76 °C, 41.03 °C and 42.42 °C, respectively.

An example of the AUC of available DOX for a treatment starting at 10 minutes is shown in Figure 5A. The linear regression analysis of the influence of the AUC on the accumulated sample dose yielded a coefficient of correlation $R^2$ of 0.74, a proportionality factor of $3.46 \cdot 10^{-5}$ and an intercept of $-7.32 \cdot 10^{-3}$ %ID/g (Figure 5B).
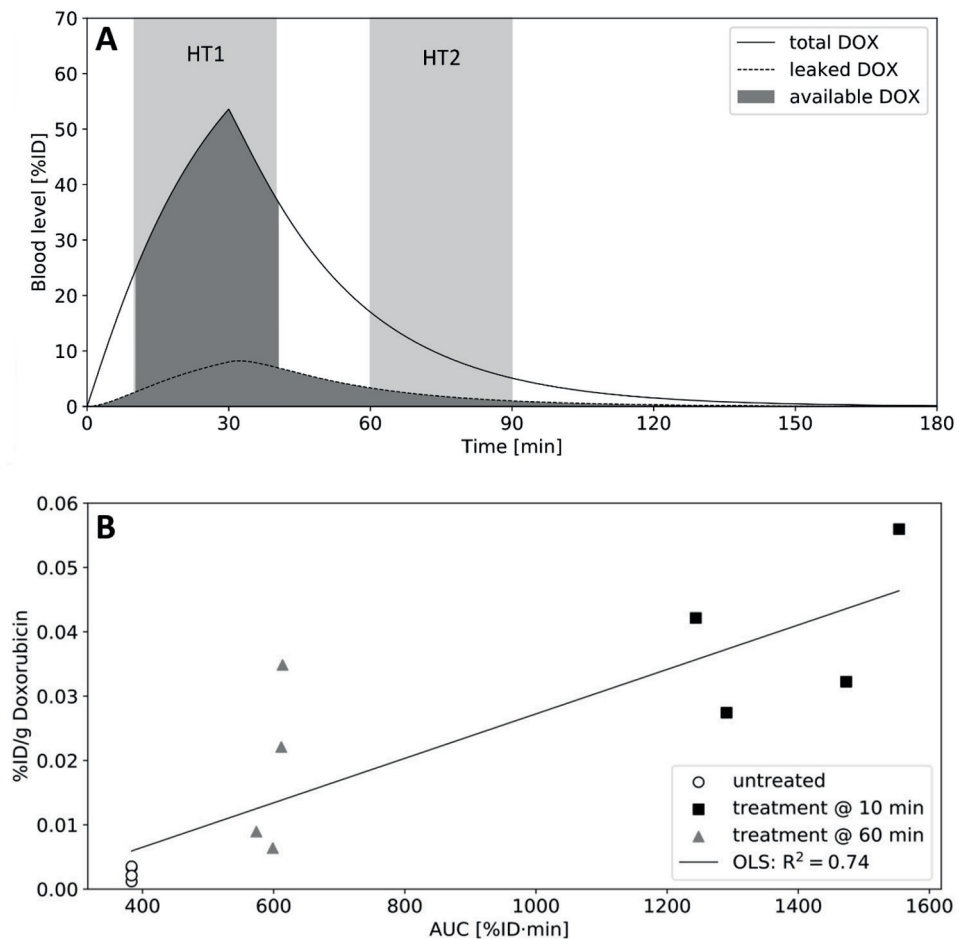


**Figure 5:** (**A**) Visualization of one example AUC of available (free) DOX used for the %ID versus AUC analysis of a treatment starting 10 minutes after the start of infusion. (**B**) DOX concentration in muscle samples versus their respective AUC of available DOX.

## Fluorescence microscopy

In the cells which underwent ablation (Figure 6A), fluorescence was enhanced in the cytoplasm compared to other nearby cells (Figure 6B). Fluorescence of the cell nuclei was observed throughout all samples (Figure 6C). No fluorescence was observed in the control sample.
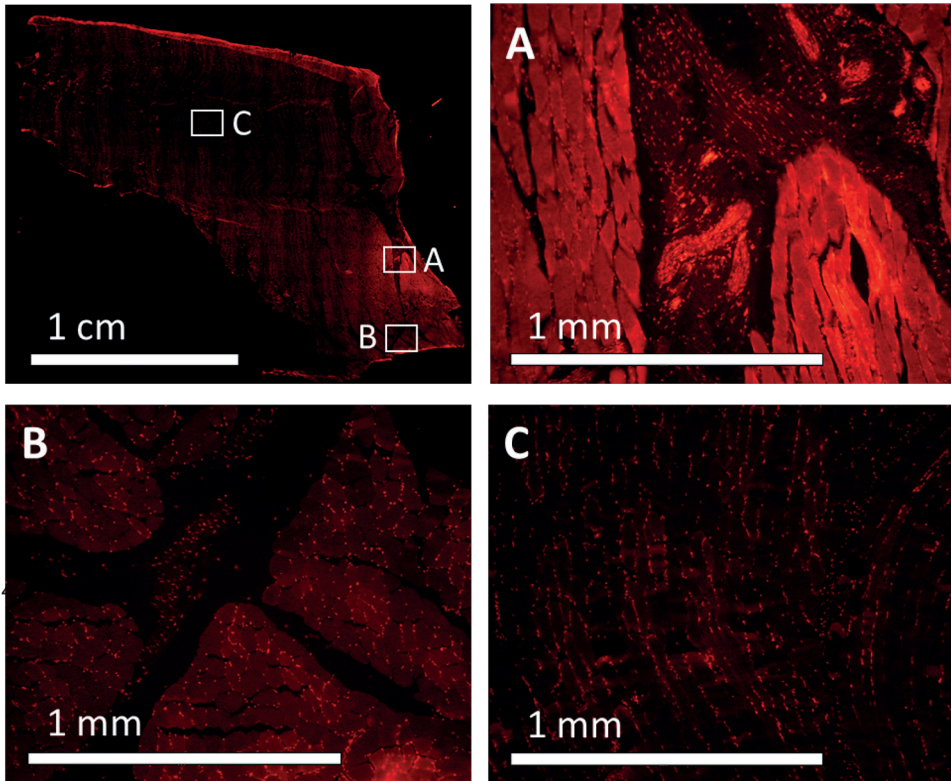


**Figure 6:** Representative fluorescence microscopy image. Cells in the treatment focus exhibit pronounced fluorescence of both the nucleus and the plasma (**A**). Fluorescence of the nuclei is present throughout all samples (**B**, **C**).

## DISCUSSION

Here, we present a large animal drug delivery study performed in a healthy swine model demonstrating hyperthermia-triggered DOX release from DPPG$_2$-TSLs using MR-HIFU as a hyperthermia device. Hyperthermia over a time span of thirty minutes with tight spatial and temporal temperature control was achieved using MR-HIFU together with a model predictive control (MPC) algorithm [55]. The MPC algorithm employs a tissue

model comprising local diffusion and perfusion values and utilizes near-real time MR-thermometry data to spatially direct MR-HIFU heating at locations with the highest thermal washout, see chapter 3 of this thesis. In contrast to small animal studies, the DPPG$_2$-TSL-DOX was administered in our study as an infusion over a time period of thirty minutes, mimicking a clinically useable protocol. One treatment session comprised two hyperthermia time spans of thirty minutes each with a target temperature of 42.0 °C that started 10 min and 50 min after begin of infusion. The hyperthermia targets were placed in the porcine thigh muscle. Pharmacokinetic data of DPPG$_2$ and DOX in blood as well as biodistribution data of DOX in all organs and the heated volume were measured for the first time in a pig model.

The synthetic lipid DPPG$_2$ has been extensively studied as a constituent for TSLs *in-vitro* and *in-vivo* [33-36,63,64]. Measurements carboxyfluorescein-loaded DPPG$_2$-TSLs demonstrated a long circulation time of this carrier system, which was superior to other TSL formulations relying on lyso-lipids [33]. The half-life of carboxy fluorescein loaded into DPPG$_2$-TSLs as a model drug was $t_{1/2}$ = 9.6 h in hamsters and $t_{1/2}$ = 5.0 h in rats [33]. A study performed with DPPG$_2$-TSL-DOX in domestic cats suffering from a spontaneous feline sarcoma, found a DOX half-life of approx. 40 minutes after infusion for a dose of 0.4 mg/kg DOX [34]. Plasma concentrations of DOX comprise TSL-encapsulated-DOX together with free DOX that leaked from its carrier but is still present in circulation. Importantly, the blood concentration and circulation time of the DPPG$_2$-TSL carrier itself was so far not assessed. We measured the blood concentration of DPPG$_2$ directly using mass spectrometry as well as that of DOX, which allowed to determine the circulation time of the TSLs. Using a simplified pharmacokinetic model, we calculated the leakage rate of DOX from the carrier and the plasma concentration of free DOX as well as DOX still encapsulated within the DPPG$_2$-TSL carrier.

## Pharmacokinetics

The blood concentration of the liposomal carrier DPPG$_2$-TSL showed a slow double exponential clearance leveling off at approx. 60% ID after 3 hours. As soon as DPPG$_2$-TSL-DOX is infused, leakage of DOX from the carrier occurs with a leakage time of $\tau_{leak}$ = 24.91 min, while free DOX is cleared from blood with an elimination time $\tau_{leak}$ = 4.89 min, from simultaneous fitting of a set of differential equations described above.

Our model simplifies the clearance of free DOX by assuming a simple mono-exponential elimination, though pharmacokinetic studies of free DOX in pigs demonstrated a triphasic elimination [65]. However, as the elimination is strongly dominated by the first rapid alpha phase, we chose to approximate DOX clearance with a simple mono-exponential model. The elimination time of free DOX obtained from modelling is similar to the experimental half-life found by Andreson *et al.* A second simplification

of our model is the assumption that the concentration of DPPG$_2$-TSL remains constant after end of infusion, while the experimental data show a noticeable double exponential clearance of DPPG$_2$-TSL of approx. 37% by the timepoint of euthanasia referred to peak concentration. Consequently, our model underestimates the value of total DOX especially at later times after end of infusion and most likely overestimates the leakage accordingly.

While our measurements demonstrate a long circulation of DPPG$_2$-TSL in pigs, the DOX blood concentrations is considerably lower compared to data obtained cats due to a significant leakage of DOX at body temperature. These results point to a possible destabilization of the DPPG$_2$-TSLs in pigs by blood components leading to a stronger leakage of DOX without leading to a rapid clearance of the carrier. The exact nature of this interaction and identification of the responsible blood constituents was not further pursued in this study. Another explanation may be the higher body temperature of pigs with a normal range between 38–39 °C [66]. Though esophageal temperature probes showed an average body temperature of 37.5 °C, it can't be ruled out that core organs were still at higher temperatures leading to an increased leakage. Whatever the exact cause may be, current PK data indicate that circulation times of DPPG$_2$-TSL and the leakage of DOX from the carrier are strongly species dependent, which also applies to other TSL formulations. For example, a TSL formulations comprising lyso-lipids showed a higher leakage in small animals compared to DPPG$_2$-TSLs but seem to be more stable in swine with a DOX plasma half-life of $t = 4.8h$ [33,67]. Unfortunately, information on animal body temperatures are not given. Interestingly, a clinical hyperthermia study with Thermodox® reported a dose independent average9plasma half-life of only $t_{1/2,exp} = 35.15$ min (N = 18) [32].

**Hyperthermia**

The on average, the hyperthermia sonications resulted in a mean temperature of 41.76 °C, which is 0.24 K below the target temperature of 42 °C. A possible cause for these tracking errors is the stimulation of perfusion over time, which has been observed in a previous study, see chapter 3 of this thesis. However, temperature variations between 40 to 42 °C are not expected to significantly affect release rate of TSLs as the temperature range where paid release occurs is fairly broad [63]. The implementation of an offset-free MPC may become important when treating malignant tissue in close proximity to large vessels, where even lower temperatures could be expected due to thermal washout. Thanks to the spatially resolved allocation of heating power to blood vessels provided by the MPC, the lowest average that was observed in this study was 40.41 °C, which is above the presumed release temperature of these liposomes. Consequently, we believe that drug release occurred with comparable rate across the entire heated tissue and above-mentioned minor tracking errors don't lead to variations in deposited drug concentrations.

## Biodistribution

The DOX concentration in the target muscle volume heated at the earlier time span was on average 15 times higher (p = 0.0048, student t-test) compared to untreated muscle. For the later hyperthermia treatment, an averaged 7-fold increase was found (p = 0.049). Uptake of DOX was also visible on fluorescence imaging showing homogeneous uptake of DOX in cell nuclei across the heated tissue.

The hyperthermia exposed muscle tissues were marked about 110 minutes after the beginning of the DPPG$_2$-TSL-DOX infusion with small ablation spots to serve as a visual marker during tissue extraction. A third additional ablation spot within the muscle that did not undergo hyperthermia served as control to measure if an ablation performed at t = 110 minutes adds extra DOX to the measured tissue concentration. As the DOX concentration measured for this third spot was comparable to untreated muscle (0.0025 ± 0.016 %ID/g vs. 0.00255 ± 0.00097 %ID/g), we conclude that DOX concentrations measured in HT treated muscle were not affected by the small additional ablation spot but solely related to the DOX delivered during HT. The DOX concentration within the first HT treated tissue may have been more affected by washout due to perfusion compared to the second HT treated volume as the time from the HT treatment to euthanasia was longer.

Using our pharmacokinetic model, the AUC of free DOX (AUC$_{freeDox}$) could be calculated for treated and untreated muscle tissue. For treated muscle tissue, the AUC$_{freeDox}$ is composed of free DOX released from the DPPG$_2$-TSL carrier during hyperthermia plus the AUC of the free DOX that originated from leaking of the DPPG$_2$-TSL-DOX at body temperature over the entire time span of the experiment. The AUCfreeDox for untreated tissue only comprises the leaked, free DOX. Importantly, we found a linear correlation of the DOX uptake in the untreated muscle as well as the two HT treated muscles with respective AUC$_{freeDox}$, which is in agreement with the computer model proposed by Gasselhuber *et. al.* [60]. Any clinical application therefore benefits from an optimal timing of DPPG$_2$-TSL-DOX infusion and hyperthermia application, which can be predicted using pharmacokinetic modeling.

Uptake of DOX in the spleen and liver is most likely a result of DPPG$_2$-TSL-DOX clearance by phagocytic cells present in these organs. The latter also contribute to the DOX concentration found in the kidney in addition to a contribution from clearance of free DOX. Similar biodistribution was reported for different DOX-TSLs in small animal studies [28,45,68,69].

Infusion of DPPG$_2$-TSL-DOX was well tolerated in all animal experiments, as adverse or allergic reactions such as an anaphylactic shock due to possible liposome-induced compliment activation was managed using suitable premedication [70].

5

## CONCLUSIONS

We have shown in a large animal study that MR-HIFU is a suitable technology for well controlled, focal hyperthermia, which can be used for temperature-triggered drug delivery in deep seated tissue. In our study, we used as a temperature sensitive drug carrier a formulation based on the synthetic lipid $DPPG_2$, i.e. $DPPG_2$-TSL-DOX. $DPPG_2$-TSL-DOX was infused over 30 minutes, and 30-minute long HT treatments were started at 10 and 60 minutes after the start of the infusion. Uptake of DOX scaled with the $AUC_{freeDOX}$ and reached 15- and 7-times higher concentrations compared to untreated tissue, for the treatments starting at 10 and 60 minutes, respectively. No serious adverse effects were observed during the experiments. The present study is of high importance for clinical translation, as the protocol could directly be applied for treatment of sarcomas, where DOX is used in an adjuvant or neoadjuvant setting. In addition, MR-HIFU offers the additional possibility of combined treatment protocols comprising a hyperthermia drug delivery step followed by focal thermal ablation of the tissue.

## DECLARATION OF INTEREST

Edwin Heijman is employed by Philips. Sin Yuin Yeo is partly employed by Profound Medical.

## ACKNOWLEDGEMENT

# REFERENCES

[1] Datta NR, Ordóñez SG, Gaipl US, et al. Local Hyperthermia Combined with Radiotherapy and-/or Chemotherapy: Recent Advances and Promises for the Future. Cancer Treat. Rev. 2015;41:742–753.

[2] Issels RD. Hyperthermia Adds to Chemotherapy. Eur. J. Cancer. 2008;44:2546–2554.

[3] Horsman MR, Overgaard J. Hyperthermia: A Potent Enhancer of Radiotherapy. Clin. Oncol. 2007;19:418–426.

[4] Dewhirst MW, Vujaskovic Z, Jones E, et al. Re-setting the Biologic Rationale for Thermal Therapy. Int. J. Hyperth. 2005;21:779–790.

[5] Wust P, Hildebrandt B, Sreenivasa G, et al. Hyperthermia in cancer treatment (I). Lancet Oncol. 2002;3:487–497.

[6] Falk MH, Issels RDRD. Hyperthermia in Oncology. Int. J. Hyperth. 2001;17:1–18.

[7] Issels RD, Lindner LH, Verweij J, et al. Effect of Neoadjuvant Chemotherapy Plus Regional Hyperthermia on Long-Term Outcomes Among Patients With Localized High-Risk Soft Tissue Sarcoma. JAMA Oncol. 2018;4:483–492.

[8] Datta NR, Rogers S, Klingbiel D, et al. Hyperthermia and Radiotherapy with or without Chemotherapy in Locally Advanced Cervical Cancer: A Systematic Review with Conventional and Network Meta-Analyses. Int. J. Hyperth. 2016;32:809–821.

[9] Datta NR, Rogers S, Ordóñez SG, et al. Hyperthermia and Radiotherapy in the Management of Head and Neck Cancers: A Systematic Review and Meta-Analysis. Int. J. Hyperth. 2016;32:31–40.

[10] Maluta S, Kolff MW. Role of Hyperthermia in Breast Cancer Locoregional Recurrence: A Review. Breast Care. 2015;10:408–412.

[11] Wessalowski R, Schneider DT, Mils O, et al. Regional Deep Hyperthermia for Salvage Treatment of Children and Adolescents with Refractory or Recurrent Non-Testicular Malignant Germ-Cell Tumours: An Open-Label, Non-Randomised, Single-Institution, Phase 2 Study. Lancet Oncol. 2013;14:843–852.

[12] Issels RD, Lindner LH, Verweij J, et al. Neo-adjuvant Chemotherapy Alone or with Regional Hyperthermia for Localised High-Risk Soft-Tissue Sarcoma: A Randomised Phase 3 Multicentre Study. Lancet Oncol. 2010;11:561–570.

[13] Franckena M, Lutgens LC, Koper PC, et al. Radiotherapy and Hyperthermia for Treatment of Primary Locally Advanced Cervix Cancer: Results in 378 Patients. Int. J. Radiat. Oncol. Biol. Phys. 2009;73:242–250.

[14] Franckena M, Stalpers LJA, Koper PCM, et al. Long-Term Improvement in Treatment Outcome After Radiotherapy and Hyper-thermia in Locoregionally Advanced Cervix Cancer: An Update of the Dutch Deep Hyperthermia Trial. Int. J. Radiat. Oncol. Biol. Phys. 2008;70:1176–1182.

[15] Van der Zee J, Van Rhoon GC. Cervical Cancer: Radiotherapy and Hyperthermia. Int. J. Hyperth. 2006;22:229–234.

[16] Zee J Van Der, González DG, Rhoon GC Van, et al. Comparison of Radiotherapy alone with Radiotherapy plus Hyperthermia in Locally Advanced Pelvic Tumors. Lancet. 2000;355:1119–1125.

[17] Yatvin M, Weinstein J, Dennis W, et al. Design of liposomes for enhanced local release of drugs by hyperthermia. Science (80-. ). 1978;202:1290–1293.

[18] Weinstein J, Magin R, Yatvin M, et al. Liposomes and local hyperthermia: selective delivery of methotrexate to heated tumors. Science (80-. ). 1979;204:188–191.

[19] Landon CD. Nanoscale Drug Delivery and Hyperthermia: The Materials Design and Preclinical and Clinical Testing of Low Temperature-Sensitive Liposomes Used in Combination with Mild Hyperthermia in the Treatment of Local Cancer. 2011;3:24–37.

[20] Al-Ahmady Z, Kostarelos K. Chemical Components for the Design of Temperature-Responsive Vesicles as Cancer Therapeutics. Chem. Rev. 2016;116:3883–3918.

[21] Kneidl B, Peller M, Winter G, et al. Thermo-sensitive liposomal drug delivery systems: state of the art review. Int J Nanomedicine. 2014;9:4387–4398.

5

[22] Hijnen N, Langereis S, Grüll H. Magnetic resonance guided high-intensity focused ultrasound for image-guided temperature-induced drug delivery. Adv. Drug Deliv. Rev. 2014;72:65–81.

[23] Grüll H, Langereis S. Hyperthermia-triggered drug delivery from temperature-sensitive liposomes using MRI-guided high intensity focused ultrasound. J. Control. Release. 2012;161:317–327.

[24] Seynhaeve ALB, Amin M, Haemmerich D, et al. Hyperthermia and smart drug delivery systems for solid tumor therapy. Adv. Drug Deliv. Rev. 2020;

[25] Van Rhoon GC, Franckena M, Ten Hagen TLM. A moderate thermal dose is sufficient for effective free and TSL based thermo-chemotherapy. Adv. Drug Deliv. Rev. 2020;

[26] Lokerse WJM, Kneepkens ECM, ten Hagen TLM, et al. In depth study on thermosensitive liposomes: Optimizing formulations for tumor specific therapy and in vitro to in vivo relations. Biomaterials. 2016;82:138–150.

[27] Gasselhuber A, Dreher MR, Partanen A, et al. Targeted drug delivery by high intensity focused ultrasound mediated hyperthermia combined with temperature-sensitive liposomes: Computational modelling and preliminary in vivo validation. Int. J. Hyperth. 2012;28:337–348.

[28] Hijnen N, Kneepkens E, De Smet M, et al. Thermal Combination Therapies for Local Drug Delivery by Magnetic Resonance-Guided High--Intensity Focused Ultrasound. Proc. Natl. Acad. Sci. 2017;114:E4802–E4811.

[29] Lencioni R, Cioni D. RFA plus lyso-thermosensitive liposomal doxorubicin: In search of the optimal approach to cure intermediate-size hepatocellular carcinoma. Hepatic Oncol. 2016;3:193–200.

[30] Tak WY, Lin SM, Wang Y, et al. Phase III HEAT study adding lyso-thermosensitive liposomal doxorubicin to radiofrequency ablation in patients with unresectable hepatocellular carcinoma lesions. Clin. Cancer Res. 2018;24:73–83.

[31] Lyon PC, Gray MD, Mannaris C, et al. Safety and feasibility of ultrasound-triggered targeted drug delivery of doxorubicin from thermosensitive liposomes in liver tumours (TARDOX): a single-centre, open-label, phase 1 trial. Lancet Oncol. 2018;19:1027–1039.

[32] Zagar TM, Vujaskovic Z, Formenti S, et al. Two phase I dose-escalation/pharmacokinetics studies of low temperature liposomal doxorubicin (LTLD) and mild local hyperthermia in heavily pretreated patients with local regionally recurrent breast cancer. Int. J. Hyperth. 2014;30:285–294.

[33] Lindner LH, Eichhorn ME, Eibl H, et al. Novel Temperature-Sensitive Liposomes with Prolonged Circulation Time. Clin. Cancer Res. 2004;10:2168–2178.

[34] Zimmermann K, Hossann M, Hirschberger J, et al. A pilot trial of doxorubicin containing phosphatidyldiglycerol based thermo-sensitive liposomes in spontaneous feline soft tissue sarcoma. Int. J. Hyperth. 2017;33:178–190.

[35] Peller M, Willerding L, Limmer S, et al. Surrogate MRI markers for hyperthermia-induced release of doxorubicin from thermo-sensitive liposomes in tumors. J. Control. Release. 2016;1–10.

[36] Willerding L, Limmer S, Hossann M, et al. Method of hyperthermia and tumor size influence effectiveness of doxorubicin release from thermosensitive liposomes in experimental tumors. J. Control. Release. 2016;222:47–55.

[37] De Smet M, Hijnen NM, Langereis S, et al. Magnetic Resonance Guided High-Intensity Focused Ultrasound Mediated Hyperthermia Improves the Intratumoral Distribution of Temperature-Sensitive Liposomal Doxo-rubicin. Invest. Radiol. 2013;48:395–405.

[38] Kheirolomoom A, Lai C-Y, Tam SM, et al. Complete regression of local cancer using temperature-sensitive liposomes combined with ultrasound-mediated hyperthermia. J. Control. Release. 2013;172:266–273.

[39] Staruch RM, Ganguly M, Tannock IF, et al. Enhanced drug delivery in rabbit VX2 tumours using thermosensitive liposomes and MRI-controlled focused ultrasound hyperthermia. Int. J. Hyperth. 2012;28:776–787.

[40] Bing C, Patel P, Staruch RM, et al. Longer Heating Duration Increases Localized Doxorubicin Deposition and Therapeutic Index in Vx2 Tumors Using MR-HIFU Mild Hyperthermia and Thermosensitive Liposomal Doxorubicin. Int. J. Hyperth. 2018;0:1–8.

[41] Staruch R, Chopra R, Hynynen K. Localised drug release using MRI-controlled focused ultrasound hyperthermia. Int. J. Hyperth. 2011;27:156–171.

[42] Farr N, Wang Y-N, D'Andrea S, et al. Hyperthermia-enhanced targeted drug delivery using magnetic resonance-guided focussed ultrasound: a pre-clinical study in a genetic model of pancreatic cancer. Int. J. Hyperth. 2018;34:284–291.

[43] Staruch RM, Hynynen K, Chopra R. Hyperthermia-mediated doxorubicin release from thermosensitive liposomes using MR-HIFU: therapeutic effect in rabbit Vx2 tumours. Int. J. Hyperth. 2015;31:118–133.

[44] De Smet M, Heijman E, Langereis S, et al. Magnetic Resonance Imaging of High Intensity Focused Ultrasound Mediated Drug Delivery from Temperature-Sensitive Liposomes: An In Vivo Proof-of-Concept Study. J. Control. Release. 2011;150:102–110.

[45] De Smet M, Langereis S, Van den Bosch S, et al. SPECT/CT Imaging of Temperature-Sensitive Liposomes for MR-Image Guided Drug Delivery with High Intensity Focused Ultrasound. J. Control. Release. 2013;169:82–90.

[46] Kneepkens E, Heijman E, Keupp J, et al. Interleaved Mapping of Temperature and Longitudinal Relaxation Rate to Monitor Drug Delivery During Magnetic Resonance-Guided High-Intensity Focused Ultrasound-Induced Hyperthermia. Invest. Radiol. 2017;52:620–630.

[47] Hijnen NM, Heijman E, Köhler M, et al. Tumour Hyperthermia and Ablation in Rats Using a Clinical MR-HIFU System Equipped with a Dedicated Small Animal Setup. Int. J. Hyperth. 2012;28:141–155.

[48] Ranjan A, Jacobs GC, Woods DL, et al. Image-guided drug delivery with magnetic resonance guided high intensity focused ultrasound and temperature sensitive liposomes in a rabbit Vx2 tumor model. J. Control. Release. 2012;158:487–494.

[49] Negussie AH, Yarmolenko PS, Partanen A, et al. Formulation and characterisation of magnetic resonance imageable thermally sensitive liposomes for use with magnetic resonance-guided high intensity focused ultrasound. Int. J. Hyperth. 2011;27:140–155.

[50] Wong AW, Fite BZ, Liu Y, et al. Ultrasound ablation enhances drug accumulation and survival in mammary carcinoma models. 2015;126:99–111.

[51] Salomir R, Vimeux FC, De Zwart JA, et al. Hyperthermia by MR-Guided Focused Ultrasound: Accurate Temperature Control Based on Fast MRI and a Physical Model of Local Energy Deposition and Heat Conduction. Magn. Reson. Med. 2000;43:342–347.

[52] Quesson B, Vimeux F, Salomir R, et al. Automatic Control of Hyperthermic Therapy Based on Real-Time Fourier Analysis of MR Temperature Maps. Magn. Reson. Med. 2002;47:1065–1072.

[53] Mougenot C, Salomir R, Palussie J, et al. Automatic spatial and temporal temperature control for MR-guided focused ultrasound using fast 3D MR thermometry and multispiral trajectory of the focal point. Magn. Reson. Med. 2004;52:1005–1015.

[54] Tillander M, Hokland S, Koskela J, et al. High Intensity Focused Ultrasound Induced In Vivo Large Volume Hyperthermia under 3D MRI Temperature Control. Med. Phys. 2016;43:1539–1549.

[55] Sebeke L, Deenen DA, Maljaars E, et al. Model predictive control for MR-HIFU-mediated uniform hyperthermia. Int. J. Hyperth. 2019;36:1040–1050.

[56] Matyash V, Liebisch G, Kurzchalia T V., et al. Lipid extraction by methyl-terf-butyl ether for high-throughput lipidomics. J. Lipid Res. 2008;49:1137–1146.

[57] Greenblatt D, Koch-Weser J. Clinical Pharmacokinetics (First of Two Parts). New Engl. J. Med. 1975;293:702–705.

[58] Greenblatt D, Koch-Weser J. Clinical Pharmacokinetics (Second of Two Parts). N. Engl. J. Med. 1975;293:964–970.

[59] Newville M, Otten R, Nelson A, et al. LMFIT: Non-Linear Least-Square Minimization and Curve-Fitting for Python. 2019.

[60] Gasselhuber A, Dreher MR, Negussie A, et al. Mathematical spatio-temporal model of drug delivery from low temperature sensitive liposomes during radiofrequency tumour ablation. Int. J. Hyperth. 2010;26:499–513.

[61] Varoquaux G, Buitinck L, Louppe G, et al. Scikit-learn. GetMobile Mob. Comput. Commun. 2015;19:29–33.

5

[62]  Virtanen P, Gommers R, Oliphant TE, et al. SciPy 1.0: Fundamental Algorithms for Scientific Computing in Python. Nat. Methods. 2020;

[63]  Hossann M, Syunyaeva Z, Schmidt R, et al. Proteins and cholesterol lipid vesicles are mediators of drug release from thermosensitive liposomes. J. Control. Release. 2012;162:400–406.

[64]  Hossann M, Wang T, Wiggenhorn M, et al. Size of thermosensitive liposomes influences content release. J. Control. Release. 2010;147:436–443.

[65]  Anderson M, Domellöf L, Eksborg S, et al. Pharmacokinetics and central haemodynamic effects of doxorubicin and 4'epi-doxorubicin in the pig. Acta Oncol. (Madr). 1989;28:709–714.

[66]  Irving L. Physiological Insulation of Swine as Bare-Skinned Mammals. J. Appl. Physiol. 1956;9:414–420.

[67]  Swenson CE, Haemmerich D, Maul DH, et al. Increased duration of heating boosts local drug deposition during radiofrequency ablation in combination with thermally sensitive liposomes (ThermoDox) in a porcine model. PLoS One. 2015;10:1–15.

[68]  Dicheva BM, Seynhaeve ALB, Soulie T, et al. Pharmacokinetics, Tissue Distribution and Therapeutic Effect of Cationic Thermosensitive Liposomal Doxorubicin Upon Mild Hyperthermia. Pharm. Res. 2016;33:627–638.

[69]  Morita K, Friedrich Z, Kakinuma K, et al. Efficacy of doxorubicin thermosensitive liposomes (40 °C) and local hyperthermia on rat rhabdomyosarcoma. Oncol. Rep. 2008;20:365–372.

[70]  Szebeni J, Muggia F, Gabizon A, et al. Activation of complement by therapeutic liposomes and other lipid excipient-based therapeutic products: Prediction and prevention. Adv. Drug Deliv. Rev. 2011;63:1020–1030.

# Chapter 6

## General Discussion

## INTRODUCTION

Radio- and chemotherapy are the main tools that are used today to treat inoperable tumors and these modalities have drastically improved the prognosis for cancer patients. However, the power of radio- and chemotherapy is self-limiting due to their toxic effect on healthy tissue. Adjuvant treatment options are therefore investigated to both enhance their effectiveness and limit their side-effects. Besides the more recent addition of immune therapy to cancer treatment options, thermal therapy has already proven itself to be a valuable addition to radio- and chemotherapy [1-3]. Many clinical trials have shown the benefits of adding hyperthermia to radio-, chemo- and chemoradiotherapy over corresponding monotherapies while adding only limited additional toxicity [4-9]. However, there have also been studies that did not find statistically significant benefits due to poor temperature control [10,11], and even with the most modern clinical devices for hyperthermia, the accuracy and reproducibility of temperature elevations is lacking [12]. It therefore stands to reason that an advancement in temperature control would greatly improve upon the already impressive results seen with hyperthermia today [13,14]. Magnetic resonance-guided high-intensity focused ultrasound (MR-HIFU) has great potential to enable this advancement as a hyperthermia device that provides conformal and uniform hyperthermia. Magnetic resonance imaging (MRI) is not only valuable as a tool for treatment planning due to the high soft-tissue contrast it provides, but it can also be used to noninvasively gather accurate temperature information on a sub-second interval that is spatially resolved on the millimeter scale [15,16]. This synergizes extremely well with high intensity focused ultrasound, as HIFU generates an extremely tight energy deposition field. This leads to a local temperature increase in a small volume of only a few millimeters in diameter that can be steered with high accuracy. MR-HIFU therefore has all components necessary for tight temperature control and first steps are already being taken in bringing MR-HIFU-mediated hyperthermia to the clinic [17,18]. This would not only enable uniform and conformal hyperthermia but also the subsequent noninvasive ablation of the tumor, which has been the mainstay of MR-HIFU for more than a decade. This would presumably yield even greater returns, as a preclinical study recently demonstrated the superiority of the three-pronged approach of local delivery of chemotherapy, hyperthermia and ablation over the two-pronged approaches using either hyperthermia or ablation [19]. This development has tremendous implications for patients with tumors that are highly resistant to chemotherapy and radiotherapy. Therefore, the aim of this thesis is to advance the clinical translation of MR-HIFU hyperthermia and ablation for malignant tumors such as pancreatic cancer.

## *IN-VIVO* ABLATION OF THE PORCINE PANCREAS *VIA* MR-HIFU

Pancreatic cancer has a five-year survival rate of nine percent, which is the lowest of any cancer [20]. This stems from a confluence of unfavorable characteristics, including the late onset of symptoms, the rapid formation of metastases and the rapid involvement of nearby arteries. Consequently, five out of six patients are ineligible for surgery at the time of diagnosis, which is currently the only available curative treatment [21]. If the tumor mass cannot be resected, it exerts growing pressure on the surrounding structures, leading to severe pain in the abdomen and in the back as well as digestive problems and nausea [21]. The available options for pain management are often ineffective [22]. It has already been shown that ultrasound-guided HIFU ablation relieves pain, reduces the tumor volume in pancreatic cancer patients and may even offer a survival benefit [23]. However, the lack of real-time temperature feedback at the relevant temperatures during ultrasound-guided HIFU compromises the technique's safety and potential effectiveness as the thermal buildup in the target volume and surrounding structures cannot be tracked effectively [24]. We therefore performed a feasibility study of magnetic-resonance guided HIFU ablation of the pancreas in a healthy swine model and presented it in **chapter 2**. The pig was chosen as a model as the anatomical dimensions encountered in these animals closely resemble the human situation and the porcine pancreas is structured in a similar way as the human pancreas [25]. However, the arrangement of the bowels poses an additional obstacle in the pig, as most of the colon is arranged in a spiral that obstructs the acoustic access to the pancreas [26]. This is problematic, as solid bowel contents and gas pockets would strongly absorb ultrasound, leading to rapid prefocal heating. We addressed this problem *via* a bowel preparation protocol involving a laxative and by using an acoustically transparent hydrogel pad with an added dome shape during the experiments. This gel pad compressed the bowels and shortened the length of the intraabdominal beam path without a significant impact on the overall distance of the pancreas from the HIFU window. Eight of ten attempts at sonication of the pancreas were successful after the addition of the compression device, five of which induced clearly visible thermal lesions in the pancreas. The lesion sizes that were predicted by thermometry and contrast enhanced MRI for these lesions matched the lesion sizes that were measured in gross examination on the scale of the thermometry protocol's voxel size. The factors that were found to prohibit a successful ablation of the pancreas were the obstruction of the beam path, the application of too little acoustic power, spontaneous respiratory motion, the displacement of the pancreas between the acquisition of the planning image and the sonication, and the rapid cooling of the target volume by the adjacent portal vein. In one case, severe bowel damage was observed in gross examination.

The obstacles that were encountered in the preclinical study provide us with useful guidelines for upcoming clinical trials. The treatment planning must be swift to avoid

6

the displacement of the bowels between the acquisition of the planning scan and the treatment. This demands that the operator is experienced in the use of the clinical HIFU software, knows which acoustic power is going to be required and is aware of the tremendous cooling effect of the adjacent blood vessels. It is furthermore of the utmost importance for the safety of the patient and the success of the treatment that no solid bowel content or air pockets intersect the beam path. Bowel preparation will presumably be easier to accomplish in humans than in pigs due to the well-established bowel preparation methods for colonoscopy. Additionally, a hydrogel compression device should be used and to shorten the intraabdominal beam path and to displace bowels and stomach tissue. This is vital because most pancreatic cancer tumors arise in the head of the pancreas [21], which is situated behind the transverse mesocolon in humans [27]. Finally, the treatment will require active participation of the anesthesiologist to ensure that the patient's respiration remains suspended for the duration of the treatment. These guidelines will first be implemented and practiced in an upcoming preclinical study. The study will also investigate the precision with which HIFU ablation can be performed in the pancreas using online control of the thermal dose applied to the target area [28].

In summary, the ablation of the porcine pancreas is feasible, and the size of the induced thermal lesion can be tracked accurately using noninvasive MR-thermometry. By implementing the discussed improvements in the next preclinical experiments, the workflow could be further optimized for clinical translation.

## DEVELOPMENT AND VALIDATION OF A MODEL-BASED CONTROLLER FOR MR-HIFU HYPERTHERMIA

Even with the improved control MRI provides over diagnostic ultrasound for the guidance of HIFU treatments, not all areas of a tumor will be safe to ablate. This is especially true for pancreatic cancer, which rapidly infiltrates adjacent organs and encases major blood vessels [21]. Pancreatic cancer is furthermore highly resistant to radiation and chemotherapy. Such tumors might be receptive to sensitization by hyperthermia, but current clinical hyperthermia devices lack the control and precision necessary to induce therapeutic temperature levels in proximity to blood vessels [29].

MR-HIFU has the potential to enable hyperthermia treatments in pancreatic cancer as MR-guidance provides both near real-time temperature feedback, with which local heat sinks can be identified, and HIFU provides the precision and high focal energy deposition rates necessary to heat tissue close to such heat sinks. With Sonalleve®, there is a clinical MR-HIFU system available at hospitals today that is capable of inducing hyperthermia. The hyperthermia routines implemented in the control software already include a mechanism for the management of nearfield heating, which is necessary for

applications that require high acoustic powers over long timespans, and the capability to heat clinically relevant volumes by switching the transducer position among multiple sub-volumes [30]. However, the high precision that HIFU affords over the heating pattern is not fully utilized by the binary feedback algorithm which is used to regulate the temperature within the sub-volumes. We have therefore developed a novel model-predictive control (MPC) algorithm which uses a thermal model of the target tissue to calculate the optimal heating pattern to achieve a uniform temperature distribution. In **chapter 3**, we described the architecture of the controller and measured its performance under various conditions *in-silico* and *in-vitro*. We found that even at large mismatches in the used model parameters, the controller maintains high performance and provides both smaller tracking errors and more controlled temperature distributions than the binary controller of the Sonalleve® software. Our experiments demonstrated that the controller automatically allocates additional heating power to regions of elevated heat loss in experiments with target volumes close to an artificial blood vessel that was integrated in the tissue mimicking phantom used for the study. This behavior was also observed *in-vivo*. In **chapter 4**, we investigated the controller's performance in a series of experiments performed with target volumes in the biceps femori of five German landrace pigs. We found that the power applied to the target area is allocated in heterogenous patterns and passes a minimum after an initial warmup period of approximately three hundred seconds. When the heating pattern was overlaid on the contrast enhanced MRI images acquired after the treatments, a clear colocalization of elevated power allocation with the presence of blood vessels was observed. The heat sink effect of the blood vessels was verified by superimposing the contrast enhanced MRI images with perfusion maps that were calculated from the thermometry data acquired after the end of the sonication. We also found that during the sonication, the evolution of the prediction error over time exhibited a negative slope, indicating an increase in heat loss over time. This effect was stronger in the voxels close to blood vessels, indicating that the increase in heat loss was indeed caused by an increase in perfusion. Using the applied power that was required to maintain hyperthermia as a measure for the enhancement of perfusion, an increase by a factor of approximately 1.86 was found, which is in accordance with the values previously reported by Lokshina *et al.* [31]. Despite the increase in perfusion, the MPC maintained high performance throughout the treatments.

To our knowledge, this is the first time the heat sink effect of individual blood vessels was visualized and the thermoregulation response was demonstrated in a large animal model. The visualization and real-time estimation of perfusion-induced heat loss during MPC-MR-HIFU hyperthermia presents an opportunity for future research investigating the stimulation of perfusion in poorly perfused and hypoxic tumor regions, as most research concerning the physiological response of tumor vasculature to heat was conducted in the 1980s and only quantified averages across the whole tumor [32]. As the MPC

6

performs well in highly perfused muscle tissue even while perfusion is increasing due to hyperthermia, we consider MPC development as successfully concluded. However, there are still a few issues to address before the controller can be used in a clinical setting. In two of the ten experiments that were performed, the thermometry failed due to the occurrence of situations that the drift correction algorithm was not designed to handle. As the performance of any feedback controller will critically depend on the quality of the feedback it receives, the pairing with a robust thermometry algorithm will be vital for uniform and safe hyperthermia in the clinic. The controller is also only designed to regulate the temperature in the volume that is accessible *via* electronic beam steering. An integration with a second control layer which can dynamically reposition the transducer during treatment will therefore be necessary to treat clinically relevant tissue volumes. Finally, an extension of the controller with a mechanism that can adapt the controller's model to the perfusion changes triggered by hyperthermia may further improve the uniformity of the created temperature distribution. This would be of special interest for drug delivery applications, where the temperature of the blood vessels will determine the rate of release [33].

## LOCAL DRUG DELIVERY *VIA* MR-HIFU-HYPERTHERMIA IN A LARGE ANIMAL MODEL

The benefit of adding hyperthermia to chemotherapy (thermochemotherapy) with freely circulating drug has already been shown in the clinical setting [34]. However, the use of freely circulating drug fundamentally limits the potential of thermochemotherapy. The rapid clearance of freely circulating drugs from the blood pool leads to low plasma concentrations and thereby low availability of the drug in the tumor while being taken up in healthy, off-target tissues such as the heart. Temperature sensitive liposomes (TSLs), which were first proposed in the late seventies by Yatvin and Weinstein *et al*. [35,36], solve this problem by encapsulating the drug in long-circulating nanoparticles that protect the drug from being cleared and releasing the drug locally when hyperthermia is applied. Consequently, preclinical studies investigating thermochemotherapy with doxorubicin-loaded TSLs showed an enhancement of the drug uptake into the tumor by a factor of 5 to 25 times compared to freely circulating drug [37], vastly increasing the cytotoxic effect. For the clinical translation of MR-HIFU hyperthermia-mediated drug delivery, it is essential that clinical workflows are developed, and promising drugs are evaluated in large animal models. In **chapter 5**, we therefore presented a study in a healthy swine model concerning the delivery of doxorubicin (DOX) from temperature sensitive liposomes (TSLs) using the newly developed MPC algorithm for hyperthermia control. The used drug was $DPPG_2$-TSL-DOX, a novel liposomal DOX formulation by Thermosome (Munich, Germany). Four

animals were anesthetized and positioned on the patient table of the MR-HIFU. Once the treatment planning was complete and the two selected treatment sites in the thigh muscle of the pig had been co-registered with MR-visible markings on the pig's skin, $DPPG_2$-TSL-DOX was infused for half an hour. Starting at 10 minutes and at 60 minutes after the beginning of the infusion, two hyperthermia treatments with target temperatures of 42 °C were initiated and were each maintained for half an hour. Blood samples were drawn regularly from the initiation of the $DPPG_2$-TSL-DOX until the animal was euthanized 3 hours after the initiation. Analysis of the blood samples *via* mass spectroscopy and HPLC showed that the liposomal drug carrier is cleared very slowly, following a double-exponential clearance behavior, and levelling off at approximately 60 % of the injected dose by the 3-hour timepoint. Using a pharmacodynamic model for the leaking of DOX from the liposomes and its subsequent clearance, we found that DOX leaks from the carrier with an exponential decay time of approximately 25 minutes, though this number is likely to be too small due to simplifications that were made in the model. Compared to an earlier study in cats [38], the measured DOX plasma half life was considerably shorter. As body temperature has an influence on drug leakage , the pigs' body temperature was stabilized around 37.5 °C as measured with an esophageal temperature probe. However, it cannot be ruled out that the intrinsically higher physiological body temperature in pigs of up to 39 °C [39] may have an influence on leakage, as thermoregulation tends to maintain the physiological temperature in major organs even if the rest of the animal's body cools down during anesthesia. Furthermore, differences in the chemical environment of the blood may cause additional destabilization of the TSL lipid bilayer, leading to a more rapid release of the payload. The temperature during the hyperthermia treatments was slightly below the target temperature on average, which may have been caused by the additional heat loss due to stimulated perfusion that was observed in chapter 4. However, due to the high uniformity of the temperature distribution enabled by the MPC algorithm, the temperature necessary for effective drug delivery was still maintained throughout the target ROI. The analysis of the biodistribution showed that in comparison to untreated muscle, the concentration of DOX was 15 and 7 times higher in the muscle volumes that had undergone hyperthermia starting at 10 and 60 minutes after the start of the infusion, respectively. Using the pharmacodynamic model to estimate the AUC of the bioavailable "free" DOX for each target volume, we found a linear relationship between the AUC of bioavailable DOX and the concentration in the respective muscle sample. This finding is in accordance with *in-silico* studies by Gasselhuber *et al*. [40] and will help to plan treatment schedules to maximize the beneficial effect of hyperthermia-mediated drug delivery. This study shows that MR-HIFU is a suitable technology for hyperthermia-mediated drug delivery from temperature-sensitive liposomes. As the workflow used in this study was developed for a large animal model, it may serve as a starting point and accelerator for the development of clinical workflows.

6

## OUTLOOK: THE PATH TO CLINICAL TRANSLATION

The studies in this thesis were deliberately performed in a large animal model to bridge the gap between preclinical research and clinical application. The purpose of the feasibility study presented in chapter 2 was designed with the aim to develop a workflow that could be implemented in an upcoming clinical trial on the MR-guided HIFU ablation of pancreatic cancer. There are still some questions that still need to be addressed beforehand, especially concerning the precision that can be achieved with feedback-controlled ablation protocols in the pancreas and whether the whole target area is reliably ablated. These questions will be addressed in a follow-up study in the second half of 2020 before the clinical trial will commence in Q1 of 2021 at the University Hospital of Cologne (UHC).

In a review article of 2014, Hijnen *et al.* [37] outlined five requirements that needed to be met for MR-HIFU hyperthermia-mediated drug delivery to become a clinical reality. These requirements are (1) the availability of uniform and conformal hyperthermia, (2) the development of clinical protocols, (3) the availability of liposome formulations for clinical use, (4) the identification of suitable applications and (5) funding. The studies presented in this thesis are steppingstones towards the first two requirements. The model-based controller developed in the scope of this thesis is in the progress of being integrated into a dedicated hyperthermia release of the Sonalleve® software in close collaboration with Profound Medical (Mississauga, Canada). As soon as the integration is completed, a preclinical study will be performed at the UHC to develop a clinical protocol for the application of MR-HIFU hyperthermia and drug delivery in abdominal targets. This will fulfill the second requirement and lay the technological foundation for a first clinical of MR-HIFU hyperthermia-mediated drug delivery. The target application may be the pancreas, but as the temperature sensitive liposomal doxorubicin formulation of Thermosome (Munich, Germany) will likely reach a stage within three years at which clinical trials in combination with MR-HIFU hyperthermia may be considered, other tumor entities that respond to doxorubicin, like soft-tissue sarcoma, are also likely candidates. This will leave funding as the final hurdle for the clinical translation of MR-HIFU hyperthermia-mediated drug delivery. If this step succeeds will depend in large parts on the availability of public grants for joint projects of public and private partners due to the high financial risks involved [19]. In close partnerships between hospitals and companies, such as Profound Medical, the manufacturer of Sonalleve®, and Thermosome, a manufacturer of drug-loaded temperature-sensitive liposomes, strategies can be developed to secure funding for clinical pilot trials.

## CONCLUSION

MR-HIFU has great potential in oncology as an enabler for potent combination therapies with minimal toxicity. In this thesis we have explored two applications of MR-HIFU in a large animal model, with the aim to show their feasibility and to develop workflows that can swiftly be adapted into clinical practice. The magnetic resonance-guided ablation of pancreatic cancer and the local release of cytostatic drugs have both reached a stage at which they could soon yield benefits for patients who only have limited treatment options left. With continued research effort, a combination therapy of hyperthermia, local drug delivery, and ablation that allows to noninvasively treat unresectable chemo- and radioresistant tumors with reduced side effects may soon be a clinical reality. We hope and believe that the work presented in this thesis will help to accelerate this process.

6

# REFERENCES

[1] Issels RD. Hyperthermia Adds to Chemotherapy. Eur. J. Cancer. 2008;44:2546–2554.

[2] Horsman MR, Overgaard J. Hyperthermia: A Potent Enhancer of Radiotherapy. Clin. Oncol. 2007;19:418–426.

[3] Datta NR, Ordóñez SG, Gaipl US, et al. Local Hyperthermia Combined with Radiotherapy and-/or Chemotherapy: Recent Advances and Promises for the Future. Cancer Treat. Rev. 2015;41:742–753.

[4] Issels RD, Lindner LH, Verweij J, et al. Effect of Neoadjuvant Chemotherapy Plus Regional Hyperthermia on Long-Term Outcomes Among Patients With Localized High-Risk Soft Tissue Sarcoma. JAMA Oncol. 2018;4:483–492.

[5] Vernon CC, Hand JW, Field SB, et al. Radiotherapy with or without hyperthermia in the treatment of superficial localized breast cancer: Results from five randomized controlled trials. Int. J. Radiat. Oncol. Biol. Phys. 1996;35:731–744.

[6] Zee J Van Der, González DG, Rhoon GC Van, et al. Comparison of Radiotherapy alone with Radiotherapy plus Hyperthermia in Locally Advanced Pelvic Tumors. Lancet. 2000;355:1119–1125.

[7] Datta NR, Rogers S, Ordóñez SG, et al. Hyperthermia and Radiotherapy in the Management of Head and Neck Cancers: A Systematic Review and Meta-Analysis. Int. J. Hyperth. 2016;32:31–40.

[8] Datta NR, Rogers S, Klingbiel D, et al. Hyperthermia and Radiotherapy with or without Chemotherapy in Locally Advanced Cervical Cancer: A Systematic Review with Conventional and Network Meta-Analyses. Int. J. Hyperth. 2016;32:809–821.

[9] Hu Y, Li Z, Mi D-H, et al. Chemoradiation combined with regional hyperthermia for advanced oesophageal cancer: a systematic review and meta-analysis. Jounral Clin. Pharm. Ther. 2017;42:155–164.

[10] Vasanthan A, Mitsumori M, Park JH, et al. Regional hyperthermia combined with radiotherapy for uterine cervical cancers: A multi-institutional prospective randomized trial of the international atomic energy agency. Int. J. Radiat. Oncol. Biol. Phys. 2005;61:145–153.

[11] Emami B, Scott C, Perez CA, et al. Phase III study of interstitial thermoradiotherapy compared with interstitial radiotherapy alone in the treatment of recurrent or persistent human tumors: A prospectively controlled randomized study by the radiation therapy oncology group. Int. J. Radiat. Oncol. Biol. Phys. 1996;34:1097–1104.

[12] Mulder HT, Curto S, Paulides MM, et al. Systematic Quality Assurance of the BSD2000-3D MR-Compatible Hyperthermia Applicator Performance Using MR Temperature Imaging. Int. J. Hyperth. 2018;35:305–313.

[13] Van Rhoon GC. Is CEM43 Still a Relevant Thermal Dose Parameter for Hyperthermia Treatment Monitoring? Int. J. Hyperth. 2016;6736:1–13.

[14] Leopold KA, Dewhirst M, Samulski T, et al. Relationships among tumor temperature, treatment time, and histopathological outcome using preoperative hyperthermia with radiation in soft tissue sarcomas. 1992;22:989–998.

[15] Ishihara Y, Calderon A, Watanabe H, et al. A Precise and Fast Temperature Mapping Using Water Proton Chemical Shift. Magn. Reson. Med. 1995;34:814–823.

[16] Odéen H, Parker DL. Magnetic resonance thermometry and its biological applications - Physical principles and practical considerations. Prog. Nucl. Magn. Reson. Spectrosc. 2019;110:34–61.

[17] Chu W, Staruch RM, Pichardo S, et al. MR-HIFU Mild Hyperthermia for Locally Recurrent Rectal Cancer: Temperature Mapping and Heating Quality in First Patient. 12th Int. Congr. Hyperthermic Oncol. 2016. p. 144.

[18] Heijman E, Yeo SY, Sebeke L, et al. Volumetric Hyperthermia of Soft Tissue Sarcoma using MR-Guided High Intensity Focussed Ultrasound. 6th Int. Symp. Focus. Ultrasound. 2018.

[19] Hijnen N, Kneepkens E, De Smet M, et al. Thermal Combination Therapies for Local Drug Delivery by Magnetic Resonance-Guided High--Intensity Focused Ultrasound. Proc. Natl. Acad. Sci. 2017;114:E4802–E4811.

[20] Siegel RL, Miller KD, Jemal A. Cancer Statistics, 2019. CA. Cancer J. Clin. 2019;69:7–34.

[21] Ryan DP, Hong TS, Bardeesy N. Pancreatic Adenocarcinoma. N. Engl. J. Med. 2014;371: 1039–1049.

[22] Moffat GT, Epstein AS, O'Reilly EM. Pancreatic Cancer—A Disease in Need: Optimizing and Integrating Supportive Care. Cancer. 2019;0:1–9.

[23] Marinova M, Huxold HC, Henseler J, et al. Clinical Effectiveness and Potential Survival Benefit of US-Guided High-Intensity Focused Ultrasound Therapy in Patients with Advanced-Stage Pancreatic Cancer. Ultraschall Med. 2019;40:625–637.

[24] Lewis MA, Staruch RM, Chopra R. Thermometry and Ablation Monitoring with Ultrasound. Int. J. Hyperth. 2015;31:163–181.

[25] Ligresti D, Kuo YT, Baraldo S, et al. EUS Anatomy of the Pancreatobiliary System in a Swine Model: The WISE Experience. Endosc. Ultrasound. 2019;8:249–254.

[26] Swindle MM, Smith AC. Comparative Anatomy and Physiology of the Pig. Scand. J. Lab. Anim. Sci. 1998;25:11–21.

[27] Mahadevan V. Anatomy of the Pancreas and Spleen. Surgery. 2016;34:261–265.

[28] Enholm JK, Köhler M, Quesson B, et al. Improved Volumetric MR-HIFU Ablation by Robust Binary Feedback Control. IEEE Trans. Biomed. Eng. 2010;57:103–113.

[29] Datta NR, Kok HP, Crezee H, et al. Integrating Loco-Regional Hyperthermia Into the Current Oncology Practice: SWOT and TOWS Analyses. Front. Oncol. 2020;10:819.

[30] Tillander M, Hokland S, Koskela J, et al. High Intensity Focused Ultrasound Induced In Vivo Large Volume Hyperthermia under 3D MRI Temperature Control. Med. Phys. 2016;43:1539–1549.

[31] Lokshina AM, Song CW, Rhee JG, et al. Effect of fractionated heating on the blood flow in normal tissues. Int. J. Hyperth. 1985;1:117–129.

[32] Vaupel PW, Kelleher DK. Pathophysiological and vascular characteristics of tumours and their importance for hyperthermia: heterogeneity is the key issue. Int. J. Hyperth. 2010;26:211–223.

[33] Lokerse WJM, Kneepkens ECM, ten Hagen TLM, et al. In depth study on thermosensitive liposomes: Optimizing formulations for tumor specific therapy and in vitro to in vivo relations. Biomaterials. 2016;82:138–150.

[34] Issels RD, Lindner LH, Verweij J, et al. Neo-adjuvant Chemotherapy Alone or with Regional Hyperthermia for Localised High-Risk Soft-Tissue Sarcoma: A Randomised Phase 3 Multicentre Study. Lancet Oncol. 2010;11:561–570.

[35] Yatvin M, Weinstein J, Dennis W, et al. Design of liposomes for enhanced local release of drugs by hyperthermia. Science (80-. ). 1978;202:1290–1293.

[36] Weinstein J, Magin R, Yatvin M, et al. Liposomes and local hyperthermia: selective delivery of methotrexate to heated tumors. Science (80-. ). 1979;204:188–191.

[37] Hijnen N, Langereis S, Grüll H. Magnetic resonance guided high-intensity focused ultrasound for image-guided temperature-induced drug delivery. Adv. Drug Deliv. Rev. 2014;72:65–81.

[38] Zimmermann K, Hossann M, Hirschberger J, et al. A pilot trial of doxorubicin containing phosphatidyldiglycerol based thermo-sensitive liposomes in spontaneous feline soft tissue sarcoma. Int. J. Hyperth. 2017;33:178–190.

[39] Irving L. Physiological Insulation of Swine as Bare-Skinned Mammals. J. Appl. Physiol. 1956;9:414–420.

[40] Gasselhuber A, Dreher MR, Negussie A, et al. Mathematical spatio-temporal model of drug delivery from low temperature sensitive liposomes during radiofrequency tumour ablation. Int. J. Hyperth. 2010;26:499–513.

6

# Ethical Paragraph

Pancreatic cancer has the lowest five-year survival rate of any cancer and the mortality of this condition is rising steadily. There is a strong body of evidence that supports the beneficial effect of high-intensity focused ultrasound (HIFU) for pancreatic cancer patients. Likewise, there is strong evidence that hyperthermia enhances the effectiveness of radio- and chemotherapy in tumors that are otherwise highly refractory to these therapies, one of which is pancreatic cancer. Magnetic resonance guidance of HIFU enables a combination of chemotherapy, hyperthermia and ablation that has been shown to be highly effective in the preclinical setting. The animal experiments performed within the scope of this thesis were aimed at the clinical translation of this combination therapy, which may improve the prognosis of pancreatic cancer patients. The studies were planned according to the 3R principle to minimize the animal suffering caused by the experiments. Where possible, animal experiments were **replaced** using *in-silico* and *in-vitro* methods. The number of animal experiments was furthermore **reduced** to the absolute minimum necessary to obtain meaningful results. The experimental protocols were also **refined** *via* the implementation of adequate acclimatization periods, housing arrangements, and analgesia to minimize the distress experienced by the animals.

All preclinical studies performed in this thesis were approved by the State Agency for Nature, Environment and Consumer Protection of North Rhine Westphalia, Germany. For each experiment, the number of animals used and the discomfort they experienced were weighted against the importance of the obtained information. The maintenance and care of the experimental animals was in compliance with the EU guideline 2010/63/EU and the TierSchVersV accredited by the German Federal ministry of Food, Agriculture and Consumer protection.

# Summary

The **aim** of this dissertation is the clinical translation of magnetic resonance-guided high-intensity focused ultrasound (MR-HIFU) for the treatment of pancreatic cancer and other malignant tumors that are highly refractory to chemo- and radiotherapy. The envisioned treatment scheme comprises the application of conformal and highly uniform MR-HIFU-mediated hyperthermia, the local release of a cytostatic drug from temperature sensitive liposomes, and the subsequent ablation of the tumor.

An overview of the background of this thesis is given in **chapter 1**. It includes an introduction to the principles of thermal therapy and the medical heating technologies that are available today. This is followed by a historical account of the development of the MR-HIFU technology and a discussion of the value of MR-HIFU for two established applications, uterine fibroids and painful bone metastases, and one upcoming application, pancreatic cancer. The chapter is concluded with an introduction to feedback control in MR-HIFU.

In **chapter 2**, the feasibility of ablating the porcine pancreas using a clinical MR-HIFU system is investigated. The prognosis of pancreatic cancer is exceptionally poor as the disease is often discovered only at a late stage. At the time of diagnosis, the tumor has often already encased the adjacent arteries or even metastasized. In addition, pancreatic tumors are highly resistant to chemo- and radiotherapy, which only leaves palliative treatment for most patients. Pharmaceutical pain palliation is often insufficient. The analgesic effect of sonography-guided HIFU ablation on inoperable pancreatic tumors has already been demonstrated in multiple clinical studies over the last two decades and recent studies have found a possible survival benefit in comparison to historical data. However, sonography guidance lacks the soft-tissue contrast and real-time temperature feedback that is available under MR-guidance. Consequently, MR-HIFU might allow a safer and more complete ablation of pancreatic cancer tumors. We have therefore conducted a translational study concerning MR-HIFU ablation of the porcine pancreas to develop a workflow that can be adapted to clinical practice. Five healthy German landrace pigs were anesthetized and positioned in prone position on the HIFU table of a clinical MR-HIFU system. Acoustic access to the pancreas was supported by a preceding bowel preparation and the addition of a newly developed acoustically transparent hydrogel spacer for the compression of the abdomen. During short periods of apnea, two volumes with diameters of 4 mm in the pancreas of each animal were sonicated using a sonication protocol that is already in use for the treatment of uterine fibroids. This resulted in clearly visible changes in eight of ten sonications, five of which resulted in a thermal lesion of coagulated tissue. The five sonications that did not lead to a thermal lesion were analyzed

to discern the modes of failure. It was found that in three of the attempts, insufficient acoustic energy had been delivered due to premature cancellation of the sonications. These treatments were aborted early due to strong prefocal heating observed in MR-thermometry, spontaneous breathing of the animal, and an error in judgement by the operator, respectively. In one treatment that did not show a thermal lesion in the pancreas, severe damage in an adjacent bowel loop was observed instead, suggesting a displacement of the pancreas out of the HIFU focus. The final sonication was attempted in a volume adjacent to the portal vein, which prevented sufficient thermal buildup due to the rapid cooling by the blood vessel. In the sonications that did produce a thermal lesion, the size of the lesion found in gross examination was in close agreement with the measurements using MR-thermometry derived dose profiles and contrast enhanced MRI. We conclude that, if the points of failure that were identified in this study are avoided, it is feasible to ablate the porcine pancreas under magnetic resonance-guidance using equipment and software that is already available in the clinic today.

In pancreatic cancer patients, the adjacency of sensitive structures like the stomach, the bowels, and blood vessels will often prevent a complete ablation of the tumor due to safety concerns. It may be possible to sensitize these areas to chemo- and radiotherapy *via* the application of local hyperthermia. However, the proximity of large blood vessels like the celiac artery and the mesenteric artery create heat sink effects that current clinical hyperthermia equipment may not be able to compensate. MR-HIFU may provide a solution to this problem, as heat sink effects can be identified during treatment using MR-thermometry feedback and compensated *via* the focused heating HIFU provides. We have therefore developed a novel model predictive control (MPC) algorithm for MR-HIFU hyperthermia. In **chapter 3** we describe the controller's architecture as well as a study of its robustness. The robustness of the controller against model errors was assessed both in simulations and in a tissue-mimicking phantom. The MPC algorithm was set to heat nine different simulated tissues with diffusion and absorption values that deviated from the controller's predictive model by large factors. A similar experiment was performed in the tissue mimicking phantom, where the controller's predictive model was intentionally mismatched to the phantom's thermal properties. Both experiments showed that the controller creates highly uniform temperature distributions even at large model mismatches but performs best if an accurate model is provided. Finally, the controller's performance was compared to the performance of the binary hyperthermia control algorithm of the Sonalleve® platform (Profound Medical, Mississauga, Canada) both in a homogenous phantom and in a volume directly adjacent to a perfused water channel, which acted as a localized heat sink. We found that the MPC algorithm generates much more uniform temperature distributions and smaller tracking errors than the binary controller in both cases. The main reason for this was that the MPC algorithm primarily allocated acoustic power to the edge of the target region after the warmup was complete

and relied on diffusion to warm the center of the target, leading to an even temperature distribution. The binary controller on the other hand formed a bell-shaped temperature distribution. We also showed that the MPC algorithm automatically allocated additional power to the edge of the target region that was adjacent to the perfused water channel in the second experiment, which allowed the controller to maintain high performance.

The artificial blood vessel used in the phantom study is limited in its transferability to the clinical setting as it only provides a single localized heat sink effect that remains constant over time. It can therefore not properly mimic the perfusion *in-vivo*, which is both heterogeneous in space and reacts to elevated temperatures. We have therefore performed a large animal study investigating the interplay between hyperthermia and spatiotemporally heterogenous perfusion, and the effect of the latter on the performance of the MPC algorithm. This study is presented in **chapter 4**. Five healthy female German landrace pigs were anesthetized and placed on the HIFU table in lateral recumbency with the biceps femori centered above the HIFU transducer. In each animal, up to three hyperthermia experiments were performed targeting the biceps femori, resulting in a total of 8 hyperthermia treatments of 30 minutes and two shorter treatments of 10 and 15 minutes. As in chapter 3, the observed controller performance was better than values reported for binary controller in an analogous experiment. The heterogenous heating patterns generated by the controller were superimposed in contrast enhanced MRI images to investigate the interplay between perfusion and heating power allocation. This revealed that areas of increased power allocation were colocalized with blood vessels inside or next to the target volume. Using a spatially resolved model of perfusion that was fitted to the temperature maps acquired after the end of the hyperthermia treatments, we showed that the blood vessels do indeed act as local heatsinks in the areas to which the MPC algorithm had allocated elevated heating power. Analysis of the dynamic behavior of the controller over the timespan of the treatments furthermore revealed a linear increase in heat loss over time that was localized at the blood vessels. Using the increase in power that was required to maintain hyperthermia as an indicator for the increase in perfusion, we estimated that, on average, the perfusion in the target areas had increased at least by a factor 1.86 over 25 minutes, which is close to values reported in the literature for similar hyperthermia regimes in rats. We also found that the increase in perfusion does not necessarily negatively impact controller performance due to the rapid temperature feedback that is enabled by MR-thermometry.

The requirements for the clinical translation of MR-HIFU hyperthermia-mediated drug delivery include high performance temperature control, suitable drug formulations, and the development of clinical workflows. In **chapter 5**, we therefore present a drug delivery study in a large animal model in which a promising novel drug formulation was used and the MPC was applied for hyperthermia control. The drug used in the study was $DPPG_2$-TSL-DOX, a temperature-sensitive liposomal formulation of doxorubicin (DOX) developed by Thermosome (Munich, Germany). For the study, four female German

landrace pigs were prepared several days beforehand with premedication to prevent anaphylactic reactions to the drug. On the day of the experiment, the pigs anesthetized and placed on the MR-HIFU table in lateral recumbency with the hind limb centered above the transducer. Two target volumes were selected in the thigh muscle of each pig. Once the treatment planning was completed and the target volumes had been coregistered with MR-visible markers on the skin of the pig, DPPG$_2$-TSL-DOX was infused over a timespan of 30 minutes. Starting at 10 minutes and 60 minutes after the initiation of the infusion, two separate hyperthermia treatments with target temperatures of 42 °C were initiated and continued for 30 minutes each. After the end of the second treatment, small volumes inside the hyperthermia-treated muscle were ablated to provide a visual reference during excision. Blood samples were drawn regularly until the euthanization at 3 hours after the initiation of the DPPG$_2$-TSL-DOX infusion. The concentrations of the liposomal carrier and DOX in the blood samples were analyzed *via* high precision liquid chromatography and mass spectrometry. The analysis of the pharmacokinetic revealed a long circulation time of the drug carrier but a shorter than expected circulation of the drug. Reasons for this may include the specific chemical environment in the blood of pigs and elevated temperatures in core organs. The analysis of the biodistribution showed that the muscle samples that had undergone hyperthermia at 10 minutes and 60 minutes after initiation of the DPPG2-TSL-DOX infusion had on average accumulated 15- and 7 times more DOX than muscle samples that had not undergone hyperthermia, respectively. The analysis of the temperature maps acquired during the hyperthermia treatments showed that the temperatures in the target area were slightly below the target temperature on average, which may have been caused by the stimulation of perfusion that was already observed in chapter 4. However, due to the high uniformity of the temperature distribution enabled by the MPC algorithm and the rapid thermometry feedback enabled by noninvasive MR-thermometry, the minimum temperature required for effective drug delivery was still maintained throughout the target area in all treatments. Using the MR-thermometry data and a pharmacodynamic model of the drug, the AUC of bioavailable DOX in the hyperthermia-treated muscle volumes and untreated muscle volumes was calculated. The comparison with the DOX concentrations found in the corresponding muscle samples revealed a linear correlation between the AUC of bioavailable DOX and the resulting DOX accumulation, which is in agreement with theoretical predictions. This study may therefore serve as a resource for the optimization of clinical treatment schedules. As the workflow used in this study was furthermore developed for a large animal model, it may serve as a starting point and accelerator for the development of clinical workflows.

In **chapter 6**, the results obtained over the course of this thesis are summarized and discussed. Finally, an outlook on the clinical translation of MR-HIFU for the treatment of malignant tumors is given and the final conclusions are drawn.

# Acknowledgements

One of the most important lessons I learned during my projects is that collaboration is not only necessary for most projects, but that it will also greatly enhance the quality of the results and not least of all, that it will make the project more enjoyable. Over the past years I had the privilege and pleasure to work with some of the smartest, most resourceful and kind people I know and I am deeply grateful for this experience. Outside of the lab I enjoyed the support of my family and friends who constantly confirm my decision to start on this path. Their help in keeping me grounded and engaged after setbacks was just as vital to the successful conclusion of my projects as the help and advice I received from my collaborators. Here I would like to say thank you to the people who made this thesis possible, though the list is almost certainly incomplete, and the words are far from adequate to properly acknowledge their contributions.

**Holger**, thank you for your vote of confidence in a student who did not have any prior experience in biomedical engineering, mistook you for a postdoc in our first email exchange and was late for his interview because he did not think it necessary to look up the correct campus before traveling 500 km to Eindhoven. You told me several times that a PhD is granted mainly for the personal growth of the candidate, and not so much his achievements. While I cannot fully embrace that view (yet?), I am convinced that one grows with their tasks. Thank you for showing confidence when suggesting steps that I would not have dared to attempt otherwise and for holding me to a higher standard than I thought myself capable of. At the same time I am grateful that you always made time for a meeting when I felt like I needed help and for proofreading every single piece of writing that I have produced over the past five years. There is much more that I am grateful for and I have probably already forgotten more of such things than I can still remember, but lastly I would like to say thank you for the attitude you inspire in the people who work for you. "Go home and get a life" is a piece of advice that you frequently shared when you still found people working at the time you went home yourself (and you probably oftentimes went right back to work after cooking for your family, don't deny it!). Your consideration for the people who work for you and your interest in their personal lives and health is a beautiful thing.

**Edwin**, thank you for your patient supervision these past five years. Thank you for all the advice you shared and all the times you helped with my experiments or when the system behaved in an unexpected way. But most of all: Thank you for the times where you pushed me towards handling a challenge myself. I count these lessons in autonomy and confidence among the most valuable of my PhD.

**Lapo** and **Christian**, thank you for your continued support and encouragement during my Master and Bachelor projects. You both took much time to mentor me despite the need to finish your own projects and the turbulences of that period. I only now begin to appreciate how demanding that probably was. I thoroughly enjoyed my time with you as my supervisors. If it weren't for you, I may never have begun this undertaking.

**Joo Ha**, **Maurice**, **Prof. David Maintz**, **Prof. Peter Hilbers** and **Richard**, thank you for joining my doctorate committee, your evaluation and for the kind words that you have found for my thesis. **Joo Ha**, thank you for joining our first experiment on the ablation of the pancreas in Utrecht and sharing your expertise. I am also very grateful for your words of encouragement and the "KISS"-rule, they have gone a long way. **Maurice**, thank you for the pleasant and fruitful collaboration on the Control To Act project. Your advice helped a lot in bringing the MR-HIFU Hyperthermia project forward and I am excited to see how far we have come and what is next. **Prof. David Maintz**, thank you for welcoming us at the Radiology department and your efforts in bringing research and clinical routine closer together. **Prof. Peter Hilbers**, thank you for taking time for our update meetings and your critical questions and suggestions. **Richard**, thank you for taking time out of your busy schedule to review the PhD thesis of a complete stranger. Finally: Thank you, **Prof. Maarten Merkx** for chairing my defense. It is a day that I will remember vividly for a long time.

Thank you **Rajiv** and **Rob**, for welcoming and hosting me in Texas for a month. I was still trying to get my bearings in MR-HIFU at the time and had never been in the US before that point. But your help in preparation, getting me settled and your hospitality made my time with you a wonderful experience that I am incredibly grateful for. Thank you also for taking me out for dinner so often and showing me all the good restaurants around Dallas, Rob. You were right, I have not found anything that is quite like Texan barbecue since.

**Daniel**, **Bert** and **Bram**, thank you for the pleasant collaboration during the Control To Act project. I have learned a lot of valuable and interesting things during the project, both about control engineering and working together in a team where progress depends so heavily on all parts working together. You made the learning process a pleasure and I think we have come far together. I am excited to see what is next.

**Sin Yuin**, **Juan**, and **Ileana**, with the three of you the line between friends and colleagues first started to blur for me when I came to Eindhoven. I am grateful for all the times where we helped each other out and I really enjoyed spending time with you, be it at 6 am in the lab, watching a British TV show while having a hot chocolate with cheese or having

dinner (hopefully without mussels) in a restaurant on Malta. I really hope that we will keep in contact and I will cherish the memories that we created together.

**Alex** and **Pia**, thank you for the incredible amount of support with setting up and executing all my animal studies and your constant readiness to help. Thank you for making me feel welcome at the experimental medicine and for creating such a pleasant working atmosphere. Without you, most of the experiments in this thesis would not have been possible and certainly would have been a lot more terrifying to plan and perform.

**Irmgard**, **Claudia**, **Jenni**, **Katrin**, **Susann**, **Caro**, **Petra**, **Andrea**, **Tülay** and **Kirsten**, thank you for the incredible support before, during and after the experiments. Knowing that I can rely on you took a lot of stress out of the whole affair and allowed me to concentrate on what I personally needed to do. In that sense you very directly enhanced the quality of the results, for which I am also exceedingly grateful.

**Patrick**, **Markus**, **Steffi** and **Johannes**, thank you being awesome colleagues. I have experienced kindness, generosity and empathy for my high stress level over the past few months from all of you. I feel privileged to work with you and hope that we can spend a lot more time together, both inside and outside of the lab.

**Janina** and **Kira**, thank you for making my first experience as a supervisor awesome. To some degree the two of you were my lab rats in my attempts to figure out how to provide guidance while letting you organize and execute your own projects. Fortunately for me, both of you were incredibly self-reliant and showed a lot of initiative. I hope I can use the feedback you provided to improve my supervising-skills in the future.

**Pieter** and **John**, thank you for welcoming me in Eindhoven and letting me live in your house. Moving to a new city can be a lonely endeavor, but you made me feel at home immediately. **John**, thank you for giving me a second chance and your help with my internet problems. **Pieter**, thank you for being my first friend in the Netherlands and for being a great listener.

**Andi** and **Homes**, thank you for your friendship and for not holding it against me whenever I did not reach out for months at a time. Our games have really helped me to stay sane during my thesis. Just talking to you about this and that and getting lost in a fictional world together is something I have come to appreciate on an entirely new level in the past few years.

**Jana**, thank you for your love and showing me a more colorful side of life. Having you with me for the last stretch of my thesis really helped me to cope with the pressure and the brief weekends we have together are times that I can enjoy even in the middle of the greatest rush. I love you.

**Mama** and **Papa**, thank you for supporting and encouraging me for the past thirty-one years. From the trip to the library where I got my first WAS-IST-WAS book to your help in finding my PhD position, you have done more than anyone else to help me get where I am today. I am beyond grateful for your love and all the small and large ways in which you helped me to grow to a point from which I had the freedom to choose this path. **Jannik** and **Marius**, thank you for being awesome brothers. I may be the oldest (no, my hairline is not in "full retreat" (yet)!), but I nonetheless feel like I can still learn a lot from both of you about life and how to enjoy it. **Jannik**, thank you for finding fun things we can do as a family and getting us together every once in a while. **Marius**, your enthusiasm for biology and your high spirits are nothing short of inspirational. Keep it up. I love all of you.

# List of publications

## FULL PAPERS

1. Deenen DA, Maljaars E, **Sebeke L**, *et al*. Offset-Free Model Predictive Control for Enhancing MR-HIFU Hyperthermia in Cancer Treatment. IFAC-PapersOnLine. 2018;51:191–196.
2. **Sebeke LC**, Deenen DA, Maljaars E, *et al*. Model Predictive Control for MR-HIFU-Mediated Uniform Hyperthermia. Int. J. Hyperth. 2019;36:1040–1050.
3. **Sebeke LC**, Rademann P, Maul AC, *et al*. Feasibility Study of MR-guided Pancreas Ablation using High-Intensity Focused Ultrasound in a Healthy Swine Model. Int. J. Hyperth. 2020;37:786–798.
4. **Sebeke LC**, Rademann P, Maul AC, *et al*. Visualization of Thermal Washout due to Spatiotemporally Heterogenous Perfusion in the 29 Application of a Model-based Control Algorithm for MR-HIFU Mediated Hyperthermia.
   *Submitted to International Journal of Hyperthermia*
5. Deenen DA, Maljaars E, **Sebeke L**, *et al*. Robust temperature control for MR-HIFU hyperthermia cancer treatments using offset-free MPC.
   *Submitted to IFAC-PapersOnLine*
6. ***Sebeke LC**, *Castillo Gómez JD, Heijman E *et al*. Visualization of Thermal Washout due to Spatiotemporally Heterogenous Perfusion in the Application of a Model-based Control Algorithm for MR-HIFU Mediated Hyperthermia.
   *Manuscript in preparation*

## CONFERENCE ABSTRACTS

1. **Sebeke LC**, Luo X, De Jager B, Heemels, WPMH, Grüll H. Model predictive control algorithm for large-area regional hyperthermia. 5th International Symposium on Focused Ultrasound, Washington DC, USA, 2016
2. **Sebeke LC**, Luo X, De Jager B, Heemels, WPMH, Heijman E, Grüll H. Prediction-based controller for MR-HIFU mediated hyperthermia. 4th European Symposium on Focused Ultrasound, Leipzig, Germany, 2017
3. **Sebeke LC**, Luo X, De Jager B, Heijman E, Heemels, WPMH, Grüll H. Model Predictive Control of MRI-Guided HIFU for Hyperthermia. Joint Annual Meeting ISMRM-ESMRMB, Paris, France, 2017

4. **Sebeke LC**, Heijman E, Deenen DA, Maljaars E, De Jager, B, Heemels WPMH, Grüll H. Model-Based Control for Conformal Hyperthermia Using MR-HIFU. 6th International Symposium on Focused Ultrasound, Washington DC, USA, 2018

5. Heijman E, Yeo SY, **Sebeke LC**, Staruch R, Bratke G, Püsken M, Tuchscherer A, Maintz D, Grüll H. Volumetric Hyperthermia of Soft Tissue Sarcoma Using MR Guided High Intensity Focused Ultrasound: Case Report. 6th International Symposium on Focused Ultrasound, Washington DC, USA, 2018

6. Yeo SY, Castillo Gomez JD, Heijman E, Maul AC, **Sebeke LC**, Rademann P, Schröder HJ, Grüll H. MR-HIFU Ablation of Lumbar Facet Joints: Effects of Varying Acoustic Powers. 6th International Symposium on Focused Ultrasound, Washington DC, USA, 2018

7. **Sebeke LC**, Heijman E, Rademann P, Maul AC, Schubert C, Henke I, Castillo Gomez JD, Yeo SY, Grüll H. Thermal Therapy of the Porcine Pancreas in-vivo Using MR-Guided HIFU. 33rd Annual Meeting of the European Society for Hyperthermic Oncology, Warsaw, Poland, 2019

8. **Sebeke LC**, Heijman E, Rademann P, Maul AC, Schubert C, Henke I, Castillo Gomez JD, Yeo SY, Grüll H. In-vivo validation of a Model-Based Control Algorithm for MR-HIFU Hyperthermia. 33rd Annual Meeting of the European Society for Hyperthermic Oncology, Warsaw, Poland, 2019

9. **Sebeke LC**, Rademann P, Maul AC, Heijman E, Castillo Gomez JD, Yeo SY, Grüll H. In-vivo Validation of a Model-Based Control Algorithm for MR-HIFU Hyperthermia. 19th International Symposium for Therapeutic Ultrasound, Barcelona, Spain, 2019

# Curriculum Vitae

**Lukas Christian Sebeke** was born on 15.08.1989 in Hannover, Germany. After finishing Abitur in 2009 at the Otto Hahn Gymnasium in Böblingen, he studied Physics at the University of Stuttgart. In 2015 he graduated within the Department of Physics on functionalized graphene devices for spintronics applications. The project aimed to exploit the deformation of the electronic band structure of graphene for the conversion of charge- and spin currents.

From May 2015 he started a PhD project at the Eindhoven University of Technology, Eindhoven, the Netherlands, in the group of Prof. Holger Grüll. His PhD project comprised translational research on MR-guided HIFU interventions in the pancreas and MR-HIFU mediated hyperthermia. During the project, he received a student award for the 2019 joint annual meeting of the EUFUS and ISTU. Lukas currently works in the group of Prof. Holger Grüll at the University Hospital of Cologne, Cologne, Germany as a researcher.